

# **Ultra Wideband Wearable Sensors for Motion Tracking Applications**

**Manmohan Sharma**

A thesis submitted to the faculty of the University of London in partial  
fulfilment of the requirements for the degree of

Doctor of Philosophy

School of Electronic Engineering and Computer Science  
Queen Mary University of London  
London E1 4NS  
United Kingdom

September 2015

*In loving memory of my grandparents*

# Abstract

The increasing interest and advancements in wearable electronics, biomedical applications and digital signal processing techniques have led to the unceasing progress and research in novel implementations of wireless communications technology. Human motion tracking and localisation are some of the numerous promising applications that have emerged from this interest. Ultra-wideband (UWB) technology is particularly seen as a very attractive solution for microwave-based localisation due to the fine time resolution capabilities of the UWB pulses. However, to prove the viability of utilizing UWB technology for high precision localisation applications, a considerable amount of research work is still needed. The impact of the presence of the human body on localisation accuracy needs to be investigated. In addition, for guaranteeing accurate data retrieval in an impulse-radio based system, the study of pulse distortion becomes indispensable. The objective of the research work presented in this thesis is to study and carry out experimental investigations to formulate new techniques for the development of an Impulse-radio UWB sensor based localisation system for human motion tracking applications. This research work initiates a new approach for human motion tracking by making use of pulsed UWB technology which will allow the development of advanced tracking solutions with the capacity to meet the needs of professional users.

Extensive experimental studies involving several ranging and three dimensional localisation investigations have been undertaken, and the potential of achieving high precision localisation using ultra-wideband technology has been demonstrated. Making use of the upper portion of the UWB band, a novel miniature antenna designed for integration in the UWB localisation system is presented and its performance has been examined. The key findings and contributions of this research work include UWB antenna characterisation for pulse based transmission, evaluation of comprehensive antenna fidelity patterns, impact of pulse fidelity on the communication performance of a UWB radio system, along with studies regarding the effect of the human body on received pulse quality and localisation accuracy. In addition, an innovative approach of making use of antenna phase centre information for improving the localisation accuracy has been presented.

# Acknowledgement

Firstly, I want to thank the Almighty God for helping me get this far in my life against all odds. Thank you for giving me the determination, courage and wisdom to embark upon and complete this journey.

I want to express my deepest gratitude towards my supervisor Professor Clive Parini who has been exceptionally generous, friendly and supportive throughout the course of my PhD. I cannot thank him enough for giving me the opportunity to undertake this research and for all the assistance and invaluable advice he has been providing me. Without him, it would have been impossible for me to accomplish this work. Special thanks to my second supervisor Dr. Akram Alomainy for his continuous guidance and fruitful suggestions at all stages of my studies.

Most of all, I am extremely grateful to my parents, Harinder Kumar Sharma and Veena Sharma for all the sacrifices they have made for me and for teaching me the importance of education. They have always been my best friends, my heroes, my mentors, and the source of my strength. I will remain indebted to them for the unconditional support they have always given me, with all my decisions throughout life. Thanks to my sister Ruchi for her selfless cooperation at every stage of my studies. I want to thank Mr. Gopi Chand for always being a well-wisher of my family.

My earnest thanks to my dear friend Shahidul Islam for his assistance during some really difficult times of my life, when I was in need of help the most.

Many thanks to Dr. Khaleda Ali and her family for all the good wishes and blessings they bestowed upon me and especially for her friendship, support and encouragement over the years. My utmost appreciations to them for treating me like a part of their own family.

A special mention goes to my work colleagues in the Wines Section at John Lewis Partnership, Oxford Street; Lisa Wilkins, Osbert Drakes, Andy Evans, William Parker and Ben Dodwell for all their cooperation over these past few years of my PhD. I want to sincerely thank my section manager, Mrs. Annette Buttler for her exceptional

support and understanding, so that I could effectively manage my studies along with my part-time job.

I would also like to thank my colleagues and friends at Queen Mary University of London, Sabri Zaman, Amna Abdul Wahid, Deepak Singh Nagarkoti, Guangwei Jiang, Xiang Li, Dr. Melusine Pigeon, Dr. Oleksandr Sushko, Berit Greinke, Majid Naeem, Muhammad Qureshi, Nishtha Chopra, Qiao Cheng, Dr. Zhijiao Chen and many others for always being so nice and helpful towards me. I am also thankful to Dr. Massimo Candotti and Viren Joshi for their assistance with the measurements in the Antenna Lab at Queen Mary.

**Manmohan Sharma**

**London, May 2015**

# Table of Contents

<b>Abstract</b> .....	<b>3</b>
<b>Acknowledgement</b> .....	<b>4</b>
<b>Table of Contents</b> .....	<b>6</b>
<b>List of Publications</b> .....	<b>10</b>
<b>List of Figures</b> .....	<b>12</b>
<b>List of Tables</b> .....	<b>20</b>
<b>List of Abbreviations</b> .....	<b>21</b>
<b>1 Introduction</b> .....	<b>24</b>
1.1 Research Motivation .....	26
1.2 Research Objectives and Challenges .....	28
1.3 Overview of Localisation Approaches.....	30
1.3.1 Signalling Scheme.....	30
1.3.2 Position-related Parameters.....	30
1.3.3 Location Estimation Unit .....	31
1.3.4 Centralized and Distributed Localisation.....	31
1.3.5 Relative and Absolute Coordinate Localisation.....	31
1.3.6 Indoor and Outdoor Localisation .....	31
1.4 Organisation of the Thesis .....	32
References .....	34
<b>2 UWB Ranging and Position Estimation Techniques</b> .....	<b>36</b>
2.1 Measurement Categories for UWB Positioning.....	37
2.1.1 Time of Arrival.....	38
2.1.2 Time Difference of Arrival.....	39
2.1.3 Angle of Arrival .....	41
2.1.4 Received Signal Strength .....	43
2.1.5 Other Measurement Types .....	44
2.2 Position Estimation Mechanisms .....	44
2.3 Sources of Error in Time Based Ranging .....	48

2.4	UWB Signal Propagation Measurement Setup .....	51
2.4.1	Time Domain Measurement Techniques .....	51
2.4.2	Frequency Domain Measurement Techniques .....	52
2.5	IEEE 802.15.4a Standard for Ranging .....	54
2.6	Target Operational Requirements for UWB-based Sensor Nodes.....	56
2.7	Summary .....	58
	References .....	59
<b>3</b>	<b>Ultra Wideband Technology for Localisation and Motion Tracking.....</b>	<b>66</b>
3.1	UWB Technology .....	67
3.1.1	Overview .....	67
3.1.2	Advantages of UWB .....	69
3.1.3	Requirements for UWB Antennas.....	70
3.1.4	Challenges .....	72
3.2	Impulse Radio .....	73
3.3	Recent Trends in UWB based Positioning and Motion Tracking.....	74
3.4	Commercially Available UWB Localisation and Positioning Systems.....	77
3.4.1	Time Domain.....	77
3.4.2	DecaWave .....	78
3.4.3	Zebra Technologies .....	79
3.4.4	Ubisense .....	79
3.4.5	PLUS Location System .....	80
3.5	Motion Tracking Technologies .....	81
3.5.1	Optical Motion Tracking Systems.....	81
3.5.2	Mechanical Motion Tracking Systems.....	82
3.5.3	Inertial Motion Tracking Systems.....	83
3.5.4	Magnetic Motion Tracking Systems .....	84
3.6	Summary .....	85
	References .....	87
<b>4</b>	<b>Miniature Ultra Wideband Antenna Design .....</b>	<b>95</b>
4.1	Suitable Antenna Designs .....	96
4.1.1	Tapered-slot Antenna .....	96
4.1.2	Quasi Self-complementary Antenna .....	102
4.1.3	Printed Compact UWB Antenna .....	106

4.1.4	Performance Comparison of the Three Antennas .....	112
4.2	Miniaturised Design of Tapered-Slot Antenna .....	113
4.2.1	Antenna Geometry .....	113
4.2.2	Fabricated Miniature Tapered-Slot Antenna Performance .....	115
4.3	Analysis with Simplified Human Body Models .....	119
4.4	Summary .....	128
	References .....	130
<b>5</b>	<b>Fidelity Analysis of the Miniature UWB Antenna Using Different Excitation Pulses .....</b>	<b>132</b>
5.1	Measurements of the Miniature UWB Antenna System .....	133
5.1.1	Measurement Setup and System Details .....	134
5.1.2	Measurement Results and Analysis.....	135
5.2	Pulse Fidelity Analysis of the Miniature UWB Antenna.....	139
5.2.1	Use of Different Excitation Pulses for Fidelity Analysis.....	141
5.2.2	Received Pulse Waveforms.....	142
5.3	Investigation of Fidelity Patterns of Miniature UWB Antenna .....	146
5.4	UWB System Modelling and Communication Link Performance Analysis .	150
5.4.1	Impulse Radio UWB Systems.....	151
5.4.2	System-level Modelling and Performance Analysis .....	151
5.5	Summary .....	154
	References .....	156
<b>6</b>	<b>Experimental Investigation of Ranging and 3D Localisation using the Miniature UWB Antenna .....</b>	<b>159</b>
6.1	Ranging Accuracy Investigation of the Miniature UWB Antenna System ...	160
6.1.1	Measurements with Antennas in Free-space .....	161
6.1.2	Measurements with Antennas Mounted on the Human Body.....	168
6.1.3	Non-line-of-sight Range Measurements .....	175
6.2	Three Dimensional Localisation Analysis .....	176
6.2.1	Base Station Antenna Design.....	177
6.2.2	Localisation Method and Measurement Setup .....	179
6.3	3D Localisation Measurements and Results .....	183
6.3.1	Localisation of Mobile Tag Being Moved Along the $x$ -axis .....	183
6.3.2	Localisation of Mobile Tag Being Moved in the $xy$ and $xz$ planes ..	185
6.3.3	Localisation of Two Mobile Tags Simultaneously .....	187

6.3.4	Repeatability of the Localisation Measurements .....	188
6.3.5	Calibration of Localisation System to Minimise Error .....	189
6.4	Summary .....	194
	References .....	195
<b>7</b>	<b>Measurements and Experimental Analysis using the UWB Localisation System.....</b>	<b>197</b>
7.1	DecaWave Ultra Wideband Chip.....	198
7.1.1	Overview .....	198
7.1.2	Range Estimation Mechanisms .....	200
7.2	Ultra Wideband 3D Localisation System.....	205
7.2.1	Base Station and Mobile Tag PCBs .....	205
7.2.2	Measurement Setup for UWB Localisation System.....	208
7.2.3	Three Dimensional Localisation Method .....	210
7.3	Three Dimensional Localisation Experiments .....	211
7.3.1	Mobile Tag Placed in Free-space .....	211
7.3.2	Mobile Tag Placed on the Human Body .....	213
7.3.3	Hand Mounted Mobile Tag Tilted by 90° .....	214
7.3.4	Non-line-of-sight Measurements.....	216
7.4	Summary .....	218
	References .....	219
<b>8</b>	<b>Conclusions and Future Work.....</b>	<b>222</b>
8.1	Conclusions .....	222
8.2	Key Contributions .....	225
8.3	Future Work .....	226

# List of Publications

## Journal Publications

1. M. Sharma, A. Alomainy and C.G. Parini, “Fidelity Pattern Analysis of a CPW-fed Miniature UWB Antenna Using Different Excitation Pulses”, *IEEE Antennas and Wireless Propagation Letters*, Volume 14, pp. 494-498, November 2014.
2. M. Sharma, A. Alomainy and C.G. Parini, “Study of 3D Localisation of Body-worn Miniature UWB Antennas for Motion Tracking Applications”, to be submitted in the *IEEE Transactions on Antennas and Propagation*.

## Conference Publications

1. M. Sharma, C.G. Parini and A. Alomainy, “UWB Sensor Nodes for Tracking of Human Motion in Medical and Rehabilitation Applications”, accepted in 5<sup>th</sup> International Conference on Wireless Mobile Communication and Healthcare (MobiHealth), London, United Kingdom, 2015.
2. M. Sharma, C.G. Parini and A. Alomainy, “Influence of Antenna Alignment and Line-of-sight Obstruction on the Accuracy of Range Estimates between a Pair of Miniature UWB Antennas”, 9<sup>th</sup> European Conference on Antennas and Propagation (EuCAP), Lisbon, Portugal, 2015.

3. M. Sharma, C.G. Parini and A. Alomainy, "Investigative Analysis of the Influence of Different Simplified Human Body Models on a Miniature Ultra-Wideband Antenna", International Microwave Workshop Series on RF and Wireless Technologies for Biomedical and Healthcare Applications (IMWS-Bio), London, United Kingdom, 2014.
4. M. Sharma, C.G. Parini and A. Alomainy, "Experimental investigation of 3D localisation of an on-body UWB antenna using several base stations", Loughborough Antennas and Propagation Conference (LAPC), Loughborough, United Kingdom, 2014.
5. M. Sharma, C.G. Parini and A. Alomainy, "Investigation of TOA-Based Ranging Accuracy of a Miniature Ultra-Wideband Antenna for Human Motion Capture Applications", 11<sup>th</sup> International Conference on Wearable and Implantable Body Sensor Networks (BSN), Zurich, Switzerland, 2014.
6. M. Sharma, C.G. Parini and A. Alomainy, "Time domain analysis of a miniature tapered-slot UWB antenna", International Workshop on Antenna Technology: Small Antennas, Novel EM Structures and Materials, and Applications (iWAT), Sydney, Australia, 2014.
7. M. Sharma and C.G. Parini, "A miniature wideband antenna for wearable systems", Loughborough Antennas and Propagation Conference (LAPC), Loughborough, United Kingdom, 2013.

# List of Figures

Figure 1.1: Various possible applications of the ultra-wideband wireless technology [3].	..... 25
Figure 1.2: Comparison of various wireless positioning technologies [5].	..... 26
Figure 2.1: Two different approaches for position estimation: (a) direct positioning and (b) two-step positioning [10].	..... 37
Figure 2.2: In a TOA measurement, the black node determines the distance $d$ between itself and the target node (red node). The distance information defines a circle around the black node with a radius of $d$ [2].	..... 39
Figure 2.3: Position estimation based on TDOA measurements, which define a hyperbola passing through the target node (red node) with foci at the reference nodes (black nodes) [2].	..... 40
Figure 2.4: The reference node (black node) measures the AOA and determines the angle $\psi$ between itself and the target node (red node) [2].	..... 41
Figure 2.5: Signal arriving at a uniform linear array with angle $\psi$ and the relation between arrival time differences and AOA [2].	..... 42
Figure 2.6: Position estimation based on TOA or RSS measurements via trilateration. The intersection of the three circles around the reference nodes (black nodes) can be calculated to obtain the position of the target node (red node) [10].	..... 45
Figure 2.7: Position estimation based on TDOA measurements. Position of the target node (red node) can be deduced from the intersection of two hyperbolas, corresponding to two TDOA measurements [2].	..... 46
Figure 2.8: Position estimation based on AOA measurements via triangulation. The angles measured by the reference (black) nodes determine two lines, the intersection of which yields the position of the target (red) node [2].	..... 47
Figure 2.9: TOA estimation scenario in a multipath channel. The first path is considerably weaker and arrives much earlier at the receiver than the strongest component [2].	..... 49
Figure 2.10: Four different simple scenarios for channel realisations in LOS and NLOS situations. (a) The direct path is unobstructed (LOS). (b) The direct path is unobstructed, but attenuated due to antenna pattern (LOS). (c) The direct path is obstructed. The attenuation due to the obstruction makes the direct path weaker than the strongest path. The delay due to the obstruction is neglected since it is insignificant (NLOS). (d) The direct path is obstructed. The obstruction both attenuates and delays the direct path. Note that in certain cases the direct path may completely disappear (NLOS) [2].	..... 50
Figure 2.11: Schematic diagram of the time domain measurement setup for UWB channel characterisation [49].	..... 52

Figure 2.12: Schematic diagram of the frequency domain measurement setup for UWB channel characterisation [49].....	53
Figure 2.13: Flow diagram for Hermitian signal processing [3].....	53
Figure 2.14: IEEE 802.15.4a packet structure [55].....	55
Figure 3.1: UWB spectrum overlaying with other existing narrowband systems [9].....	67
Figure 3.2: An Impulse Radio UWB signal containing short pulses with a low duty cycle. Here, $T$ represents the signal duration and $Tf$ represents the pulse repetition interval or the frame interval [35]. .....	74
Figure 3.3: Potential applications of UWB technology for positioning and motion tracking..	75
Figure 3.4: Time Domain's P410 Ranging and Communications Module [57] .....	78
Figure 3.5: DecaWave's evaluation board with DW1000 chip for real time location applications [58]. .....	78
Figure 3.6: Dart UWB Real Time Location System from Zebra Technologies [59].....	79
Figure 3.7: Ubisense Series 7000 Sensors and compact tags [60].....	80
Figure 3.8: PLUS real-time location system [61]. .....	80
Figure 3.9: Measurement setup for an optical motion tracking system [64].....	82
Figure 3.10: Exoskeleton of a mechanical motion capture system [68], [69].....	83
Figure 3.11: A typical body-worn inertial motion tracking system [70]. .....	84
Figure 3.12: Measurement setup for a magnetic motion tracking system [75].....	85
Figure 4.1: Geometry of the tapered-slot antenna design. ....	96
Figure 4.2: Fabricated prototype of the tapered-slot antenna design. ....	97
Figure 4.3: Measured S11 of the tapered-slot antenna in free-space and on human body.....	97
Figure 4.4: Simulated 3D radiation patterns of the tapered-slot antenna at three different frequencies.....	98
Figure 4.5: Simulated S11 of the tapered-slot antenna for different lengths of semi-minor axis $x_2$ of the smaller ellipse.....	99
Figure 4.6: Simulated S11 of the tapered slot antenna for different lengths of semi-major axis $y_2$ of the smaller ellipse.....	100
Figure 4.7: Simulated S11 of the tapered slot antenna for different lengths of semi-minor axis $x_1$ of the bigger ellipse. ....	100

Figure 4.8: Simulated S11 of the tapered-slot antenna for different lengths of semi-major axis $y1$ of the bigger ellipse. ....	101
Figure 4.9: Geometry of the quasi self-complementary antenna design. ....	102
Figure 4.10: Fabricated prototype of the quasi self-complementary antenna design. ....	102
Figure 4.11: Measured S11 of the quasi self-complementary antenna in free-space and on human body. ....	103
Figure 4.12: Simulated 3D radiation patterns of the quasi self-complementary antenna for three different frequencies. ....	104
Figure 4.13: Simulated S11 of the quasi self-complementary antenna for different widths of the triangular notch $w$ . ....	105
Figure 4.14: Simulated S11 of the quasi self-complementary antenna for different heights of the triangular notch $h$ . ....	105
Figure 4.15: Simulated S11 of the quasi self-complementary antenna for different disc radii $r$ . ....	106
Figure 4.16: Geometry of the printed compact UWB antenna design. ....	106
Figure 4.17: Fabricated prototype of the printed compact UWB antenna design. ....	107
Figure 4.18: Measured S11 of the printed compact UWB antenna in free-space and on human body. ....	107
Figure 4.19: Simulated 3D radiation patterns of the printed compact UWB antenna for three different frequencies. ....	108
Figure 4.20: Simulated S11 of the printed compact UWB antenna for different lengths of the semi-minor axis of the bigger ellipse $x1$ . ....	109
Figure 4.21: Simulated S11 of the printed compact UWB antenna for different lengths of the semi-major axis of the bigger ellipse $y1$ . ....	109
Figure 4.22: Simulated S11 of the printed compact UWB antenna for different lengths of the semi-minor axis of the smaller ellipse $x2$ . ....	110
Figure 4.23: Simulated S11 of the printed compact UWB antenna for different lengths of the semi-major axis of the smaller ellipse $y2$ . ....	111
Figure 4.24: Simulated S11 of the printed compact UWB antenna for different widths of central patch $w$ . ....	111
Figure 4.25: Dimensions and geometry of the miniature tapered-slot UWB antenna. ....	114
Figure 4.26: Fabricated prototype of the miniature tapered-slot UWB antenna. ....	115
Figure 4.27: Measured and simulated S11 of the miniature tapered-slot UWB antenna. ....	116

Figure 4.28: On-body radiation pattern measurement setup with the miniature UWB antenna attached to test subject's body inside an anechoic chamber.....	116
Figure 4.29: Coordinate frame and antenna orientation for the radiation pattern measurements in the (a) azimuth and (b) elevation planes.....	117
Figure 4.30: Free-space and on-body radiation patterns of the miniature UWB antenna at 6, 7.5 and 9 GHz in (a) $xy$ -plane, (b) $yz$ -plane. The radiation patterns have been normalized (maximum=0 dB). ....	118
Figure 4.31: Simulated current distributions of the miniature UWB antenna at (a) 6 GHz, (b) 7.5 GHz, (c) 9 GHz and (d) 10.6 GHz.....	118
Figure 4.32: Four simplified human body models used in simulations, namely (a) flat, (b) rectangular, (c) half-cylindrical and (d) cylindrical.....	120
Figure 4.33: Simulated S11 of the antenna using the four simplified non-dispersive body models for distance $d = 1, 4,$ and $6$ mm.....	121
Figure 4.34: Simulated normalized radiation patterns of the miniature UWB antenna using four simplified non-dispersive body models at 6, 7.5 and 9 GHz in (a) $xy$ -plane ( $0^\circ$ is in $y$ -direction) and (b) $yz$ -plane ( $180^\circ$ is in $y$ -direction).....	122
Figure 4.35: Simulated S11 of the antenna using the four simplified dispersive body models for distance $d = 1, 4,$ and $6$ mm along with the on-body measurements. ....	123
Figure 4.36: Simulated normalized radiation patterns of the miniature antenna using the four simplified dispersive body models at 6, 7.5 and 9 GHz in (a) $xy$ -plane ( $0^\circ$ is in $y$ -direction) and (b) $yz$ -plane ( $180^\circ$ is in $y$ -direction).....	124
Figure 4.37: Size variation of the (a) flat and (b) half-cylindrical body models.....	125
Figure 4.38: Simulated S11 of the antenna with different sizes of the (a) flat and (b) half-cylindrical body models. ....	126
Figure 4.39: Miniature UWB antenna mounted on a test subject's wrist for on-body S11 measurements. ....	127
Figure 4.40: On-body S11 measurements of the antenna for three different separation gaps. ....	127
Figure 5.1: Measurement setup of the miniature tapered-slot UWB antenna pair.....	134
Figure 5.2: Face-to-face and side-by-side antenna orientations used in the analysis.....	134
Figure 5.3: Miniature UWB antennas mounted on the fingertips of a human test subject for on-body measurements.....	135
Figure 5.4: Measured (a) transfer function magnitude and (b) group delay for the miniature UWB antenna system in free-space.....	136
Figure 5.5: Measured (a) transfer function magnitude and (b) group delay for the miniature UWB antenna system when mounted on the fingertips.....	137

Figure 5.6: Received signal waveforms in free-space for two different antenna orientations using a sine-modulated Gaussian input. ....	138
Figure 5.7: Received signal waveforms for two different antenna orientations when mounted on fingertips, using a sine-modulated Gaussian input. ....	139
Figure 5.8: Excitation pulses used in the fidelity analysis, namely (a) First-Order, (b) Second-Order, (c) Fourth-Order and (d) Sine-modulated Gaussian. ....	142
Figure 5.9: Normalized power spectral density curves of the four different excitation pulses in frequency domain. ....	142
Figure 5.10: Received signal waveforms, namely (a) First-Order Gaussian, (b) Second-Order Gaussian, (c) Fourth-Order Gaussian and (d) Sine-modulated Gaussian for free-space fidelity measurements. ....	143
Figure 5.11: Received signal waveforms, namely (a) First-Order Gaussian, (b) Second-Order Gaussian, (c) Fourth-Order Gaussian and (d) Sine-modulated Gaussian for on-body fidelity measurements. ....	145
Figure 5.12: Experimental setup for fidelity pattern measurements inside the Anechoic Chamber. ....	147
Figure 5.13: Miniature UWB antenna position with respect to the coordinate frame used for the fidelity pattern measurements. ....	148
Figure 5.14: Fidelity patterns of the miniature UWB antenna in (a) Horizontal plane and (b) Vertical plane for free-space measurements. ....	149
Figure 5.15: Fidelity patterns of the miniature UWB antenna in (a) Horizontal plane and (b) Vertical plane for on-body measurements. ....	150
Figure 5.16: Simplified block diagram of the UWB communication system modelled to study the effect of fidelity factor on system performance. ....	152
Figure 5.17: Comparison of BER values at various angles around the antenna in the horizontal plane for free-space measurements using bi-phase modulation. ....	153
Figure 5.18: Comparison of BER values at various angles around the antenna in the horizontal plane for on-body measurements using bi-phase modulation. ....	154
Figure 6.1: Measurement setup for free-space ranging experiment with the two antennas aligned face-to-face and side-by-side to each other. ....	162
Figure 6.2: Absolute error values in range estimation for two different antenna orientations at varying separation distance $d$ between the antennas in free-space. ....	163
Figure 6.3: Probability density distribution of the ranging error obtained when the antennas were placed in free-space. ....	163
Figure 6.4: Coordinate frame used to represent rotation of the miniature UWB antenna in various directions. ....	164

Figure 6.5: Miniature UWB antenna tilted sideways by varying angles. It is to be noted that the tilt angles towards left side are represented by a negative sign. ....	165
Figure 6.6: Miniature UWB antenna tilted forwards and backwards by varying angles. It is to be noted that the tilt angles towards antenna's back side are represented by a negative sign.....	165
Figure 6.7: Absolute error values in range estimation for varying tilt angles of the transmitter antenna for side-by-side orientation. ....	166
Figure 6.8: Absolute error values in range estimation for varying tilt angles of the transmitter antenna for face-to-face orientation.....	167
Figure 6.9: Measurement setup with the receiver antenna attached to a test subject's body and the transmitter antenna in free-space. ....	169
Figure 6.10: Absolute error values in range estimation with one antenna attached to a test subject's body and another antenna in free-space. ....	169
Figure 6.11: Probability density distribution of the ranging error obtained when one antenna was attached to a human test subject's body. ....	170
Figure 6.12: Experimental setup for on-body ranging measurements with the two antennas and different bend-angles of the elbow. ....	171
Figure 6.13: Absolute error values in range estimation with both the antennas mounted on-body for different bend angles of the elbow. ....	172
Figure 6.14: Measurement setup for on-body ranging measurements with the two antennas mounted on a human test subject's arm and the forearm bent by different angles in the vertical plane. ....	173
Figure 6.15: Absolute error values in range estimation for on-body measurements, with the forearm tilted by different angles in the vertical plane.....	174
Figure 6.16: Different types of materials: wood, cardboard, human hand and plastic, used as obstruction between the antenna pair for non-line-of-sight ranging analysis....	175
Figure 6.17: Absolute error values for non-line-of-sight ranging measurements of UWB antenna pair using different materials as obstructions.....	176
Figure 6.18: The Vivaldi antenna (a) geometry and its (b) fabricated prototype.....	177
Figure 6.19: Measured and simulated S11 of the Vivaldi antenna in free-space.....	178
Figure 6.20: Coordinate frame used for the radiation pattern measurements of the Vivaldi antenna.....	178
Figure 6.21: Normalized radiation patterns of the Vivaldi antenna at 6, 7.5 and 9 GHz in (a) $xy$ -plane ( $0^\circ$ is in $x$ -direction) and (b) $yz$ -plane ( $0^\circ$ is in $y$ -direction). ....	179
Figure 6.22: The coordinate system for three dimensional localisation of the unknown coordinates of point $P$ .....	180

Figure 6.23: L-shaped configuration of the base stations (BSs) for 3D localisation of the mobile station (MS).....	181
Figure 6.24: 3D localisation experimental setup with the finger-mounted mobile station (MS) and the three base stations (BS1 - 3). Miniature antenna mounted on the finger is shown in the inset. ....	182
Figure 6.25: Three dimensional plots of the estimated and actual positions of the mobile station for (a) 10 cm increments and (b) 3 cm increments. ....	184
Figure 6.26: Three dimensional plots of the estimated and actual positions of the mobile station being moved in the $xy$ plane.....	185
Figure 6.27: Three dimensional plots of the estimated and actual positions of the mobile station being moved in the $xz$ plane. ....	186
Figure 6.28: Three dimensional plots of the estimated and actual positions of two mobile stations fixed on thumb and index finger, being localised simultaneously. ....	187
Figure 6.29: Deviation in the estimated locations of the MS from the localisation measurements done on two different occasions. ....	188
Figure 6.30: Simulated phase centres of the (a) miniature UWB antenna and the (b) Vivaldi antenna at 8.3 GHz frequency. ....	190
Figure 6.31: Three dimensional plots of the actual positions of the mobile station along with its calibrated estimated positions, with the MS being moved along $x$ -axis, for (a) 10 cm increments and (b) 3 cm increments.....	191
Figure 6.32: Three dimensional plots of the actual positions of the mobile station along with its calibrated estimated positions, with the MS being moved in the $xy$ plane. .	192
Figure 6.33: Three dimensional plots of the actual positions of the mobile station along with its calibrated estimated positions, with the MS being moved in the $xz$ plane...	192
Figure 6.34: Three dimensional plots of the actual positions of thumb and finger mounted mobile stations, along with the calibrated estimated positions.....	193
Figure 7.1: DecaWave's DW1000 location and communication chip [12], [13].....	199
Figure 7.2: Range calculation mechanism of the DecaWave chip using the two-way ranging algorithm [11].....	201
Figure 7.3: Cramer-Rao Lower Bounds on the ranging error in terms of SNR for four different frequency bandwidths.....	204
Figure 7.4: Fabricated prototype of the base station sensor node along with the Vivaldi antenna.....	206
Figure 7.5: DecaWave's EVB1000 evaluation board connected to the miniature UWB antenna.....	207

Figure 7.6: Block diagram of the prototype ultra-wideband localisation system (shows just two base stations for clarity).....	207
Figure 7.7: Base station receivers aligned in a Y-shaped configuration along with the mobile station positions. ....	208
Figure 7.8: Measurement setup of the UWB localisation system placed on top of a table. The 5-by-5 matrix used to place the mobile station is shown in the inset. ....	209
Figure 7.9: Measurement setup for 3D localisation of the mobile station kept in free-space. ....	212
Figure 7.10: Localisation measurements with the mobile tag fixed on the hand of a real human test subject. ....	213
Figure 7.11: Localisation measurements with the hand-mounted mobile tag tilted by 90° ...	215
Figure 7.12: Localisation measurements setup with a human hand kept 10 cm away from one base station receiver, blocking its direct line-of-sight communication with the mobile station. ....	216

# List of Tables

Table 4.1: Size and performance comparison of the three preliminary UWB antenna designs. .....	112
Table 4.2: Electrical properties of human body tissues at 8.3 GHz frequency.....	121
Table 5.1: Calculated Fidelity Factor values for the four different excitation pulses.....	146
Table 6.1: Average and standard deviation of error values obtained for ranging experiments with the transmitter antenna tilted in the vertical plane. ....	168
Table 6.2: Average error in estimating the $x$ , $y$ and $z$ coordinates of the MS for various localisation experiments.....	189
Table 7.1: Average error in estimating the $x$ , $y$ and $z$ coordinates of the mobile tag in free-space for each row of the matrix locations. ....	212
Table 7.2: Average error in estimating the $x$ , $y$ and $z$ coordinates of the hand mounted mobile tag for each row of the matrix locations.....	214
Table 7.3: Average error in estimating the $x$ , $y$ and $z$ coordinates of the hand-mounted mobile tag when tilted by $90^\circ$ for each row of the matrix locations. ....	215
Table 7.4: Average error in estimating the $x$ , $y$ and $z$ coordinates of the hand-mounted mobile tag for non-line-of-sight measurements. ....	217

# List of Abbreviations

ADS	Advanced Design System
AOA	Angle Of Arrival
AWGN	Additive White Gaussian Noise
BER	Bit Error Rate
BPM	Bi-Phase Modulation
BS	Base Station
CDMA	Code Division Multiple-Access
CMOS	Complementary Metal-Oxide Semiconductor
CPW	Co-Planar Waveguide
CRE	Coarse Range Estimation
CRLB	Cramer-Rao Lower Bound
CSS	Chirp Spread Spectrum
CST	Computer Simulation Technology
dB	Decibels
dBm	Decibels relative to 1mW
DC	Direct Current
$E_b/N_0$	Energy per bit to noise power spectral density
FCC	Federal Communications Commission
IC	Integrated Circuit
IEEE	Institute of Electrical and Electronics Engineers
IFFT	Inverse Fast Fourier Transform
IR-UWB	Impulse Radio Ultra Wideband
ISM	Industrial, Scientific and Medical

LCD	Liquid Crystal Display
LOS	Line-Of-Sight
MB-OFDM	Multiband Orthogonal Frequency Division Multiplexing
MC-UWB	Multicarrier Ultra Wideband
MPC	Multipath Component
MS	Mobile Station
NLOS	Non Line-Of-Sight
OFDM	Orthogonal Frequency Division Multiplexing
PAM	Pulse Amplitude Modulation
PC	Personal Computer
PCB	Printed Circuit Board
PHR	Physical Layer Header
PLUS	Precision Location Ultra Wideband System
PNA	Programmable Network Analyser
PPM	Pulse Position Modulation
PSD	Power Spectral Density
PSM	Pulse Shape Modulation
RF	Radio Frequency
RMS	Root Mean Square
RSS	Received Signal Strength
RX	Receiver
SDP	Synchronization Distribution Panel
SFD	Start of Frame Delimiter
SHR	Synchronization Header
SMA	Sub miniature Version A
SMP	Sub miniature Push-on

SNR	Signal-to-Noise Ratio
SPI	Serial Peripheral Interface
TDOA	Time Difference Of Arrival
TOA	Time Of Arrival
TOF	Time Of Flight
TW-TOF	Two Way Time-Of-Flight
TX	Transmitter
USB	Universal Serial Bus
UWB	Ultra Wideband
VNA	Vector Network Analyser
WBAN	Wireless Body Area Network
WLAN	Wireless Local Area Network
WPAN	Wireless Personal Area Network
WSN	Wireless Sensor Network

# Introduction

Wireless communication technology has significantly changed our lives over the past many years and has considerably transformed and contributed to several aspects of human development. Due to its increasing reliability and convenience, wireless technology has seen a phenomenal growth in its usage all over the world. In countless homes and offices, the cordless telephones provide us the freedom from the limited reach of handset cables. Mobile phones give us even more freedom such that we can communicate with others at any time and in any place. Wireless local area network (WLAN) technology provides us access to the internet without the trouble to deal with hideous and expensive cables.

Cellular networks, satellite communication, WLANs and wireless sensor networks (WSNs) are only a few of the wireless technologies that we use on a daily basis. These make the everyday life easier by keeping us connected anywhere, anytime [1]. This rapid development in wireless communication technology, along with continuous miniaturisation of sensors, is leading to a new generation of wearable gadgets. Microwave-based localisation and motion tracking is one such thing that has emerged as a prospective application from the advancements in wireless technology.

In 2002, the United States Federal Communications Commission (FCC) adopted the First Report and Order that validated the commercial operation of UWB technology [2]. This has allowed the unlicensed use of UWB devices subject to some emission constraints. Since then, UWB has been considered as an excellent wireless technology that could provide the high data rate transmission required by the latest and future wireless and portable devices. Some prospective applications of the UWB technology have been depicted through Figure 1.1.

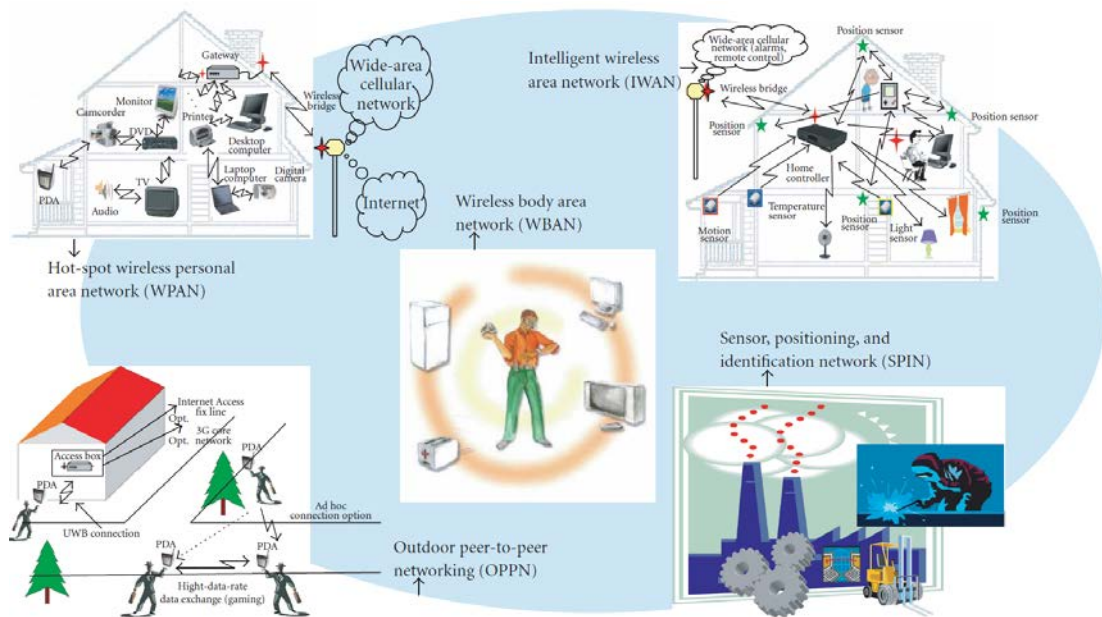


Figure 1.1: Various possible applications of the ultra-wideband wireless technology [3].

One of the most promising aspects of UWB radios are their potential for high-precision localisation. The use of ultra-short duration pulse waveforms enable Impulse Radio UWB (IR-UWB) receivers to resolve individual multipath components and hence accurately estimate the arrival time of the first signal path transmitted from another UWB transmitter. This implies that the distance between a wireless transmitter and receiver can be precisely determined, delivering high localisation accuracy [1]. Time of Arrival and Time Difference of Arrival based ranging approaches can be utilized to take advantage of the fine time resolution capabilities of the UWB pulses for obtaining accurate range estimates. The low-cost circuitry and the low power consumption potential of UWB are well suited for systems such as WSNs

and wireless personal area networks (WPANs). All these features make UWB an ideal technology for localisation and ranging purposes. The IEEE also acknowledged this potential of UWB technology for future wireless communication networks and adopted UWB in the IEEE 802.15.4a WPAN standard for the creation of a specific physical layer to enable precise wireless ranging. UWB based positioning systems are also of particular interest for human motion tracking applications as such a kind of system does not require any external infrastructure [4].

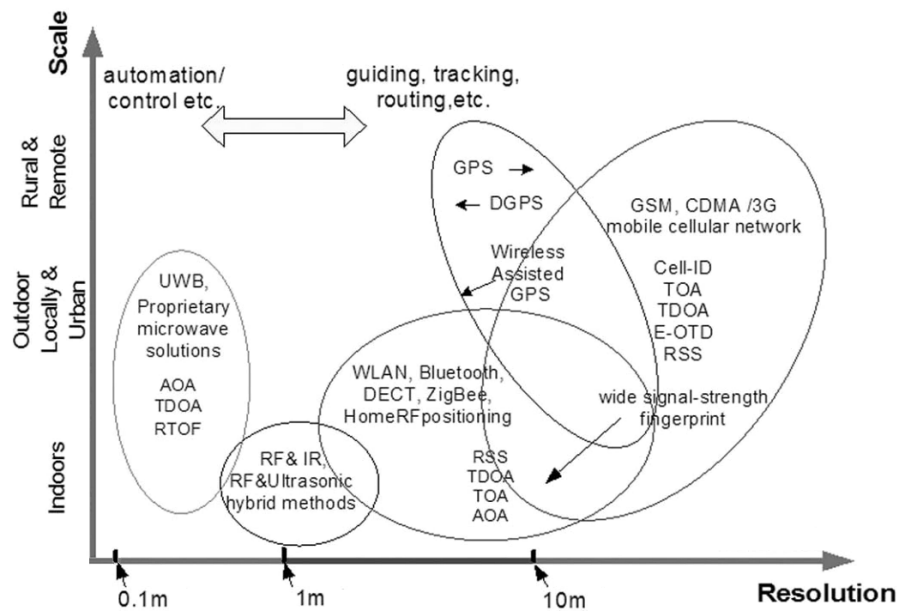


Figure 1.2: Comparison of various wireless positioning technologies [5].

## 1.1 Research Motivation

Motion tracking is studied in several fields including sports and athletic training, medical care and rehabilitation, animation, human-computer interaction, robotics etc. [6]–[10]. For rehabilitation or injury prevention, motion tracking solutions could allow continuous and accurate monitoring of physical activities, supplying the data concerning important movement parameters in order to evaluate exercise effectiveness, provide feedback or diagnose disordered movement. The monitoring of athletes in sports such as football (knee), golf (spine), tennis (shoulder), rugby (knee) etc. could provide detailed information to enhance athletic performance and reduce the risk of injury [11].

Presently, there are several motion tracking schemes available in the market, such as based on mechanical, acoustic, magnetic, optical and inertial technologies. Optical systems such as *Vicon MX* and *Codasport* have been the main focus in the development of traditional motion tracking systems since they can provide high spatial precision and high update rates. However, these systems suffer from some fundamental limitations like restricted tracking volume due to the coverage of available cameras, occlusion, high sensitivity to lighting conditions that restricts most optical systems being used in an indoor studio environment only, and demanding requirement on equipment and infrastructure. All these factors result in the motion tracking systems that are very expensive and not easy to use. Also, there are some inertial motion tracking techniques available nowadays that can provide tracking solutions without the requirement of external infrastructure. But, such systems use a wired network of sensors and provide limited accuracy when used to monitor complex movements.

Most current research on RF wireless motion tracking systems has used inertial tracking techniques using accelerometers and gyroscopes attached to joints of the subject's body as these can provide a tracking solution without the requirement for external infrastructure. However, the measurement accuracy of current inertial sensors suffers from accumulated drifts caused by accelerometer bias error and non-linearity in accelerometer sensitivity [12]. No existing system has been demonstrated to be capable of tracking multiple nodes in a low latency networked environment as required for full body motion tracking [13]. The conventional microwave sensing device has not been exploited much in motion tracking due to its high cost and large size. However, with the development in UWB technology, emerging applications of UWB are foreseen for precise ranging and localisation in sensor networks as well. UWB signalling is especially suitable in this context because it allows centimetre accuracy in ranging, and low-power and low-cost implementation of communication systems [14]. Its wideband characteristics together with miniaturized hardware make UWB a promising candidate for wireless body area communications. Additionally, UWB signals do not cause significant interference to other systems operating in the vicinity and do not pose a threat to users' safety. UWB has emerged as a technology which offers great advantages for high speed digital wireless networks. The UWB sensors can be used to detect tiny movement inside the human body such as the heart

rate, blood pressure and respiration and the viability of using the same transceiver for both radar sensing and IR-UWB communications has been proven in [15].

Improvements in IR-UWB based positioning techniques could potentially generate unprecedented commercial opportunities for various industrial sectors and make motion tracking solutions much more affordable and accessible to a wider range of users. Though IR-UWB based localisation and motion tracking may find usage in an extensive array of applications in different areas, substantial amount of research and study is still required to demonstrate the feasibility of using IR-UWB technology for high precision 3D positioning. Moreover, the presence of human body and its effect on the level of localisation accuracy needs to be studied extensively as the complex electromagnetic properties of human tissues can significantly affect the characteristics of radio waves. In addition, use of impulse radio technique involves transmission of very narrow pulses. The successful reception of such pulses requires minimal distortion of the pulse shape by the antenna system. This makes the study of fidelity factor of a pulse waveform extremely important to ensure accurate retrieval of the sent data. From an impulse-radio system viewpoint, very limited work is available in the open literature regarding the impact of fidelity on the communication performance of a UWB system. Hence, before the idea could be deployed for professional applications, the actual system performance evaluation needs to be undertaken based on measured experimental results.

## **1.2 Research Objectives and Challenges**

The aim of the research work presented in this thesis is to investigate and carry out experimental analysis to formulate new techniques and methods for the development of an IR-UWB sensor based localisation system for human motion tracking applications, exhibiting high accuracy and ease of use, but still low cost. This will allow the development of advanced motion tracking solutions with the calibre of those being used in sports, healthcare and industrial applications. This research will initiate a new approach for motion tracking by making use of microwave sensors based on IR-UWB technology. The key idea is to replace optical markers with electromagnetic markers deploying UWB nano-pulses.

The fundamental challenge that will have to be tackled in this project by means of novel research is the need for a high precision wireless wearable system that gives minimal disturbance to its user, to prevent any performance degradation and chances of physical injury. The system will need to be portable and easy to use, with simple and uncomplicated techniques for quick deployment. Such a three-dimensional UWB positioning system will be required to be fully operational regardless of the environment in which it is being used, either indoors or outdoors, rather than demanding an artificial “studio” environment. There will be a demand for measurements with good repeatability and high accuracy, particularly for reliably interpreting rapid motion. Some other challenges involved in realising an accurate and compact UWB positioning system include identification and mitigation of non-line-of-sight scenarios, along with designing and integration of suitable miniature antennas having the required electromagnetic characteristics.

This work investigates a totally novel concept of an intelligent UWB body-worn sensor network. UWB is also suitable in the context of wearable electronics due to the potential advantages it offers, such as low cost, high data rate, low power and low-complexity implementation. The human body is an integral part of any wearable system or a network that operates in close proximity to the body. Hence, it is very important to study the effect of human body on UWB localisation and the accuracy achieved while localising the sensors present on different parts of the body. The main objectives of this research work are as follows:

- To design a novel miniature antenna with compact size, ultra-wideband characteristics and decent on-body and off-body performance, suitable for wearable applications.
- To characterize the designed UWB antenna’s overall performance for pulse-based transmission. For this, pulse distortion, antenna fidelity etc. need to be analysed since data may be contained in the shape or precise timing of the pulse. This involves analysing the effect of the antenna and the propagation channel on the received pulse quality.
- To study the effect of different excitation pulses and the vicinity of human body on the level of distortion experienced by the received pulse, to ensure optimal performance of the system. Since UWB antennas tend to radiate

different signals in different spatial directions when fed with an impulse, the spatial properties of the radiated signal also need to be explored.

- To investigate the impact of pulse fidelity on the communication performance of an impulse-based ultra wideband system, in order to analyse how accurately the sent data could be retrieved from the received pulse.
- To undertake different static as well as pseudo-dynamic ranging and three-dimensional localisation experiments, and study the influence of antenna orientation and the presence of human body on the localisation accuracy.
- Development of a prototype ultra-wideband positioning system as a technology demonstrator for highlighting the feasibility and potential of IR-UWB technology in precision localisation.

### **1.3 Overview of Localisation Approaches**

This section discusses some of the main categories of various approaches for localisation [1] which have been presented in the literature.

#### **1.3.1 Signalling Scheme**

The type of signalling scheme which a localisation technology uses is one of the key classifications. A commonly used signalling scheme for localisation applications is through *Radio Frequency* (RF) signals since they can cover long distances and also penetrate through obstacles. Several RF technologies like ultra-wideband (UWB), code division multiple-access (CDMA), and orthogonal frequency division multiplexing (OFDM) could be utilized for localisation depending on the specific requirements of accuracy and range. Some other signalling schemes include use of *Infrared* signals, *Optical* signals as well as *Ultrasound* waves. A major disadvantage of these three signalling schemes is their limited operation in non-line-of-sight (NLOS) scenarios.

#### **1.3.2 Position-related Parameters**

Different position-related parameters extracted from the received signals could be employed for localisation purposes. These include parameters such as the *received*

*signal strength (RSS), time of arrival (TOA), time difference of arrival (TDOA) and angle of arrival (AOA)*. Moreover, a number of *hybrid* techniques are also possible by using a combination of these parameters. All these different approaches are discussed in detail in Chapter 2.

### **1.3.3 Location Estimation Unit**

Depending on where the localisation is carried out, localisation technologies can be classified as *handset-based* or *network-based* systems. In handset-based localisation, the target node estimates its own position through the signals it receives from the reference nodes. This is also known as self-positioning. In network-based localisation, the reference nodes forward the information acquired from the received signal (such as TOA, AOA etc.) to a central processing unit, where the location of the target is estimated.

### **1.3.4 Centralized and Distributed Localisation**

Another classification for the localisation systems is the *Centralized* or *Distributed* localisation. In centralized localisation systems, position-related information like the TOA, AOA etc. is sent to a data fusion centre, where position of the target is estimated. For a distributed localisation system, the nodes jointly resolve their position by communicating with each other.

### **1.3.5 Relative and Absolute Coordinate Localisation**

Localisation technologies can also be classified depending upon the kind of coordinate scheme they utilize for position estimation. *Absolute* localisation provides the actual physical coordinates of a target with respect to a global reference. Alternatively, in *relative* localisation the position of a target is estimated with respect to a local reference within the network.

### **1.3.6 Indoor and Outdoor Localisation**

In addition, localisation systems are also commonly classified as *indoor* and *outdoor* systems, since there are substantial differences in the propagation characteristics of the environments in which they are used.

## 1.4 Organisation of the Thesis

Following this introductory chapter, the rest of the thesis is organised as follows:

**Chapter 2** highlights some prospective measurement techniques that can be utilized for ranging purposes, including the various position estimation mechanisms and their underlying principles. It also gives an insight of the IEEE 802.15.4a standard for range estimation and common sources of error in time-based ranging, as well as a discussion on the tentative operational requirements of a UWB sensor node.

**Chapter 3** exhibits the fundamental concepts and principles of the ultra-wideband technology and the advantages as well as challenges involved when working with UWB. Latest developments that have been taking place in the area of UWB-based positioning are discussed briefly. In addition, the operating principles and limitations of various other technologies that are being used for motion tracking purposes are highlighted.

**Chapter 4** presents a novel miniature ultra-wideband antenna that has been designed to be used for the sensor node. The performance and characteristics of this antenna have been analysed in detail. Besides, a study of the influence of various simplified human body models and real human body on the operation of the miniature UWB antenna is also provided.

**Chapter 5** investigates the miniature UWB antenna from a system perspective. The fidelity factor analysis of the antenna is presented, by making use of different kinds of excitation pulses. The fidelity analysis of the antenna has been carried out both in the azimuth and elevation planes, thereby creating comprehensive antenna fidelity patterns. Both free-space and on-body scenarios have been studied. The effect of antenna fidelity on the communication performance of a UWB antenna system has been assessed based on the bit error rate and signal-to-noise ratio parameters.

**Chapter 6** provides a detailed analysis involving several ranging experiments in different measurement scenarios. The accuracy with which the point-to-point distance between a transmitter-receiver pair of the miniature UWB antennas could be estimated has been studied. An experimental investigation of the three dimensional localisation of the body mounted miniature UWB antenna is presented. The results of

various localisation experiments using the body-worn miniature ultra-wideband antennas as transmitters and off-body Vivaldi antennas in the vicinity as receivers are provided. The geometry and performance of the ultra-wideband Vivaldi antenna designed as part of this study is also given.

**Chapter 7** discusses the experimental and investigational work carried out towards the development of a prototype ultra-wideband localisation system. The specifications and operating principles of the commercially available DW1000 IR-UWB chip from DecaWave are highlighted, and a development system is used to gain practical experience of three-dimensional localisation. Results of various 3D localisation measurements carried out using the developed prototype system are presented, demonstrating the feasibility and potential of IR-UWB technology for precise location of body mounted mobile tags.

**Chapter 8** presents a summary to the research work that has been presented in this thesis along with the main contributions and findings. It also provides details about the prospective future research activities that can be undertaken.

## References

- [1] Z. Sahinoglu, S. Gezici, and I. Guvenc, *Ultra-Wideband Positioning Systems: Theoretical Limits, Ranging Algorithms, and Protocols*. Cambridge University Press, 2008.
- [2] *FCC First Report and Order, Revision of Part 15 of the commission's rules regarding ultra-wideband transmission systems*. Washington D.C., 2003, ET-Docket 98-153.
- [3] M.-G. Di Benedetto, T. Kaiser, A. F. Molisch, I. Oppermann, C. Politano, and D. Porcino, Eds., *UWB Communication Systems: A Comprehensive Overview*. Hindawi Publishing Corporation, 2006.
- [4] Z. W. Mekonnen and A. Wittneben, "Localization via Taylor series approximation for UWB based human motion tracking," in *8th Workshop on Positioning, Navigation and Communication*, 2011, pp. 77-82.
- [5] H. Liu, H. Darabi, P. Banerjee, and J. Liu, "Survey of Wireless Indoor Positioning Techniques and Systems," *IEEE Trans. Syst. Man Cybern. Part C Applications Rev.*, vol. 37, no. 6, pp. 1067-1080, Nov. 2007.
- [6] Z. Chaczko, A. Kale, and C. Chiu, "Intelligent health care — A Motion Analysis system for health practitioners," in *Sixth International Conference on Intelligent Sensors, Sensor Networks and Information Processing*, 2010, pp. 303-308.
- [7] J. Li and Y. Ya, "Animation system of virtual human using motion capture devices," in *IEEE International Conference on Computer Science and Automation Engineering*, 2011, vol. 3, pp. 544-547.
- [8] K. F. Li, K. Takano, and M. G. Johnson, "Motion Tracking and Processing for Multimedia Sport E-Learning," in *International Conference on Broadband and Wireless Computing, Communication and Applications*, 2011, pp. 75-82.
- [9] O. Mirabella, A. Rauceo, F. Fisichella, and L. Gentile, "A motion capture system for sport training and rehabilitation," in *4th International Conference on Human System Interactions (HSI)*, 2011, pp. 52-59.

- [10] J. Rosell, R. Suarez, A. Perez, and C. Rosales, "Including virtual constraints in motion planning for anthropomorphic hands," in *IEEE International Symposium on Assembly and Manufacturing (ISAM)*, 2011, pp. 1–6.
- [11] K. Herman, C. Barton, P. Malliaras, and D. Morrissey, "The effectiveness of neuromuscular warm-up strategies, that require no additional equipment, for preventing lower limb injuries during sports participation: a systematic review.," *BMC Med.*, vol. 10, no. 1, p. 75, Jan. 2012.
- [12] D. Roetenberg, "Inertial and Magnetic Sensing of Human Motion," PhD Thesis, Twente University, 2006.
- [13] A. D. Young, "Wireless realtime motion tracking system using localised orientation estimation," PhD Thesis, University of Edinburgh, 2010.
- [14] L. Taponecco, A. A. D'Amico, and U. Mengali, "Joint TOA and AOA Estimation for UWB Localization Applications," *IEEE Trans. Wirel. Commun.*, vol. 10, no. 7, pp. 2207–2217, Jul. 2011.
- [15] C. G. Bilich, "Bio-Medical Sensing using Ultra Wideband Communications and Radar Technology: A Feasibility Study," in *Pervasive Health Conference and Workshops*, 2006, pp. 1–9.

# UWB Ranging and Position Estimation Techniques

Wireless technology is used extensively in our everyday lives. It can be utilized for localisation and tracking applications too. Positioning based on the use of radio signals has a long history. UWB technology is especially suited for this purpose because of its very large bandwidth which provides a fine accuracy in ranging [1]. For estimating the position of a target node in a wireless network, signals are exchanged between the target node and a number of reference nodes. Generally, a single parameter is estimated for each received signal, such as the arrival time of the signal. However, it is also possible to estimate multiple signal parameters [2]. Several different position estimation techniques under different scenarios are available for various purposes. Methods such as time of arrival, angle of arrival, signal strength etc. can all be employed for the purpose of position estimation [3]. Each of these techniques has its own drawbacks and plus points. A number of studies are available in the literature that provide a comparison of the different measurement techniques for positioning applications [4]–[8]. Depending upon individual requirements such as accuracy, design complexity etc., any of these techniques can be employed.

In this chapter, different kinds of measurement techniques that can be utilized for ranging purposes will be presented. The main principles and characteristics including the underlying position estimation mechanisms for each measurement type are outlined. Some of the potential error sources that may degrade the accuracy of the range estimation in a simplistic environment are discussed. Moreover, the ranging aspect of the recent IEEE 802.15.4a UWB standard is studied in detail and the two main approaches employed for the measurement of UWB signal propagation are also provided.

## 2.1 Measurement Categories for UWB Positioning

Position estimation could be described as the mechanism for estimating the position of a node, called the target node, in a wireless network by exchanging signals between the target node and a number of reference nodes in the vicinity [9]. Two types of techniques could be utilized for position estimation, depending upon whether the position is estimated from the signals travelling between the nodes directly or not, as shown in Figure 2.1 [10]. Using the direct positioning technique, position estimation could be achieved directly from the signals traveling between the nodes [2]. Alternatively, in a two-step positioning approach, certain signal parameters are first extracted from the exchanged signals and then position estimation is done based on those signal parameters.

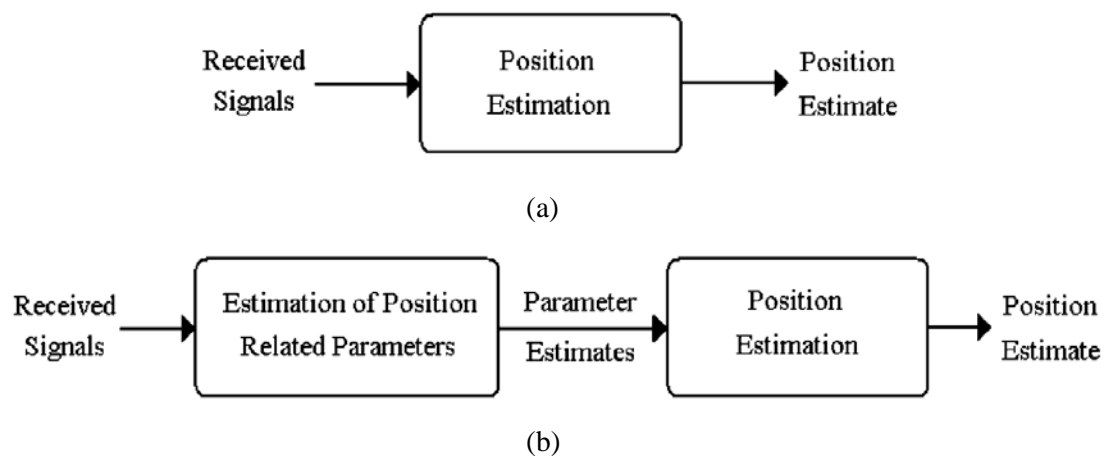


Figure 2.1: Two different approaches for position estimation: (a) direct positioning and (b) two-step positioning [10].

Even though the two-step positioning techniques are not optimal in general, their algorithm complexity is considerably lower as compared to the direct technique. Moreover, the performance of the two methods is typically quite similar for very high signal bandwidths or signal-to-noise ratios (SNR) [10]. Hence, the two-step approach is the most popular technique adopted by positioning systems, which is also the main focus of the investigations presented in this thesis.

Measurement of a set of signal parameters is the first step to estimate the position of a target node using the two-step technique. The signal parameters could be associated with the energy, timing, and/or direction of the signals propagating between the target node and the reference nodes. Different signal parameters could be utilized, depending upon the accuracy requirements and system constraints [9]. Generally, a single parameter is estimated for each signal between the target node and a reference node, such as the arrival time of the signal. However, it is also possible to estimate multiple position related parameters in order to enhance positioning accuracy [2]. Some of the common measurement categories that can be used to extract these signal parameters are discussed in the following sub-sections.

### **2.1.1 Time of Arrival**

Time of arrival (TOA) measurements estimate the time-of-flight of a signal that travels from one node to the other, thus providing information about the distance between two nodes. Hence, an uncertainty region in the shape of a circle is obtained from TOA measurement at a node, as shown in Figure 2.2. For avoiding ambiguity in the TOA estimates, the two nodes need to have a common clock or should exchange timing information via certain protocols, such as a two-way ranging protocol (discussed in detail in Chapter 7). The conventional TOA estimation technique involves use of matched filtering or correlation operations [2] [11]. Let the received signal at a node be expressed as

$$r(t) = \alpha s(t - \tau) + n(t), \quad (2.1)$$

where  $\tau$  represents the TOA,  $\alpha$  is the channel coefficient, and  $n(t)$  is additive white Gaussian noise (AWGN). A conventional correlator based scheme searches for the peak of the correlation of  $r(t)$  with a shifted version of the template signal,  $s(t - \hat{\tau})$ ,

for various delays  $\hat{\tau}$  and calculates the delay corresponding to the correlation peak [10]; that is

$$\hat{\tau}_{TOA} = \arg \max_{\hat{\tau}} \int r(t) s(t - \hat{\tau}) dt, \quad (2.2)$$

Similarly, a matched filter scheme, in which the filter is matched to the transmitted signal, estimates the instant at which the filter output attains its largest value, which results in equation (2.2) as well. Both the correlator and matched filter techniques are optimal for single-path AWGN channels.

The accuracy of a TOA measurement could be improved by increasing the SNR and/or the effective bandwidth of the signal. As UWB signals have very large bandwidth, this characteristic helps in obtaining highly accurate distance estimation using TOA measurements with the help of UWB radios [2], [10]. TOA-based techniques have been studied extensively in the literature [12]–[16]. In [17], Almazrouei *et al.* investigated the performance of the TOA method for ranging in indoor channels. Enyang *et al.* investigated the problem of source localisation in wireless sensor networks based on the received signal TOA measurements [18].

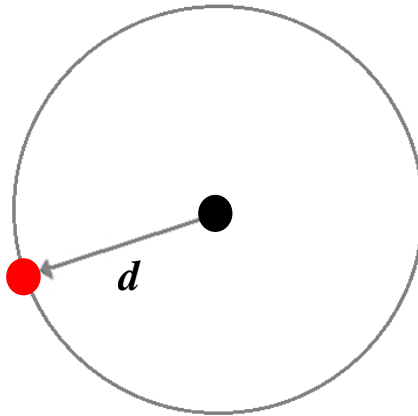


Figure 2.2: In a TOA measurement, the black node determines the distance  $d$  between itself and the target node (red node). The distance information defines a circle around the black node with a radius of  $d$  [2].

### 2.1.2 Time Difference of Arrival

In time difference of arrival (TDOA) measurements, the difference between the arrival times of two signals travelling between the target node and the two reference nodes is estimated. This locates the target node on a hyperbola, with foci at the two

reference nodes, as shown in Figure 2.3. A considerable number of works have explored the TDOA approach for a wide range of positioning applications [19]–[24]. Usually, TOA-based range measurements need synchronization among the target node and the reference nodes. However, TDOA measurements can be obtained even in the absence of synchronization between the target node and the reference nodes, if there is synchronization among the reference nodes [2], [10].

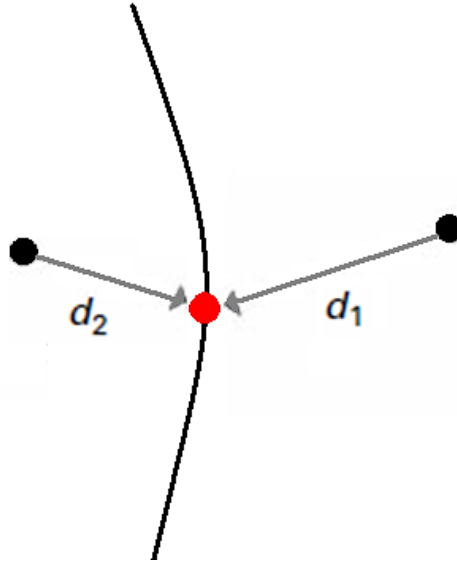


Figure 2.3: Position estimation based on TDOA measurements, which define a hyperbola passing through the target node (red node) with foci at the reference nodes (black nodes) [2].

One technique for obtaining a TDOA measurement is to first estimate TOA at each reference node and then calculate the difference between the two estimates. If the received signals are given by  $r_1(t)$  and  $r_2(t)$  as in equation (2.1), then  $\tau_1$  is estimated from  $r_1(t)$  and  $\tau_2$  is estimated from  $r_2(t)$ . The TOA estimates at the reference nodes also include a timing offset in addition to the time-of-flight because there is no synchronization between the target node and the reference nodes. Since the reference nodes are synchronized, the timing offset is the same for each TOA estimate. This timing offset gets cancelled out when subtracting two TOA measurements [2], [25]. Therefore, the TDOA measurement can be obtained as

$$\hat{\tau}_{TDOA} = \hat{\tau}_1 - \hat{\tau}_2, \quad (2.3)$$

where  $\hat{\tau}_1$  and  $\hat{\tau}_2$  denote the TOA estimates at the first and second nodes, respectively. Another way to obtain a TDOA measurement is to perform cross-correlations of the

received signals  $r_1(t)$  and  $r_2(t)$ , and to calculate the delay corresponding to the largest cross-correlation value. The cross-correlation function can be expressed as

$$\varphi_{1,2}(\tau) = \frac{1}{T} \int_0^T r_1(t) r_2(t + \tau) dt, \quad (2.4)$$

where  $T$  is the observation interval, and the TDOA estimate is given by

$$\hat{\tau}_{TDOA} = \arg \max_{\tau} |\varphi_{1,2}(\tau)| \quad (2.5)$$

Although the cross-correlation based TDOA estimation in equation (2.5) works well for single-path channels, its performance can degrade significantly over multipath channels.

### 2.1.3 Angle of Arrival

Angle of arrival (AOA) measurements provide information regarding the direction of an incoming signal, which stipulates the angle between the two nodes. AOA measurement given an uncertainty region in the shape of a line, as illustrated in Figure 2.4.

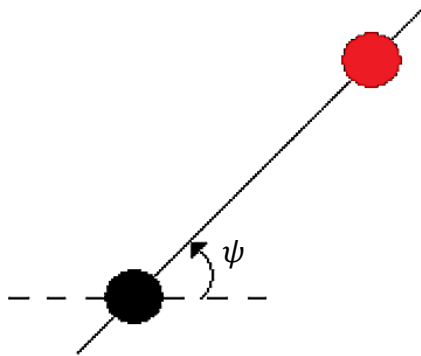


Figure 2.4: The reference node (black node) measures the AOA and determines the angle  $\psi$  between itself and the target node (red node) [2].

To estimate the AOA of the signal arriving at a node, several antennas in the form of an antenna array are generally utilized at that node. The principle behind using an antenna array for AOA estimation is that by measuring the differences in arrival times of an incoming signal at different antenna elements, the angle information for a known array geometry can be obtained. For example, a uniform linear array (ULA) is

considered as shown in Figure 2.5. It is assumed that the distance between the transmitting and receiving nodes are sufficiently large and hence the incoming signal can be modelled as a planar wave-front. The incoming signal arrives at consecutive array elements with time difference of  $(l \sin \psi)/c$  seconds, where  $l$  is the inter-element spacing,  $\psi$  is the AOA and  $c$  is the speed of light. Thus, estimation of the time differences of arrivals provides the angle information [2], [10].

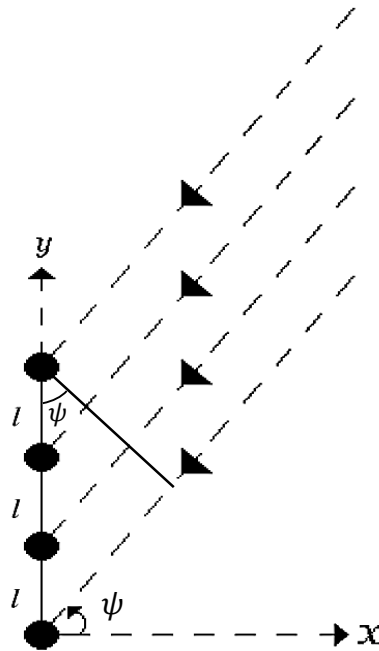


Figure 2.5: Signal arriving at a uniform linear array with angle  $\psi$  and the relation between arrival time differences and AOA [2].

The AOA technique requires multiple antenna elements, which could potentially lead to increased sensor device cost, size and complexity [11]. Moreover, the measurement of angles could be difficult in a multipath environment. The absence of line of sight or increasing distance between the transmitting and receiving nodes will also lead to an increase in the location error and give poor system performance [1] [26]. Many studies presented in the literature have employed AOA techniques for localisation [27]–[30]. The accuracy of AOA estimation increases as the SNR, effective bandwidth, number of antenna elements and/or inter-element spacing are increased. Also, the accuracy of an AOA estimate increases linearly with the effective bandwidth, which implies that UWB signals can provide high-precision AOA estimates [10].

#### 2.1.4 Received Signal Strength

Received signal strength (RSS) measurements provide information about the distance between two nodes based on certain channel characteristics. The operating principle behind this technique is that if the relation between distance and signal energy loss is known, the RSS measurement at a node can be used to estimate the distance between that node and the transmitting node, assuming that the transmitted signal's energy is known [2]. Several methods have been proposed to estimate the position of a target node based on RSS measurements [31]–[33]. RSS is one of the simplest ways of range estimation. The signal from a transmitter gradually falls off in strength as it moves further away from the transmitter [26]. Path loss is one such parameter that affects the signal energy in relation to distance. It refers to the reduction of signal power/energy as it propagates through space. Hence, by measuring the RSS, it is possible to estimate the range to a target node [34]. A common model for path loss is given by [10]:

$$\bar{P}(d) = P_0 - 10n \log_{10}(d/d_0), \quad (2.6)$$

where  $n$  is the path loss exponent,  $\bar{P}(d)$  is the average received power (dB) at a distance  $d$ , and  $P_0$  is the received power (dB) at reference distance  $d_0$ . Even though there is a simple relation between average signal power and distance, the exact relation between distance and signal energy in a practical environment is quite complex because of propagation mechanisms like reflection, scattering and diffraction. These can lead to substantial variations in RSS even for short distances and small time intervals. For acquiring a reliable range estimate, signal power is commonly obtained as

$$P(d) = \frac{1}{T} \int_0^T |r(t, d)|^2 dt \quad (2.7)$$

where  $r(t, d)$  is the received signal at distance  $d$  and  $T$  is the integration interval. The averaging process in equation (2.7) can diminish the short-term fluctuations called small scale fading. Despite this, the average received power (or RSS) still varies about its local mean due to shadowing effects, which represent signal energy variations due to the obstacles in the environment. Shadowing is commonly modelled by a zero-

mean Gaussian random variable in the logarithmic scale. Thus, the received power  $P(d)$  in decibels can be modelled with a log-normal random variable, expressed as

$$10 \log_{10} P(d) \sim \mathcal{N}(\bar{P}(d), \sigma_{\text{sh}}^2) \quad (2.8)$$

where  $\sigma_{\text{sh}}^2$  is the variance of a Gaussian random variable  $\mathcal{N}$ .

RSS measurements are relatively inexpensive and simple to implement in hardware, but are notoriously unpredictable [11]. Generally, the RSS scheme is unable to provide very accurate range estimates because of its heavy dependence on the channel parameters, which is also the case for UWB systems [10]. Also, the accuracy of RSS measurements declines with the increasing distance between the transmitter and receiver nodes [26].

### 2.1.5 Other Measurement Types

It is also possible that a node estimates a combination of position-related parameters instead of performing a single measurement such as RSS or TOA. Such hybrid schemes can provide more accurate information about the position of the target node than the schemes that estimate a single position parameter [2]. Various combinations of measurements, such as TOA/AOA [35]–[38], TOA/TDOA [39], [40], TOA/RSS [41]–[43] etc. have been presented and studied extensively in literature. The selection of these hybrid schemes depends upon the accuracy requirements and complexity constraints on the system.

## 2.2 Position Estimation Mechanisms

Once a set of position-related parameters have been extracted from the received signals by one of the techniques described in the previous section, the next step is to use the acquired parameters to estimate the position of the target node. Position estimation schemes can be divided into groups such as geometric, statistical, fingerprinting techniques etc. [2].

A geometric positioning technique solves for the position of the target node as the intersection of position lines obtained from a set of measurements at a number of

reference nodes. This technique employs a deterministic approach and computes the target node's position based on estimated angles or distances using simple geometric and algebraic relationships. The statistical techniques provide a theoretical framework for position estimation in the presence of multiple position-related parameter estimates and try to evaluate the most likely position of the target node. Fingerprinting techniques make use of a database, which contains previously estimated signal parameters at known positions, for estimating the position of the target node [10]. Systems utilizing parameters like TOA, TDOA and RSS are mostly based on geometric positioning techniques. The data fusion mechanism combines measurements from different reference nodes to estimate the location of target node.

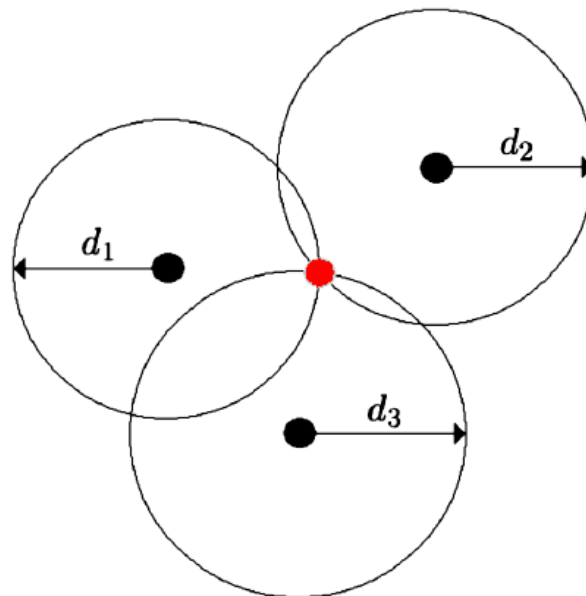


Figure 2.6: Position estimation based on TOA or RSS measurements via trilateration. The intersection of the three circles around the reference nodes (black nodes) can be calculated to obtain the position of the target node (red node) [10].

A range measurement (obtained from either a TOA or RSS measurement) determines a position line for the target's location as a circle around the reference node. Then, the intersection of three position lines, obtained from three TOA or RSS measurements, can be used to solve for the position of the target as shown in Figure 2.6. Determination of the target position from a set of range measurements is called trilateration. Let  $d_1$ ,  $d_2$  and  $d_3$  represent the range measurements obtained from three TOA measurements. Then, the following three equations must be solved jointly in order to estimate the position of the target via trilateration [2]:

$$d_i = \sqrt{(x_i - x)^2 + (y_i - y)^2}, \quad i = 1, 2, 3, \quad (2.9)$$

where  $(x_i, y_i)$  is the known position of the  $i^{\text{th}}$  reference node, and  $(x, y)$  is the position of the target node. The position  $(x, y)$  can be solved from equation (2.9) as

$$x = \frac{(y_2 - y_1)\gamma_1 + (y_2 - y_3)\gamma_2}{2[(x_2 - x_3)(y_2 - y_1) + (x_1 - x_2)(y_2 - y_3)]}, \quad (2.10)$$

$$y = \frac{(x_2 - x_1)\gamma_1 + (x_2 - x_3)\gamma_2}{2[(x_2 - x_1)(y_2 - y_3) + (x_2 - x_3)(y_1 - y_2)]}, \quad (2.11)$$

where

$$\gamma_1 = x_2^2 - x_3^2 + y_2^2 - y_3^2 + d_3^2 - d_2^2, \quad (2.12)$$

$$\gamma_2 = x_1^2 - x_2^2 + y_1^2 - y_2^2 + d_2^2 - d_1^2, \quad (2.13)$$

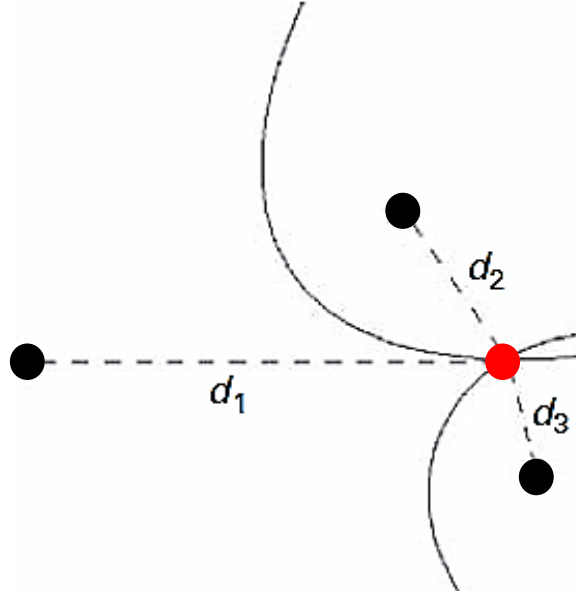


Figure 2.7: Position estimation based on TDOA measurements. Position of the target node (red node) can be deduced from the intersection of two hyperbolas, corresponding to two TDOA measurements [2].

For TDOA-based positioning, each TDOA parameter defines a hyperbola for the position of the target node. Hence, in the presence of three reference nodes, two

TDOA measurements can be obtained with respect to one of the reference nodes. Then, the intersection of two hyperbolas, corresponding to two TDOA measurements, determines the position of the target node. For three reference nodes, two range differences (obtained from TDOA measurements) can be expressed as follows [2]:

$$d_{i1} \triangleq d_i - d_1 = \sqrt{(x - x_i)^2 + (y - y_i)^2} - \sqrt{(x - x_1)^2 + (y - y_1)^2}, \quad (2.14)$$

for  $i = 2$  and  $3$ , which define two hyperbolas as shown in Figure 2.7.

The position of the target node can be obtained from the two equations in (2.14) and from the relation  $d_1 = \sqrt{(x - x_1)^2 + (y - y_1)^2}$ . Note that there are three unknowns in this case,  $x$ ,  $y$  and  $d_1$ . The equations in (2.14) can be expressed as two linear relations in terms of these three unknowns:

$$\begin{bmatrix} x_1 - x_2 & y_1 - y_2 \\ x_1 - x_3 & y_1 - y_3 \end{bmatrix} \begin{bmatrix} x - x_1 \\ y - y_1 \end{bmatrix} = d_1 \begin{bmatrix} d_{21} \\ d_{31} \end{bmatrix} + \frac{1}{2} \begin{bmatrix} d_{21}^2 & \tilde{d}_{21}^2 \\ d_{31}^2 & \tilde{d}_{31}^2 \end{bmatrix}, \quad (2.15)$$

where  $\tilde{d}_{i1}^2 = (x_i - x_1)^2 + (y_i - y_1)^2$ , for  $i = 2$  and  $3$ .

Combination of (2.15) and  $d_1 = \sqrt{(x - x_1)^2 + (y - y_1)^2}$  yields a quadratic equation for  $d_1$ . Under geometric regularity conditions, a unique value of  $d_1$  can be determined and the position of the target node,  $(x, y)$  can be obtained.

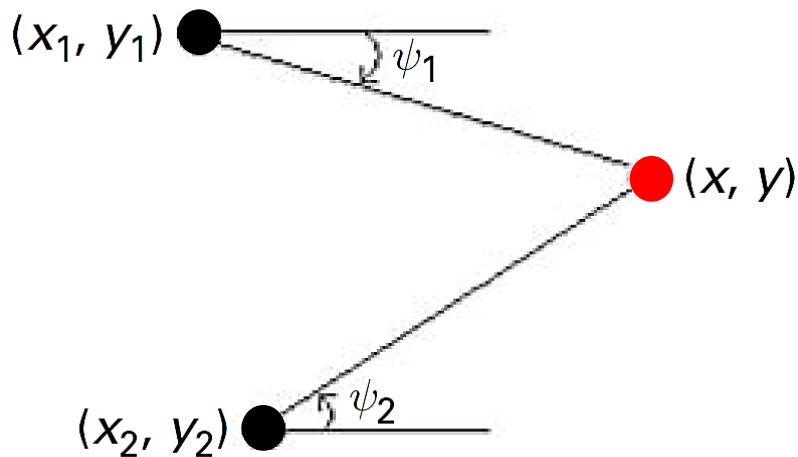


Figure 2.8: Position estimation based on AOA measurements via triangulation. The angles measured by the reference (black) nodes determine two lines, the intersection of which yields the position of the target (red) node [2].

Angle of arrival (AOA) estimates can be obtained at the reference node using an antenna array. The direction of arrival of the target node signal can be calculated by measuring the phase difference between the antenna array elements. For AOA measurements, two reference nodes (antenna arrays) are sufficient to determine the position of the target node by intersecting two lines, which is called triangulation. The number of reference nodes needed for the location process is less than that of the TOA and TDOA methods. Another advantage of AOA location methods is that they do not require reference node or target node clock synchronization [25].

As depicted in Figure 2.8, each measured AOA gives us an uncertainty in the shape of a line; so, we can estimate the target node's position as the intersection of these two lines. Let  $\psi_1$  and  $\psi_2$  denote the angles measured by reference node 1 and 2, respectively. Then, the following two equations are solved for the position of the target

$$\tan \psi_i = \frac{y - y_i}{x - x_i}, \quad i = 1, 2, \quad (2.16)$$

Solving these two equations jointly yields [2]

$$x = \frac{x_2 \tan \psi_2 - x_1 \tan \psi_1 + y_1 - y_2}{\tan \psi_2 - \tan \psi_1}, \quad (2.17)$$

$$y = \frac{(x_2 - x_1) \tan \psi_2 \tan \psi_1 + y_1 \tan \psi_2 - y_2 \tan \psi_1}{\tan \psi_2 - \tan \psi_1}, \quad (2.18)$$

### 2.3 Sources of Error in Time Based Ranging

There are various sources of error that can drastically affect the accuracy of the range estimations. Multipath propagation introduces challenges for UWB ranging due to a large number of multipath components and relatively long excess delays compared to the transmitted pulse duration. In the absence of multipath propagation, estimation of the arrival time of a signal is relatively easy; the cross-correlation of the received signal with a local template is obtained and the TOA is given by the correlation peak.

[2], [44]. In a multipath environment, a transmitted signal reaches the receiver via multiple signal paths. Reflections from scatterers in the environment arrive at the receiver as replicas of the transmitted signal with various attenuation levels and delays. The maximum excess delay of the received multipath signal can be on the order of a hundred nanoseconds, and the strongest multipath component may arrive much later than the first path (See Figure 2.9). In such a scenario, instead of finding the highest peak of the cross-correlation, in the multipath channel, the receiver must find the first-arriving peak. Thus, first path detection algorithms [45]–[47] have to be employed here to estimate the TOA accurately.

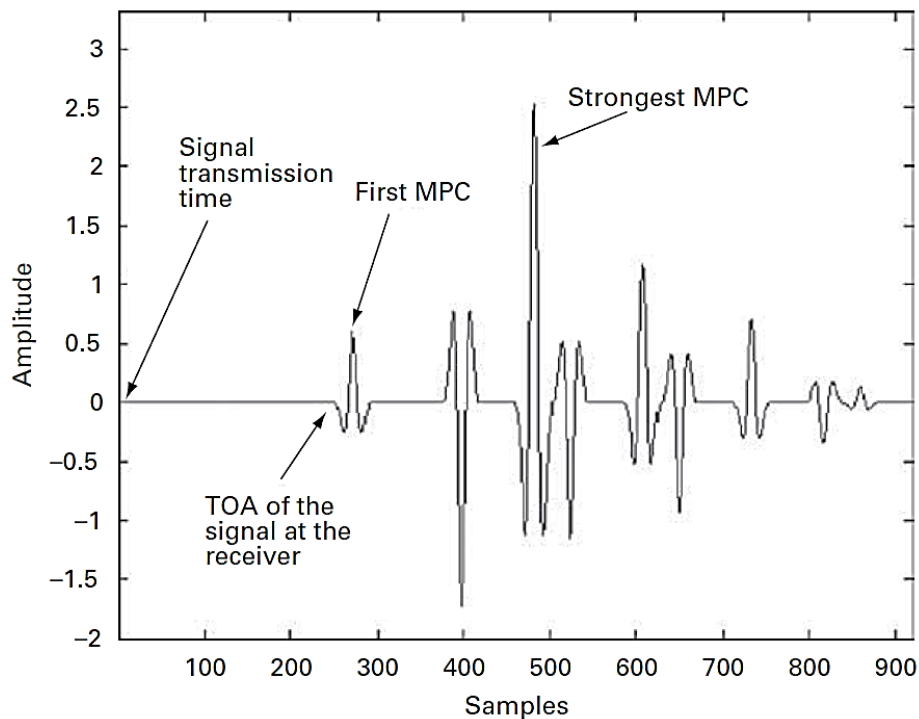


Figure 2.9: TOA estimation scenario in a multipath channel. The first path is considerably weaker and arrives much earlier at the receiver than the strongest component [2].

The first path component could be significantly weaker than the strongest multipath component at the receiver for a typical UWB channel. This problem has been illustrated in Figure 2.9, where the first path component arrives at the receiver several nanoseconds before the strongest component. Figure 2.10 demonstrates many simple situations in which the first path could be weaker than the later paths because of the characteristics of the antenna or due to non-line-of-sight (NLOS) signal propagation. When there is an obstructing medium between the direct path of a transmitter and a

receiver, the first arriving multipath component (MPC) can be attenuated more than some other MPCs. Thus, first-path detection techniques will be required to mitigate the effects of NLOS propagation.

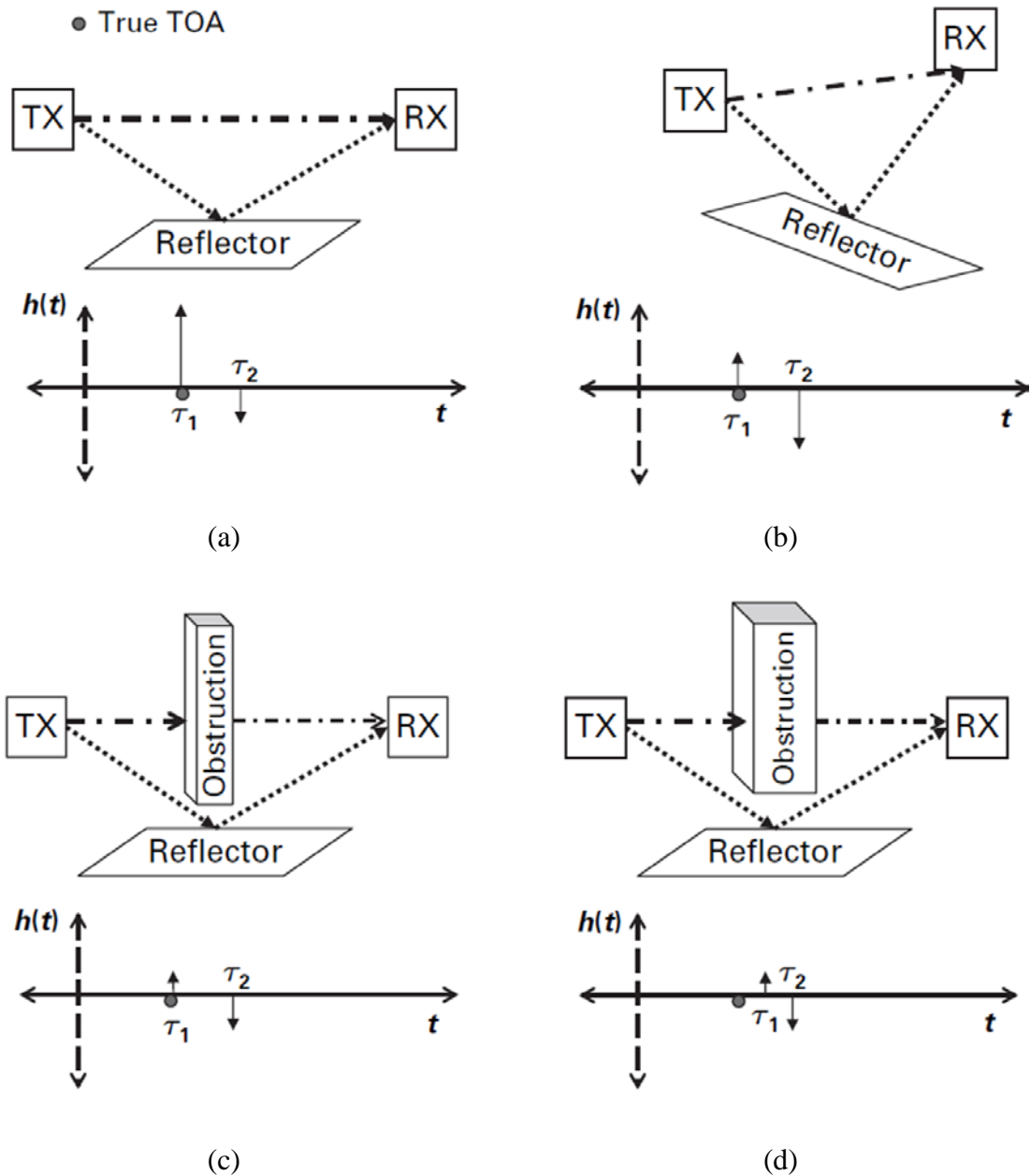


Figure 2.10: Four different simple scenarios for channel realisations in LOS and NLOS situations. (a) The direct path is unobstructed (LOS). (b) The direct path is unobstructed, but attenuated due to antenna pattern (LOS). (c) The direct path is obstructed. The attenuation due to the obstruction makes the direct path weaker than the strongest path. The delay due to the obstruction is neglected since it is insignificant (NLOS). (d) The direct path is obstructed. The obstruction both attenuates and delays the direct path. Note that in certain cases the direct path may completely disappear (NLOS) [2].

Timing inaccuracies between reference devices in infrastructure-based ranging and clock drifting between transmitter and receiver nodes in the round-trip TOA measurements lead to further errors in range estimation. UWB receivers are more susceptible to the effects of timing jitter and clock drifting because of their large signal bandwidths [48]. The clocks in the transmitting and receiving nodes also need to be stable in relation to each other for the duration of time period over which the ranging measurements are carried out [26].

In order to realise low-cost and low-power system implementation, it is always essential that ranging is done with lower sampling rates. This is particularly necessary for the case of UWB signals as sampling them at or above the Nyquist rate proves to be rather expensive. Sampling UWB signals below the Nyquist rate leads to additional error and reduces the accuracy of UWB ranging systems. The received signal needs to be sampled at or above the Nyquist rate to reconstruct the signal from its samples accurately. In UWB systems, this may increase the cost and complexity of the receiver.

## **2.4 UWB Signal Propagation Measurement Setup**

Measurement of UWB signal propagation can be carried out using a variety of methods that may be broadly divided into two categories: time domain and frequency domain techniques. Both these measurement techniques are discussed in this section.

### **2.4.1 Time Domain Measurement Techniques**

Time domain techniques can be used as a direct way to characterize UWB communication channels. Ideally, the impulse response provides complete characterisation of a device or a system over the entire frequency band of use. However, it is not possible to directly measure the true impulse response of a device or a system since that requires the availability of an ideal dirac-delta excitation signal. In practice, very short duration pulses are used for the time domain characterisation of UWB channels. The shorter the duration of the pulses used, the wider the bandwidth for which the UWB propagation characteristics can be measured.

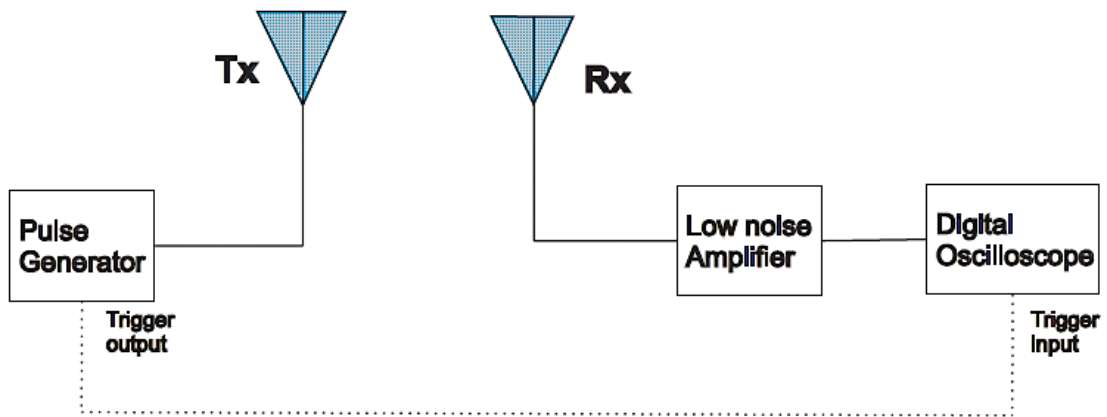


Figure 2.11: Schematic diagram of the time domain measurement setup for UWB channel characterisation [49].

The basic idea of time domain measurements is to excite one end of the UWB channel with a periodic train of very short duration pulses separated by a sufficiently long quiet period so that all multipath components are received at the other end during the quiet period (prior to the next occurrence of the pulse). On the receiving side, the signal is detected using a wideband detector (e.g., a digital sampling oscilloscope in a lab demo) [50]. A typical time domain measurement setup for UWB channel characterisation has been shown in Figure 2.11. The pulse generator represents the UWB signal source. The receiving antenna and the digital oscilloscope constitute the receiver. To enhance the received signal power, a low-noise amplifier may be used right at the output port of the receiving antenna.

#### 2.4.2 Frequency Domain Measurement Techniques

Channel measurements can also be performed using a vector network analyser (VNA) in the frequency domain (See Figure 2.12). Measurement antennas are connected to the ports of the analyser and a sweep of discrete frequency tones, which include the S-parameters of the wireless channel, is taken by the analyser. The  $S_{21}$  response measures the transmission from one antenna to the other and it also represents the channel frequency response ( $H(\omega)$ ), which includes the effect of the two antennas and of the radio channel [51].

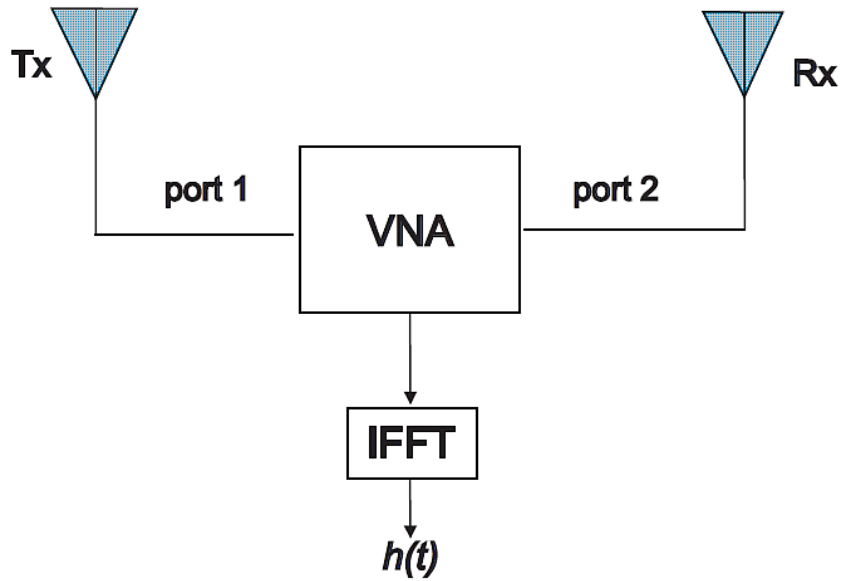


Figure 2.12: Schematic diagram of the frequency domain measurement setup for UWB channel characterisation [49].

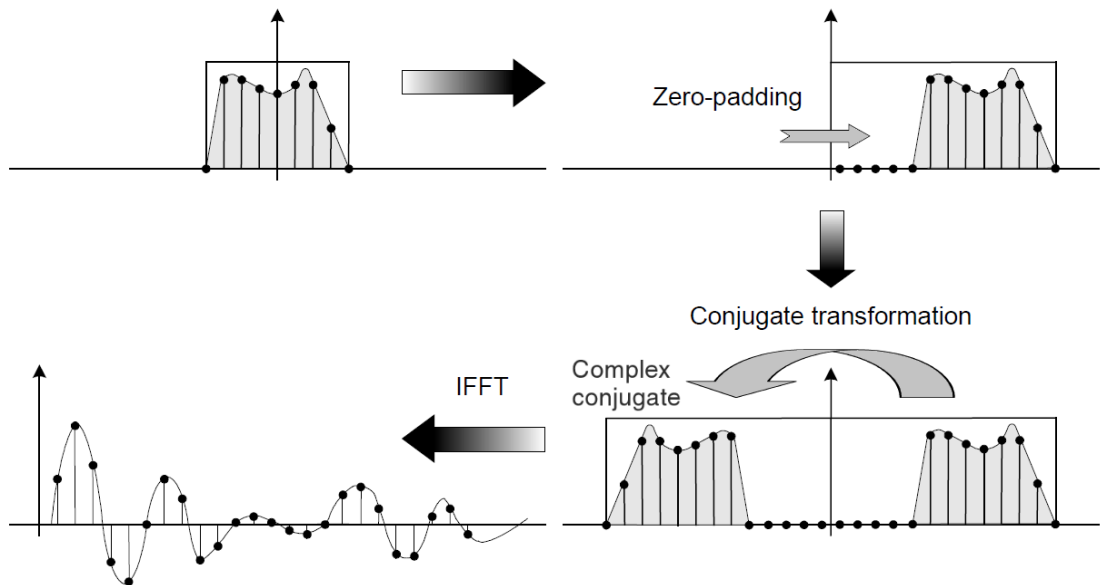


Figure 2.13: Flow diagram for Hermitian signal processing [3].

Analysing both the magnitude and phase of  $S_{21}$  enables a transition of the frequency domain information to the time domain. The Hermitian processing [3] is used for the data conversion, as illustrated in Figure 2.13. Firstly, the pass-band signal is obtained with zero-padding from the lowest frequency down to DC (direct current). Next, the conjugate of the signal is taken and reflected in the negative frequency axis. The

resulting double-sided spectrum corresponds to a real signal, i.e. the system impulse response. It is then transformed to the time domain using inverse fast fourier transform (IFFT) [52].

The chief advantage of the frequency domain technique over the time domain method is the availability of a much larger dynamic range, resulting in improved measurement precision [50]. One of the disadvantages of the frequency domain method is the restriction applied on measurement area freedom, since both the transmitter and receiver antennas are connected to the same VNA. However, such problems can be avoided by the use of ultra-low loss long cables and applying advance calibration techniques.

## **2.5 IEEE 802.15.4a Standard for Ranging**

The IEEE 802.15.4a is the first international standard that provides a specific physical layer to enable precise wireless ranging, extended range, and enhanced robustness and mobility. IEEE 802.15.4a added two additional physical layers to the original IEEE 802.15.4 standard. In 2011, the 802.15.4a was incorporated into the main body of the IEEE 802.15.4 standard and was denoted as IEEE 802.15.4-2011 [53]. The world's first IEEE 802.15.4a UWB wireless packet was transmitted and successfully coherently received in real time in March 2009 [54].

The IEEE 802.15.4a specifies two signalling formats; one based on impulse radio ultra-wideband (IR-UWB) signals and another based on chirp spread spectrum (CSS) signals. The IR-UWB systems can use frequencies of 3 - 5 GHz, 6 - 10 GHz and less than 1 GHz, whereas CSS uses the 2.45 GHz ISM band [55] [56]. In this standard, the IR-UWB has the optional capability of precise ranging. CSS, on the other hand can only be used for data communication [34]. An IR-UWB system employs very narrow pulses to transmit information, which is usually conveyed by the positions and/or polarities of the pulses [2]. In contrast to the conventional IR-UWB, the IEEE 802.15.4a standard conveys the information through the positions and polarities of pulse bursts. The signalling structure in the payload field of an IEEE 802.15.4a packet is a modified version of the classical IR-UWB signal. However, for the

synchronization preamble of the packet, UWB pulses with a low duty cycle are transmitted, similar to a classical IR-UWB system [54], [55].

In a highly scattered environment, multiple copies of the transmitted signal arrive at the receiver, with different time delays and various levels of attenuation. In this case, matched filtering or correlation-based time of arrival techniques would return multiple peaks. But for precision ranging, the time of only the first peak is required. The first peak may not be the strongest if the direct line-of-sight between the transmitter and receiver nodes gets obstructed or multiple reflections from scatterers in the environment get superimposed [57], [58]. For making the detection of the first path easier, the packet preamble in IEEE 802.15.4a is designed with multipath channels in consideration.

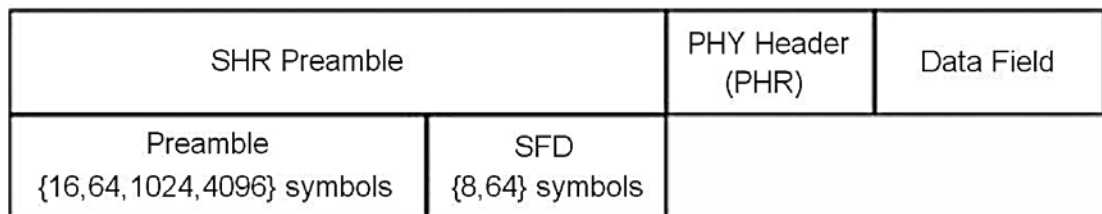


Figure 2.14: IEEE 802.15.4a packet structure [55].

The IEEE 802.15.4a packet consists of a synchronization header (SHR) preamble, a physical layer header (PHR) and a data field. The format of the IEEE 802.15.4a packet has been illustrated in Figure 2.14. Any device compliant to the IEEE 802.15.4a standard will use this packet format. The SHR preamble is composed of a ranging preamble and the start of frame delimiter (SFD). The ranging preamble is used for acquisition, channel sounding and leading-edge detection. The length of the ranging preamble can be 16, 64, 1024 or 4096 symbols and needs to be specified according to requirements of the application. A larger packet size helps low quality receivers in improving their SNRs. On the other hand, a smaller packet size reduces the channel occupancy, which helps in improving the system's energy efficiency.

The SFD helps a receiver to synchronize to the beginning of the data portion of a frame. It can consist of 8 or 64 symbols. Only after establishing acquisition during the preamble, the receiver knows that it is receiving the preamble of a packet. However, it

does not know when to expect the end of the preamble yet. It is the SFD that flags the end of the preamble and the beginning of the PHR.

A single ranging operation is started by the Initiator sending a poll message addressed to the Responder and notes the send time. The Initiator then listens for the response message. When the Responder receives the poll, it notes the receive time and sends a response message back to the Initiator. The Initiator then receives the response message and sends a final message with embedded transmit and receive timestamps for the poll, response and the final message itself. In ranging protocols, the arrival time of the signal and the process time between arrival and sending back an acknowledgement packet need to be measured accurately. The SFD is the trigger that starts and stops counting of time, which is necessary for a precise timing [34]. The PHR comes after the SHR and contains data rate and frame length information. Finally, the data field is the part that carries the communication data [2], [59]. In Chapter 7, the ranging and localisation capabilities of an IR-UWB IEEE 802.15.4a based single-chip implementation from DecaWave using 900 MHz bandwidth pulses at 6.5 GHz frequency is investigated.

## **2.6 Target Operational Requirements for UWB-based Sensor Nodes**

Attempting to overcome the limitations and technological difficulties associated with the prevailing motion tracking approaches, this thesis presents the research work and experimental investigations undertaken in a bid to devise new techniques and methods for the development of an ultra-wideband (UWB) electromagnetic sensor-based body motion tracking system. The conventional microwave sensing device has not been exploited much in motion tracking due to its high cost and large size. However, with the advancement in UWB technology, emerging applications of UWB are foreseen for precise ranging and localisation in sensor networks as well. Such a system has the potential of being adept in tracking sporting movements due to the high precision localisation and data rate transmission capabilities of UWB signals.

The UWB sensor nodes of the proposed motion tracking system will be using the upper part of the UWB frequency spectrum from 6 GHz to 10.6 GHz. The reason for selecting this frequency range is that this part of the UWB band has been less used

and hence is not very crowded. Moreover, operation at higher frequency would help to realise the need for compact antennas and hence compact sensor nodes with low cost. Also, this frequency range selected would provide us the required broad spectrum, necessary to ensure high accuracy [60] as well as deliver high data-rates to handle the intensive data traffic generated when using several sensor nodes simultaneously. It is desirable from the system that accurate ranging is achieved at feasible sampling rates to facilitate low-cost and low-power designs. Low power consumption curtails the need to replace batteries, as well as offering the use of physically smaller batteries, and thus helps in reducing system size and operational costs. This is particularly important for UWB signals since sampling them at very high rates is not practical as it demands large processing power.

The sensors are required to have a high spatial resolution so that small movements could be detected with ease. The accuracy and precision requirements for three dimensional localisation and tracking applications are highly dependent on the application characteristics. When dealing with tracking of the human motion, the required accuracy is in the order of millimetres [61], [62]. Discussions with colleagues from the Human Performance Lab at Queen Mary University of London and the Shadow Robot Company have revealed that a minimum precision of 10 mm is necessary in order to accurately track the motion of the human limbs, whereas if the target is to track the fingers of a human hand, an accuracy of 1 mm or better is required [63], [64]. Hence, the targeted localisation accuracy in the context of the UWB motion tracking system application is 10 mm.

UWB technology is especially suitable in this context because the ultra-short duration of the UWB waveforms gives the potential ability to achieve high-precision ranging and localisation in communication systems. In order to accurately capture the fast movements, especially in sports applications, the system would require high update rates. Since the UWB sensor nodes will be mounted on the human body, it is important that they are of a physical size which is consistent with the wearable applications. A compact and light-weight sensor node will ensure that it gives minimal disturbance to the users and also doesn't restrict their movement. The tentative target for the dimensions of the node is 30 mm × 30 mm × 15 mm, with a weight less than 30 grams.

Fast and easy deployability is another crucial requirement from a motion tracking system. The target setup time for the UWB motion tracking system will be around 10 to 15 minutes. The use of the compact wearable UWB markers as on-body tags and relative simplicity of UWB technology as compared to other prevalent techniques will help in meeting the objective of quick deployment. Use of Velcro straps could be one of the potential methods for attaching the sensor nodes to the body. Velcro straps have a sturdy grip and could be fastened and unfastened very conveniently to everyday clothing.

## **2.7 Summary**

This chapter focussed on the ranging and position estimation techniques from the UWB perspective. Some of the most common positioning techniques for radio systems were looked at. The wideband nature of their waveforms allows UWB systems to offer potentially very high positioning accuracy in simple propagation environments. The position of a target node can be estimated in a wireless network based on TOA, TDOA, RSS and AOA of the received signals. Both TOA and TDOA techniques exploit the fine time resolution of UWB signals, giving high accuracy ranging and localisation. While AOA method can also provide good precision, implementations based on AOA technique have high complexity. Despite being relatively cheaper and easier to implement, RSS measurements can be quite erratic and thus are unable to provide very high ranging accuracy. Hence, positioning based on TOA or TDOA estimation is the method of choice in UWB-based positioning systems. Some of the potential error sources in time-based ranging have been addressed in this chapter, and some of the means to detect and possibly avoid or mitigate these errors were conversed. In addition, the tentative specifications and operational requirements for the intended UWB sensor nodes which could help in realising a simple, compact and accurate motion tracking system are discussed. Further chapters will present the analysis and experimental investigations carried out for the actualisation of a system of such kind.

## References

- [1] H. Nikookar and R. Prasad, *Introduction to Ultra Wideband for Wireless Communications*. Springer, 2009.
- [2] Z. Sahinoglu, S. Gezici, and I. Guvenc, *Ultra-Wideband Positioning Systems: Theoretical Limits, Ranging Algorithms, and Protocols*. Cambridge University Press, 2008.
- [3] I. Oppermann, M. Hämäläinen, and J. Inatti, Eds., *UWB: Theory and Applications*. John Wiley and Sons, 2004.
- [4] M. Yassin, E. Rachid, and R. Nasrallah, “Performance comparison of positioning techniques in Wi-Fi networks,” in *10th International Conference on Innovations in Information Technology (IIT)*, 2014, pp. 75–79.
- [5] H. Liu, H. Darabi, P. Banerjee, and J. Liu, “Survey of Wireless Indoor Positioning Techniques and Systems,” *IEEE Trans. Syst. Man Cybern. Part C (Applications Rev.)*, vol. 37, no. 6, pp. 1067–1080, Nov. 2007.
- [6] D. Zhang, F. Xia, Z. Yang, L. Yao, and W. Zhao, “Localization Technologies for Indoor Human Tracking,” in *5th International Conference on Future Information Technology*, 2010, pp. 1–6.
- [7] U. I. Khan, K. Pahlavan, and S. Makarov, “Comparison of TOA and RSS based techniques for RF localization inside human tissue,” in *Annual International Conference of the IEEE Engineering in Medicine and Biology Society*, 2011, vol. 2011, pp. 5602–5607.
- [8] I. Jami, M. Ali, and R. . Ormondroyd, “Comparison of methods of locating and tracking cellular mobiles,” in *IEE Colloquium Novel Methods of Location and Tracking of Cellular Mobiles and their System Applications*, 1999, vol. 1999, pp. 1–6.
- [9] S. Gezici, “A Survey on Wireless Position Estimation,” *Wirel. Pers. Commun.*, vol. 44, no. 3, pp. 263–282, Oct. 2008.

- [10] S. Gezici and H. V. Poor, "Position Estimation via Ultra-Wide-Band Signals," *Proc. IEEE*, vol. 97, no. 2, pp. 386–403, Feb. 2009.
- [11] N. Patwari, J. N. Ash, S. Kyperountas, A. O. Hero, R. L. Moses, and N. S. Correal, "Locating the nodes: cooperative localization in wireless sensor networks," *IEEE Signal Process. Mag.*, vol. 22, no. 4, pp. 54–69, Jul. 2005.
- [12] M. M. Pietrzyk and T. von der Grun, "Ultra-wideband technology-based ranging platform with real-time signal processing," in *4th International Conference on Signal Processing and Communication Systems*, 2010, pp. 1–5.
- [13] A. F. Molisch, "Passive location estimation using TOA measurements," in *IEEE International Conference on Ultra-Wideband (ICUWB)*, 2011, pp. 253–257.
- [14] C. Xu, Y. Zhao, and Y. Zhang, "Localization Technology in Wireless Sensor Networks Based on UWB," in *International Conference on Wireless Networks and Information Systems*, 2009, pp. 35–37.
- [15] I. Sharp and K. Yu, "Indoor TOA Error Measurement, Modeling, and Analysis," *IEEE Trans. Instrum. Meas.*, vol. 63, no. 9, pp. 2129–2144, Sep. 2014.
- [16] G. Bellusci, G. J. M. Janssen, and C. C. J. M. Tiberius, "Performance Evaluation of a Low-Complexity Receiver Concept for TOA-Based Ultrawideband Ranging," *IEEE Trans. Veh. Technol.*, vol. 61, no. 9, pp. 3825–3837, Nov. 2012.
- [17] E. Almazrouei, N. Al Sindi, S. R. Al-Araji, N. Ali, Z. Chaloupka, and J. Aweya, "Measurements and characterizations of spatial and temporal TOA based ranging for indoor WLAN channels," in *7th International Conference on Signal Processing and Communication Systems (ICSPCS)*, 2013, pp. 1–7.
- [18] E. Xu, Z. Ding, and S. Dasgupta, "Source Localization in Wireless Sensor Networks From Signal Time-of-Arrival Measurements," *IEEE Trans. Signal Process.*, vol. 59, no. 6, pp. 2887–2897, Jun. 2011.

- [19] O. H. Woon and S. Krishnan, "Investigation of methods to extract TDOA from UWB-IR waveforms," in *IEEE International Conference on Communication Systems*, 2010, pp. 228–232.
- [20] H. Matsumoto, H. Kusano, T. Morokuma, and K. Sakamura, "Numerical and experimental investigation of TDOA-based positioning system by ultra-wideband impulse radio," in *IEEE Topical Conference on Wireless Sensors and Sensor Networks*, 2011, pp. 25–28.
- [21] G. I. Mary and V. Prithiviraj, "UWB localization techniques for precision automobile parking system" in *IEEE Region 10 Conference (TENCON)*, 2008, pp. 1–4.
- [22] M. Mandlik and Z. Nemeč, "An accurate Time-Difference measurement method for passive radar applications," in *23rd International Conference Radioelektronika*, 2013, pp. 406–409.
- [23] C. Gentner and T. Jost, "Indoor positioning using time difference of arrival between multipath components," in *International Conference on Indoor Positioning and Indoor Navigation*, 2013, pp. 1–10.
- [24] L. Zwirello, M. Janson, C. Ascher, U. Schwesinger, G. F. Trommer, and T. Zwick, "Localization in industrial halls via ultra-wideband signals," in *7th Workshop on Positioning, Navigation and Communication*, 2010, pp. 144–149.
- [25] A. H. Sayed, A. Tarighat, and N. Khajehnouri, "Network-based wireless location: challenges faced in developing techniques for accurate wireless location information," *IEEE Signal Process. Mag.*, vol. 22, no. 4, pp. 24–40, Jul. 2005.
- [26] S. Goswami, *Indoor Location Technologies*. New York, NY: Springer New York, 2013.
- [27] H.-C. Liu and C.-W. Hsuan, "AOA estimation for coexisting UWB signals with multipath channels," in *International Conference on Telecommunications and Multimedia (TEMU)*, 2014, pp. 173–178.

- [28] R. P and M. Sichitiu, “Angle of Arrival Localization for Wireless Sensor Networks,” in *3rd Annual IEEE Communications Society on Sensor and Ad Hoc Communications and Networks*, 2006, vol. 1, pp. 374–382.
- [29] M. Biguesh and S. Gazor, “On Proper Antenna Pattern for a Simple Source Detection and Localization System,” *IEEE Trans. Antennas Propag.*, vol. 57, no. 4, pp. 1073–1080, Apr. 2009.
- [30] J. Xu, M. Ma, and C. L. Law, “AOA Cooperative Position Localization,” in *IEEE Global Telecommunications Conference*, 2008, pp. 1–5.
- [31] A. E. Waadt, S. Wang, C. Kocks, A. Burnic, D. Xu, G. H. Bruck, and P. Jung, “Positioning in multiband OFDM UWB utilizing received signal strength,” in *7th Workshop on Positioning, Navigation and Communication*, 2010, pp. 308–312.
- [32] C. Feng, W. S. A. Au, S. Valaee, and Z. Tan, “Received-Signal-Strength-Based Indoor Positioning Using Compressive Sensing,” *IEEE Trans. Mob. Comput.*, vol. 11, no. 12, pp. 1983–1993, Dec. 2012.
- [33] J.-S. Leu and H.-J. Tzeng, “Received Signal Strength Fingerprint and Footprint Assisted Indoor Positioning Based on Ambient Wi-Fi Signals,” in *IEEE 75th Vehicular Technology Conference (VTC Spring)*, 2012, pp. 1–5.
- [34] M. Yavari and B. G. Nickerson, “Ultra Wideband Wireless Positioning Systems.” University of New Brunswick, 2014.
- [35] S. Galler, W. Gerok, J. Schroeder, and T. Kaiser, “Combined AOA/TOA UWB localization,” in *International Symposium on Communications and Information Technologies*, 2007, pp. 1049–1053.
- [36] F. Shang, B. Champagne, and I. Psaromiligkos, “A novel ML based joint TOA and AOA estimator for IR-UWB systems,” in *IEEE International Conference on Acoustics, Speech and Signal Processing*, 2013, pp. 5190–5194.
- [37] L. Taponecco, A. A. D’Amico, and U. Mengali, “Joint TOA and AOA Estimation for UWB Localization Applications,” *IEEE Trans. Wirel. Commun.*, vol. 10, no. 7, pp. 2207–2217, Jul. 2011.

- [38] M. W. Khan, N. Salman, and A. H. Kemp, "Enhanced hybrid positioning in wireless networks I: AoA-ToA," in *International Conference on Telecommunications and Multimedia (TEMU)*, 2014, pp. 86–91.
- [39] A. Gholoobi and S. Stavrou, "A hybrid TDoA-ToA localization method," in *20th International Conference on Telecommunications (ICT)*, 2013, pp. 1–4.
- [40] M. R. Gholami, S. Gezici, and E. G. Strom, "Improved Position Estimation Using Hybrid TW-TOA and TDOA in Cooperative Networks," *IEEE Trans. Signal Process.*, vol. 60, no. 7, pp. 3770–3785, Jul. 2012.
- [41] C. Kim, S. Lee, and K. Kim, "3D Underwater Localization with Hybrid Ranging Method for Near-Sea Marine Monitoring," in *IFIP 9th International Conference on Embedded and Ubiquitous Computing*, 2011, pp. 438–441.
- [42] T. Panichcharoenrat and W. Lee, "Hybrid location awareness in cognitive radio system," in *International Electrical Engineering Congress (iEECON)*, 2014, pp. 1–4.
- [43] M. Laaraiedh, S. Avrillon, and B. Uguen, "Hybrid Data Fusion techniques for localization in UWB networks," in *6th Workshop on Positioning, Navigation and Communication*, 2009, pp. 51–57.
- [44] M. R. Mahfouz, B. C. Merkl, M. J. Kuhn, and A. E. Fathy, "Investigation of High-Accuracy Indoor 3-D Positioning Using UWB Technology," *IEEE Trans. Microw. Theory Tech.*, vol. 56, no. 6, pp. 1316–1330, Jun. 2008.
- [45] Z. Sahinoglu and I. Guvenc, "Threshold-Based TOA Estimation for Impulse Radio UWB Systems," in *IEEE International Conference on Ultra-Wideband*, 2005, pp. 420–425.
- [46] O. Bialer, D. Raphaeli, and A. J. Weiss, "Efficient Time of Arrival Estimation Algorithm Achieving Maximum Likelihood Performance in Dense Multipath," *IEEE Trans. Signal Process.*, vol. 60, no. 3, pp. 1241–1252, Mar. 2012.
- [47] G. Shen, R. Zetik, H. Yan, O. Hirsch, and R. S. Thoma, "Time of arrival estimation for range-based localization in UWB sensor networks," in *IEEE International Conference on Ultra-Wideband*, 2010, vol. 2, pp. 1–4.

- [48] Y. Shimizu and Y. Sanada, “Accuracy of relative distance measurement with ultra wideband system,” in *IEEE Conference on Ultra Wideband Systems and Technologies*, 2003, pp. 374–378.
- [49] A. Sani, “Modelling and Characterisation of Antennas and Propagation for Body-Centric Wireless Communication,” PhD Thesis, Queen Mary University of London, 2010.
- [50] J. H. Reed, *An Introduction to Ultra Wideband Communication Systems*. Prentice Hall, 2005.
- [51] I. Kovacs, G. Pedersen, P. Eggers, and K. Olesen, “Ultra wideband radio propagation in body area network scenarios,” in *IEEE Eighth International Symposium on Spread Spectrum Techniques and Applications*, 2004, pp. 102–106.
- [52] C. Parini, S. Gregson, J. McCormick, and D. J. van Rensburg, *Theory and Practice of Modern Antenna Range Measurements*. The Institution of Engineering and Technology (IET), 2014.
- [53] “IEEE802.15.4a standard - ScenSor - DecaWave.” [Online]. Available: <http://www.decawave.com/technology/ieee802154a-standard>.
- [54] T. Ye, M. Walsh, P. Haigh, J. Barton, and B. O’Flynn, “Experimental impulse radio IEEE 802.15.4a UWB based wireless sensor localization technology: Characterization, reliability and ranging,” in *22nd IET Irish Signals and Systems Conference*, 2011.
- [55] Z. Sahinoglu and S. Gezici, “Ranging in the IEEE 802.15.4a Standard,” in *IEEE Annual Wireless and Microwave Technology Conference*, 2006, pp. 1–5.
- [56] “Part 15.4: Wireless Medium Access Control (MAC) and Physical Layer (PHY) Specifications for Low-Rate Wireless Personal Area Networks (WPANs),” IEEE, 2007.
- [57] H. Arslan, Z. N. Chen, and M.-G. Di Benedetto, Eds., *Ultra Wideband Wireless Communication*. Wiley, 2006.

- [58] A. F. Molisch, K. Balakrishnan, C. Chong, S. Emami, A. Fort, J. Karedal, J. Kunisch, H. Schantz, U. Schuster, and K. Siwiak, "IEEE 802.15.4a channel model - final report," 2005.
- [59] E. Karapistoli, F.-N. Pavlidou, I. Gragopoulos, and I. Tsetsinas, "An overview of the IEEE 802.15.4a Standard," *IEEE Commun. Mag.*, vol. 48, no. 1, pp. 47–53, Jan. 2010.
- [60] W. C. Chung and D. S. Ha, "An accurate ultra wideband (uwb) ranging for precision asset location," in *IEEE Conference on Ultra Wideband Systems and Technologies*, 2003, pp. 389–393.
- [61] D. Roetenberg, "Inertial and Magnetic Sensing of Human Motion," PhD Thesis, Twente University, 2006.
- [62] K. S. Hale and K. M. Stanney, Eds., *Handbook of Virtual Environments: Design, Implementation, and Applications (Human Factors and Ergonomics)*. CRC Press, 2002.
- [63] "Shadow Robot Company Ltd." [Online]. Available: <http://www.shadowrobot.com/>.
- [64] "William Harvey Research Institute: Queen Mary University of London" [Online]. Available: <http://www.whri.qmul.ac.uk/about-us/418-sports-exercise-medicine>.

# Ultra Wideband Technology for Localisation and Motion Tracking

Human motion analysis has attracted great interest from the research community due to its promising applications in various fields like sports performance analysis, animation, medicine and rehabilitation, robotics etc. Given the wide range of applications, numerous technical approaches are available today to realise human motion tracking. However, not all of them could adequately satisfy the professional requirements. The extra complexity inherent in full body movement capture has prevented cutting-edge systems from being sufficient to fulfil the professional needs. One alternative approach for motion tracking is by means of ultra wideband (UWB) based radio communication. UWB technology has been identified as one of the most promising techniques in future body area networks to enhance a mobile node or a sensor with accurate ranging and tracking capabilities [1], [2]. Due to the progress in the area of UWB chipset technology and their ease of availability in the market, emerging applications of UWB are being foreseen for precise localisation in sensor networks. Impulse radio ultra wideband (IR-UWB) systems have much better distance resolution capabilities than any other wireless system. This makes IR-UWB

technology ideally suited for localisation applications since the use of very short pulses enables precise time and distance assessment [3]–[5].

This chapter presents a detailed overview of the ultra-wideband technology, along with the advantages as well as challenges involved when working with UWB. A brief description of the operating principles and limitations of various other technologies that are being used for motion tracking applications is provided. In addition, some of the commercially available devices based upon UWB technology for localisation applications are discussed.

### 3.1 UWB Technology

#### 3.1.1 Overview

Ultra-wideband has emerged as a technology which offers abundant potential to satisfy the ever increasing demand for low-cost, high-speed digital wireless indoor and home networks [6]. This technology is based on the transmission of digital data over a wide frequency spectrum with very low energy and at very high data rates [7]. The very large bandwidth of UWB offers several advantages including low power consumption, high data rate, high time resolution, low-cost implementation, obstacle penetration, resistance to interference, covert transmission, coexistence with narrowband systems and so on [8].

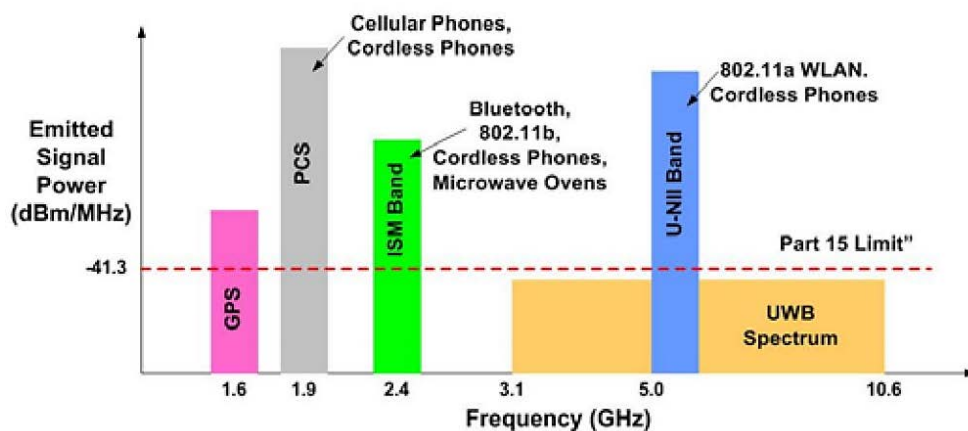


Figure 3.1: UWB spectrum overlaying with other existing narrowband systems [9].

The world of UWB has changed dramatically in the very recent history. Up until the current decade, UWB was mainly used for sensing, military communications and niche applications. In February 2002, a significant change took place in which the Federal Communications Commission (FCC) of the United States mandated that UWB radio transmission can legally operate in the frequency range of 3.1 GHz to 10.6 GHz, with the power spectral density (PSD) satisfying a specific spectral mask assigned by the FCC [10]. Since then, UWB has been rapidly progressing as a promising high data rate wireless technology for a diverse range of applications like data communications, imaging, radars, positioning, defence etc. [11]–[16].

In general, the spectral mask related with the FCC’s UWB regulation was designed to protect other spectrum users from undesirable interference caused by UWB operations. For wireless communications, the power levels regulated by the FCC are extremely low (i.e., -41.3 dBm/MHz), which permits the UWB technology to overlay with existing services such as the GPS (Global Positioning System) and the WLAN (Wireless Local Area Network) [10]. Perhaps the greatest advantage of UWB is most evident from the famous Shannon formula for the capacity of a band-limited channel operating with Gaussian noise:

$$C = W \log \left( 1 + \frac{P}{WN_0} \right), \quad (3.1)$$

where  $C$  is the channel capacity in bits/second (bps),  $W$  is the channel bandwidth in Hertz,  $P$  is the signal power in Watts and  $N_0$  is the noise power spectral density in Watts/Hz. The Shannon formula shows that, given the noise power spectral density  $N_0$  of the channel, the signal power  $P$  can be traded off with the bandwidth  $W$  while maintaining the same channel capacity  $C$ . In particular, we can decrease  $P$  if more bandwidth is available. On the other hand, given  $P$ , the capacity  $C$  will increase with  $W$ . From an information-theoretic perspective, this trade-off between power and bandwidth motivated the development of wideband communication systems such as spread spectrum and UWB [8].

Because of the low power spectral density of UWB, its interference can often be ignored by many existing systems occupying the same frequency bands. This property enables the unlicensed operation of UWB devices. Moreover, the short pulses of

UWB provide robust performance even in dense multipath environments due to their fine time resolution. This fine time resolution is also extremely beneficial for ranging and positioning applications. Besides, there is no need of carrier modulation of pulse-based UWB, which helps in reducing the size and cost of UWB devices compared to conventional narrowband systems [17].

### **3.1.2 Advantages of UWB**

Because of its various unique aspects and benefits, ultra wideband technology has been seen as a promising solution for future wireless communication applications. The principal advantages of UWB can be outlined as follows:

- Potential for high data rates.
- Extensive multipath diversity.
- Potential small size and processing power together with low equipment cost.
- High-precision ranging and localisation for positioning and tracking applications.

The extremely large bandwidth occupied by UWB gives the potential of very high theoretical capacity, yielding very high data rates. Also, due to the low energy density and the pseudo-random characteristics of the transmitted signal, the UWB signal is noise-like. This makes unintended detection quite difficult [11].

Conveying information with ultra-short duration waveforms, UWB signals have low susceptibility to multipath interference. Multipath interference occurs when a modulated signal arrives at a receiver from different paths. Combining signals at the receiver can result in distortion of the signal received. The ultra-short duration of UWB waveforms gives rise to a fine resolution of reflected pulses at the receiver. As a result, UWB transmissions can resolve many paths, and are thus rich in multipath diversity.

The low complexity and low cost of UWB systems arises from the carrier-free nature of the signal transmission. Specifically, due to its ultra-wide bandwidth, the UWB signal may span a frequency commonly used as a carrier frequency. This eliminates the need for an additional radio-frequency (RF) mixing stage as required in

conventional radio technology. Such an omission of up/down-conversion processes and RF components allows the entire UWB transceiver to be integrated with a single CMOS implementation. Single-chip CMOS integration of a UWB transceiver contributes directly to low cost, small size, and low power.

The ultra-short duration of UWB waveforms gives rise to the potential ability to provide high-precision ranging and localisation. Together with good material penetration properties, UWB signals offer opportunities for short-range radar applications such as rescue and anti-crime operations, as well as in surveying and in the mining industry [6].

### **3.1.3 Requirements for UWB Antennas**

A major step in the development of UWB technology for wireless communications is the antenna. Just like in any wireless communication system, the antenna performs an imperative part in a UWB system. The interest in UWB technology for wearable applications has been growing significantly over the last few years. Consequently, body-mounted UWB antennas have attracted a lot of attention from the research community. A range of such UWB antennas, with different designs and physical sizes have been proposed in literature [18]–[25].

The UWB antenna acts like a filter and is a critical component in the UWB radio systems. The basic effect of antennas is that they produce the derivative of the transmitted or received pulse waveform. This also has the effect of extending the duration of the transmitted and received pulse. This extension of pulse duration decreases the time resolution of the system. The antenna has a greater impact in UWB than in narrowband systems because of the very large bandwidth of a UWB signal [11]. In UWB communications, the antennas are significant pulse-shaping filters. Any distortion of the signal in the frequency domain leads to distortion of the transmitted pulse shape, which would necessitate the requirement for a more complex detection mechanism for successful data retrieval [26]. The extremely large frequency bandwidth of a UWB antenna is what differentiates it from other kinds of antennas. According to the FCC, a UWB antenna should possess an absolute bandwidth of minimum 500 MHz or a fractional bandwidth of at least 20%. Fractional bandwidth [9] is defined as

$$B_f = \frac{2(f_H - f_L)}{f_H + f_L}, \quad (3.2)$$

where  $f_H$  and  $f_L$  are the highest and lowest transmitted frequencies (at the -10 dB point) of a UWB pulse spectrum, respectively. The UWB antenna's radiation characteristics should be consistent across the whole operational frequency band. To prevent dispersion of the transmitted pulse, the antenna gain needs to be smooth across the operating frequency band [11], [27]. Sometimes, there is a requirement for specific spatial radiation properties, depending upon the practical application of the antenna. The UWB antennas for on-body applications should have omnidirectional radiation pattern [28]. Directional radiation characteristics are required for radar systems and other directional systems where high gain is desired [7], [29].

Other requirements of UWB antennas for wireless communications emanate from the spectrum sharing of the UWB and the existence of other narrowband services. Such UWB antennas should be able to be modified by introducing notches or filtering to some frequencies occupied by other services [30]. Another important requirement is the integration of the UWB antenna with the system. For wireless communications, an ultra-wideband antenna should be an integral part of the system and not just a standalone element. This is an important issue in the successful implementation of UWB technology for wireless communication applications [7]. Investigations carried out by Sipal et al. have successfully shown that for ideal system performance, UWB antennas need to be designed and optimised taking into consideration their specific deployment scenarios [31]. Moreover, a well-designed UWB antenna will have a constant surface current distribution over the bandwidth of interest and will give minimal distortion to the transmitted UWB waveform [32]. Also, the suitable antenna needs to be compact enough in order to be compatible with UWB systems especially for portable devices and mobile applications.

Furthermore, a UWB antenna is required to achieve good time domain characteristics. In the case of narrowband antennas, it is approximated that the antenna's characteristics are consistent over the entire bandwidth and the basic parameters, such as gain and return loss, have little variation across the operational band. In contrast, UWB systems often employ extremely short pulses for data transmission. In other words, enormous bandwidth has been occupied. Thus the antenna cannot be treated as

a “spot filter” any more but a “band-pass” filter. In this case, the antenna imposes more significant impacts on the input signal. As a result, a good time domain performance, i.e. minimum pulse distortion in the received waveform, is a primary concern of a suitable UWB antenna because the signal is the carrier of useful information [3].

#### **3.1.4 Challenges**

Although UWB has several attractive properties that make it a promising technology for upcoming wireless communications and many other applications, some challenges must be overcome to fulfil these expectations. The transmitter power levels of UWB signals are strictly limited in order for UWB devices to coexist peacefully with other wireless systems. Such strict power limitation poses significant challenges when designing UWB systems. One major difficulty is to achieve the desired performance at a satisfactory communication range with limited transmitter power. Another challenge lies in designing UWB waveforms that could utilize the bandwidth and power allowed by the FCC spectral mask in an efficient manner.

The ultra-short duration of UWB pulses leads to a large number of resolvable multipath components at the receiver. In particular, the received UWB signal contains many delayed and scaled replicas of the pulses transmitted. Additionally, each resolvable pulse undergoes different channel fading, which makes multipath energy capture a challenging problem in UWB system design. For example, if a Rake receiver is used to collect the multipath energy, a large number of fingers are needed to achieve the performance desired. Design challenges also exist in the fields of modulation and coding techniques that are suitable for UWB systems. UWB radio was initially used for defence applications, where multi-user transmission and achieving high multi-user capacity are not major concerns. However, these issues become very important in commercial applications, such as high-speed wireless home networks. Effective coding and modulation schemes are thus necessary to improve UWB multi-user capacity as well as system performance [9].

Other design challenges include scalable system architectures and spectrum flexibility. Potential applications of UWB include both high data rate applications (e.g., images and video) and lower data rate applications (e.g., computer peripheral

support). Thus, the UWB transceiver must be able to support a wide range of data rates. Furthermore, the unlicensed nature of the UWB spectrum makes it essential for UWB devices to coexist with devices that share the same spectrum [6]. All kinds of interference from existing narrowband services across the extremely large bandwidth of UWB may result in considerably stronger disturbances than background noise. This would mean that the equivalent noise power spectral density might be considerably larger, which may undermine the capacity promise of UWB [33]. The promise of low-cost implementation might also be undermined if simple circuits for signal reception and interference combating were unavailable. Moreover, it is significantly more difficult to design UWB antennas as compared to the conventional antennas. Conventional wideband antennas will be unable to transmit UWB signals without causing distortions. It is also more difficult to characterise UWB antennas, as traditional narrowband antenna parameters are not directly useful to UWB [8].

### **3.2 Impulse Radio**

Because of the inverse relation between the bandwidth and the duration of a signal, UWB systems are characterized by very short duration waveforms, typically in the order of sub-nanosecond. Usually, a UWB system transmits pulses of very short duration with a low duty cycle. This means that the ratio between the pulse transmission instant and the average time between two consecutive transmissions is kept small. Due to very narrow pulses, the spectrum of the signal reaches a bandwidth of several gigahertz. Such a pulse based UWB signalling scheme is called impulse radio (IR) [7], [34]. In an IR-UWB system, a number of pulses are transmitted per information symbol and information is generally conveyed by the positions or the polarities of the pulses, as illustrated in Figure 3.2.

The IR-UWB does not require the use of additional carrier modulation for transmission, as the pulse will propagate well in the radio channel. The technique is therefore a baseband signal approach [3]. As there is no requirement for a mixer, the implementation of the impulse radio technique becomes simpler. This also helps in reducing the costs of the transmitters and receivers [7]. This technology has a low transmit power and also has a fine time resolution due to the sharp transmitted pulses, which can be utilized for ranging and localisation.

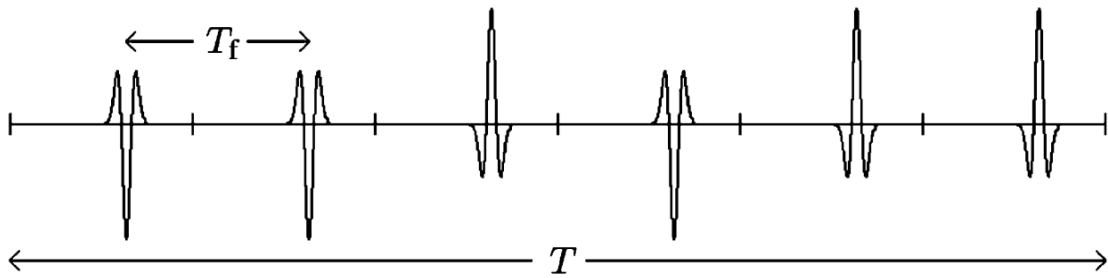


Figure 3.2: An Impulse Radio UWB signal containing short pulses with a low duty cycle. Here,  $T$  represents the signal duration and  $T_f$  represents the pulse repetition interval or the frame interval [35].

Capability of IR-UWB technology for precise distance measuring and positioning in body area networks has been established in recent times [36]–[38]. Because of this, IR-UWB is viewed for its potential application in through-wall radar, medical imaging, sensor networks, robot positioning, tracking and supervision. The key point of these applications is to locate the position of a target [39]. Owing primarily to the fine time resolution on the order of sub nanosecond pulses, accuracy of a few centimetres or above in distance measurement can be achieved using the IR-UWB scheme. Its high quality communication and accurate ranging capabilities make Impulse UWB a promising technology for location aware sensor networks [40].

Another competing technology for UWB wireless communications is the Multiband Orthogonal Frequency Division Multiplexing (MB-OFDM). In this technique, the 7.5 GHz UWB frequency spectrum is divided into multiple non-overlapping sub-bands with a -10 dB bandwidth of at least 500 MHz. The information is then interleaved across the sub-bands and the OFDM technique is applied for transmission. [41]. The research work presented in this thesis will specifically address the IR-UWB techniques only.

### 3.3 Recent Trends in UWB based Positioning and Motion Tracking

In recent years, there has been a growing demand for wearable technologies, especially in the domain of localisation and motion tracking. This demand is projected to remain strong in the near future. The revenues for wearable electronics industry are expected to reach US \$11.61 billion by 2020, with healthcare, wellbeing and fitness

being the dominant sectors [42]. According to [43], the worldwide market for real-time location systems is expected to witness a compound annual growth rate of 31.2% between 2013 and 2020 and the overall market is projected to reach US \$3.7 billion by 2020.

Analysis of the motion and posture of the human body is of interest in many different disciplines. During rehabilitation, the body movement of a patient needs to be monitored continuously and accurately in order to rectify any undesired motion pattern. Thus, motion tracking systems can provide a means to record and analyse the patient's gait and assist in the rehabilitation process [44]. The monitoring of the body movements of professional athletes in different sports can provide detailed information for improving performance and training while avoiding injury. In physiotherapy, motion tracking systems make it possible to accurately monitor the physical activities of an individual, which helps in analysing the effectiveness of the remedial exercises. Motion tracking is also utilized in the entertainment industry for recording the body movements of real human actors, which can then be used for the animation of computer generated characters or virtual reality [45].

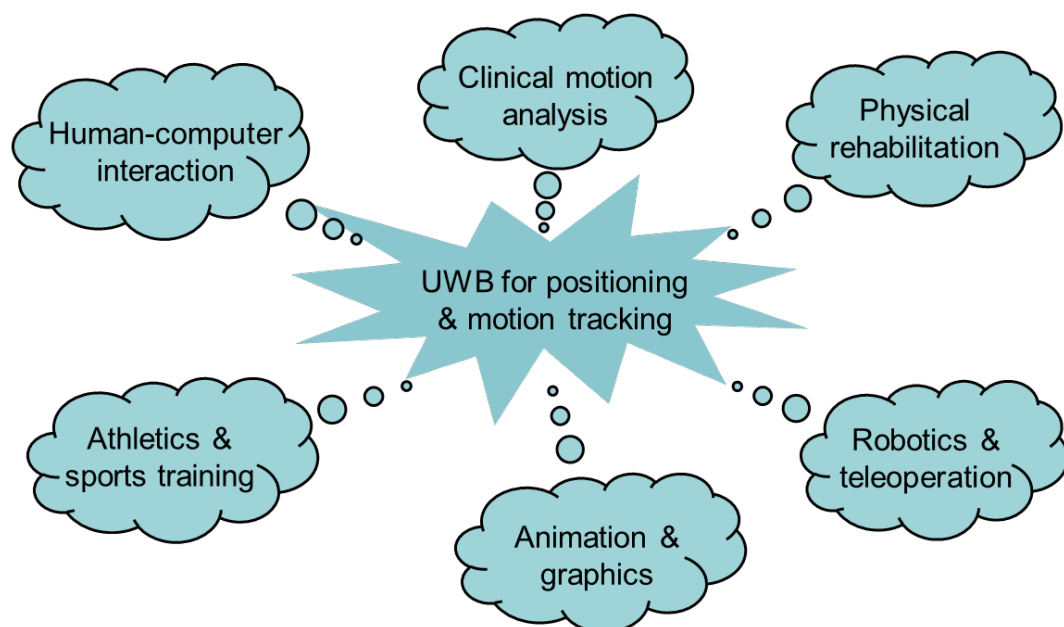


Figure 3.3: Potential applications of UWB technology for positioning and motion tracking.

One of the most promising approaches for localisation and motion tracking is by making use of ultra wideband technology. Other than its fine spatial and temporal

resolution, UWB fulfils several other crucial requirements for wireless human motion tracking such as low power, small form factor and low cost. In addition, such a system does not require any external infrastructure [46]. Some of the prospective applications of UWB technology for motion tracking have been depicted in Figure 3.3. UWB-based localisation and tracking has attracted a lot of attention from the research community. Recently published books on UWB communication systems and more general works on wireless networks, study UWB positioning techniques too [7], [47]–[49]. In [50], El-Nasir et al. investigated a UWB-based motion tracking system for gait analysis and reported sub-centimetre level ranging accuracy. Mahfouz et al. proposed a 3D indoor positioning system by implementing UWB technology in [51]. A human motion tracking systems based on ultra wideband radio nodes was investigated in [52]. The benefits of using UWB techniques for achieving high precision localisation in comparison to other available technologies has been nicely discussed by Zhang et al. in [53].

Recent progress in the field of millimetre wave technology has led to an interest for its utilization for positioning and localisation applications. In the 60 GHz frequency band (57 to 64 GHz in the United States, 59 to 66 GHz in Japan, 57 to 66 GHz in Europe), 7 to 9 GHz wide unlicensed spectrum is available globally. Due to its availability for licence free use, the 60 GHz band is seen as a promising candidate for multi-gigabit wireless indoor communication systems [54]. The wide frequency band can offer the advantages of ensuring good ranging and localisation accuracy. Compact size is another major benefit of millimetre wave equipment. While ICs keep the circuitry small, the high frequency makes it possible to realise very small sized antennas. The 60 GHz band can permit much higher data rates as compared to the microwave frequencies. The continuous improvement in miniaturisation and low-cost devices has triggered research activities aiming at developing future millimetre wave body area networks [55].

One of the key shortcomings of the 60 GHz band is its limited range due to increased atmospheric absorption. This is caused by the resonance of the oxygen molecules which results in high radio wave absorption. This effect is compounded by other perceived unfavourable characteristics of millimetre wave communication, such as increased free space path loss, decreased signal penetration through obstacles, directional communication due to high-gain antenna requirements and substantial

inter symbol interference due to many reflective paths over massive operating bandwidths. This disadvantage may be partially mitigated through good receiver sensitivity, high transmit power and high antenna gains. A millimetre wave system that uses omnidirectional antennas can suffer from severe inter symbol interference due to the multipath channels that cause successive symbols arriving at a receiver to overlap and interfere with each other. Moreover, 60 GHz circuitry and devices have traditionally been very expensive to build and only in the past few years have circuit solutions become viable in low-cost silicon. Communications signal processing is also more challenging at millimetre wave frequencies. Another challenge presented by the 60 GHz and millimetre wave band is in the development of power-efficient RF circuitry [56].

### **3.4 Commercially Available UWB Localisation and Positioning Systems**

Many systems and devices are currently available in the market-place that make use of UWB technology for localisation and positioning applications. This section discusses a few such commercially available devices and their operating principles.

#### **3.4.1 Time Domain**

The *PulsON 410 (P410)* is a UWB module developed by *Time Domain* [57], providing advanced real-time ranging and communication capabilities. The module supports two techniques for range measurements; two way time-of-flight (TW-TOF) and coarse range estimation (CRE). CRE method estimates the range by the signal strength and is less accurate than the TW-TOF technique. The dimensions of the module are 76 mm × 80 mm × 16 mm. Its operating range is 354 m and can provide range estimates with an accuracy of 2.1 cm in line-of-sight scenarios and 10 cm in non-line-of-sight scenarios. It operates at a centre frequency of 4.3 GHz with a 2.2 GHz bandwidth. This latest UWB module from Time Domain offers the advantage of high accuracy, however, it does not provide a tag module which is smaller, inexpensive and consumes less power to be suitable for use in a mobile node.



Figure 3.4: Time Domain's P410 Ranging and Communications Module [57]

### 3.4.2 DecaWave

The *DW1000* sensor chip developed by *DecaWave* [58] is able to perform positioning by using TOA (Time of arrival) or TDOA (Time difference of arrival) with a 10 cm precision and has a communication range of 300 m. It can work at six different frequency bands with centre frequencies from 3.5 GHz to 6.5 GHz. The two frequency bands centred at 4 GHz and 6.5 GHz can have a maximum bandwidth of up to 900 MHz, while the rest of the bands have a maximum bandwidth of 500 MHz. The EVB1000 Evaluation Board is a complete device which includes the DW1000 chip, ARM programmable processor, USB connection, LCD screen and a replaceable antenna. The evaluation board has the dimensions of 7 cm × 7 cm. This product provided by DecaWave is more suitable for research and development work because it is programmable, compact in size and has embedded LCD and USB connections.



Figure 3.5: DecaWave's evaluation board with DW1000 chip for real time location applications [58].

### 3.4.3 Zebra Technologies

The *Dart* UWB location system is a product developed by *Zebra Technologies* [59] which can provide a positioning accuracy of 30 cm for a 200 m operating range. The system comprises of a hub, sensors and mobile tags. The small mobile tags are 4 cm in diameter and include an embedded battery that can last for years depending upon mode. The Dart hub implements the positioning software and provides power, data and clock for the Dart sensors. The Dart sensors receive UWB signals from the mobile Dart tags, using the TDOA approach.



Figure 3.6: Dart UWB Real Time Location System from Zebra Technologies [59].

### 3.4.4 Ubisense

The *Series 7000* sensors from *Ubisense* [60] are precision UWB measurement devices which contain an array of antennas and ultra-wideband radio receivers. These sensors detect UWB pulses from Ubisense tags, allowing the Ubisense location system to find the tag's positions in real-time with an accuracy of 15 cm. They operate over a frequency range of 6 to 8 GHz. Ubisense sensors make use of both angle of arrival (by means of antenna arrays) and time difference of arrival to determine the tag location. The dimensions of the sensor are 20 cm × 14 cm × 6.5 cm and its weight is 580 g. The small tool tags are 4.2 cm × 3.2 cm × 2.1 cm in size. The sensors can communicate with each other with wires or through a wireless connection. The Ubisense sensor is however not programmable for research and development purposes.



Figure 3.7: Ubisense Series 7000 Sensors and compact tags [60].

### 3.4.5 PLUS Location System

The *Precision Location Ultra Wideband System (PLUS)* [61] is a real-time location system comprising of tags, readers, synchronization distribution panels (SDPs) and location software. The compact battery operated UWB transmitter tags weigh 22 g, are 13 mm × 36 mm × 33 mm in size and operate at a centre frequency of 6.6 GHz. The SDPs provide data connectivity, timing synchronization, and power to the network of PLUS readers. They also pass tag location information from the readers to the location software. The PLUS reader is a receive-only device that receives tag transmissions and determines the signal time of arrival from each tag. The reader passes tag data and TOA information to a server hosting the PLUS Location Software. This system can provide sub-meter localisation accuracy. Both TOA and TDOA techniques could be used for positioning.



Figure 3.8: PLUS real-time location system [61].

### **3.5 Motion Tracking Technologies**

Motion tracking involves recording movements of the human body (or any other movement) which could be translated on to a digital model, where post-processing of the captured data could be carried out to retrieve the relevant information for immediate or delayed analysis and playback [62]. The interdisciplinary characteristic of human motion analysis makes it a very fascinating and challenging field. Over the last few years, several systems have been developed that are capable of tracking human motion. In such systems, the human body is often considered as a system of rigid links connected by joints. Human body parts are not actually rigid structures, but they are customarily treated as such during studies of human motion [45]. In the present day world, the most prominent approaches for motion tracking could mainly be categorised into optical, mechanical, inertial and magnetic technologies. Each approach has different advantages and limitations depending upon its operating principles. These have been discussed in the subsequent sections.

#### **3.5.1 Optical Motion Tracking Systems**

The optical systems (such as *Vicon T-Series* from *Vicon* [63]) operate by tracking the motion of markers attached to a special suit worn by the user. The locations of the markers on the suit are designed such that the required body parts (e.g. joints) are covered. These systems tend to utilize proprietary video cameras which track the motion of markers on the subject's body segments, aligned with specific bony landmarks. About eight to sixteen such cameras are necessary for full body motion tracking. A typical measurement setup of an optical motion tracking system has been illustrated in Figure 3.9.

This optical shooting through several synchronized cameras leads to the synthesis of (x, y) coordinates of the same marker from different angles which ultimately allows the calculation of the (x, y, z) coordinates and hence the position of the marker in virtual space. Optical motion tracking systems have the advantage of being very configurable. The markers could be easily fixed to anything that needs to be tracked. Also, these systems are capable of providing high spatial precision and high update rates.



Figure 3.9: Measurement setup for an optical motion tracking system [64].

However, there are several drawbacks of these systems too, the most prominent being their exorbitant costs and requirement for a large dedicated studio setup. Moreover, these systems are not of much use outdoors because of their high sensitivity to lighting conditions and their limited tracking volume due to the coverage of available cameras. Most vision-based approaches to human motion tracking involve intensive computations, such as temporal differencing, background subtraction or occlusion handling. Also, these systems are extremely complex to install and suffer from occlusion (line-of-sight) problems whenever a required light path is blocked. Interference from other light sources or reflections may also lead to a problem.

### 3.5.2 Mechanical Motion Tracking Systems

Mechanical motion tracking systems (such as *Gypsy 7* from *Animazoo* [65]) utilize an exoskeleton that is fastened to the user's body. The users attach the skeletal-like structure to their body and as they move their joints, the articulated mechanical segments move with them and measure the relative motion of the user. The rigid segments are linked together with electromechanical transducers like potentiometers that directly track the angles of joints of the human body [66]. These potentiometers

provide joint angle data to kinematic algorithms which are used to determine the body posture [45].

One such mechanical motion tracking system has been shown in Figure 3.10. The benefits of this technology include their relatively low-cost, freedom from occlusion and flexibility to be used in any environment. These systems can acquire data at a high sampling rate as the sensed data does not require a lot of processing to extract motion information [67]. Their drawbacks include a very rigid and bulky structure, which leads to restriction of movements that one could make while using such systems. Also, these systems are not very comfortable to wear especially when being used for longer periods.



Figure 3.10: Exoskeleton of a mechanical motion capture system [68], [69].

### 3.5.3 Inertial Motion Tracking Systems

The Inertial motion tracking technology is based on use of inertial sensors such as gyroscopes and accelerometers, which are used to measure the relative motion of the object being tracked. One such inertial motion tracking system, *Xsens MVN* from *Xsens* [70] has been illustrated in Figure 3.11. The inertial motion sensors are placed on each body segment to be tracked and provide the absolute orientation estimates, which are also used to calculate the 3D linear accelerations in world coordinates. This

sequentially provides translation estimates of the body segments. These systems require calibration before use as the rotation from sensor to body segment and its position with respect to the axes of rotation are initially unknown [71], [72].

The inertial systems have several advantages like immunity to visual occlusion, data acquisition at a high sampling rate, low processing power and lower costs compared to optical systems. Also, these systems can be used in any environment without the need for a set studio room. There are some drawbacks too. The accumulation of errors through time (drift) makes it impractical to use these systems for long time periods if no compensation is applied. Moreover, there is a dense network of thick connecting wires between the sensors.



Figure 3.11: A typical body-worn inertial motion tracking system [70].

### 3.5.4 Magnetic Motion Tracking Systems

Magnetic motion tracking systems (such as *MotionStar* from *Ascension* [73]) utilize sensors placed on the body to measure the low-frequency magnetic fields generated by a transmitter source. The transmitter is a set of three coils which induces magnetic fields into the environment. For every measurement cycle, electric current is sent to these coils sequentially, thereby creating three mutually perpendicular fields. The sensors measure the strength of those fields, which is proportional to the distance of each coil from the field emitter assembly. The location of the sensors is estimated by a

processor connected to the transmitter and each sensor, based on the measured field values [74].

Since the magnetic fields could penetrate the human body, magnetic systems do not face any occlusion problem. These systems can measure absolute positioning of an object in 3D space. But there are several negative aspects of these systems. These systems are highly sensitive to magnetic interference and hence their performance gets affected by the presence of magnetic (ferric) materials in the vicinity. This makes it unsuitable for consumer-level motion tracking, which will demand such systems to operate in any kind of environment. These systems restrict user movement due to the thick cabling. Magnetic fields decrease in power rapidly as the distance from the generating source increases. This effectively limits the motion tracking area of such systems [67].



Figure 3.12: Measurement setup for a magnetic motion tracking system [75].

### 3.6 Summary

In this chapter, an outline of the UWB technology has been presented, along with the benefits and unique characteristics it offers. Recent developments taking place in the field of human motion tracking, especially in the context of UWB technology have been discussed. The monitoring of the human body movements, body kinematics, is a

growing research area for a wide range of applications such as healthcare, entertainment and athletics. IR-UWB technique offers a great potential to simplify the complexities and shortcomings of current motion tracking technologies and make such systems accessible to a wider range of users at an affordable price. The utilization of UWB technology for motion tracking presents an exciting and challenging area for the future and will lead to the development of more compact, accurate and easy to use motion tracking systems. Details of some commercial UWB devices presently available in the market have been discussed. Many of these systems are quite expensive and bulky in size, and provide an accuracy of within a range of several centimetres. Future trends could be towards the development of more compact localisation modules with an improved accuracy. This would be a significant improvement in the field of UWB-based positioning and will make it possible to realise the full potential of the benefits UWB technology could offer. The system provided by DecaWave appeared to be the most suitable for utilization in research and development tasks because of its many advantages like lower cost, compact size and easy programmability. Whilst not fulfilling all the desired requirements like lower operating frequency band and limited bandwidth, it is seen as a useful research and investigational tool for this work. A review of other technical approaches for tracking human motion was also undertaken and their advantages and limitations were discussed.

## References

- [1] M.-G. Di Benedetto, T. Kaiser, A. F. Molisch, I. Oppermann, C. Politano, and D. Porcino, Eds., *UWB Communication Systems: A Comprehensive Overview*. Hindawi Publishing Corporation, 2006.
- [2] H. Cao, V. Leung, C. Chow, and H. Chan, “Enabling technologies for wireless body area networks: A survey and outlook,” *IEEE Commun. Mag.*, vol. 47, no. 12, pp. 84–93, Dec. 2009.
- [3] L. Guo, “Study and Miniaturisation of Antennas for Ultra Wideband Communication Systems,” PhD Thesis, Queen Mary University of London, 2009.
- [4] “Ultra Wide Band: Be Spoon.” [Online]. Available: <http://bespoon.com/technology/ultra-wide-band/>.
- [5] S. Licul, J. Noronha, W. Davis, D. Sweeney, C. Anderson, and T. Bielawa, “A parametric study of time-domain characteristics of possible UWB antenna architectures,” in *58th Vehicular Technology Conference (VTC)*, 2003, vol. 5, pp. 3110–3114.
- [6] W. P. Siriwongpairat and K. J. R. Liu, *Ultra-Wideband Communications Systems : Multiband OFDM Approach*. John Wiley and Sons, 2007.
- [7] H. Nikookar and R. Prasad, *Introduction to Ultra Wideband for Wireless Communications*. Springer, 2009.
- [8] D. Valderas, J. I. Sancho, D. Puente, C. Ling, and X. Chen, *Ultrawideband Antennas: Design and Applications*. Imperial College Press, 2011.
- [9] C. Chong, F. Watanabe, and H. Inamura, “Potential of UWB Technology for the Next Generation Wireless Communications,” in *IEEE Ninth International Symposium on Spread Spectrum Techniques and Applications*, 2006, pp. 422–429.

- [10] *FCC First Report and Order, Revision of Part 15 of the commission's rules regarding ultra-wideband transmission systems.* Washington D.C., 2003, ET–Docket 98–153.
- [11] I. Oppermann, M. Hämmäläinen, and J. Iinatti, Eds., *UWB: Theory and Applications.* John Wiley and Sons, 2004.
- [12] E. Pancera, “Medical applications of the Ultra Wideband technology,” in *Loughborough Antennas & Propagation Conference*, 2010, pp. 52–56.
- [13] S. Colson and H. Hoff, “Ultra-Wideband Technology for Defence Applications,” in *IEEE International Conference on Ultra-Wideband*, 2005, pp. 615–620.
- [14] L. Fu-lai, S. Qian, W. Yu-ming, Z. Han-hua, and Z. Zhi-min, “Ultra-wideband Synthetic Aperture Radar landmine detection based on landmine-enhanced imaging,” in *IEEE International Conference on Ultra-Wideband (ICUWB)*, 2013, pp. 201–204.
- [15] I. Khajenasiri, P. Zhu, M. Verhelst, and G. Gielen, “Low-energy UWB transceiver implementation for smart home energy management,” in *The 18th IEEE International Symposium on Consumer Electronics (ISCE)*, 2014, pp. 1–2.
- [16] J. E. Jamaluddin and O. H. See, “Advances in control and data transmission over the power line using the ultra-wideband technology approach,” in *International Conference on Computer Applications and Industrial Electronics*, 2010, pp. 38–42.
- [17] J. H. Reed, *An Introduction to Ultra Wideband Communication Systems.* Prentice Hall, 2005.
- [18] Q. Wang, R. Hahnel, H. Zhang, and D. Plettmeier, “On-body directional antenna design for in-body UWB wireless communication,” in *6th European Conference on Antennas and Propagation (EUCAP)*, 2012, pp. 1011–1015.

- [19] E. Joo, K. Kwon, J. Park, and J. Choi, "On-body UWB MIMO antenna for UWB application," in *Asia-Pacific Microwave Conference Proceedings (APMC)*, 2013, pp. 1130–1132.
- [20] N. Chahat, M. Zhadobov, R. Sauleau, and K. Ito, "A Compact UWB Antenna for On-Body Applications," *IEEE Trans. Antennas Propag.*, vol. 59, no. 4, pp. 1123–1131, Apr. 2011.
- [21] M. Koohestani, J.-F. Zurcher, A. A. Moreira, and A. K. Skrivervik, "A Novel, Low-Profile, Vertically-Polarized UWB Antenna for WBAN," *IEEE Trans. Antennas Propag.*, vol. 62, no. 4, pp. 1888–1894, Apr. 2014.
- [22] T. Tuovinen, K. Y. Yazdandoost, and J. Iinatti, "Ultra Wideband loop antenna for on-body communication in Wireless Body Area Network," in *6th European Conference on Antennas and Propagation (EUCAP)*, 2012, pp. 1349–1352.
- [23] M. Klemm and G. Troster, "Textile UWB antenna for on-body communications," in *First European Conference on Antennas and Propagation*, 2006, pp. 1–4.
- [24] A. Kumar, B. Jakhar, and P. Agrawal, "Design and analysis of CPW-fed quasi-self-complementary pentagonal antenna for ultra-wideband systems," in *International Conference on Signal Propagation and Computer Technology (ICSPCT)*, 2014, pp. 754–757.
- [25] A. K. Gautam, S. Yadav, and B. K. Kanaujia, "A CPW-Fed Compact UWB Microstrip Antenna," *IEEE Antennas Wirel. Propag. Lett.*, vol. 12, pp. 151–154, 2013.
- [26] A. Sani, "Modelling and Characterisation of Antennas and Propagation for Body-Centric Wireless Communication," PhD Thesis, Queen Mary University of London, 2010.
- [27] T. Tuovinen, K. Y. Yazdandoost, and J. Iinatti, "Monopole Ultra Wideband antenna for on-body communication in Wireless Body Area Network," in *Loughborough Antennas & Propagation Conference*, 2011, pp. 1–4.

- [28] N. Chahat, M. Zhadobov, R. Sauleau, and K. Ito, “A compact planar UWB antenna for on-body communications,” in *Proceedings of the 5th European Conference on Antennas and Propagation (EUCAP)*, 2011, pp. 3627–3630.
- [29] J. Liang, “Antenna Study and Design for Ultra Wideband Communication Applications,” PhD Thesis, Queen Mary University of London, 2006.
- [30] R. Movahedinia and M. N. Azarmanesh, “Ultra-wideband band-notched printed monopole antenna,” *IET Microwaves, Antennas Propag.*, vol. 4, no. 12, pp. 2179–2186, 2010.
- [31] V. Sipal, M. John, D. Neiryneck, M. McLaughlin, and M. Ammann, “Advent of practical UWB localization: (R)Evolution in UWB antenna research,” in *8th European Conference on Antennas and Propagation (EuCAP)*, 2014, pp. 1561–1565.
- [32] V. Sipal, B. Allen, and D. Edwards, “Impact of antennas on practical UWB signals,” in *7th European Conference on Antennas and Propagation (EuCAP)*, 2013, pp. 545–548.
- [33] D. Porcino and W. Hirt, “Ultra-wideband radio technology: Potential and challenges ahead,” *IEEE Commun. Mag.*, vol. 41, no. 7, pp. 66–74, Jul. 2003.
- [34] Z. Sahinoglu, S. Gezici, and I. Guvenc, *Ultra-Wideband Positioning Systems: Theoretical Limits, Ranging Algorithms, and Protocols*. Cambridge University Press, 2008.
- [35] S. Gezici and H. V. Poor, “Position Estimation via Ultra-Wide-Band Signals,” *Proc. IEEE*, vol. 97, no. 2, pp. 386–403, Feb. 2009.
- [36] J. Hamie, B. Denis, and M. Maman, “On-body localization experiments using real IR-UWB devices,” in *IEEE International Conference on Ultra-WideBand (ICUWB)*, 2014, pp. 362–367.
- [37] C. Lee, H.-S. Lee, and J.-Y. Kim, “Performance of a one-way ranging method for WBAN healthcare services,” in *9th International Symposium on Communications and Information Technology*, 2009, pp. 1460–1463.

- [38] J.-Y. Oh, J.-H. Park, M.-K. Oh, J.-Y. Kim, and H.-S. Lee, "Baseband transceiver chip for IR-UWB system," in *International SoC Design Conference (ISOCC)*, 2009, pp. 564–568.
- [39] Z. Xiao, Y. Hei, Q. Yu, and K. Yi, "A survey on impulse-radio UWB localization," *Sci. China Inf. Sci.*, vol. 53, no. 7, pp. 1322–1335, Jul. 2010.
- [40] T. Ye, M. Walsh, P. Haigh, J. Barton, and B. O'Flynn, "Experimental impulse radio IEEE 802.15.4a UWB based wireless sensor localization technology: Characterization, reliability and ranging," in *22nd IET Irish Signals and Systems Conference*, 2011.
- [41] M. Magani, L. Guo, and X. Chen, "Improved BER performance on MB-OFDM UWB system using adaptive bit loading," in *IEEE International Conference on Ultra-Wideband*, 2010, vol. 1, pp. 1–4.
- [42] "Wearable Electronics and Technology Market by Applications, Products, Form Factors and Geography - Analysis & Forecast to 2014 - 2020." [Online]. Available: [http://www.researchandmarkets.com/reports/2624237/wearable\\_electronics\\_and\\_technology\\_market\\_by#relb2](http://www.researchandmarkets.com/reports/2624237/wearable_electronics_and_technology_market_by#relb2).
- [43] "Real-Time Location Systems (RTLS) Market by Product & Geography 2013 - 2020." [Online]. Available: <http://heritagegroupusa.com/real-time-location-systems-market-growth-driven-by-emerging-technologies-such-as-uwb-and-zigbee/>.
- [44] S. Zhang, B. Y. Tan, K. H. Leo, and R. Q. F. Tham, "A hybrid human motion tracking system for virtual rehabilitation," in *6th IEEE Conference on Industrial Electronics and Applications*, 2011, pp. 1993–1998.
- [45] D. Roetenberg, "Inertial and Magnetic Sensing of Human Motion," PhD Thesis, Twente University, 2006.
- [46] Z. W. Mekonnen, E. Slotke, H. Luecken, C. Steiner, and A. Wittneben, "Constrained maximum likelihood positioning for UWB based human motion tracking," in *International Conference on Indoor Positioning and Indoor Navigation*, 2010, pp. 1–10.

- [47] S. Goswami, *Indoor Location Technologies*. New York, NY: Springer New York, 2013.
- [48] R. Thomä, R. H. Knöchel, J. Sachs, I. Willms, and T. Zwick, Eds., *Ultra-Wideband Radio Technologies for Communications, Localization and Sensor Applications*. Rijeka: InTech, 2013.
- [49] T. Zwick, W. Wiesbeck, J. Timmermann, and G. Adamiuk, Eds., *Ultra-Wideband RF System Engineering*. Cambridge: Cambridge University Press, 2013.
- [50] M. A. El-Nasr, H. A. Shaban, and R. M. Buehrer, “Key design parameters and sensor-fusion for low-power wearable UWB-based motion tracking gait analysis systems,” *Prog. Electromagn. Res. Lett.*, vol. 29, pp. 115–126, 2012.
- [51] M. R. Mahfouz, B. C. Merkl, M. J. Kuhn, and A. E. Fathy, “Investigation of High-Accuracy Indoor 3-D Positioning Using UWB Technology,” *IEEE Trans. Microw. Theory Tech.*, vol. 56, no. 6, pp. 1316–1330, Jun. 2008.
- [52] Z. W. Mekonnen and A. Wittneben, “Localization via Taylor series approximation for UWB based human motion tracking,” in *8th Workshop on Positioning, Navigation and Communication*, 2011, pp. 77–82.
- [53] D. Zhang, F. Xia, Z. Yang, L. Yao, and W. Zhao, “Localization Technologies for Indoor Human Tracking,” in *5th International Conference on Future Information Technology*, 2010, pp. 1–6.
- [54] M. Park, P. Gopalakrishnan, and R. Roberts, “Interference mitigation techniques in 60 GHz wireless networks,” *IEEE Commun. Mag.*, vol. 47, no. 12, pp. 34–40, Dec. 2009.
- [55] M. Zhadobov, N. Chahat, R. Sauleau, C. Le Quement, and Y. Le Drean, “Millimeter-wave interactions with the human body: state of knowledge and recent advances,” *Int. J. Microw. Wirel. Technol.*, vol. 3, no. 02, pp. 237–247, Mar. 2011.
- [56] T. S. Rappaport, R. W. Heath, R. C. Daniels, and J. N. Murdock, *Millimeter Wave Wireless Communications*. Prentice Hall, 2014.

- [57] “PulsON 410 RCM Product Brochure,” 2013. [Online]. Available: [http://www.timedomain.com/datasheets/TD\\_DS\\_P410\\_RCM\\_FA.pdf](http://www.timedomain.com/datasheets/TD_DS_P410_RCM_FA.pdf).
- [58] “Indoor Positioning Systems (IPS) - RTLS Solutions | DecaWave.” [Online]. Available: <http://www.decawave.com/>.
- [59] “Dart UWB Technology Product Brochure,” 2012. [Online]. Available: <https://www.zebra.com/content/dam/zebra/product-information/en-us/brochures-datasheets/location-solutions/dartuwb-tech-datasheet-en-us.pdf>.
- [60] “Ubisense RTLS Hardware - Ubisense.” [Online]. Available: <http://www.ubisense.net/en/products-and-services/rtls-products.html>.
- [61] “Real Time Location Systems - PLUS Location SystemsPLUS® Location Systems.” [Online]. Available: <http://pluslocation.com/>.
- [62] N. Magnenat-Thalmann, L. C. Jain, and N. Ichalkaranje, Eds., *New Advances in Virtual Humans: Artificial Intelligence Environment*. Springer, 2008.
- [63] “Vicon | Systems.” [Online]. Available: <http://www.vicon.com>.
- [64] “UC Merced Adopts VICON F40 Motion Capture System.” [Online]. Available: <http://dmnnewswire.digitalmedianet.com/article/UC-Merced-Adopts-VICON-F40-Motion-Capture-System-643459>.
- [65] “Animazoo Motion Capture Systems.” [Online]. Available: <http://www.animazoo.fr/>.
- [66] A. Gmitterko and T. Lipták, “Motion Capture of Human for Interaction with Service Robot,” *Am. J. Mech. Eng.*, vol. 1, no. 7, pp. 212–216, Jan. 2013.
- [67] A. Wong, “Low-Cost Visual/Inertial Hybrid Motion Capture System for Wireless 3D Controllers,” PhD Thesis, University of Waterloo, 2007.
- [68] “3D BLOOM: My Motion Capture Essay.” [Online]. Available: <http://3dbloom.blogspot.co.uk/2013/10/my-motion-capture-system-essay-brief.html>.
- [69] “Animazoo Gypsy 7 Product Brochure.” [Online]. Available: [http://www.motionwerx.com/MotionWerxAnimazoo\\_GYPSY7\\_Brochure.pdf](http://www.motionwerx.com/MotionWerxAnimazoo_GYPSY7_Brochure.pdf).

- [70] “Xsens MVN | Products | Xsens 3D motion tracking.” [Online]. Available: <https://www.xsens.com/products/xsens-mvn/>.
- [71] J. A. Corrales, F. A. Candelas, and F. Torres, “Hybrid tracking of human operators using IMU/UWB data fusion by a Kalman filter,” in *3rd ACM/IEEE International Conference on Human-Robot Interaction (HRI)*, 2008, pp. 193–200.
- [72] “Motion capture | Xsens 3D motion tracking.” [Online]. Available: <https://www.xsens.com/tags/motion-capture/>.
- [73] “Ascension Technology Corporation.” [Online]. Available: <http://www.ascension-tech.com/realtime/RTmotionStarTethered.php>.
- [74] V. G. Duffy, Ed., *Handbook of Digital Human Modeling: Research for Applied Ergonomics and Human Factors Engineering*. CRC Press, 2008.
- [75] “Task1-Existence Technology of Motion Capture.” [Online]. Available: <https://kalyankrishna4886.wordpress.com/2010/11/17/motion-capture/>.

# Miniature Ultra Wideband Antenna Design

The ultra-wideband antenna is the core design component of the UWB sensor node. Some key requirements for this antenna are compact size, reasonable performance in the vicinity of human body, reliable communication with other antennas etc. The frequency range of 6 to 10.6 GHz was chosen as the operational band for the UWB sensor node in order to realise the need for compact sensor nodes with low cost as well as to agree with the UWB licensing regulations on spectrum usage. Three preliminary antenna designs have been presented in this chapter. The three designs were modelled using the CST Microwave Studio software package and their fabricated prototypes were investigated in free-space and on-body. A comparative study of these antennas has been carried out to determine the best design for the UWB sensor node antenna.

In this chapter, a novel miniature tapered-slot antenna design is presented. This antenna has been derived from one of the three preliminary antenna designs, and is more compact in comparison. A detailed analysis of the performance of this novel miniature ultra-wideband antenna has been carried out. Moreover, the numerical and

experimental study regarding the influence of various simplified human body models and real human body on the reflection coefficient and radiation patterns of this miniature antenna is also provided.

## 4.1 Suitable Antenna Designs

### 4.1.1 Tapered-slot Antenna

This antenna is designed on the RT/Duroid board with a relative permittivity of 3 and thickness of 1.524 mm. The antenna is fed through a 50  $\Omega$  SMA coaxial connector. The geometric design of this coplanar waveguide fed tapered-slot antenna is inspired from [1] but in comparison, is much smaller in physical size with overall dimensions of 11 mm by 14 mm, with the antenna being targeted for on-body applications. The curves of the two tapered slots are characterized by the arcs of two ellipses with different lengths for semi-major and semi-minor axis. The geometry of the tapered slot antenna is illustrated in Figure 4.1.

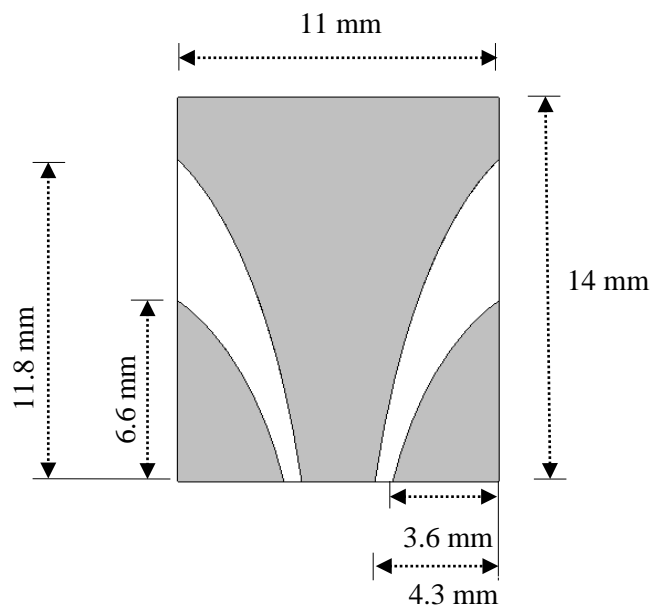


Figure 4.1: Geometry of the tapered-slot antenna design.

The lengths of the semi-major and semi-minor axes of the bigger ellipse are  $y1 = 20$  mm and  $x1 = 7.2$  mm respectively and that for the smaller ellipse are  $y2 = 12.5$  mm and  $x2 = 6.7$  mm respectively. The ratio of semi-major to semi-minor axis within the design is the most significant parameter to affect the impedance matching. There is no

ground plane on the back side of the antenna design. A prototype of the tapered-slot antenna was built in the Antenna Measurement Laboratory at Queen Mary University of London. The fabricated antenna is illustrated in Figure 4.2.



Figure 4.2: Fabricated prototype of the tapered-slot antenna design.

Figure 4.3 shows the measured  $S_{11}$  of the tapered-slot antenna in free-space and on-body. The on-body  $S_{11}$  measurement was done by placing the antenna 2 mm away from the wrist of a real human test subject. The separation gap between the body and the antenna was achieved by using a 2 mm thick cotton pad as ‘air gap’.

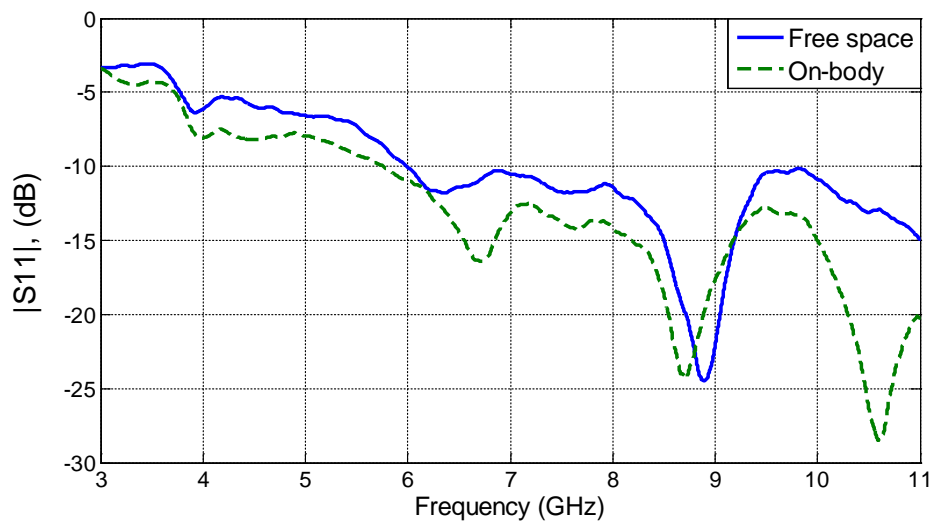


Figure 4.3: Measured  $S_{11}$  of the tapered-slot antenna in free-space and on human body.

The free-space -10 dB impedance bandwidth of the antenna is from 6 GHz to > 11 GHz, while for on-body measurements is from 5.7 GHz to > 11 GHz. The measurement confirms the UWB characteristic of the tapered-slot antenna and proves

its operation in the required 6 to 10.6 GHz frequency range. The measurement results show that the human body has a trivial effect on the antenna's input impedance. Thus, this antenna design is quite immune to the presence of human body in its vicinity.

The simulated 3D radiation patterns of the tapered-slot antenna design for 6, 7.5 and 9 GHz frequencies are presented in Figure 4.4. The simulations were carried out using the CST Microwave Studio software. The radiation patterns are almost omnidirectional in the azimuth plane for all the three frequencies. The shape of the patterns change only slightly with the increase in frequency and the patterns retain their omnidirectional character.

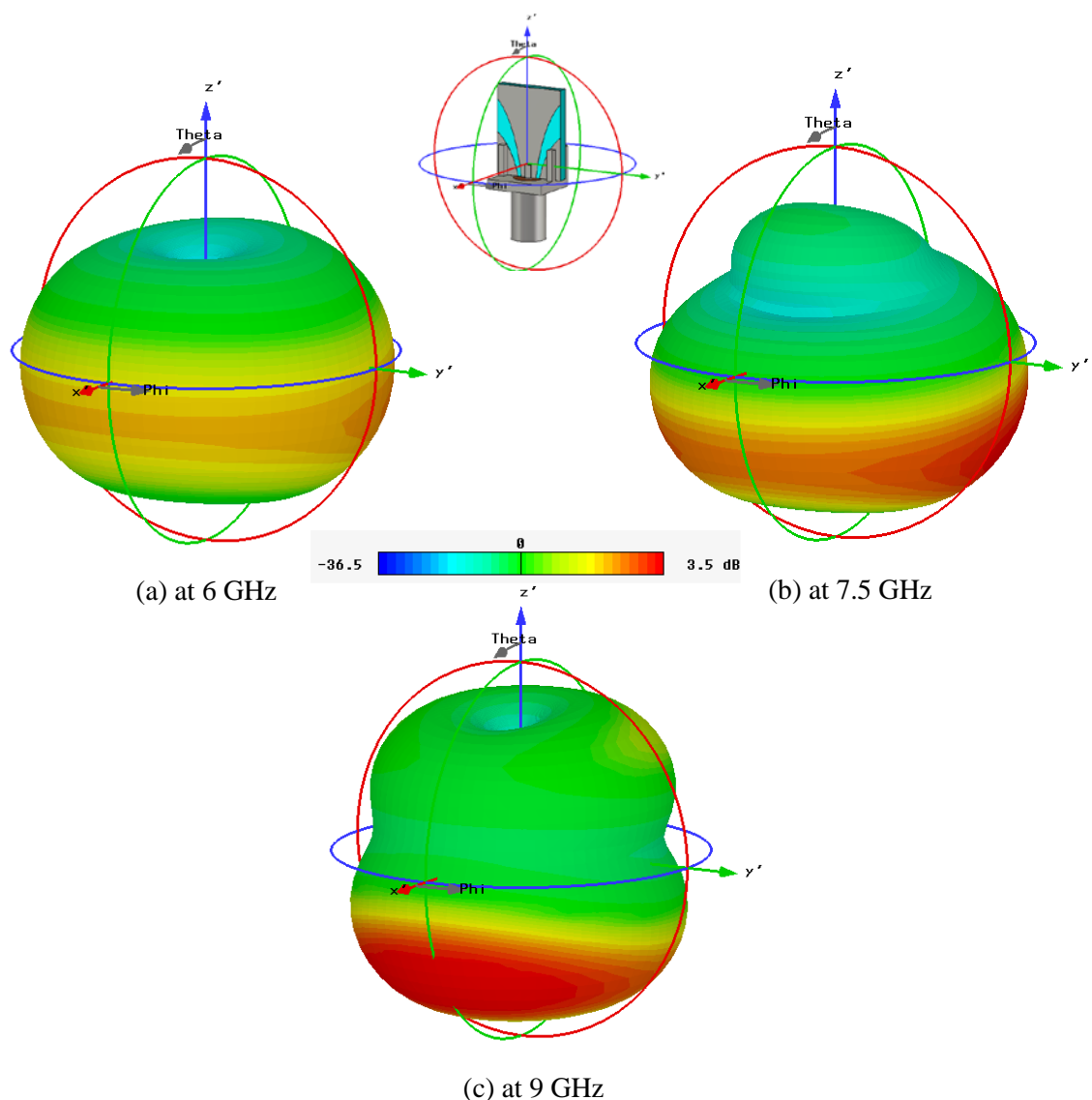


Figure 4.4: Simulated 3D radiation patterns of the tapered-slot antenna at three different frequencies.

In order to generate some design rules and to analyse the sensitivity of the tapered-slot antenna's design, the important parameters that determine the antenna performance were investigated. The lengths of semi-major and semi-minor axes of both the bigger and smaller ellipses have been varied since these are the most important parameters in the design to affect the operation of the antenna. The first parameter analysed is the length of semi-minor axis of the smaller ellipses  $x_2$ . Figure 4.5 illustrates the antenna's simulated S11 with different lengths of the semi-minor axis of the smaller ellipses ( $x_2 = 6.2, 6.7$  and  $7.2$  mm) when rest of the parameters remain fixed at their original lengths.

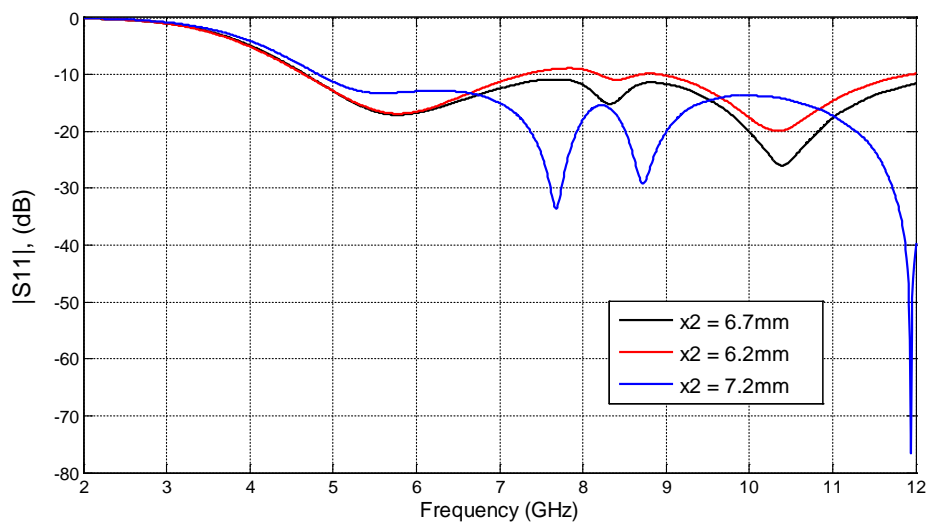


Figure 4.5: Simulated S11 of the tapered-slot antenna for different lengths of semi-minor axis  $x_2$  of the smaller ellipse.

It could be noticed in Figure 4.5 that the -10 dB impedance bandwidth of the antenna varies to some extent with the variation of the semi-minor axis of the smaller ellipses  $x_2$ . A decrease in length (as shown by red curve) degrades the -10 dB bandwidth. An increase in length (as shown by blue curve) keeps the bandwidth unchanged within the target frequency range, but reduces the gap between the central patch and side patches to 0.14 mm. The smaller gap makes the fabrication of the antenna more difficult and increases the likelihood of inaccuracies during the fabrication process. Next, the length of semi-major axis of the smaller ellipses  $y_2$  is varied. Figure 4.6 shows the simulated S11 with different lengths of semi-major axis of the smaller ellipses ( $y_2 = 12, 12.5$  and  $13$  mm) when the rest of the parameters remain fixed at their original lengths.

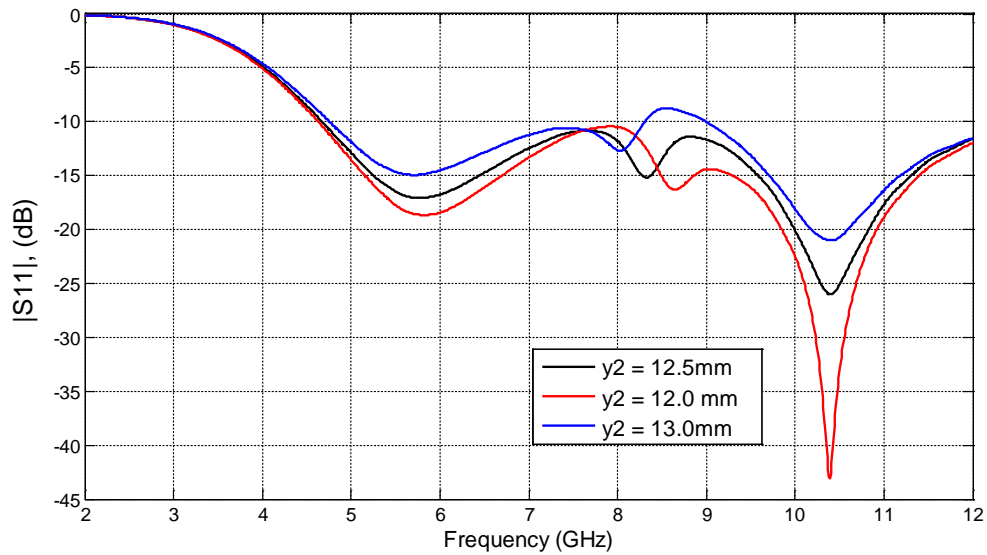


Figure 4.6: Simulated S11 of the tapered slot antenna for different lengths of semi-major axis  $y_2$  of the smaller ellipse.

It can be observed from Figure 4.6 that an increase or decrease in lengths of semi-major axis of the smaller ellipses  $y_2$  leads to a minor change in the shapes of the S11. On increasing the value for  $y_2$  the -10 dB bandwidth of the antenna gets affected slightly between 8 GHz and 9 GHz frequencies, while a decrease in  $y_2$  keeps the -10 dB bandwidth of the antenna almost unchanged. This indicates that the tapered-slot antenna design is less sensitive to variation in length of semi-major axis of the smaller ellipse in comparison to the semi-minor axis.

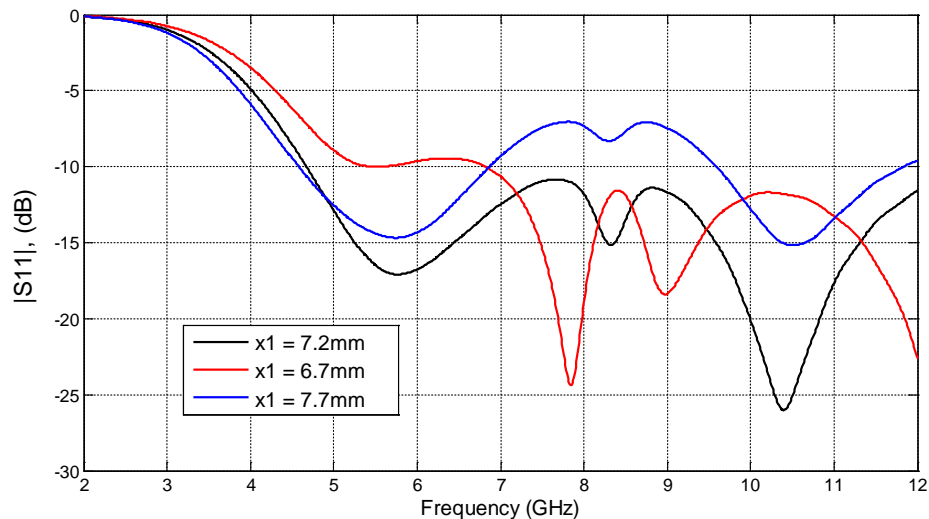


Figure 4.7: Simulated S11 of the tapered slot antenna for different lengths of semi-minor axis  $x_1$  of the bigger ellipse.

Similarly, the length of semi-minor axis of the bigger ellipses  $x1$  is varied. The simulated S11 results with different lengths of semi-minor axis of the bigger ellipses ( $x1 = 6.7, 7.2$  and  $7.7$  mm) when the rest of the parameters remain fixed at their original lengths have been shown in Figure 4.7. It can be noticed from Figure 4.7 that any variation to the length of  $x1$  has a significant effect on the -10 dB impedance bandwidth of the antenna. Any change in  $x1$  from its optimum value degrades the performance of the antenna within the target frequency range of 6 GHz to 10.6 GHz. Likewise, the length of the semi-major axis of the bigger ellipses is varied. Figure 4.8 illustrates the simulated S11 results with different lengths of semi-major axis of the bigger ellipses ( $y1 = 19.5, 20$  and  $20.5$  mm) when rest of the parameters remain fixed at their original lengths.

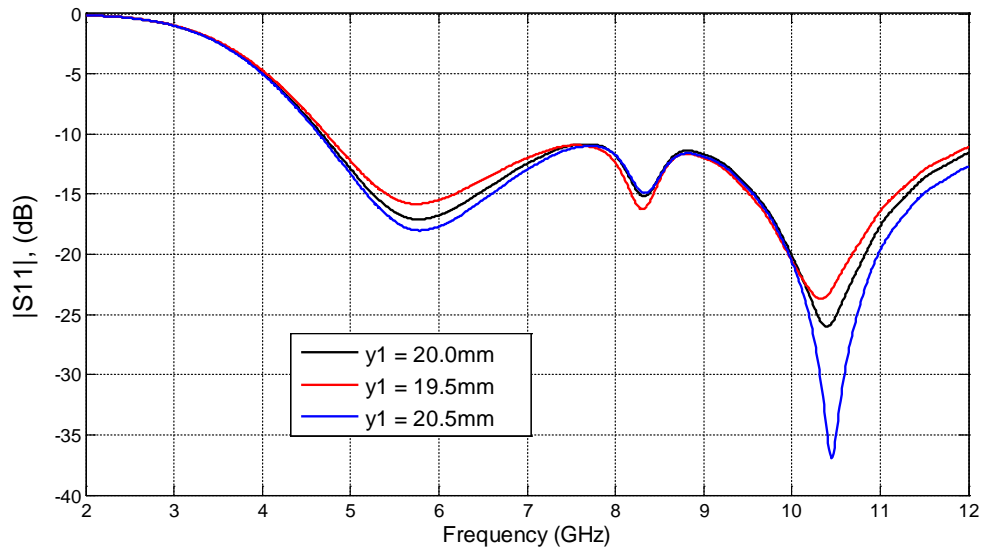


Figure 4.8: Simulated S11 of the tapered-slot antenna for different lengths of semi-major axis  $y1$  of the bigger ellipse.

It can be observed from Figure 4.8 that there is negligible effect of small variation in the lengths of semi-major axis of the bigger ellipse  $y1$  on the S11 results of the antenna. The -10 dB impedance bandwidth remains nearly unchanged. Thus, it can be inferred from this analysis that the lengths of the semi-minor axes of both the ellipses within the tapered-slot design affect the antenna performance most significantly. On the other hand, the semi-major axes of the ellipses comparatively affect the antenna operation in a limited manner.

#### 4.1.2 Quasi Self-complementary Antenna

This antenna has a half circular disc with a radius of 6.3 mm and its complementary magnetic counterpart printed on the different sides of the dielectric substrate. RT/Duroid board with a relative permittivity of 3 and thickness of 1.524 mm has been used as the substrate for this antenna design. A triangular notch is cut in the ground plane of the antenna, which improves the impedance matching. The width and height of the triangular notch are 5.8 mm and 4.8 mm respectively. The design of this antenna is derived from [2]. But in contrast, this antenna is smaller in terms of physical size. The overall size of the antenna is 12.8 mm by 18.4 mm.

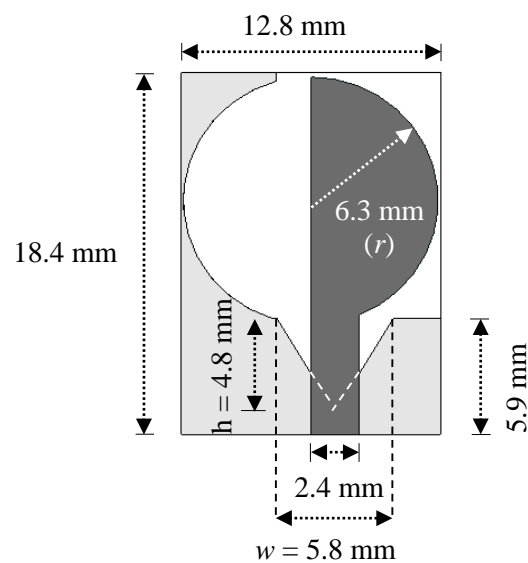


Figure 4.9: Geometry of the quasi self-complementary antenna design.



Figure 4.10: Fabricated prototype of the quasi self-complementary antenna design.

The detailed geometry of this quasi self-complementary antenna's design has been presented in Figure 4.9. A prototype of the antenna was built in the Antenna Measurement Laboratory at Queen Mary University of London. The fabricated quasi self-complementary antenna is illustrated in Figure 4.10.

Figure 4.11 illustrates the measured  $S_{11}$  for the quasi self-complementary antenna in free-space and when placed 2 mm away from a human test subject's wrist. The -10 dB impedance bandwidth of the antenna is from 6.5 GHz to > 11 GHz in free-space and from 7.3 GHz to > 11 GHz on-body. The impedance bandwidth of the antenna gets slightly affected when mounted on the human body, showing that the quasi self-complementary design is more sensitive to the presence of human body in its vicinity.

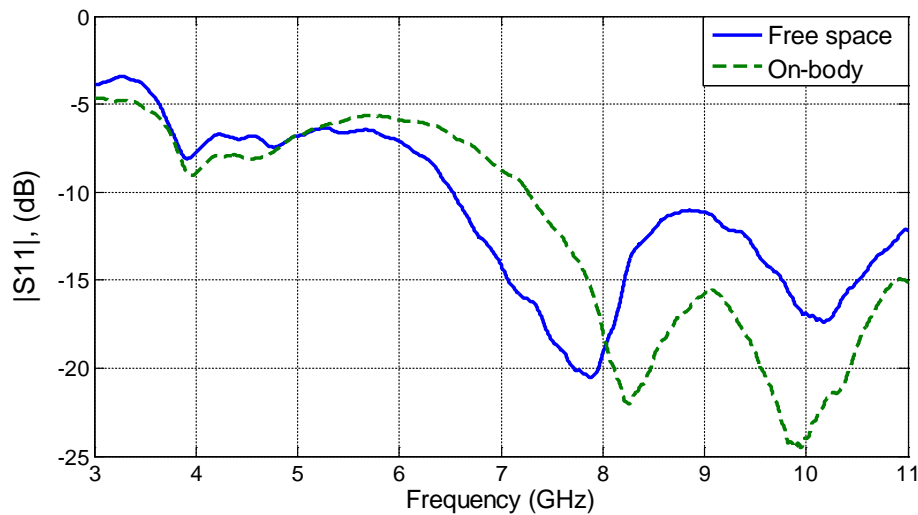


Figure 4.11: Measured  $S_{11}$  of the quasi self-complementary antenna in free-space and on human body.

Figure 4.12 presents the simulated 3D radiation patterns of the quasi self-complementary antenna design at 6, 7.5 and 9 GHz frequencies. It can be seen that the antenna's radiation is directional in nature. At 6 and 7.5 GHz frequencies the patterns are very similar, with the strongest radiation in the left side of the antenna structure. At 9 GHz, the radiation pattern changes significantly. The radiation of the antenna becomes strongest towards its front side. Thus, it can be inferred that the radiation of the quasi self-complementary antenna is directional in nature and is much more dependent on the operational frequency as compared to the tapered-slot antenna design.

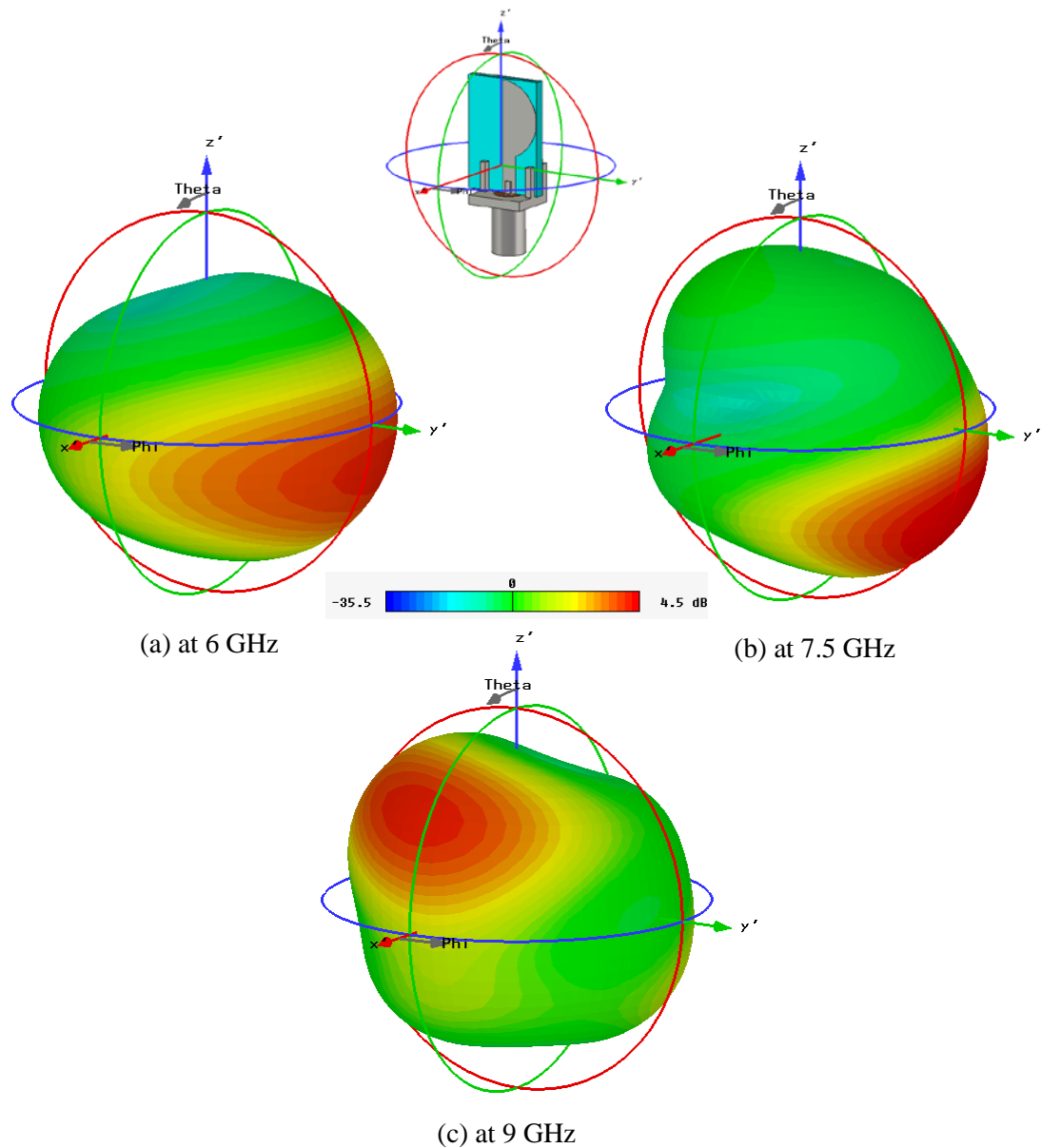


Figure 4.12: Simulated 3D radiation patterns of the quasi self-complementary antenna for three different frequencies.

Just like the tapered-slot antenna design, the important parameters that determine the performance of the quasi self-complementary design were investigated in order to analyse the sensitivity of the design and to generate some design rules. The radius of the half-circular disk and its complementary half-circular slot has been varied, along with the width and height of the triangular notch on the back side of the antenna. The first parameter to be investigated is the width of the triangular slot  $w$ . Figure 4.13 shows the  $S_{11}$  results for different widths of the triangular slot ( $w = 5.3, 5.8$  and  $6.3$  mm) while keeping the rest of the parameters unchanged.

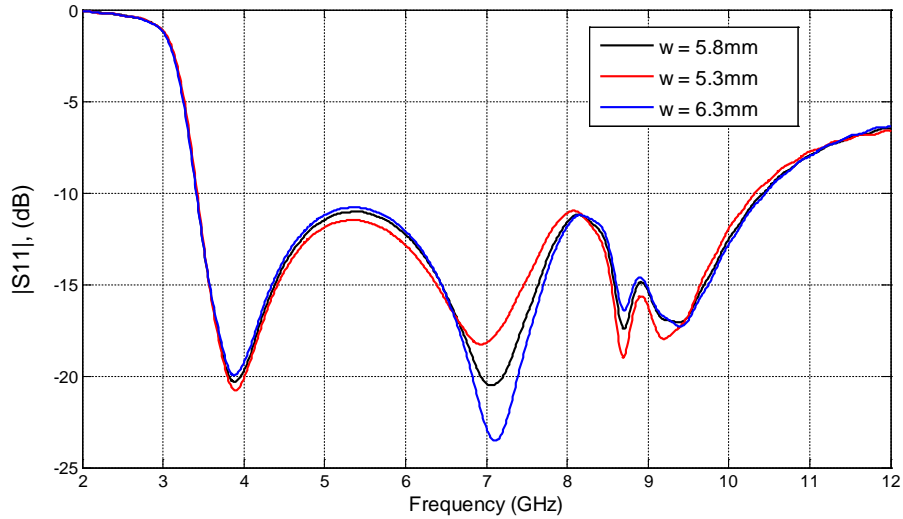


Figure 4.13: Simulated S11 of the quasi self-complementary antenna for different widths of the triangular notch  $w$ .

It can be observed from Figure 4.13 that slight variation in  $w$  has a very minor effect on the S11 results of the antenna. The -10 dB impedance bandwidth remains almost the same despite the changes. Similarly, height of the triangular notch  $h$  is varied. Figure 4.14 shows the simulated S11 with different values for different heights of the triangular notch ( $h = 4.3, 4.8$  and  $5.3$  mm) while all the other parameters remain unchanged from their original lengths. It is noticed from Figure 4.14 that on changing the value of  $h$ , there is only a slight variation in the S11 of the antenna. The -10 dB bandwidth is almost the same in all the three cases.

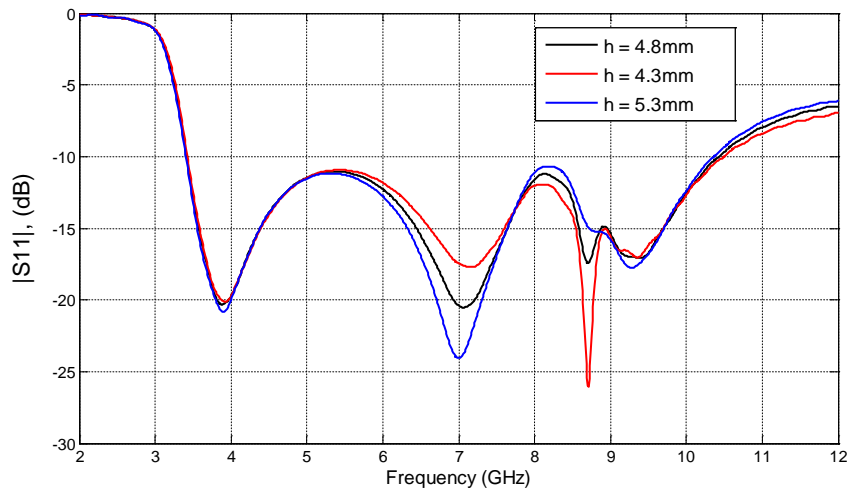


Figure 4.14: Simulated S11 of the quasi self-complementary antenna for different heights of the triangular notch  $h$ .

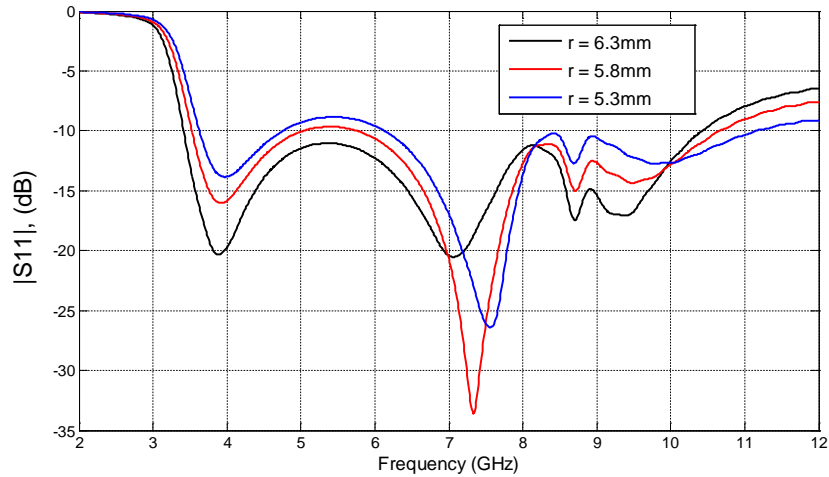


Figure 4.15: Simulated S11 of the quasi self-complementary antenna for different disc radii  $r$ .

Another design parameter affecting the antenna behaviour is the radius of the half-circular patch  $r$ . The simulated S11 with different lengths for the radius of half-circular patch and its complementary half-circular slot ( $r = 5.3, 5.8$  and  $6.3$  mm) have been shown in Figure 4.15. It can be noticed from Figure 4.15 that as the radius of half-circular patch  $r$  is reduced from its optimal value ( $6.3$  mm), the S11 of the antenna keeps deteriorating with the decreasing value of  $r$ .

### 4.1.3 Printed Compact UWB Antenna

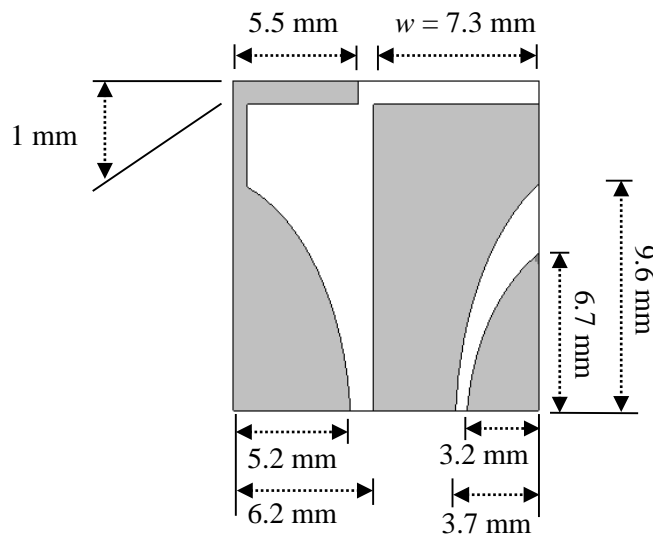


Figure 4.16: Geometry of the printed compact UWB antenna design.

This antenna design has a tapered radiating slot with a Gamma ( $\Gamma$ ) shaped quasi self-complementary structure printed on the same side of an RT/Duroid board with a

1.524 mm thickness and relative permittivity of 3. The antenna has its geometrical design derived from [3] but is comparatively smaller in overall physical dimensions. The antenna has an overall size of 13.5 mm by 14 mm, which is roughly the size of an average adult human's thumb nail. The tapered-slots in the design are formed by the arcs of three different ellipses. The slot in the right of the antenna is characterized by arcs of two ellipses. The lengths of the semi-major and semi-minor axes of the bigger ellipse are  $y1 = 11.8$  mm and  $x1 = 6.6$  mm respectively and that for the smaller ellipse are  $y2 = 8.7$  mm and  $x2 = 6.1$  mm, respectively. The tapered-slot in the left portion of the antenna is derived from an ellipse with a semi-major axis of length  $y3 = 11$  mm and semi-minor axis of length  $x3 = 6.6$  mm. The geometry of this compact ultra-wideband antenna has been illustrated in Figure 4.16. A prototype of the printed compact UWB antenna was built in the Antenna Measurement Laboratory at Queen Mary University of London. The fabricated antenna is presented in Figure 4.17.

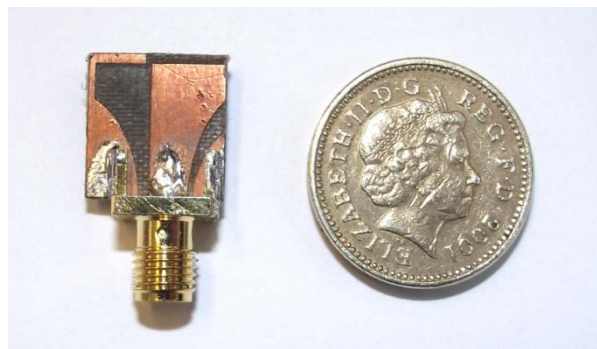


Figure 4.17: Fabricated prototype of the printed compact UWB antenna design.

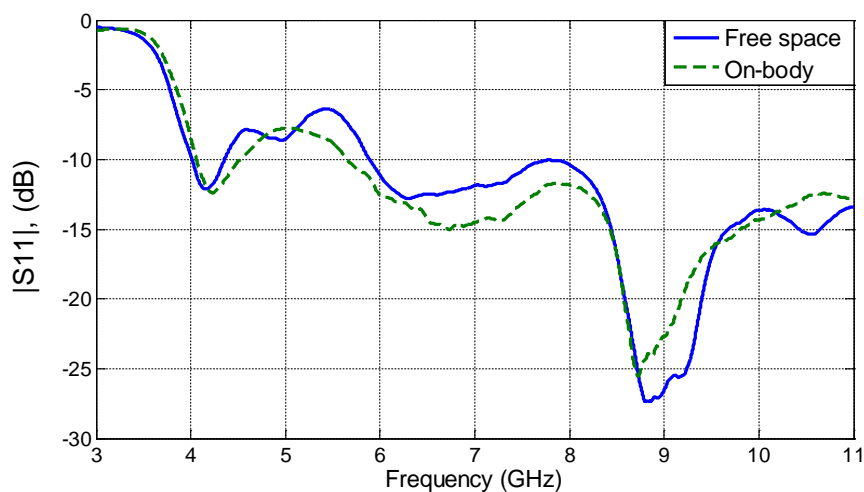


Figure 4.18: Measured S11 of the printed compact UWB antenna in free-space and on human body.

The free-space and on-body measured S11 for the antenna have been provided in Figure 4.18. The -10 dB impedance bandwidth of the antenna ranges from 5.9 GHz to > 11 GHz in free-space and 5.6 GHz to > 11 GHz on-body. Figure 4.19 illustrates the simulated 3D radiation patterns of the compact UWB antenna design at 6, 7.5 and 9 GHz frequencies. The directional nature of the antenna's radiation can be clearly noticed from the 3D patterns. The radiation of the antenna is mainly focussed towards its left side and stays like that for all the three frequencies.

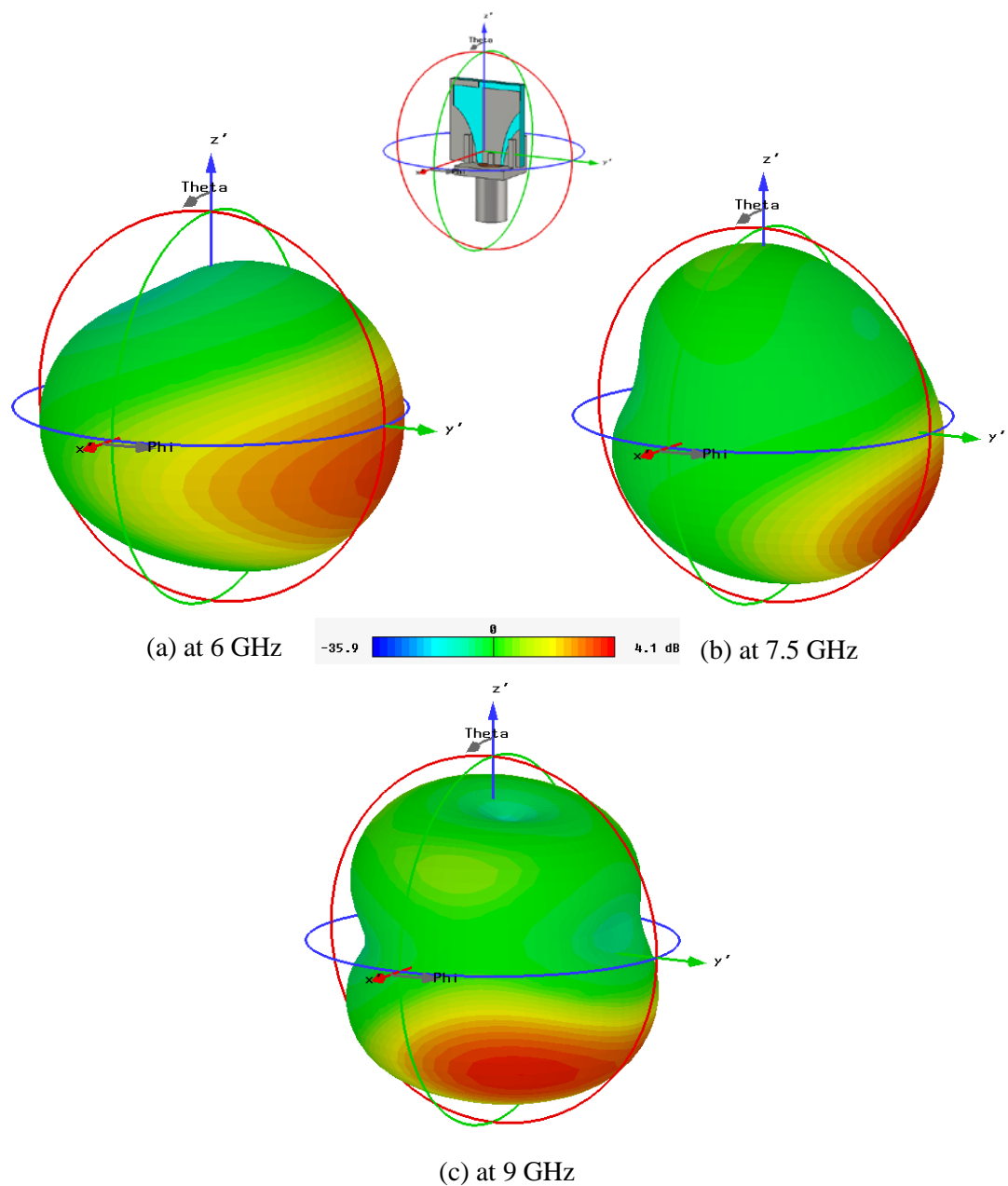


Figure 4.19: Simulated 3D radiation patterns of the printed compact UWB antenna for three different frequencies.

Just like the previous two antenna designs, the critical design parameters that determine the performance of the printed compact UWB antenna were investigated. The lengths of semi-major and semi-minor axes of the two ellipses that form the tapered slots in the left side of the antenna have been varied along with the width of the central patch  $w$ . The simulated S11 for different lengths of the semi-minor axis of the bigger ellipse ( $x1 = 6.2, 6.8$  and  $7.0$  mm) in the left side of the antenna have been illustrated in Figure 4.20. All the other parameters remained unchanged from their original values. It can be seen from Figure 4.20, that any change in length of  $x1$  from its optimum value significantly affects the S11 and also degrades the -10 dB bandwidth of the antenna.

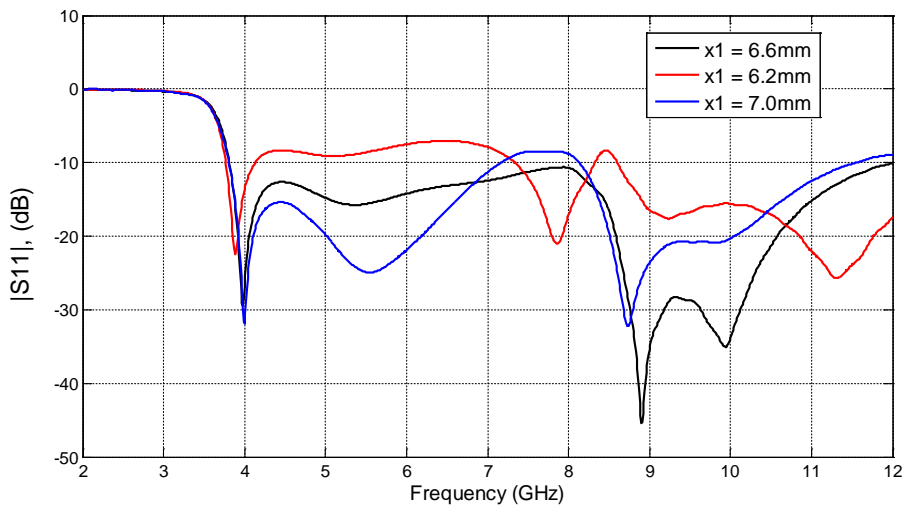


Figure 4.20: Simulated S11 of the printed compact UWB antenna for different lengths of the semi-minor axis of the bigger ellipse  $x1$ .

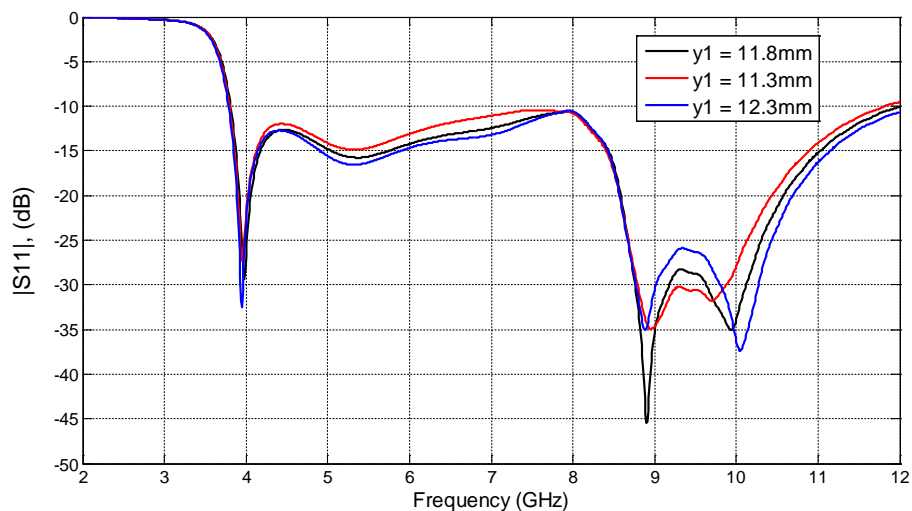


Figure 4.21: Simulated S11 of the printed compact UWB antenna for different lengths of the semi-major axis of the bigger ellipse  $y1$ .

Likewise, the length of semi-major axis of the bigger ellipse ( $y1 = 11.3, 11.8$  and  $12.3$  mm) in the left side of the antenna is varied. The simulated S11 results subsequently obtained are demonstrated in Figure 4.21. It can be noticed from Figure 4.21 that variation in the length of  $y1$  has an insignificant impact on the S11 of the antenna. The  $-10$  dB bandwidth also remained nearly unchanged despite the variations. After the bigger ellipse, the parameters of smaller ellipse in the left side of the antenna are varied.

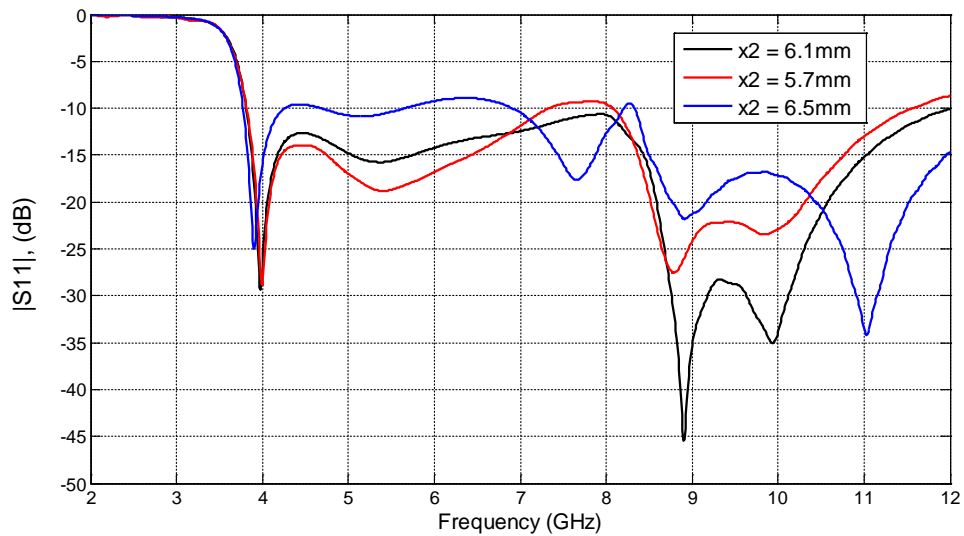


Figure 4.22: Simulated S11 of the printed compact UWB antenna for different lengths of the semi-minor axis of the smaller ellipse  $x2$ .

The simulated S11 for different lengths of the semi-minor axis of the smaller ellipse ( $x2 = 6.2, 6.8$  and  $7.0$  mm) while keeping all other parameters unchanged from their original values are provided in Figure 4.22. It can be seen from Figure 4.22 that any change in the length of  $x2$  from its optimal value has an evident impact on the S11 as well as the  $-10$  dB impedance bandwidth which gets most deteriorated in the 4 to 8 GHz range.

Similarly, the simulated S11 for different lengths of the semi-major axis of the smaller ellipse ( $y2 = 8.2, 8.7$  and  $9.2$  mm) have been illustrated in Figure 4.23 while keeping all other parameters unchanged from their original values. It is evident from Figure 4.23 that the length of the semi-major axis of the smaller ellipse  $y2$  has only minor effect on the S11 of the antenna. The  $-10$  dB impedance bandwidth of the antenna is also very similar for all the cases.

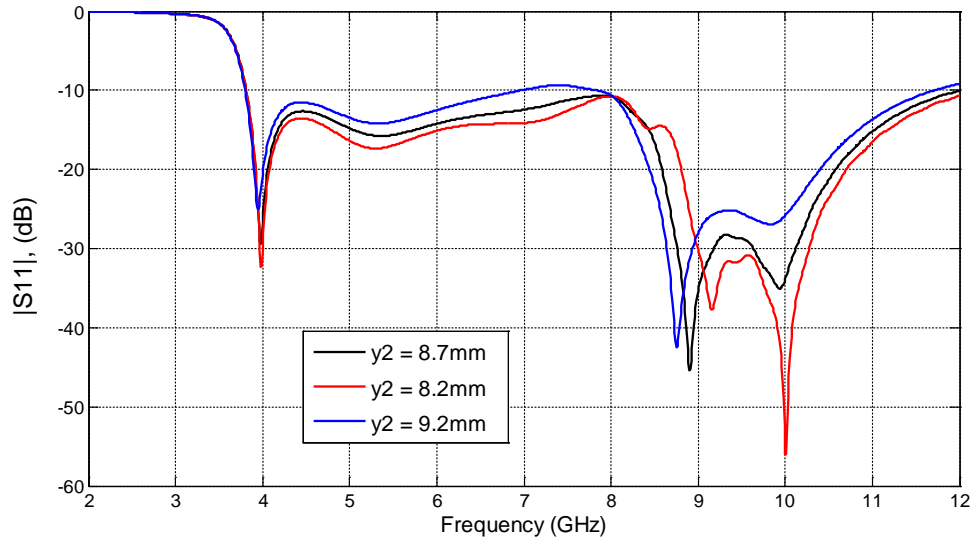


Figure 4.23: Simulated S11 of the printed compact UWB antenna for different lengths of the semi-major axis of the smaller ellipse  $y_2$ .

Lastly, the width of the central patch  $w$  is varied to assess its effect on the antenna performance. Figure 4.24 illustrates the simulated S11 results with different widths of the central patch ( $w = 6.8, 7.3$  and  $7.8$  mm). It is noticed from Figure 4.24 that any change to  $w$  from its optimal value leads to significant changes in the S11 and also substantially degrades the -10 dB impedance bandwidth of the antenna. Thus, this analysis has shown that the semi-minor axes of the two ellipses in the left side of the printed compact UWB antenna and width of the central patch are the most critical parameters to affect the operation of this antenna.

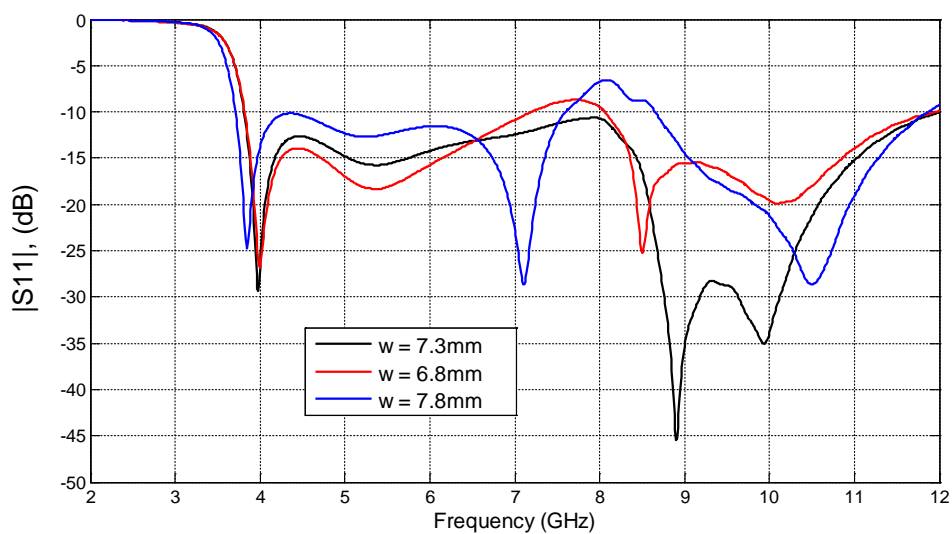


Figure 4.24: Simulated S11 of the printed compact UWB antenna for different widths of central patch  $w$ .

#### 4.1.4 Performance Comparison of the Three Antennas

All the three antenna designs presented in the previous sections are compact in size, operate close to the target frequency bandwidth of 6 to 10.6 GHz and seem appropriate to be used as the antenna for the UWB sensor at first look. The ultra-wideband antenna being the fundamental design constituent of the sensor node and hence the whole UWB localisation system, makes the selection of the suitable antenna quite crucial. In this section, a comparative study of the performance and characteristics of the three antennas has been carried out in order to choose the most appropriate design for our desired application. A comparison of the impedance bandwidths and dimensions of the three antenna designs has been provided in Table 4.1.

Table 4.1: Size and performance comparison of the three preliminary UWB antenna designs.

<b>Antenna Design</b>	<b>Dimensions (mm)</b>	<b>Surface Area (mm<sup>2</sup>)</b>	<b>Volume (mm<sup>3</sup>)</b>	<b>Free space bandwidth (GHz)</b>	<b>On-body bandwidth (GHz)</b>
Tapered-slot	11 × 14	154	234.7	6 to > 11	5.7 to > 11
Quasi self-complementary	12.8 × 18.4	235.5	358.9	6.5 to > 11	7.3 to > 11
Printed compact	13.5 × 14	189	288.1	5.9 to > 11	5.6 to > 11

All the three antennas are printed on RT/Duroid substrate with a thickness of 1.524 mm. The quasi self-complementary design has a partial ground plane at the back of the antenna. The other two antennas, namely printed compact UWB and the tapered-slot antenna have a coplanar waveguide design. The -10 dB impedance bandwidth of the tapered-slot antenna is from 6 GHz to > 11 GHz. The quasi self-complementary antenna design has a -10 dB bandwidth of 6.5 GHz to > 11 GHz. The printed compact UWB antenna's -10 dB impedance bandwidth is from 5.9 GHz to > 11 GHz. In terms of physical dimensions, the tapered-slot antenna is the smallest, with a surface area of just 154 mm<sup>2</sup>. The size of the antenna is an important feature since a physically large antenna will result in a bulky sensor node, which could potentially give disturbance to the end user and hinder smooth limb movement.

From the on-body S11 measurements of these antennas, it was observed that the tapered-slot and printed compact designs perform reasonably in the target bandwidth of 6 to 10.6 GHz and were least sensitive to the presence of human body. In contrast, the performance of the quasi self-complementary antenna design is degraded when placed near the human body. The -10 dB impedance bandwidth of the quasi self-complementary antenna becomes 7.3 GHz to > 11 GHz. This indicates that the self-complementary design might not be very suitable for on-body use. Out of the three designs, tapered-slot antenna has the most symmetrical structure. It has omnidirectional radiation patterns which are highly desirable for a wearable antenna. On the other hand, the radiation patterns of quasi self-complementary and printed compact antenna are directional in nature. Also, while investigating the design parameters it was observed that the tapered-slot design is not very sensitive to minor design variations. This helps in providing immunity to the antenna for accommodating minute inaccuracies that are unavoidable during the antenna fabrication process. Hence from these investigations, the tapered-slot antenna design appeared to be the most suitable for use in the body-mounted UWB sensor node. The tapered-slot design was further modified to create a novel miniature UWB antenna for final integration into the on-body sensor nodes. This antenna has been presented in the next section.

## **4.2 Miniaturised Design of Tapered-Slot Antenna**

### **4.2.1 Antenna Geometry**

The miniature tapered-slot UWB antenna is derived through modifications to the preliminary tapered-slot antenna design presented in Section 4.1.1. This novel antenna is designed and fabricated on Rogers RO 3210 substrate with a relative permittivity of 10.2 and thickness of 1.25 mm. The two curved side patches in the antenna design act as the ground and let the transition of impedance to occur smoothly. The overall structure of this miniature antenna is merely 7.9 mm by 16.38 mm in physical dimensions, which includes the antenna feed connector. The antenna is small enough that it can fit on a fingertip. Hence, it is ideally suited for wearable applications such as the UWB motion tracking system.

The antenna is fed through a miniature SMP connector. Just like its SMA counterpart, the SMP connector also has an impedance of  $50 \Omega$ . The SMP has a sub-miniature interface suitable for miniaturised high frequency coaxial modules up to 40 GHz [4]. It is very inexpensive and most importantly, is just 38% in volume as compared to the regular SMA end-launch. Hence the use of SMP aids in making this miniature antenna very compact and light-weight. The effect of the SMP feeding port should not be neglected because being used for this planar type of antenna it is no longer shadowed by the ground plane. Hence, the SMP port was also modelled along with the antenna structure and included in the simulations.

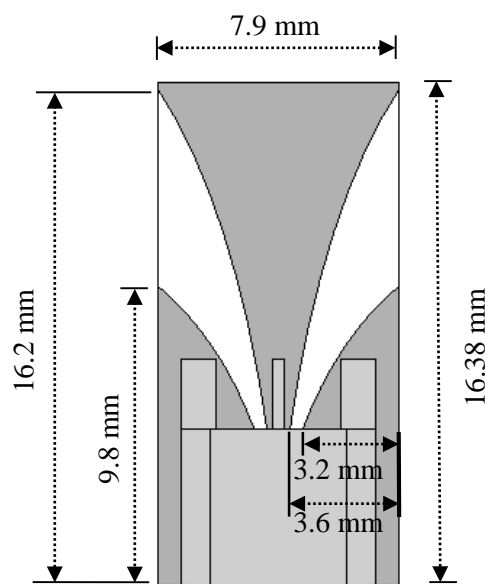


Figure 4.25: Dimensions and geometry of the miniature tapered-slot UWB antenna.

The curves of the two tapered-slots are characterized by the arcs of two ellipses with different lengths for semi-major and semi-minor axes. The lengths of the semi-major and semi-minor axes of the bigger ellipse are 21.5 mm and 7.88 mm respectively and that for the smaller ellipse are 11.95 mm and 8.05 mm respectively. In the design, the ellipses are not centred on the bottom two vertices of the antenna body. Instead, the centre points of the ellipses are located outside the structure of the antenna. The geometry of the miniature UWB antenna is illustrated in Figure 4.25. The ratio of semi-major to semi-minor axis within the design is the most significant parameter to affect the impedance matching of the antenna. There is no ground plane on the back side of this antenna design.

#### 4.2.2 Fabricated Miniature Tapered-Slot Antenna Performance

A prototype of the miniature tapered-slot antenna design was fabricated in the Antenna Measurement Laboratory at Queen Mary University of London. This is shown in Figure 4.26.



Figure 4.26: Fabricated prototype of the miniature tapered-slot UWB antenna.

Figure 4.27 shows the simulated and measured  $S_{11}$  of the miniature tapered-slot antenna in free-space and when placed on the human body. The  $S_{11}$  measurements were carried out in an anechoic chamber at Queen Mary University of London by using an Agilent N5232A PNA-L vector network analyser [5]. For on-body measurements, a real human test subject was used, with a height of 1.76 m and weight 75 kg. The antenna was placed at a gap of approximately 2 mm from the test subject's wrist.

The measured on-body -10 dB impedance bandwidth of the antenna is from 5.2 GHz to > 11 GHz. The free-space impedance bandwidth is from 5.7 GHz to 10 GHz in the simulations and from 5.4 GHz to > 11 GHz in the measurements. The measurement and simulation results demonstrate the operation of the miniature tapered-slot antenna in the upper band of UWB frequency range. The minor discrepancy between the simulation and the measurement results could be attributed to the effect of the feeding cable which had no balun. Hence, there are some surface currents on the wire which affect the antenna return loss. This problem will be solved when the antenna is integrated into the PCB of the sensor node since a feeding cable will not be there. This would eliminate the need for a balun.

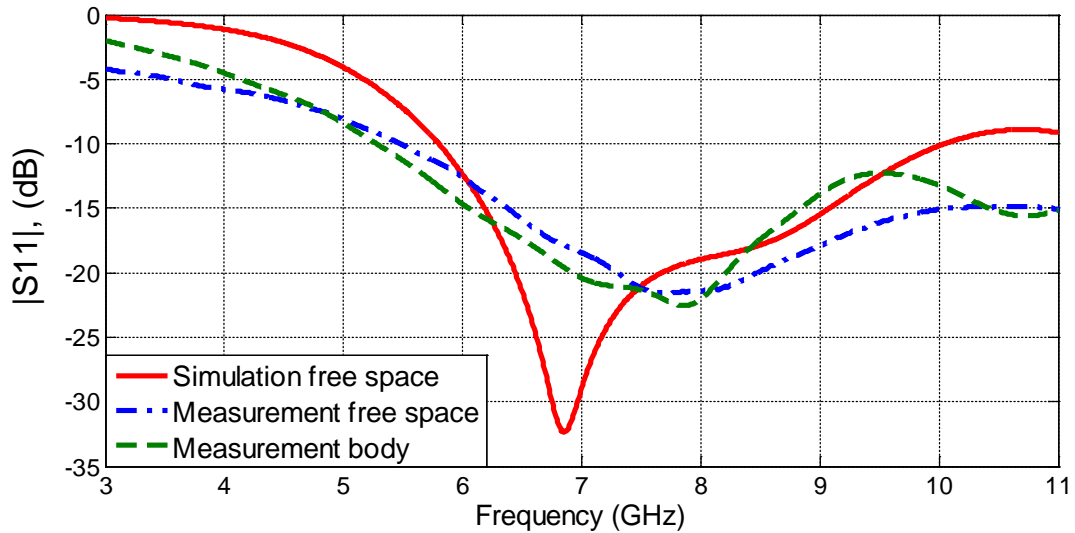


Figure 4.27: Measured and simulated S11 of the miniature tapered-slot UWB antenna.

To learn about the radiation characteristics of the fabricated antenna, some on-body radiation pattern measurements were also carried out. The radiation patterns were measured inside an anechoic chamber using an HP 8720ES vector network analyser. The same human male test subject was selected as in the case of the S11 measurements. The measurements required the test subject to stand on top of the rotating turn-table inside the anechoic chamber with the antenna placed on his body, as shown in Figure 4.28.

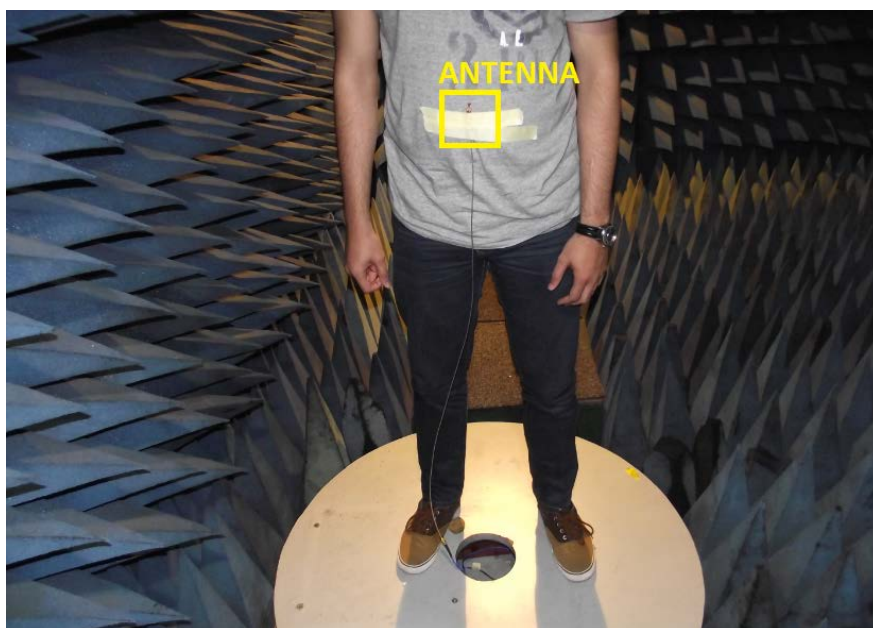


Figure 4.28: On-body radiation pattern measurement setup with the miniature UWB antenna attached to test subject's body inside an anechoic chamber.

The coordinate frame used for the radiation pattern measurements has been illustrated in Figure 4.29. The miniature UWB antenna acted as a receiver and the range horn antenna, connected to the second port of the network analyser acted as the transmitter. The free-space and on-body radiation patterns of the antenna were measured at 6, 7.5 and 9 GHz frequencies in the chamber. The antenna was placed in the middle of the test subject's abdomen with a gap of approximately 2 mm. The antenna was positioned facing outward, with its radiating elements parallel to the body of the human test subject.

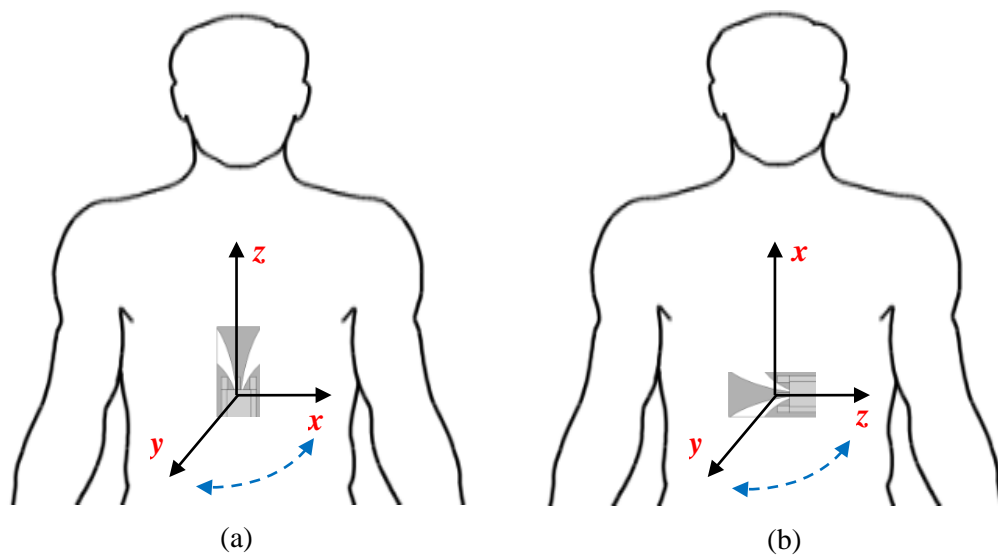


Figure 4.29: Coordinate frame and antenna orientation for the radiation pattern measurements in the (a) azimuth and (b) elevation planes.

Figure 4.30 (a) shows the normalized radiation patterns in free-space and on-body for the  $xy$ -plane, measured at 6, 7.5 and 9 GHz. The  $yz$ -plane radiation patterns were measured by placing the antenna perpendicular to its normal upright position by tilting it  $90^\circ$  towards one side. The antenna was fixed on the body with its face towards the transmitting horn antenna, which was rotated to transmit a horizontally polarised E-field. This has been illustrated in Figure 4.29 (b).

It can be observed from Figure 4.30 that the free space radiation patterns are nearly omnidirectional in the  $xy$ -plane. When the antenna is placed on the human body, the  $xy$ -plane radiation patterns become directive towards the off-body direction. This is due to the power absorption by the lossy human body tissue. Figure 4.30 (b) shows the normalized radiation patterns in free-space and on-body for the  $yz$ -plane, measured at 6, 7.5 and 9 GHz.

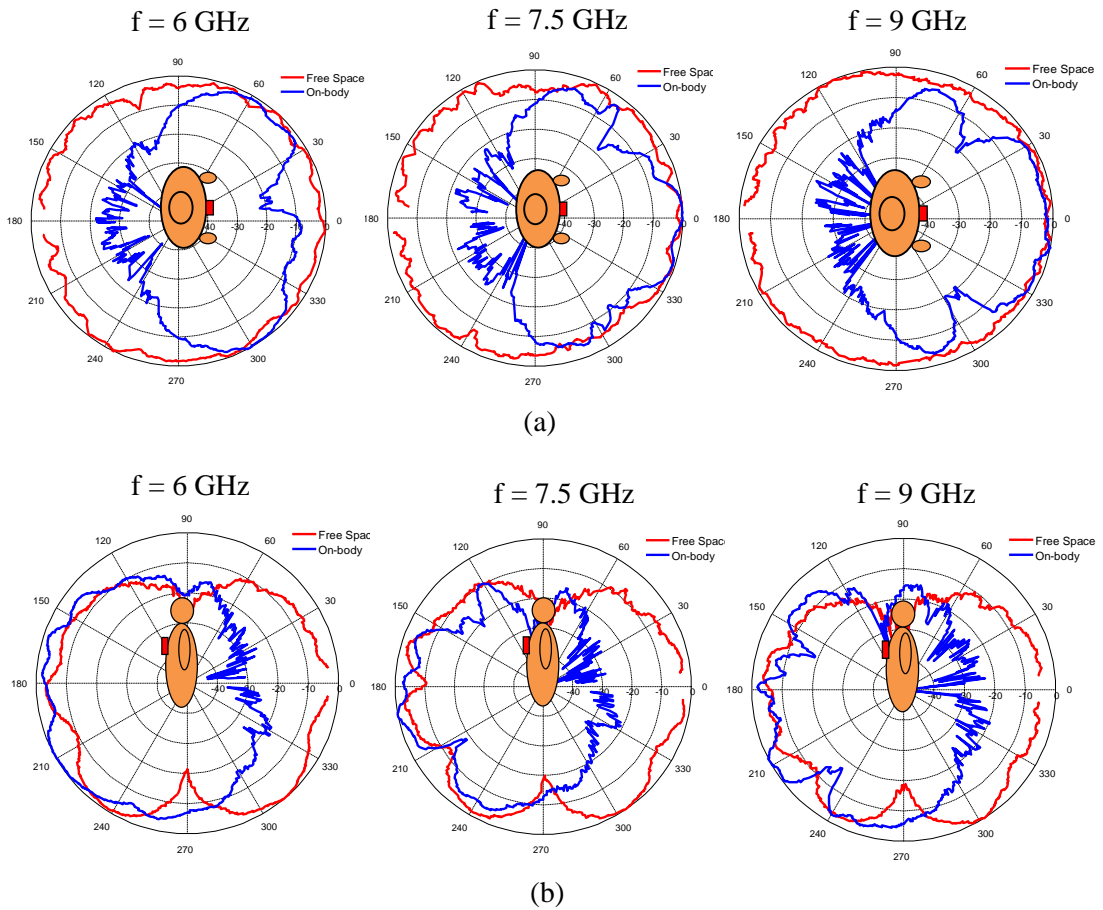


Figure 4.30: Free-space and on-body radiation patterns of the miniature UWB antenna at 6, 7.5 and 9 GHz in (a)  $xy$ -plane, (b)  $yz$ -plane. The radiation patterns have been normalized (maximum=0 dB).

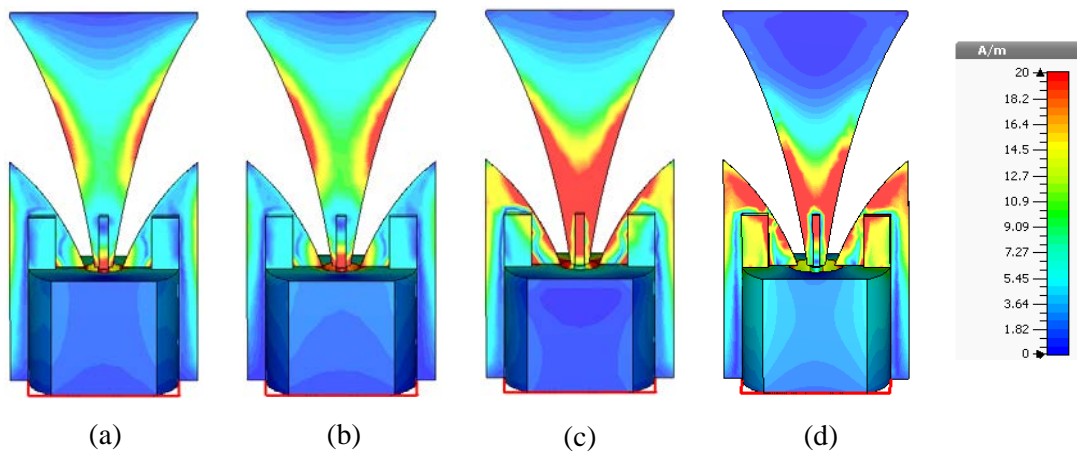


Figure 4.31: Simulated current distributions of the miniature UWB antenna at (a) 6 GHz, (b) 7.5 GHz, (c) 9 GHz and (d) 10.6 GHz.

The simulated current distributions for the miniature UWB antenna at four different frequencies, namely 6, 7.5, 9 and 10.6 GHz are presented in Figure 4.31. It can be

noticed from Figure 4.31 that the current in the antenna is mainly concentrated near the edges of the curved tapered-slots for all the four frequencies. As the frequency increases, more current is observed near the curved edges. Therefore, the performance of the antenna is pivotally dependent on the semi-major and semi-minor axes of the tapered-slot curves in the design.

### **4.3 Analysis with Simplified Human Body Models**

The human body is an indispensable entity when designing a body mounted antenna. Because of the electrical characteristics of body tissues, proximity to the human body has a considerable effect on the operation of an antenna. This is due to electromagnetic absorption in tissues, which leads to changes in the antenna input impedance, reduction in efficiency, shifting of resonant frequency and distortion in radiation patterns [6]–[9]. Hence, the design of such an antenna becomes more challenging due to the complex electromagnetic properties of body tissues. Although there are several human body models available that mimic the characteristics of the real human body in a numerical design, they demand large amounts of computational time and resources, which ultimately leads to increased costs and design timescales. One solution to this problem could be the use of simplified human body equivalent phantoms in the simulations instead of the complicated full body models. But the simple characterisation of human body can result in inaccurate estimates of antenna parameters, especially when considering the entire UWB frequency band. Moreover, it is not very clear which model, in terms of geometrical shape, size and material properties, provides more accurate results and saves computational time by correctly replicating the characteristics of real human tissues.

This analysis aims at understanding which body model provides the simulation results closest to the actual measurements with real human body, by emulating the electrical characteristics of human tissues and at the same time, not being too demanding in terms of complexity, computation time and resources. For this purpose, four simplified human body models were investigated with the miniature UWB antenna. The models were varied in terms of their cross-section, size and dispersion properties to select the best model with regard to simplicity, accuracy and reduced simulation time. These simplified four-layered human equivalent body models with different

cross sections, namely flat, rectangular, cylindrical and half cylindrical were utilized to study the effect of these models on the miniature UWB antenna's S11 and radiation patterns. These four body models have been illustrated in Figure 4.32.

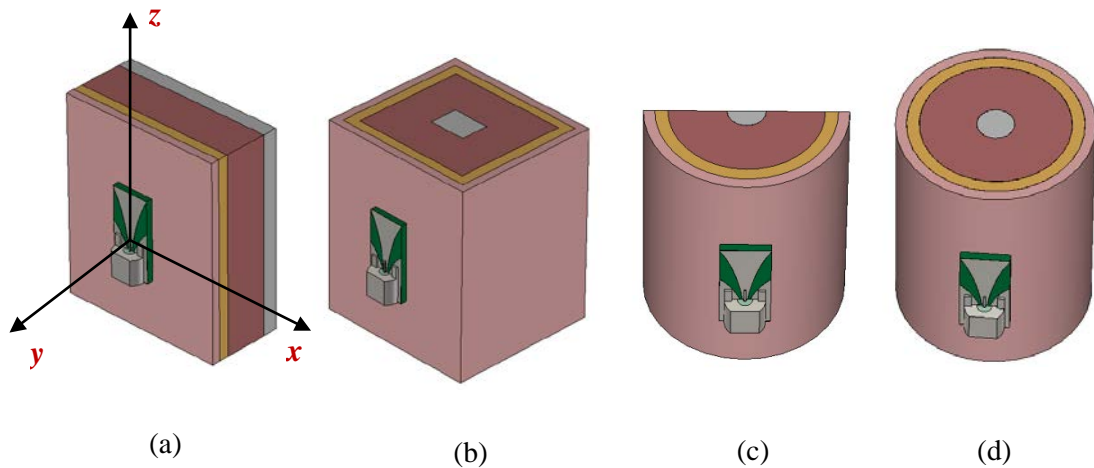


Figure 4.32: Four simplified human body models used in simulations, namely (a) flat, (b) rectangular, (c) half-cylindrical and (d) cylindrical.

The four layers considered in the body models are: skin with 1.75 mm thickness; fat with 2 mm thickness; muscle with 9 mm thickness and bone with 3 mm thickness. The thickness values of the tissues were selected to resemble a portion of the human forearm [10]. For the cylindrical and half-cylindrical models, these thickness figures are the radius values of the respective layers in the two models. The rectangular model is similar to the flat model, but has each tissue layer enclosed within another tissue layer, which makes it twice as thick as the flat model. The lengths of all these models have been limited to 40 mm. Both dispersive and non-dispersive models have been used for the analysis.

In the first scenario, the four human equivalent phantoms were modelled with non-dispersive tissue layers. For this, the electrical properties of human tissues at the centre frequency of the antenna's operating band, which is 8.3 GHz, were used. Table 4.2 provides the relative permittivity and conductivity values used for each tissue layer in the body models at 8.3 GHz frequency [11]. Figure 4.33 provides the miniature UWB antenna's simulated S11 with the four non-dispersive models kept at distance  $d$  of 1, 4 and 6 mm from the antenna back surface.

Table 4.2: Electrical properties of human body tissues at 8.3 GHz frequency.

Tissue	Relative Permittivity	Conductivity [S/m]
Skin	32.907	6.1394
Fat	4.7372	0.46415
Muscle	45.085	8.211
Bone	13.642	3.1865

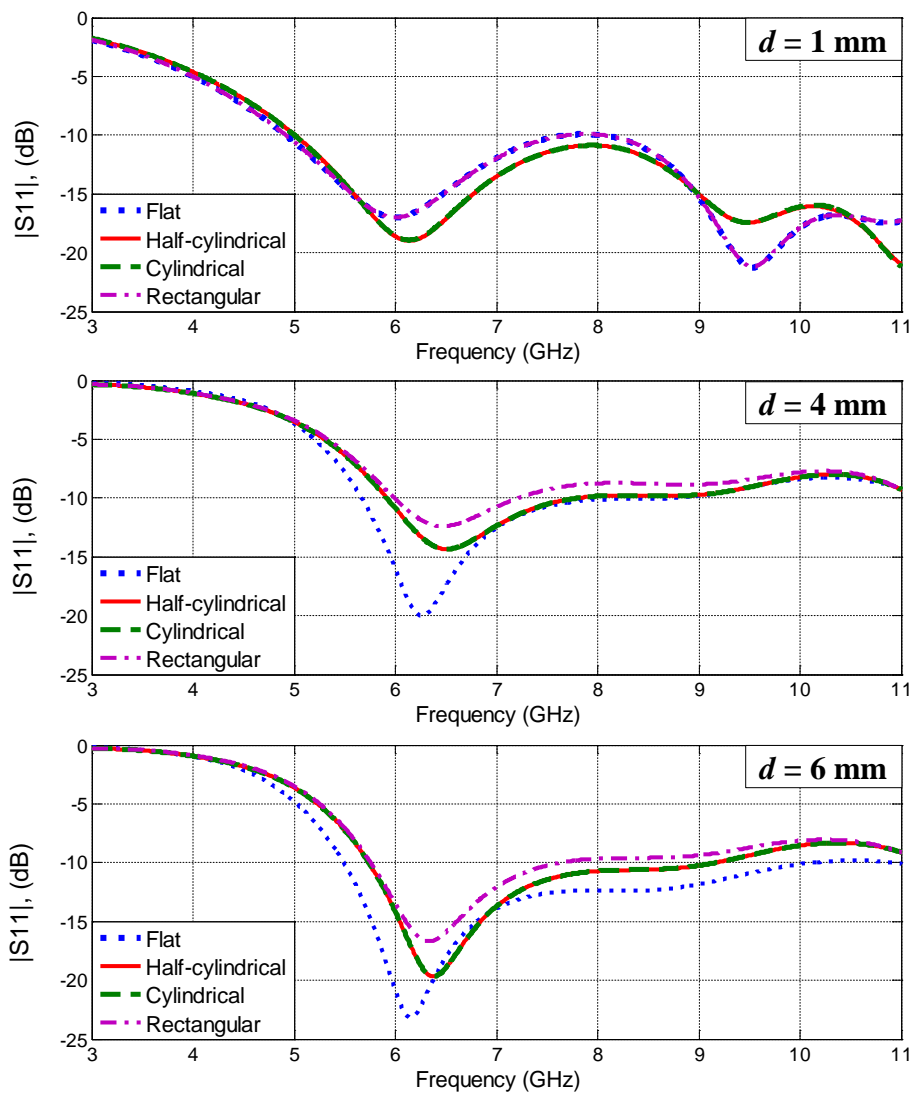


Figure 4.33: Simulated  $S_{11}$  of the antenna using the four simplified non-dispersive body models for distance  $d = 1, 4,$  and  $6$  mm.

The effect of the four body models on the radiation patterns of the miniature UWB antenna was also analysed. The simulated radiation patterns of the miniature antenna

when placed 1 mm away from the four non-dispersive body models have been presented in Figure 4.34. The patterns have been presented for 6, 7.5 and 9 GHz frequencies. The coordinate frame used for the radiation patterns has been illustrated in Figure 4.32 (a).

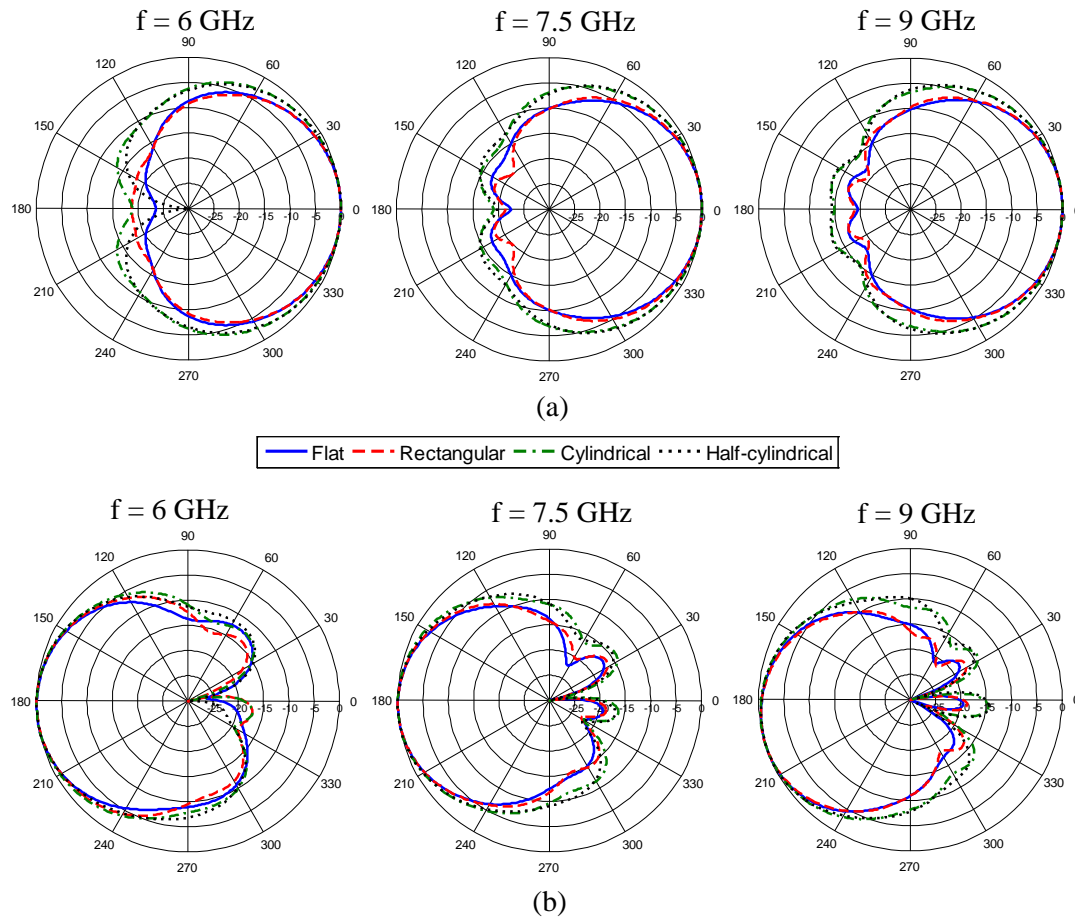


Figure 4.34: Simulated normalized radiation patterns of the miniature UWB antenna using four simplified non-dispersive body models at 6, 7.5 and 9 GHz in (a)  $xy$ -plane ( $0^\circ$  is in  $y$ -direction) and (b)  $yz$ -plane ( $180^\circ$  is in  $y$ -direction).

For further investigations, the same simplified body models were created taking into consideration the dispersive nature of the body tissues for the entire UWB frequency range, since the electrical properties of human tissues change with frequency. The physical dimensions of these models were kept exactly the same as used for the non-dispersive models. The modelling and simulations were carried out using CST Microwave Studio 2013 software package, which provides the option to include dispersive characteristics of biological tissues for the desired frequency range. Figure 4.35 provides the antenna's simulated  $S_{11}$  with the four dispersive models kept at distance  $d$  of 1, 4 and 6 mm from the antenna.

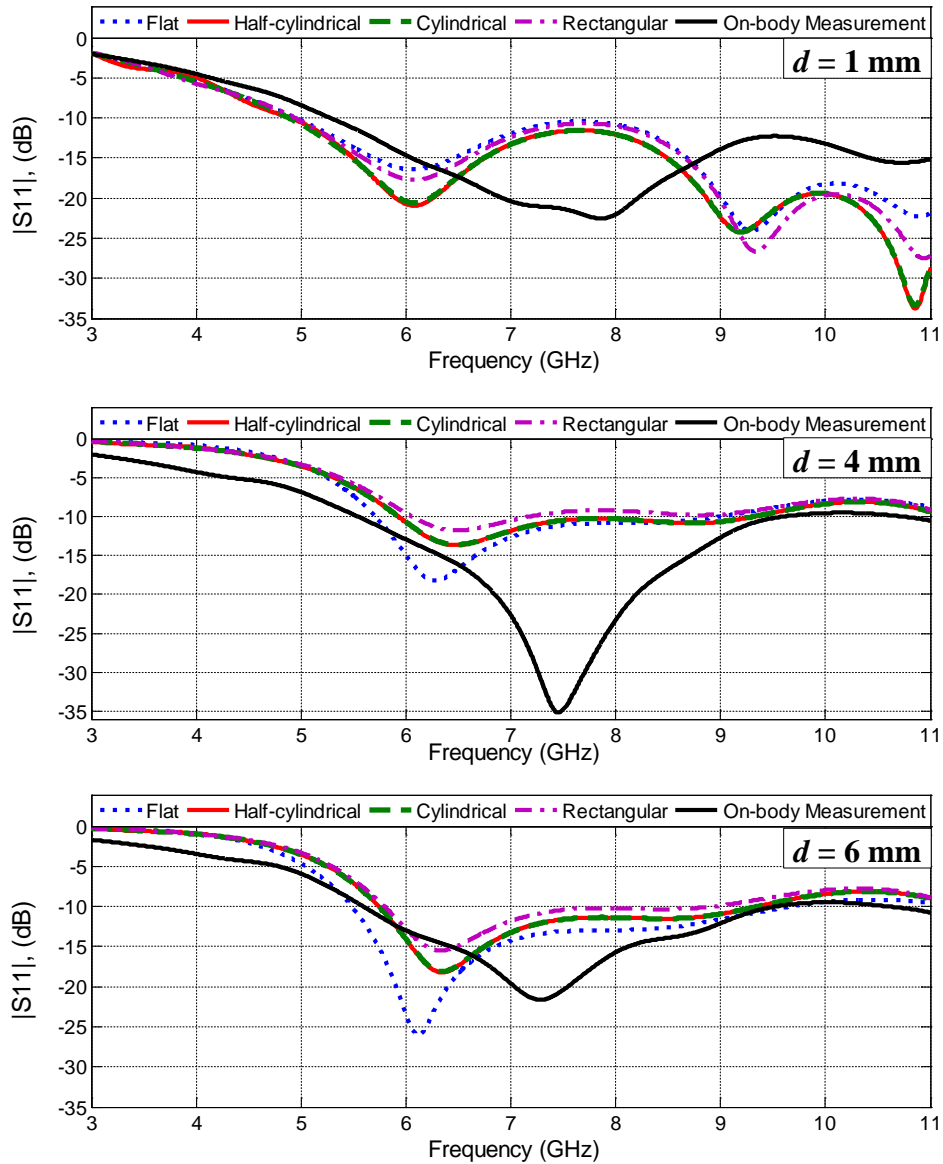


Figure 4.35: Simulated S11 of the antenna using the four simplified dispersive body models for distance  $d = 1, 4,$  and  $6$  mm along with the on-body measurements.

Figure 4.36 illustrates the simulated radiation patterns of the antenna when placed 1 mm away from the four dispersive body models at three different frequencies. It can be noticed from Figure 4.33 and Figure 4.35 that there is a slight change in the S11 compared to the results of the non-dispersive models. The changes become more pronounced at the higher frequencies. On the other hand, the simulated radiation patterns of the antenna do not show any significant difference in terms of shape whether used with the dispersive or non-dispersive body models. Both models are able to predict the shape of the actual on-body radiation patterns of the miniature antenna (as illustrated in Figure 4.30) quite closely. But, the non-dispersive models take almost four times longer for simulation compared to the dispersive models due to

sparser meshing in CST when dispersion is switched on. Since the dispersive models provide more realistic properties to actual human tissues and also consume significantly less computation time, it is reasonable to say that dispersive models are a better alternative of the two. Hence, dispersive models have been used to obtain more reliable simulation results. Also, it can be observed that the cylindrical and half-cylindrical models give exactly the same results, which shows that the half-cylindrical model can certainly substitute the cylindrical model as its simulation time is nearly half. The S11 with the rectangular model generally follow the flat body model's S11 results but with a reduced bandwidth and takes almost twice the computation time compared to the flat model. Also the radiation patterns of the flat and rectangular model are almost identical. Thus the flat model appears to be a better alternative to the rectangular model in terms of computation time.

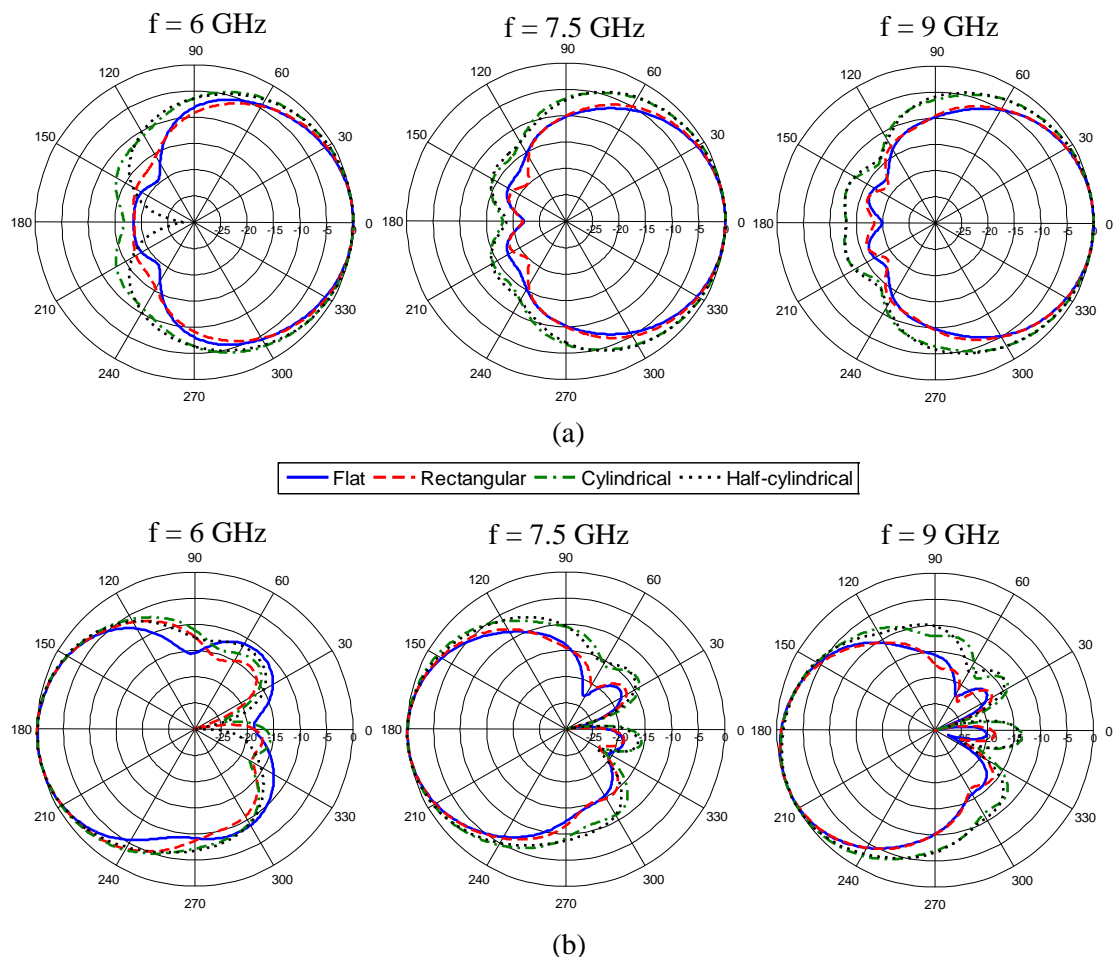


Figure 4.36: Simulated normalized radiation patterns of the miniature antenna using the four simplified dispersive body models at 6, 7.5 and 9 GHz in (a)  $xy$ -plane ( $0^\circ$  is in  $y$ -direction) and (b)  $yz$ -plane ( $180^\circ$  is in  $y$ -direction).

Next, the effect of length of the simplified body models on the impedance bandwidth of the antenna was examined. A smaller body model that gives comparable results to a bigger counterpart will provide the advantage of taking much less computation time and resources without compromising on the accuracy of the simulation estimates. The flat and half-cylindrical dispersive models were chosen for this study. Figure 4.37 illustrates the four different sizes of the flat and half-cylindrical models used in the simulations, the largest model being the original size (40 mm) and the three successive models reduced by 8, 16 and 24 mm, i.e. they are 32 mm, 24 mm and 16 mm in length respectively. The simulated S11 of the antenna when placed 1 mm away from different sizes of the two body models are provided in Figure 4.38.

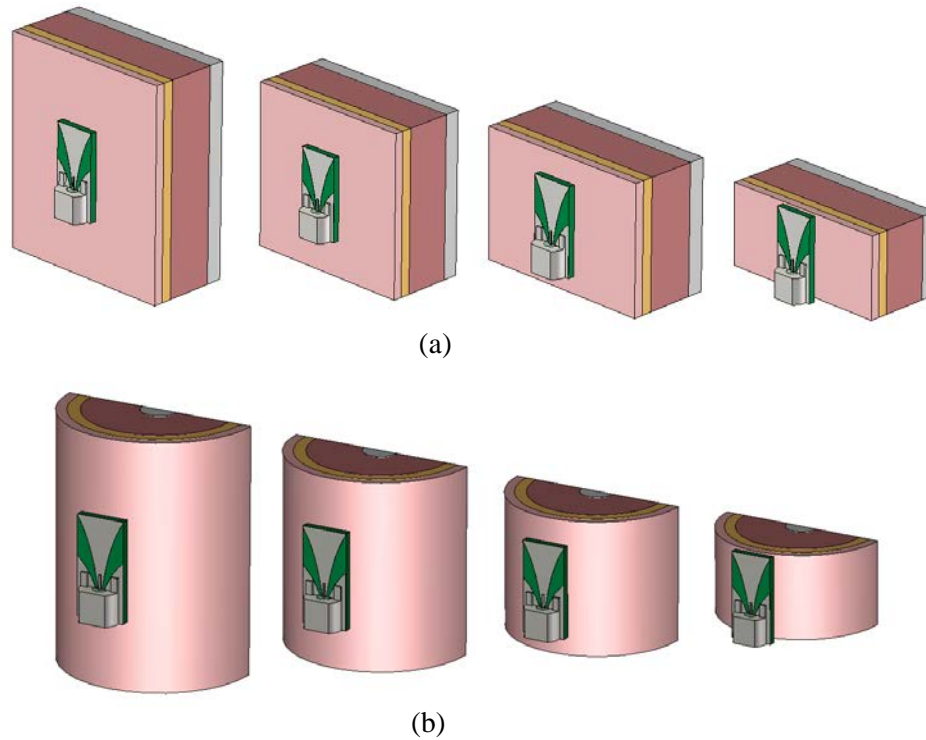
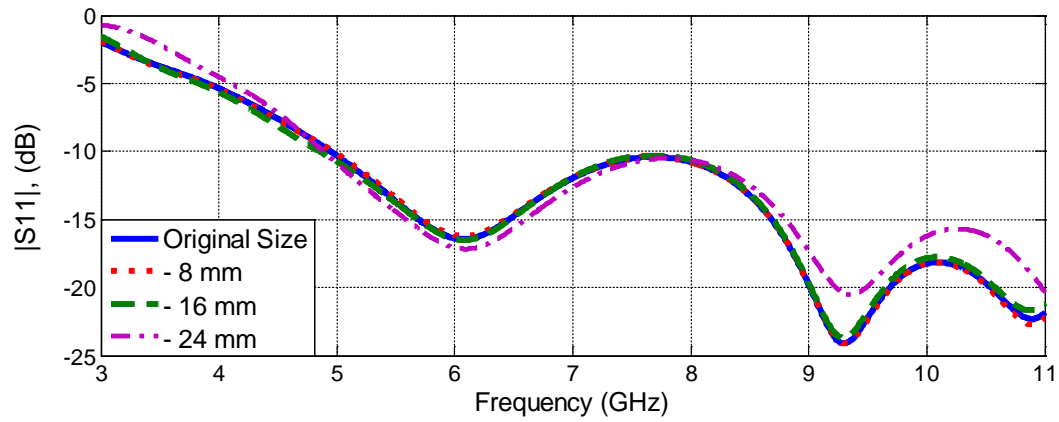


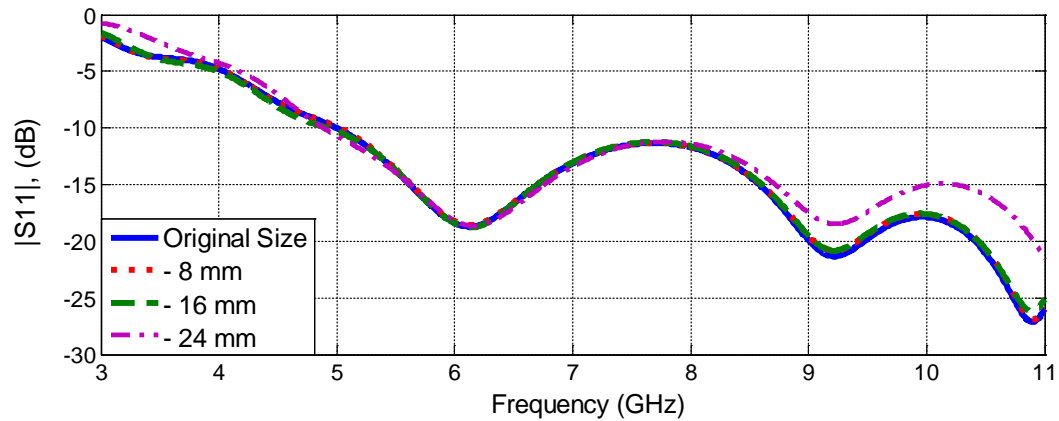
Figure 4.37: Size variation of the (a) flat and (b) half-cylindrical body models.

It can be observed from Figure 4.38 that reducing the lengths of both the flat and half-cylindrical models has a negligible effect on the antenna's reflection coefficient as long as the models are larger than the antenna structure. When the models become smaller than the structure of the antenna, the reflection coefficient curves show some variation, especially at higher frequencies. Similar results were seen with the other  $d$  values. This shows that using large sizes of simplified body models does not necessarily make the results more accurate. Hence, by keeping the body models just

slightly bigger than the antenna structure, it is possible to achieve almost the same results but with reduced computational time.



(a)



(b)

Figure 4.38: Simulated S11 of the antenna with different sizes of the (a) flat and (b) half-cylindrical body models.

Some on-body S11 measurements of the miniature UWB antenna were carried out by placing the antenna near a real human test subject's wrist. The measurements were done inside the Antenna Lab at Queen Mary University of London. For a comparative analysis, the measurements were done with separation gaps of 1, 4 and 6 mm between the antenna and the body, similar to the numerical scenarios studied earlier. The separations gaps between the body and the antenna were achieved by using layers of 1 mm thick cotton pads as 'air gap'. The measurement setup with the antenna mounted

on a test subject's wrist along with the cotton pad is illustrated in Figure 4.39. The  $S_{11}$  for the three different separation gaps are presented in Figure 4.40.

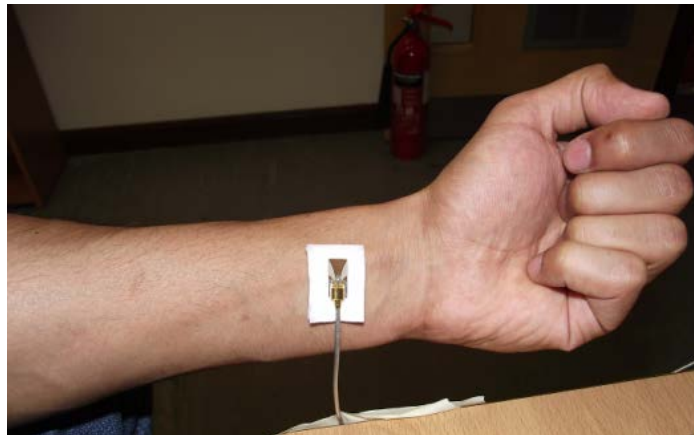


Figure 4.39: Miniature UWB antenna mounted on a test subject's wrist for on-body  $S_{11}$  measurements.

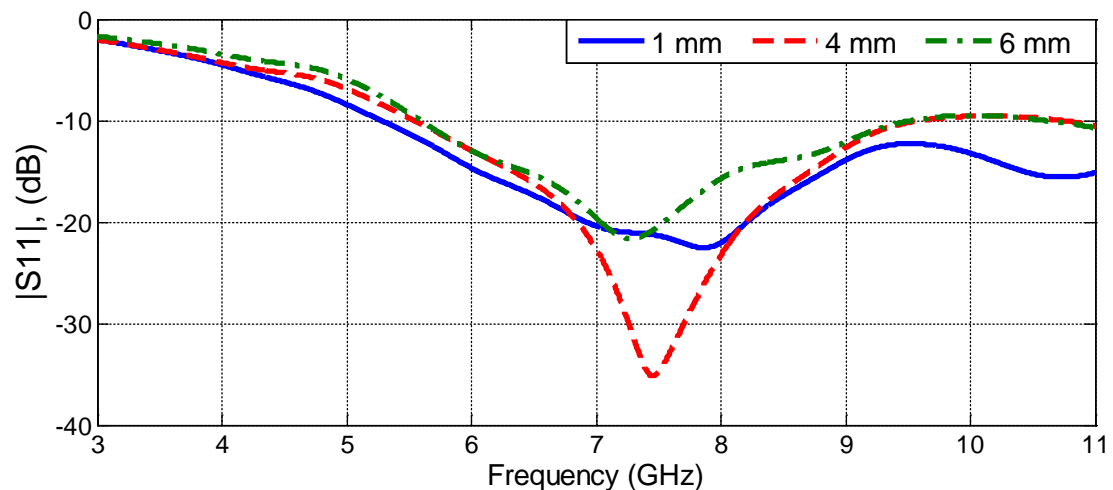


Figure 4.40: On-body  $S_{11}$  measurements of the antenna for three different separation gaps.

A comparison of the antenna's measured on-body  $S_{11}$  (solid black line) with the simulation results using dispersive body models has been provided in Figure 4.35. From Figure 4.35 and the previous analysis, it is observed that the dispersive flat body model provides the closest match to the actual measurements. The flat body model is able to predict the -10 dB impedance bandwidth of the antenna with the real human body most precisely. The measured on-body -10 dB bandwidths of the antenna are from 5.2 GHz to > 11 GHz, 5.6 GHz to 9.5 GHz and 5.5 GHz to 9.6 GHz when the antenna is kept 1, 4 and 6 mm away respectively. Using the dispersive flat model, the

simulated -10 dB bandwidths of the antenna are 5 GHz to > 11 GHz, 5.7 GHz to 9 GHz and 5.5 GHz to 9.7 GHz for 1, 4 and 6 mm separation gaps respectively. The dispersive half-cylindrical model also gives somewhat similar simulation results to the flat model, providing a reasonable estimate of the antenna reflection coefficient with human body. Besides, it can be noticed that although the flat model is able to predict the on-body -10 dB bandwidth of the antenna very closely, the resonance in the S11 curve gets shifted by 1 GHz between the simulation and measurement results. This shift could be attributed to the fact that for the free-space S11 of the antenna, the same resonance shift of about 1 GHz was observed between simulation results and measurements (See Figure 4.27). We ascribe this shift to the effects of the feeding cable since it has no balun.

#### **4.4 Summary**

In this chapter, a unique CPW-fed miniature UWB antenna has been presented. The geometry of this miniature antenna is discussed and the simulation as well as measurement results are provided. This novel antenna design uses an SMP connector and is small enough that it can fit on a fingertip. To the best of our knowledge, this is the smallest wideband planar antenna in this frequency range. The antenna is much smaller than several other compact antennas such as the ones mentioned in [7], [12] and [13], having a similar frequency range. The on-body S11 and radiation pattern measurements of the antenna clearly display its ability to operate reasonably in the vicinity of the human body. The compact size, wideband characteristics, omnidirectional radiation and decent on-body performance support the suitability of this antenna for wearable UWB applications.

Also, a numerical and experimental study of the influence of various types of simplified human equivalent phantoms and the actual human body on the reflection coefficient and radiation patterns of the miniature UWB antenna has been provided. Four multi-layered body models, with different geometries and cross-sections, along with both dispersive and non-dispersive characteristics have been used in the analysis. The study aimed at understanding which body model provides the simulation results

closest to the actual measurements with real human body, by correctly emulating the electrical characteristics of human tissues and at the same time not being too demanding in terms of complexity, computation time and resources. This could ultimately help to reduce development costs and design timescales. It has been understood that the inclusion of dispersion properties of the human tissues in simulations is necessary to accurately predict the antenna parameters and also to reduce simulation time. Measurements using a real human body have shown that the dispersive flat model estimates the antenna impedance bandwidth performance with human body most accurately. Also, it was observed that the simplified body models can be reduced in size to be just slightly bigger than the antenna structure without getting any noticeable changes to the simulation results. Overall, it can be concluded that the flat and half-cylindrical dispersive models are the best options within the studied models in terms of computational time and accurate prediction of the antenna parameters with real human body.

## References

- [1] A. Rahman, A. Alomainy, and Y. Hao, "Compact Body-Worn Coplanar Waveguide Fed Antenna for UWB Body-Centric Wireless Communications," in *2nd European Conference on Antennas and Propagation (EuCAP)*, 2007, pp. 1–4.
- [2] L. Guo, S. Wang, X. Chen, and C. Parini, "A Small Printed Quasi-Self-Complementary Antenna for Ultrawideband Systems," *IEEE Antennas Wirel. Propag. Lett.*, vol. 8, pp. 554–557, 2009.
- [3] L. Guo, S. Wang, X. Chen, and C. Parini, "A printed miniaturised antenna for ultra wideband systems," in *International Workshop on Antenna Technology (iWAT)*, 2010, pp. 1–4.
- [4] "Jyebao RF and Microwave Co., Product Catalogue." [Online]. Available: <http://www.jyebao.com.tw/files/download/SMP.pdf>.
- [5] "Agilent 2-Port and 4-Port PNA-L Network Analyzer," 2013. [Online]. Available: <http://cp.literature.agilent.com/litweb/pdf/N5235-90004.pdf>.
- [6] P. S. Hall and Y. Hao, Eds., *Antennas and Propagation for Body-Centric Wireless Communications*, 2nd ed. Artech House, 2012.
- [7] K. Y. Yazdandoost and K. Hamaguchi, "Very small UWB antenna for WBAN applications," in *5th International Symposium on Medical Information and Communication Technology*, 2011, pp. 70–73.
- [8] M. M. Khan, I. Mobin, G. Palikaras, and E. Kallos, "Study of a small printed quasi-self-complementary ultra wideband antenna for on-body applications," in *4th Computer Science and Electronic Engineering Conference (CEEC)*, 2012, pp. 179–183.
- [9] I. Oppermann, M. Hämäläinen, and J. Iinatti, Eds., *UWB: Theory and Applications*. John Wiley and Sons, 2004.
- [10] A. Christ, A. Klingenbock, T. Samaras, C. Goiceanu, and N. Kuster, "The dependence of electromagnetic far-field absorption on body tissue composition

in the frequency range from 300 MHz to 6 GHz,” *IEEE Trans. Microw. Theory Tech.*, vol. 54, no. 5, pp. 2188–2195, May 2006.

- [11] “Dielectric Properties of Body Tissues in the frequency range 10 Hz-100 GHz,” *Italian National Research Council - Institute for Applied Physics*, 2012. [Online]. Available: <http://niremf.ifac.cnr.it/tissprop>.
- [12] N. Chahat, M. Zhadobov, R. Sauleau, and K. Ito, “A compact planar UWB antenna for on-body communications,” in *Proceedings of the 5th European Conference on Antennas and Propagation (EUCAP)*, 2011, pp. 3627–3630.
- [13] T. Tuovinen, K. Y. Yazdandoost, and J. Iinatti, “Monopole Ultra Wideband antenna for on-body communication in Wireless Body Area Network,” in *Loughborough Antennas & Propagation Conference*, 2011, pp. 1–4.

# **Fidelity Analysis of the Miniature UWB Antenna Using Different Excitation Pulses**

Unlike its narrowband counterpart, the design of an ultra-wideband antenna is determined not only by its  $S_{11}$  characteristics, but also by its ability to preserve the pulse shape as it employs the unorthodox carrier-free modulation. Antennas for UWB systems are required to have very broad impedance bandwidth, and stable and constant channel transfer response. Ordinary wideband antennas will cause distortion to the transmitted short pulses because they radiate various frequency components from different parts [1]. Hence, to characterize the antenna's overall performance for pulse-based transmission, parameters like pulse distortion, antenna fidelity etc. also need to be analysed for a reliable design. Since data may be contained in the shape or precise timing of the pulse, a clean impulse response (that is, with minimal pulse distortion) can be considered as the primary requirement of a good UWB antenna [2].

This chapter presents the study of the miniature UWB antenna from a system point of view. Numerical and experimental investigations of the fidelity factor of the miniature

antenna have been undertaken. Different excitation pulse types were employed to study the effect of the antenna and the propagation channel on the received pulse quality. Since this antenna is intended to be used in a pulse-based time-of-flight motion tracking system, minimal distortion to the received pulse is required for the accurate retrieval of the sent data. The fidelity analysis has been carried out both in free-space and with the antenna mounted on the human body considering an extended spatial range compared to previously reported work in [3]–[5]. Although the distortion of pulse in various angular directions has been investigated in [6] and [7], however none of these investigations have studied the impact of human body on the received pulse. Furthermore, the effect of fidelity on the communication performance of an ultra-wideband antenna system has been investigated in this chapter, by modelling an impulse based UWB system. System performance has been evaluated based on the bit error rate (BER) and signal-to-noise ratio parameters. Such an analysis of the impact of fidelity on a UWB system's communication performance, such as BER has not been presented or discussed in any open literature previously.

## **5.1 Measurements of the Miniature UWB Antenna System**

As in any wireless communication system, the antenna performs an imperative part in an ultra-wideband system too. The UWB antenna acts like a filter and is a critical component in UWB radio systems. The basic effect of antennas is that they produce the derivative of the transmitted or received pulse waveform. This also has the effect of extending the duration of the transmitted and received pulse. This extension of pulse duration decreases the time resolution of the system. The antenna has a greater impact in UWB than in narrowband systems because of the very large bandwidth of a UWB signal [8]. In the case of narrowband antennas, it is approximated that the antenna's characteristics are consistent over the entire bandwidth and the basic parameters, such as gain and return loss, have little variation across the operational band.

In contrast, UWB systems often employ extremely short pulses for data transmission. In other words, enormous bandwidth has been occupied. Thus the antenna cannot be treated as a “spot filter” any more but a “band-pass” filter. In this case, the antenna imposes more significant impacts on the input signal. Therefore, a primary

requirement of a decent UWB antenna is to have a good impulse response, i.e. with minimal pulse distortion. The transfer function of an antenna system is determined by the characteristics of both transmitting and receiving antennas, as well as the propagation channel between them [9]–[11]. Hence, the system transfer function could be utilized to assess the behaviour of an antenna system. Since the miniature UWB antenna is meant for on-body operation, the analysis has been carried out with measurements in both free-space and with the antennas mounted on the human body.

### 5.1.1 Measurement Setup and System Details

The measurement system comprised of two identical miniature tapered-slot UWB antennas connected to an Agilent N5232A PNA-L vector network analyser [12], as shown in Figure 5.1.

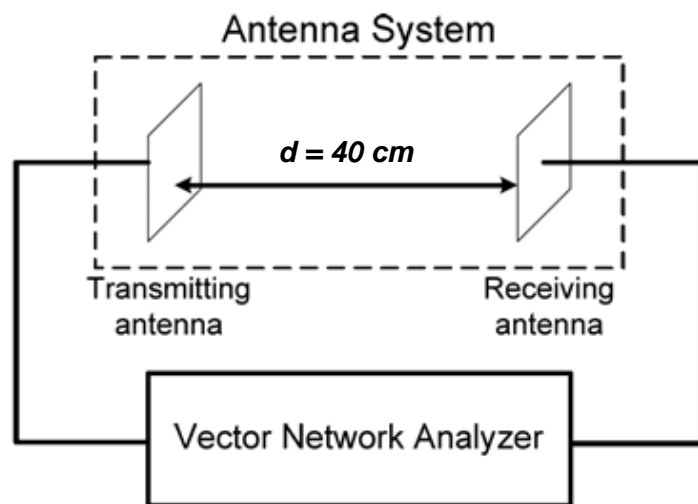


Figure 5.1: Measurement setup of the miniature tapered-slot UWB antenna pair.

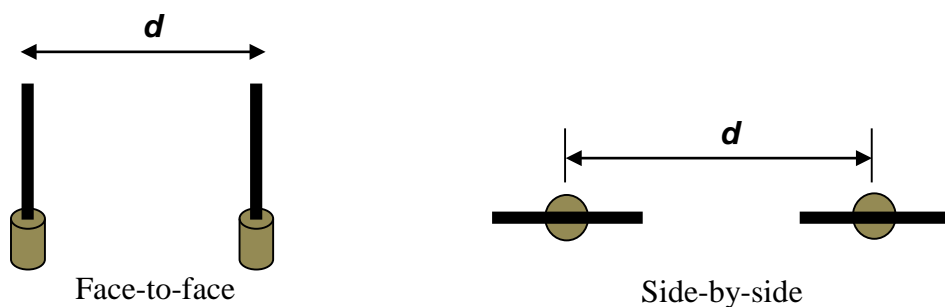


Figure 5.2: Face-to-face and side-by-side antenna orientations used in the analysis.

These antennas were aligned in two different orientations, namely face-to-face and side-by-side to each other. This has been illustrated in Figure 5.2. The distance between the two antennas was selected to be 40 cm for both the orientations. The measurements of the antenna system transfer function ( $S_{21}$ ) are carried out by using a vector network analyser. The measurements were done in the Antenna Lab at Queen Mary University of London. Two sets of measurements were undertaken, first with the antennas in free-space and second with the antennas mounted on the fingertips of a human test subject, as shown in Figure 5.3.

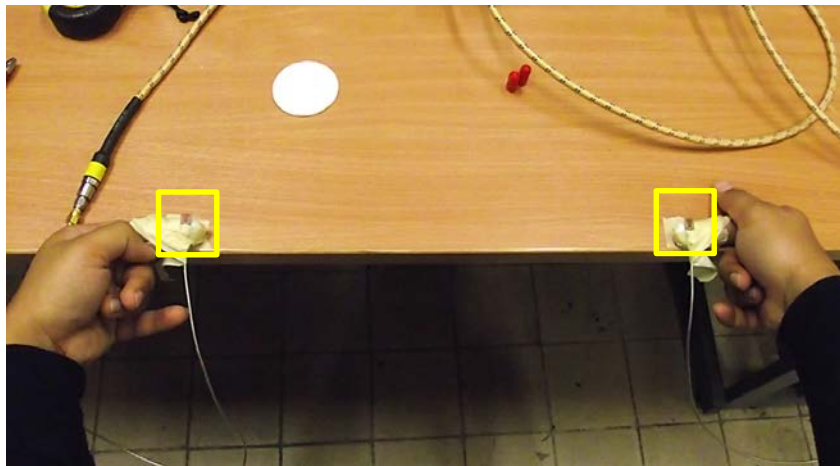
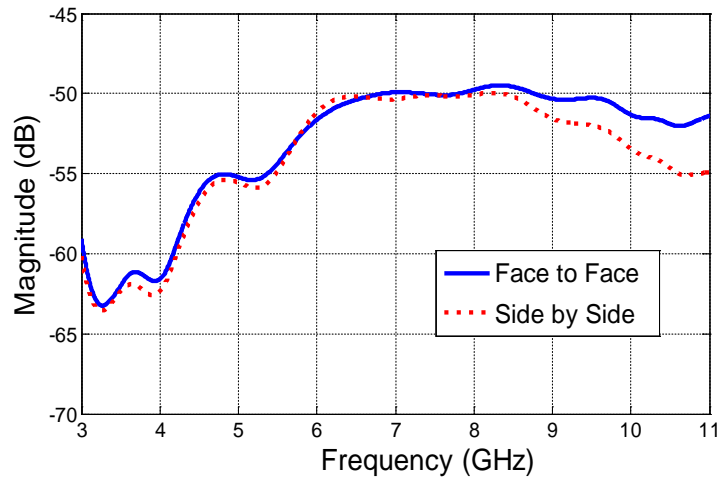


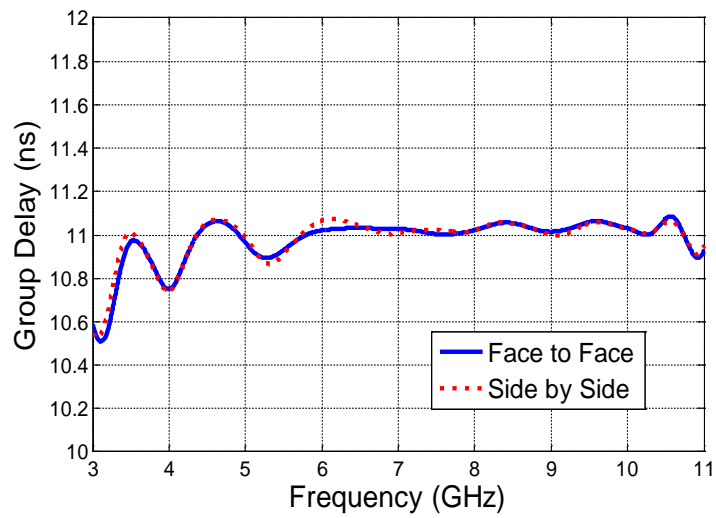
Figure 5.3: Miniature UWB antennas mounted on the fingertips of a human test subject for on-body measurements.

### 5.1.2 Measurement Results and Analysis

The measured transfer function magnitude as well as the group delay for both the antenna orientations in free-space are shown in Figure 5.4. The group delay was obtained directly from the vector network analyser. In order to have minimal distortion in the received signal, the transfer function of an antenna system should have a flat magnitude and linear phase response across the operating frequency band. To compute the phase response of the transfer function, group delay is commonly used. Group delay gives the rate of change of the transmission phase angle with respect to frequency. A constant group delay is required in most cases, which indicates a linear phase response, i.e. the phase changes linearly with frequency.



(a)



(b)

Figure 5.4: Measured (a) transfer function magnitude and (b) group delay for the miniature UWB antenna system in free-space.

It can be noticed from Figure 5.4 (a), that the magnitude of the transfer function is relatively flat within the 6 - 10.6 GHz frequency range. Similarly, it can be seen from the group delay plot in Figure 5.4 (b) that the phase response is almost linear across the 6 - 10.6 GHz frequency range. The operating band of the transfer function, which is 10 dB below the peak, for the face-to-face case is from 4.2 GHz to > 11 GHz and for side-by-side case is from 4.3 GHz to > 11 GHz. The operating bands for both the scenarios are nearly the same, which shows the omnidirectional characteristics of the antenna. The group delays for the two cases are quite stable with variation of less than 0.3 ns within the frequency range of 4.5 - 11 GHz, which corresponds to a linear

phase response within this frequency range. The same set of measurements was repeated with the two antennas mounted upon the fingertips of a human test subject, as shown in Figure 5.3. The measured on-body transfer function magnitude and group delay for both the antenna orientations have been illustrated in Figure 5.5.

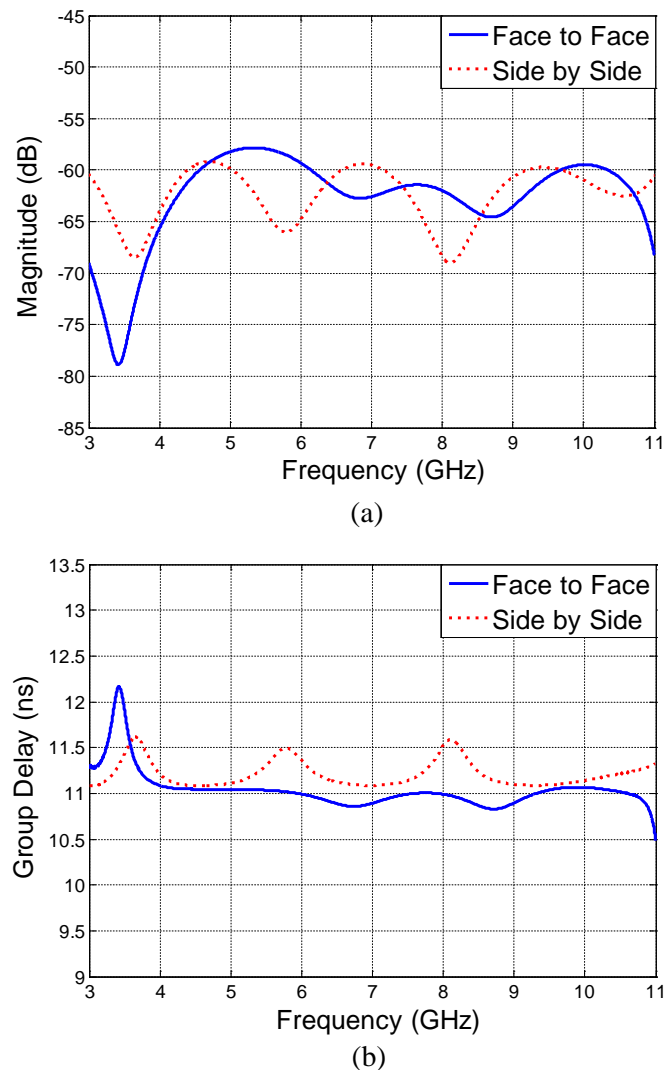


Figure 5.5: Measured (a) transfer function magnitude and (b) group delay for the miniature UWB antenna system when mounted on the fingertips.

It can be seen from Figure 5.5 that the antenna transfer function and phase response get a little distorted when the antenna pair is placed on the human body. The transfer function is not really flat, especially for the side-by-side alignment. Still, the group delay is relatively linear across the 4 - 10.6 GHz frequency range. The group delay has a variation of less than 0.2 ns for face-to-face scenario and less than 0.5 ns for the side-by-side scenario within the frequency range of 4 - 10.6 GHz. This shows that the

antenna has a fairly linear phase response within this frequency range even when mounted on the human body.

In this experimental analysis, a Gaussian pulse modulated by a continuous sine wave carrier was used to excite the antenna system. For the pulse, a carrier frequency of 6 GHz and pulse parameter  $a = 350$  ps were chosen, as the spectrum of this pulse sits entirely within the UWB band of 3.1 - 10.6 GHz, as defined by the FCC [13]. The modulated Gaussian pulse is excited to the miniature UWB antenna pair and the measured received pulse is obtained. In order to deduce the received pulse, the Inverse Fast Fourier Transform (IFFT) is carried out on the measured transfer function data. This transforms the data from frequency domain to the time domain. This IFFT of the system transfer function is actually the system impulse response. The calculated system impulse response is then convolved with the input pulse, which provides the received pulse [14]. A comparison between the received pulses for the different antenna pair orientations, namely face-to-face and side-by-side for free-space measurements have been provided in Figure 5.6.

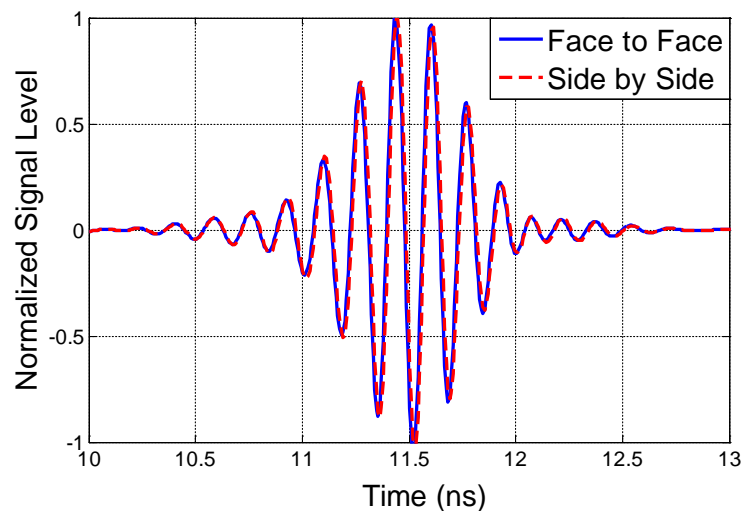


Figure 5.6: Received signal waveforms in free-space for two different antenna orientations using a sine-modulated Gaussian input.

It can be noticed from Figure 5.6 that the received waveforms for both the cases, face-to-face and side-by-side, match with each other very well. This indicates to the omnidirectional radiation characteristics of the miniature UWB antenna. The received pulses mostly follow the shape of the source pulse and only have some negligible

distortions and ringing effects. Similarly, a comparison between the measured received pulses for the two antenna orientations when mounted on the fingertips of a test subject has been shown in Figure 5.7.

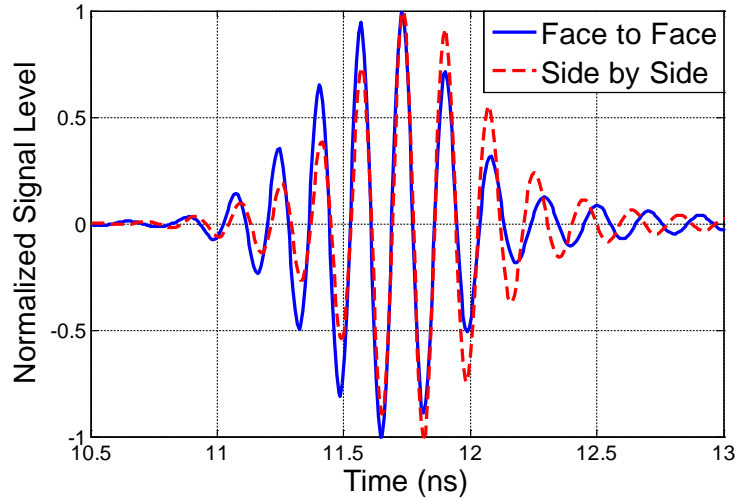


Figure 5.7: Received signal waveforms for two different antenna orientations when mounted on fingertips, using a sine-modulated Gaussian input.

It can be noticed from Figure 5.7 that the received waveforms for both the scenarios match with each other quite well, with only some minor variation between the two pulses. Both the received pulses for on-body measurement are very similar to the shape of the source pulse with some slight distortions and ringing effects, similar to the free-space measurement case. Since major energy of the modulated Gaussian pulse is completely located within the operating band of the antenna system transfer function, this leads to minimal distortions in the received pulses. Thus, an optimal input pulse can be selected to suit the specific operating bandwidth needs for different antenna systems. This has been studied extensively in the next section along with the fidelity analysis of the miniature UWB antenna in various angular directions.

## 5.2 Pulse Fidelity Analysis of the Miniature UWB Antenna

Another important parameter that needs to be studied in the context of this research work is the Fidelity. The ultra-wideband motion tracking system will involve transfer of UWB signal pulses between the antennas. But in such kind of communication, the received UWB signal pulses practically will not resemble the source pulses and will

be normally distorted in shape. Therefore, a measure of the similarity between the received pulse and the input pulse is highly desirable and valuable to indicate how well the performance of the UWB antenna system is and how well the antennas communicate with each other so that the sent data could be recovered correctly at the receiving end.

Fidelity is a well-defined parameter used to evaluate the quality of a received pulse waveform. In time-domain formulation, the fidelity between waveforms  $x(t)$  and  $y(t)$  is defined as a normalised correlation coefficient [15]:

$$F = \max_{\tau} \left[ \frac{\int_{-\infty}^{+\infty} x(t) \cdot y(t - \tau) \cdot dt}{\sqrt{\int_{-\infty}^{+\infty} |x(t)|^2 \cdot dt \int_{-\infty}^{+\infty} |y(t)|^2 \cdot dt}} \right], \quad (5.1)$$

Here, the source pulse  $x(t)$  and the received pulse  $y(t)$  are normalized by their energy. The fidelity factor  $F$  is the maximum correlation coefficient of the two signals by changing the time delay  $\tau$ . It denotes the similarity between the source pulse and the received pulse.

When the two signal waveforms are equivalent to each other, the fidelity reaches its peak, i.e. unity, which indicates the antenna system does not distort the input pulse at all. In the extreme scenario that the two pulses are totally different in shape, the fidelity reduces to the minimum value of zero. Practically, a UWB system yields fidelity between 0 and 1. Clearly, a high fidelity is always desirable. The fidelity depends not only on the antenna characteristics, but also on the excitation pulse; thus, it is also a system-dependent parameter. Fidelity factor makes use of the transmission coefficient in the frequency domain to calculate the correlation between the input and output pulses of an antenna system [16].

In this section, the fidelity analysis of the miniature tapered-slot UWB antenna is presented. The main focus here is to study the effect of different excitation pulses and the vicinity of human body on the level of distortion experienced by the received pulse. The further investigation shows that the distortions of the received signals may be mitigated if the source pulse bandwidth were to fully fit into the band of the system transfer function.

### 5.2.1 Use of Different Excitation Pulses for Fidelity Analysis

The Gaussian pulse is the classic choice for ultra-wideband communication due to its short duration in time domain and wide spectrum. In this investigative study, four different input pulses, namely first-order Gaussian, second-order Gaussian, fourth-order Gaussian and a Gaussian pulse modulated by a continuous sine-wave carrier were used to excite the antenna system. These four pulses can be defined through the following equations [17]:

$$f_1(t) = \frac{-2t}{\alpha^2} e^{-\left(\frac{t}{\alpha}\right)^2}, \quad (5.2)$$

$$f_2(t) = \left[ -\frac{2}{\alpha^2} + \frac{4t^2}{\alpha^4} \right] \cdot e^{-\left(\frac{t}{\alpha}\right)^2}, \quad (5.3)$$

$$f_4(t) = \left[ \frac{12}{\alpha^4} - \frac{48t^2}{\alpha^6} + \frac{16t^4}{\alpha^8} \right] \cdot e^{-\left(\frac{t}{\alpha}\right)^2} \quad (5.4)$$

$$f_{mod}(t) = \sin(2\pi f_c t) \cdot e^{-\left(\frac{t}{\alpha}\right)^2} \quad (5.5)$$

Here  $\alpha$  is the pulse parameter and  $f_c$  is the carrier frequency. The first, second and fourth-order Gaussian pulses have pulse parameter  $\alpha = 70$  ps. For the sine-modulated Gaussian, a carrier frequency  $f_c = 6$  GHz and pulse parameter  $\alpha = 350$  ps are chosen. The shapes of the four excitation pulses in the time domain have been illustrated in Figure 5.8.

Pulse parameter  $\alpha$  denotes the time characteristic. Larger value for  $\alpha$  corresponds to wider waveform in the time domain but narrow bandwidth in the frequency domain [18]. Decreasing the value for  $\alpha$  shortens the pulse and consequently the bandwidth increases. The normalized Power Spectral Density (PSD) curves of the four excitation pulses are presented in Figure 5.9.

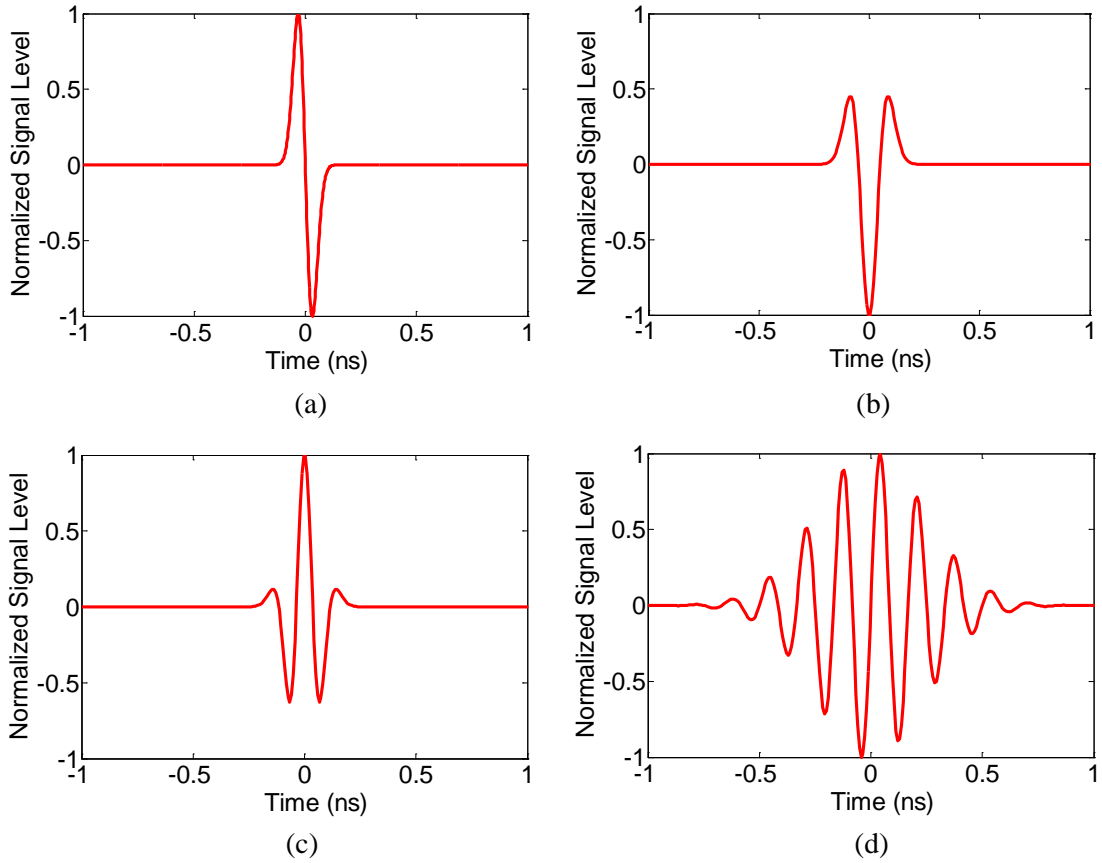


Figure 5.8: Excitation pulses used in the fidelity analysis, namely (a) First-Order, (b) Second-Order, (c) Fourth-Order and (d) Sine-modulated Gaussian.

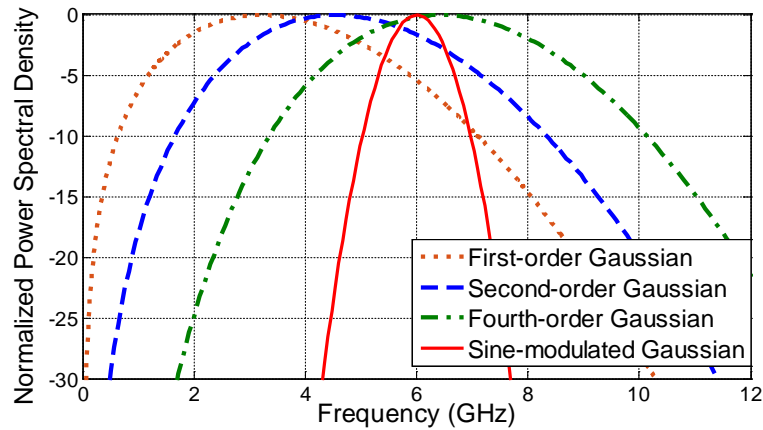


Figure 5.9: Normalized power spectral density curves of the four different excitation pulses in frequency domain.

### 5.2.2 Received Pulse Waveforms

The measurement setup comprised of two identical miniature UWB antennas aligned face-to-face and placed 100 cm away from each other (to ensure captured data were in the far-field of both antennas). The measurements were carried out inside the

Anechoic Chamber at Queen Mary University of London by using an Agilent N5232A PNA-L vector network analyser [12]. The transmitter and receiver antennas were connected to the two-port PNA and the transfer function ( $S_{21}$ ) was measured over the frequency range of 3 GHz to 11 GHz. Since the antenna is meant for on-body operation, the analysis was also carried out with the receiver antenna mounted on a real human test subject's shoulder while keeping the transmitter antenna 100 cm away in free-space, facing the receiver antenna at the same height.

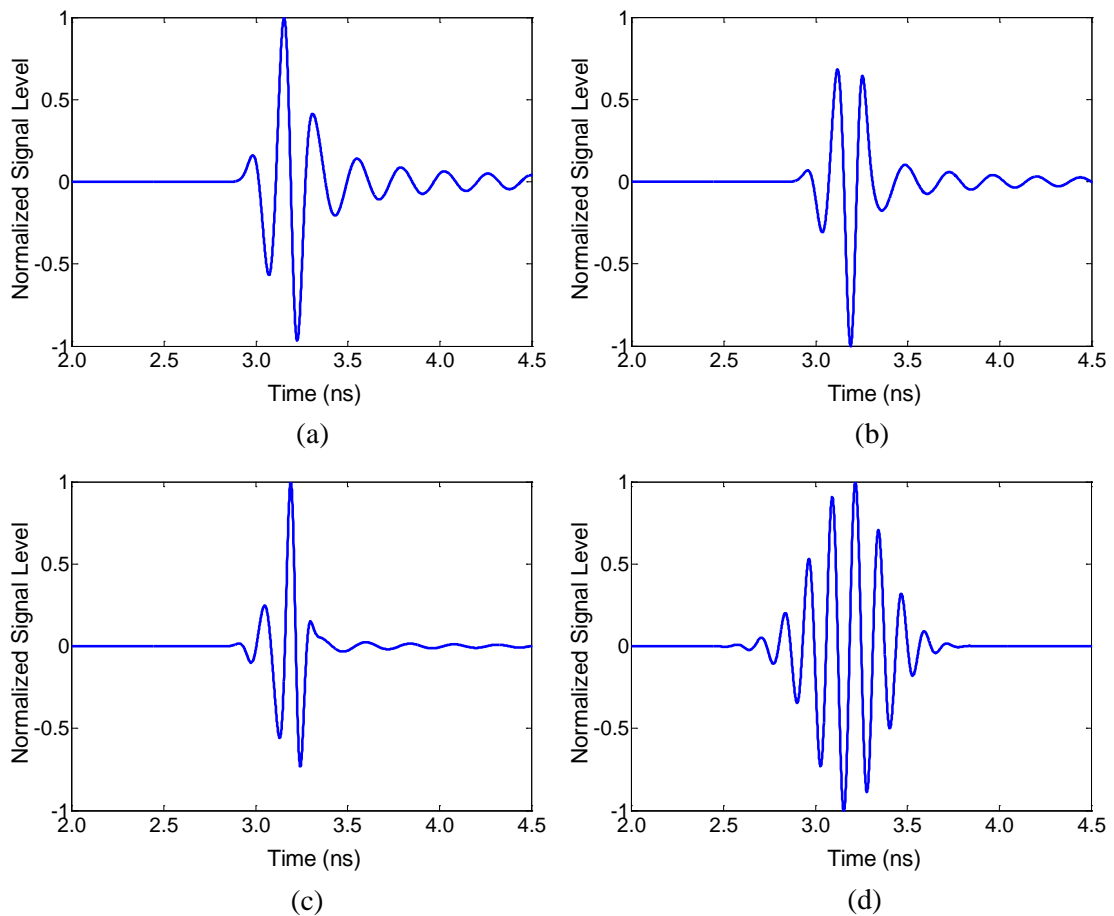


Figure 5.10: Received signal waveforms, namely (a) First-Order Gaussian, (b) Second-Order Gaussian, (c) Fourth-Order Gaussian and (d) Sine-modulated Gaussian for free-space fidelity measurements.

This setup, with the two identical antennas and the associated propagation channel could be considered as a linear time-invariant system. Any linear time-invariant system can be characterized by that system's impulse response. Using the convolution approach, the received pulse can be deduced by convolving the input pulse with the impulse response of the antenna system [14]. Firstly, the Inverse Fast Fourier

Transform (IFFT) is carried out on the measured transfer function data. This transforms the data from frequency domain to the time domain. This IFFT of the system transfer function is actually the System Impulse Response. The calculated system impulse response is then convolved with the input pulse, which provides the received pulse. The received pulse will inherit the distortion and dispersion induced by the two antennas and the propagation channel system to the input pulse.

The measured received pulses obtained by using the convolution approach for the four different excitation signals in free-space measurements have been illustrated in Figure 5.10. It could be noticed that barring the first-order Gaussian pulse, all the other received pulses are very similar to their respective input pulses, with only slight distortions and ringing effects. Even for the first-order Gaussian input, the received pulse generally follows the shape of the source pulse and only has some ringing and small variations. The slight distortions in the received pulses can be attributed to the filtering characteristics of the antenna system that acts as a band pass filter. It can be noticed from Figure 5.9 that the spectrum of the first-order Gaussian pulse does not entirely sit within the operating band of the antenna system transfer function. The spectrum bandwidth of this pulse ranges from 0.6 GHz to 7 GHz. Since some part of the energy of the first-order Gaussian is distributed outside the operating band of the antenna system, this leads to distortions in the received pulses. The upper frequency end of the signal spectrum is close to that of the transfer function, but the lower end is smaller than that of the transfer function. This leads to some low frequency components of the first-order Gaussian pulse getting filtered out by the antenna system. Thus, the fidelity value gets reduced to about 0.79 in free-space. Similarly, the second-order Gaussian pulse has the spectrum bandwidth ranging from 1.7 GHz to 8.4 GHz. Since the second-order Gaussian pulse has more of its energy distributed within the operating band of the antenna system as compared to the first-order Gaussian, this results in better fidelity factor values and reduced distortion to the source pulse.

The spectrum of the fourth-order Gaussian pulse matches better with that of the system transfer function of the miniature antenna. Its spectrum bandwidth ranges from 3.4 GHz to 10.1 GHz, which indicates that majority of the pulse spectrum lies within the operating band of the antenna system. Hence, the pulse suffers less distortion in comparison to the first and second-order Gaussian pulses. This leads to a higher

fidelity factor of greater than 0.94 in free-space. It can be noticed from Figure 5.10 that the least amount of distortion is experienced by the modulated Gaussian source pulse. This is well understood because the pulse spectrum of the modulated Gaussian is fully located within the operating band of the antenna system transfer function. Thus, most of the frequency components can be received efficiently and equally. Therefore, the antenna system incurs minimal distortions to the signal and a fidelity value of greater than 0.99 has been obtained for free-space measurements. Similarly, the received pulses with the antenna mounted on the human body have been presented in Figure 5.11.

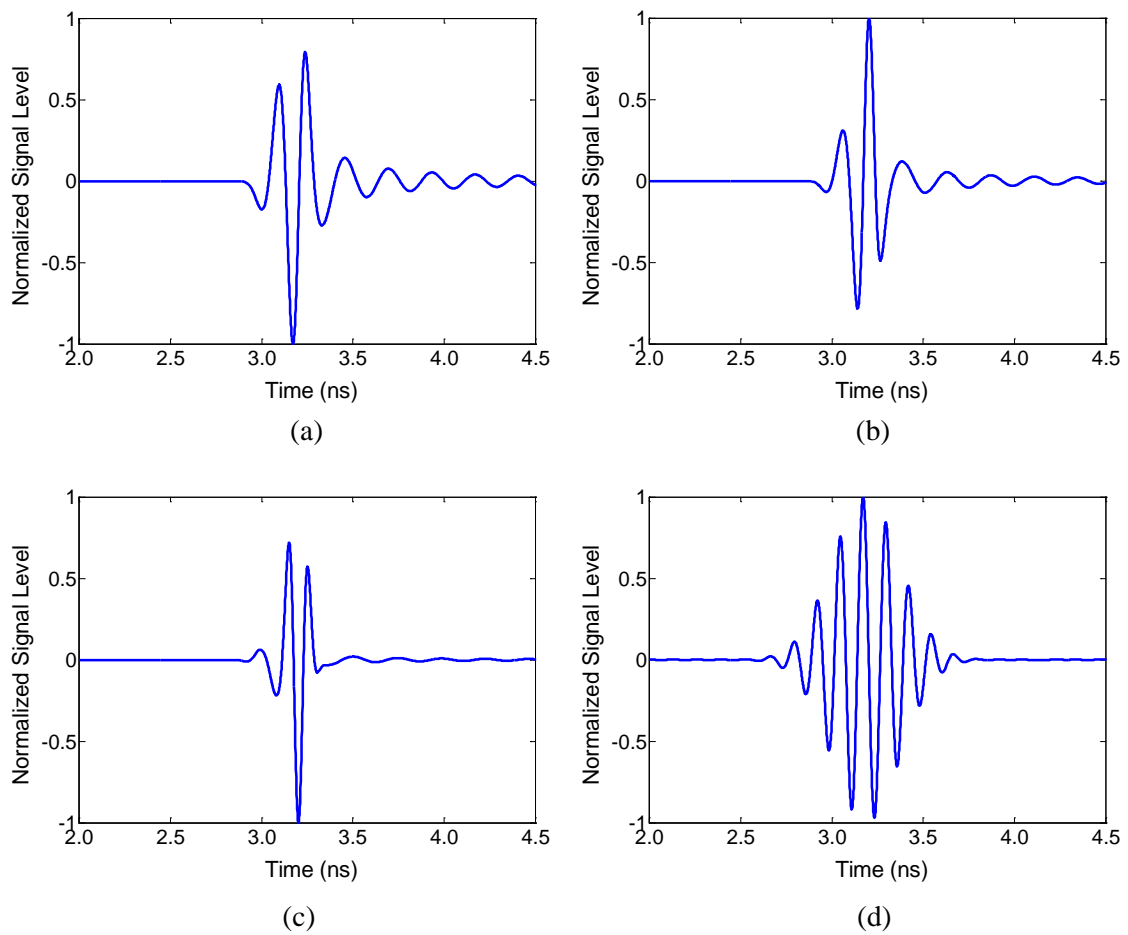


Figure 5.11: Received signal waveforms, namely (a) First-Order Gaussian, (b) Second-Order Gaussian, (c) Fourth-Order Gaussian and (d) Sine-modulated Gaussian for on-body fidelity measurements.

It can be noticed that the first, second and third-order Gaussian pulses get slightly more distorted when the receiver antenna is placed on the human body. However, the modulated Gaussian pulse is almost identical to the free-space measurements, with

only some minor ringing effects. The similarity of this pulse between the free-space and on-body measurements is 99.1%, which is computed based on the fidelity factor values of the two cases. The amount of distortion experienced by each pulse has been quantified in Table 5.1, where fidelity values for both the free-space and on-body measurements have been presented.

Table 5.1: Calculated Fidelity Factor values for the four different excitation pulses.

<b>Excitation Pulse</b>	<b>Free-space</b>	<b>On-body</b>
<i>First-order Gaussian</i>	0.7890	0.7089
<i>Second-order Gaussian</i>	0.9205	0.8061
<i>Fourth-order Gaussian</i>	0.9483	0.8174
<i>Sine-Modulated Gaussian</i>	0.9916	0.9830

It can be inferred from Table 5.1 that very high fidelity factor values have been achieved by the antenna, even in the vicinity of the human body. There is only a minor decrease in fidelity factor for the first, second and fourth-order Gaussian input pulses when the miniature antenna is mounted on the human body. In comparison, when a sine-modulated Gaussian pulse is used as input, the human body has negligible effect on the fidelity value. Hence, the analysis has demonstrated the capacity of the miniature UWB antenna system to achieve very high pulse fidelity and has demonstrated its ability to give minimal pulse distortion even with the presence of the human body. In the next section, an investigation of the fidelity patterns of the miniature tapered-slot antenna is presented for both the vertical and horizontal planes, in order to understand how the fidelity of this antenna varies in various angular directions.

### **5.3 Investigation of Fidelity Patterns of Miniature UWB Antenna**

In practice, signal fidelity is calculated for a given direction in space in order to fully characterise the spatial radiation properties of an antenna. When fed with an impulse, UWB antennas tend to radiate different signals in different spatial directions [19].

Hence, it is extremely important to study the spatial properties of the radiated or received signal from a UWB antenna. The analysis can be done for a full plane to create a complete fidelity pattern. The fidelity pattern defines how the signal varies in different angular directions. By studying the fidelity pattern of an antenna, it is possible to determine the angular region around the antenna where the distortion effects of the antenna are minimal.

The system setup for the fidelity pattern measurements consisted of two identical miniature tapered-slot UWB antennas fixed 100 cm away from each other inside an Anechoic Chamber. Each antenna was connected to a port of an Agilent N5232A PNA-L vector network analyser, which was kept outside the chamber. The transmitter antenna was kept stationary and receiver antenna was fixed on a circular turn-table that was used to rotate the receiver antenna in small steps. Two different excitation pulses, fourth-order Gaussian and sine-modulated Gaussian were used to convolve with the measured system impulse response. An illustration of the measurement setup has been provided in Figure 5.12.

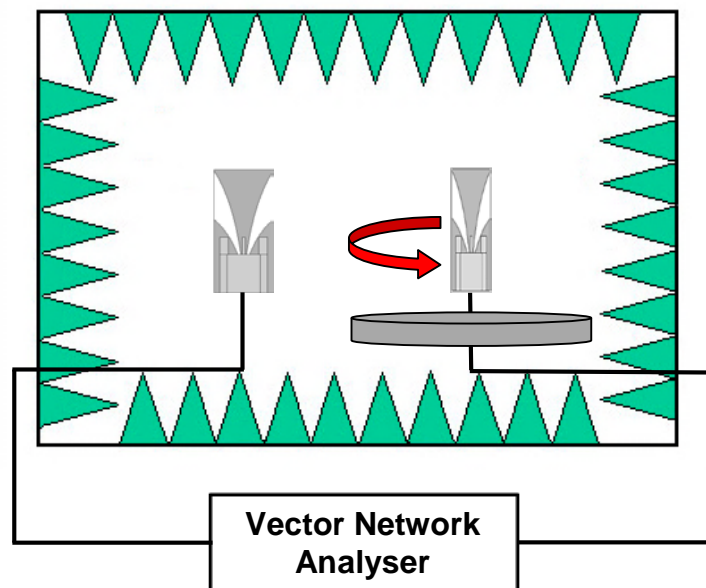


Figure 5.12: Experimental setup for fidelity pattern measurements inside the Anechoic Chamber.

The reference frame used to express the fidelity pattern measurements of the miniature antenna in vertical and horizontal planes is shown in Figure 5.13. For the fidelity pattern in the horizontal plane, the antennas were kept vertical with  $\varphi = 0^\circ$ .

Transfer function ( $S_{21}$ ) measurements were carried out between the two antennas, with the transmitter antenna kept stationary and rotating the receiver antenna by steps of  $\theta = 10^\circ$  in the horizontal plane. One new  $S_{21}$  measurement was taken at each  $\theta$  step. Hence, 36 different  $S_{21}$  measurements were done for a complete  $360^\circ$  scan.

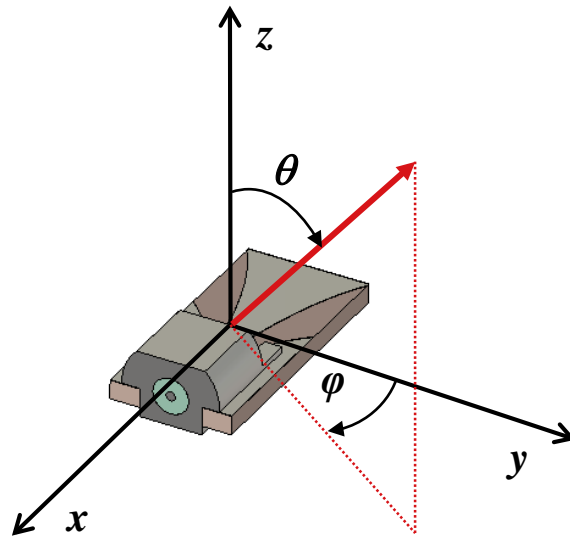


Figure 5.13: Miniature UWB antenna position with respect to the coordinate frame used for the fidelity pattern measurements.

In order to deduce an antenna's fidelity pattern in a particular plane, the fidelity factor needs to be calculated at every angle and the values can then be represented on a polar plot to visualize the fidelity pattern of the antenna. The fidelity patterns of the antenna were also obtained in the vertical plane. For this, the antennas were placed perpendicular from their normal upright position by tilting them  $90^\circ$  in the  $xy$  plane, by making  $\varphi = 90^\circ$ .

The receiver antenna fixed on the circular turn-table was then rotated in small steps of  $\theta = 10^\circ$  to create the fidelity pattern in the vertical plane. The distance between the two antennas was kept constant at 100 cm. The deduced free-space fidelity patterns in the horizontal and vertical planes for two different excitation pulses have been illustrated in Figure 5.14, with the relative position of the miniature antenna displayed for reference.

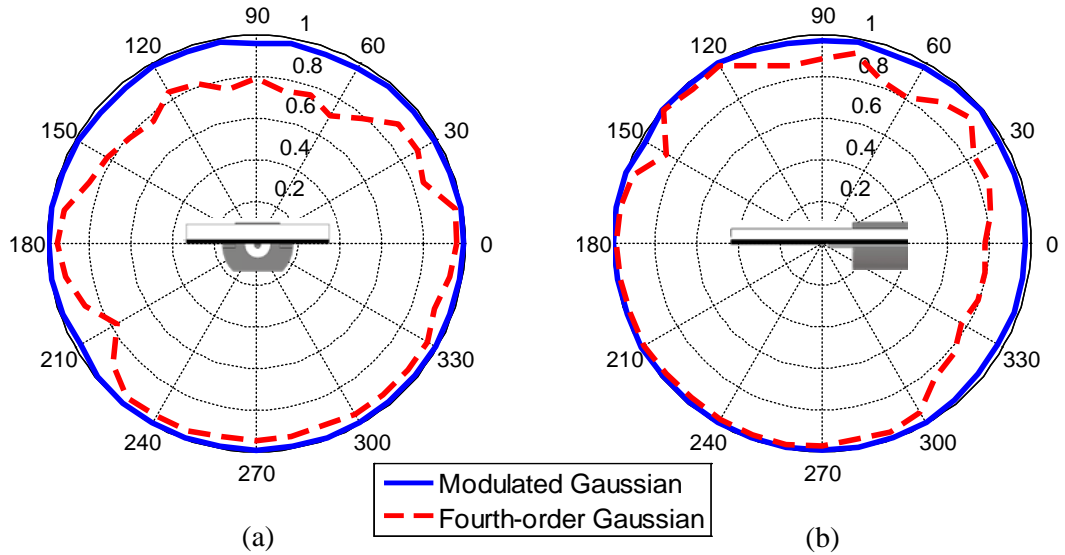


Figure 5.14: Fidelity patterns of the miniature UWB antenna in (a) Horizontal plane and (b) Vertical plane for free-space measurements.

It can be noticed from Figure 5.14 that for a sine-modulated Gaussian input, fidelity pattern is very linear for both the planes. The input pulse experiences minimal distortion in almost all angular directions around the antenna. With a fourth-order Gaussian input, fidelity pattern is better in antenna's front side compared to the back side. Similarly, fidelity is better in the upper side of antenna structure than the lower side. Overall, in the horizontal plane, the highest and lowest fidelity values for a sine-modulated input are 0.9973 and 0.9576 respectively and for a fourth-order Gaussian input are 0.9653 and 0.7049 respectively. In the vertical plane, sine-modulated input gives the highest and lowest fidelity of 0.9996 and 0.9661 respectively, whereas fourth-order Gaussian gives 0.9923 and 0.7698 respectively.

Fidelity patterns have also been obtained with the receiver antenna mounted on a real human test subject. The measurement involved placing the receiver antenna on the test subject's shoulder and making the test subject stand on the circular turn-table inside the Anechoic Chamber. The placement of the test subject's arm was such that the antenna was precisely aligned along the circular turn-table's axis of rotation. The transmitter antenna was kept at the same height as the receiver, at a distance of 100 cm. A 180° scan was done with the receiver antenna mounted on the test subject's shoulder. The turn-table was rotated with steps of  $\theta = 10^\circ$  and  $S_{21}$  measurements were done at each step. So, 19 measurements were done in total for a 180° scan to get a semi-circular fidelity pattern of the antenna in the anterior side of the body.

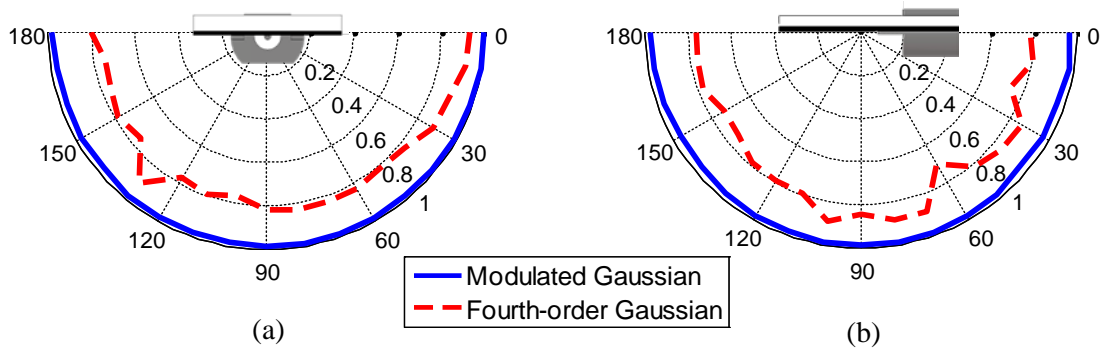


Figure 5.15: Fidelity patterns of the miniature UWB antenna in (a) Horizontal plane and (b) Vertical plane for on-body measurements.

For on-body measurements, the vertical plane fidelity patterns were obtained by tilting the antennas by  $90^\circ$  in the  $xy$  plane, with the receiver antenna fixed on the test subject's shoulder. The deduced on-body fidelity patterns in the horizontal and vertical planes for two different excitation pulses have been demonstrated in Figure 5.15, with the relative position of the miniature antenna displayed for reference. In these patterns, the position of the human body is on the back side of the antenna structure shown. It can be observed that the on-body fidelity remains almost identical to the free-space measurements in both the planes for a sine-modulated Gaussian input. With a fourth-order Gaussian input, the fidelity values do get affected by a slightly higher margin, with the lowest fidelity factor values being 0.7461 and 0.7041 in horizontal and vertical planes respectively and the average fidelity value is around 0.8, which is still very good. All these results clearly indicate that for the miniature UWB antenna, the human body has a very limited effect on the fidelity of the received pulses, which makes this compact and novel antenna suitable for wearable applications, intended to be deployed in high data rate and high efficiency wireless systems.

## 5.4 UWB System Modelling and Communication Link Performance Analysis

In the aforementioned analysis, the miniature UWB antenna has demonstrated very high and uniform pulse fidelity values in all spatial directions, both in free-space and on-body. In this section, the impact of fidelity factor on the communication

performance of an ultra-wideband radio system has been studied. The system architecture was modelled and analysed using the Agilent ADS software [20]. System performance was evaluated based on the bit error rate (BER) and signal-to-noise ratio parameters to analyse how accurately the sent data could be retrieved from the received pulse.

#### 5.4.1 Impulse Radio UWB Systems

In general, there are mainly two kinds of UWB radio systems, one is the impulse radio (IR-UWB) and other is the Multicarrier UWB (MC-UWB) system [2]. The impulse based UWB system is of particular interest in our application of the UWB motion tracking system. Conventional narrowband and wideband systems use radio frequency carriers to move the signal in the frequency domain from baseband to the actual carrier frequency where the system is allowed to operate. Impulse based UWB systems have a simple architecture. In such a system, the baseband signal is first modulated using the desired digital modulation scheme and is then sent directly in impulse form [21]. Impulse radio systems are normally implemented without a carrier; hence there is no frequency conversion stage, which makes the system relatively simpler. Various modulation schemes can be used for impulse based UWB system such as PAM (Pulse Amplitude Modulation), PPM (Pulse Position Modulation), PSM (Pulse Shape Modulation) and Bi-phase modulation.

A very commonly used shape based modulation technique is the bi-phase modulation (BPM). In this modulation, the data is encoded in the polarity of the impulses. The bi-phase modulated signal can be expressed as [22]:

$$s(t) = \sum_{k=-\infty}^{\infty} a_k p(t - kT_f), \quad \text{with } a_k = 1, -1 \quad (5.2)$$

Here,  $p(t)$  is the pulse shape and  $T_f$  is the duration of time frame.

#### 5.4.2 System-level Modelling and Performance Analysis

An impulse based UWB system was modelled using the Agilent ADS software by incorporating the measured channel impulse response data. Channel impulse responses were calculated from the measured channel transfer functions (the channel

transfer function is measured using the VNA) by taking their Inverse Fast Fourier Transform (IFFT). The system performance was evaluated based on the bit error rate (BER) and signal-to-noise ratio parameters. Bit-error-rate performance is mostly represented on a two dimensional graph. The ordinate is the normalized signal-to-noise ratio (SNR) expressed as  $E_b/N_0$ : the energy-per-bit divided by the power spectral density of the noise, expressed in decibels (dB). The abscissa is the bit-error-rate, a dimensionless quantity, usually expressed in powers of ten [23].

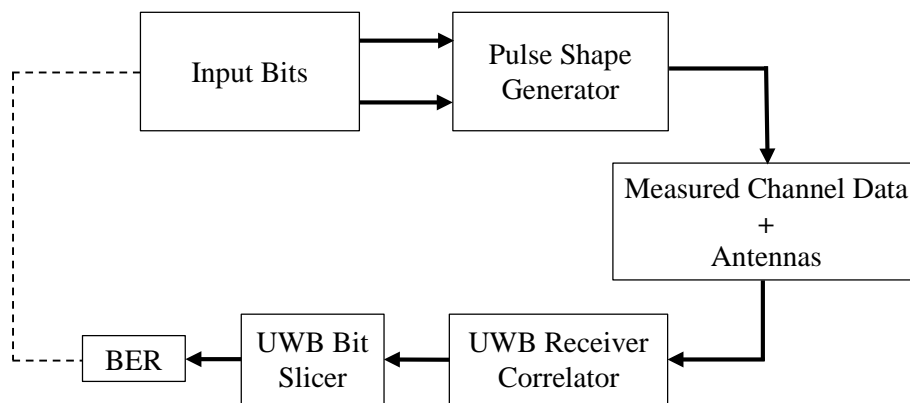


Figure 5.16: Simplified block diagram of the UWB communication system modelled to study the effect of fidelity factor on system performance.

Figure 5.16 shows a block diagram of the impulse based radio system modelled and simulated in Agilent ADS software to investigate the influence of antenna fidelity on the performance of a UWB communication system using the measured channel data. Bi-phase modulation scheme was applied in the modelled UWB communication system.

In this radio system, a long sequence of pseudo-random bits is provided as the input data to a modulator, where it is modulated with the bi-phase technique. The modulated data is then shaped to the form of a second-order Gaussian using the pulse generator. The effect of the measured channel data on the received UWB pulses is embedded into the system by convolving the transmitted pulse with the calculated channel impulse responses. The correlator is the primary element at the receiver end which carries out the demodulation of data and channel decoding. Correlator compares the template pulse and the received pulse and then detects the useful signal

from the noise. The received signal is demodulated, producing a sequence of recovered bits. Finally, the received bits are compared to the transmitted bits and the errors are tallied up to get the bit error rate.

Bit error rate was calculated for various values of  $E_b/N_0$  at different angles around the miniature UWB antenna. Figure 5.17 shows the comparison of BER values at various angular directions around the antenna in the horizontal plane for free-space measurements, using the bi-phase modulation.

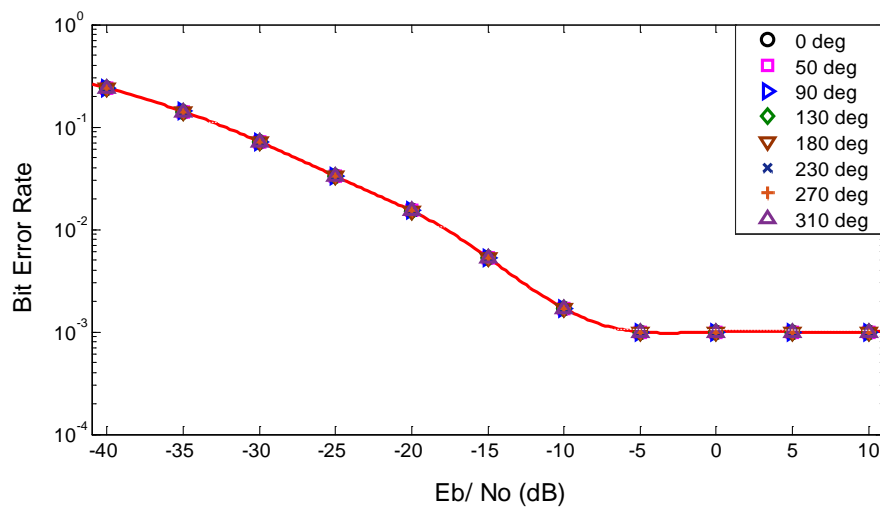


Figure 5.17: Comparison of BER values at various angles around the antenna in the horizontal plane for free-space measurements using bi-phase modulation.

From Figure 5.17, it is noticeable that the BER remains very stable in nearly all directions around the miniature UWB antenna. Since the antenna has exhibited excellent level of pulse fidelity in almost all angular directions around it, it leads to very low and consistent level of BER values. The stable fidelity patterns of the antenna in all directions lead to minimal distortion in the received pulse. Hence, the sent data could be retrieved from the pulse correctly at the receiving end. Also, it was noticed that the bit error rate saturates around the  $10^{-3}$  value, which could be attributed to the limitation of the modelled communication system since this is a fairly simple and basic simulation system.

Similarly, Figure 5.18 illustrates the BER values at various angular directions around the antenna when it is mounted on the human body. Just like the free-space scenario, the BER remains steady in nearly all directions even when the antenna is placed on

the human body. This is understandable since the fidelity factor analysis carried out in the previous section of this chapter had demonstrated that the human body had a very limited effect on the fidelity of the miniature UWB antenna. Hence, the BER values for on-body measurements were also very stable in various spatial angles, because of the consistently high fidelity of the antenna in all the directions.

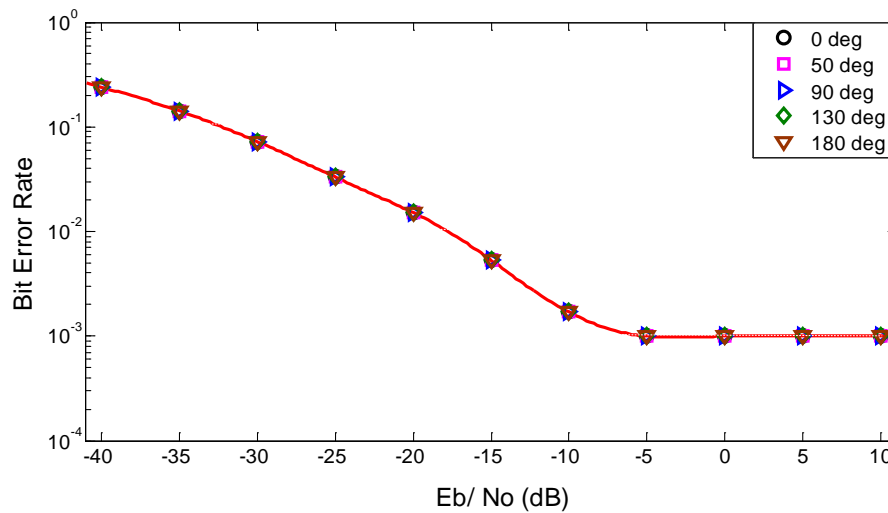


Figure 5.18: Comparison of BER values at various angles around the antenna in the horizontal plane for on-body measurements using bi-phase modulation.

## 5.5 Summary

In this chapter, the fidelity factor analysis of the miniature tapered-slot UWB antenna has been carried out. The investigation of the miniature UWB antenna from a system point of view has also been undertaken. The impact of fidelity on the design of an antenna has been discussed. Different excitation pulse types were employed to study the effect of the antenna and the propagation channel on the received pulse quality. The analysis is based on examining the extent of distortion of various excitation pulses. The fidelity patterns have been presented to study the distortion level in different angular directions for the azimuth as well as elevation planes. Both free-space and on-body scenarios have been studied in order to investigate the effect of human body on the received pulse distortion level. Very high fidelity values of up to 0.9996 have been achieved, especially when a modulated Gaussian pulse is used as the excitation signal. It has been shown that the human body has a limited effect on

the fidelity of the received signals, with a minimum fidelity value of 0.9619 achieved with a sine-modulated Gaussian input. The effect of antenna fidelity on the performance of a UWB communication system modelled in the Agilent ADS software has been assessed based on the BER and  $E_b/N_0$  parameters using the measured channel impulse responses.

To the author's knowledge, a detailed investigation of the impact of pulse fidelity on a UWB system's communication performance, such as BER has not been undertaken in any open literature earlier. It has been demonstrated through the analysis that high pulse fidelity helps in achieving low and stable BER values in the system, leading to accurate retrieval of the sent data.

## References

- [1] P. S. Hall and Y. Hao, Eds., *Antennas and Propagation for Body-Centric Wireless Communications*, 2nd ed. Artech House, 2012.
- [2] J. H. Reed, *An Introduction to Ultra Wideband Communication Systems*. Prentice Hall, 2005.
- [3] T. S. P. See and Z. N. Chen, “Experimental Characterization of UWB Antennas for On-Body Communications,” *IEEE Trans. Antennas Propag.*, vol. 57, no. 4, pp. 866–874, Apr. 2009.
- [4] M. Koohestani, N. Pires, A. K. Skrivervik, and A. A. Moreira, “Performance Study of a UWB Antenna in Proximity to a Human Arm,” *IEEE Antennas Wirel. Propag. Lett.*, vol. 12, pp. 555–558, 2013.
- [5] D.-H. Kwon, “Effect of Antenna Gain and Group Delay Variations on Pulse-Preserving Capabilities of Ultrawideband Antennas,” *IEEE Trans. Antennas Propag.*, vol. 54, no. 8, pp. 2208–2215, Aug. 2006.
- [6] E. Pancera, T. Zwick, and W. Wiesbeck, “Spherical Fidelity Patterns of UWB Antennas,” *IEEE Trans. Antennas Propag.*, vol. 59, no. 6, pp. 2111–2119, Jun. 2011.
- [7] Z. N. Chen, X. H. Wu, H. F. Li, N. Yang and M. Y. W. Chia, “Considerations for Source Pulses and Antennas in UWB Radio Systems,” *IEEE Trans. Antennas Propag.*, vol. 52, no. 7, pp. 1739–1748, 2004.
- [8] I. Oppermann, M. Hämmäläinen, and J. Iinatti, Eds., *UWB: Theory and Applications*. John Wiley and Sons, 2004.
- [9] L. Guo, “Study and Miniaturisation of Antennas for Ultra Wideband Communication Systems,” PhD Thesis, Queen Mary University of London, 2009.
- [10] S. Licul, J. Noronha, W. Davis, D. Sweeney, C. Anderson, and T. Bielawa, “A parametric study of time-domain characteristics of possible UWB antenna

- architectures,” in *58th Vehicular Technology Conference (VTC)*, 2003, vol. 5, pp. 3110–3114.
- [11] J. Powell and A. Chandrakasan, “Spiral slot patch antenna and circular disk monopole antenna for 3.1-10.6 GHz ultra wideband communication,” in *International Symposium on Antennas and Propagation (ISAP)*, 2004.
- [12] “Agilent 2-Port and 4-Port PNA-L Network Analyzer,” 2013. [Online]. Available: <http://cp.literature.agilent.com/litweb/pdf/N5235-90004.pdf>.
- [13] *FCC First Report and Order, Revision of Part 15 of the commission’s rules regarding ultra-wideband transmission systems*. Washington D.C., 2003, p. ET–Docket 98–153.
- [14] L. Guo, J. Liang, C. C. Chiau, X. Chen, C. G. Parini, and J. Yu, “Performances of ultra-wideband disc monopoles in time domain,” *IET Microwaves, Antennas Propag.*, vol. 1, no. 4, pp. 955–959, 2007.
- [15] D. Lamensdorf and L. Susman, “Baseband-pulse-antenna techniques,” *IEEE Antennas Propag. Mag.*, vol. 36, no. 1, pp. 20–30, Feb. 1994.
- [16] G. Quintero, J.-F. Zurcher, and A. Skrivervik, “System Fidelity Factor: A New Method for Comparing UWB Antennas,” *IEEE Trans. Antennas Propag.*, vol. 59, no. 7, pp. 2502–2512, Jul. 2011.
- [17] D. Valderas, J. I. Sancho, D. Puente, C. Ling, and X. Chen, *Ultrawideband Antennas: Design and Applications*. Imperial College Press, 2011.
- [18] P. R. Veena and K. A. Narayanankutty, “A Wavelet Based Pulse Shaping Method for Baseband and Multiband UWB Transmitters,” *Int. J. Recent Trends Eng.*, vol. 2, no. 5, pp. 63–69, 2009.
- [19] Z. Zeng, K. Xu, Z. Song, and Q. Zhang, “A Modified Vivaldi Antenna for Improved Angular-Dependent Fidelity Property,” *Int. J. Antennas Propag.*, vol. 2013, pp. 1–7, 2013.
- [20] “Advanced Design System (ADS) | Keysight (formerly Agilent Test and Measurement).” [Online]. Available: <http://www.keysight.com/en/pc->

1297113/advanced-design-system-ads?cc=GB&lc=eng. [Accessed: 02-Sep-2014].

- [21] A. Alomainy, "Antennas and Radio Propagation for Body-Centric Wireless Networks," PhD Thesis, Queen Mary University of London, 2007.
- [22] H. Nikookar and R. Prasad, *Introduction to Ultra Wideband for Wireless Communications*. Springer, 2009.
- [23] J. E. Gilley, "Bit-Error-Rate Simulation Using Matlab." Transcrypt International Inc., 2003.

# **Experimental Investigation of Ranging and 3D Localisation using the Miniature UWB Antenna**

The high data rate transmission capabilities, low power emission level, along with low complexity and low cost offered by UWB makes it a very promising technique for wireless body area networks (WBANs) [1]. With the development in pulse ultra-wideband chipset technology, emerging applications of UWB are foreseen for precise ranging and localisation in sensor networks. UWB pulse signalling is especially suitable in this context because the ultra-short duration of UWB waveforms provides high time resolution which is of the order of less than a nanosecond. This gives rise to the potential ability to provide high-precision ranging along with low-power and low-cost implementation [2]–[4]. Due to their large bandwidths, UWB receivers can resolve individual multipath components (MPCs); therefore, they are capable of accurately estimating the arrival time of the first signal path. This implies that the distance between a wireless transmitter and a receiver can be accurately determined, yielding high localisation accuracy [5]–[8]. Such unique aspects of UWB make it a very promising technology for positioning and tracking applications. Along

with good material penetration properties, UWB signals offer opportunities for utilization in short-range radar systems too and their fine time resolution is very useful for range measurement purposes [9].

In this chapter, an investigative study of the ranging capabilities of the miniature tapered-slot UWB antenna and influence of the human body on the accuracy of range estimates is presented. An analysis of the impact of the miniature UWB antenna's alignment in the vertical plane, on the estimated range values between a transmitter-receiver pair of such antennas is also undertaken. Moreover, the effect of non-line-of-sight communication on the range estimation between the antenna pair has also been examined by using different types of materials as obstruction to line-of-sight between the two antennas.

Several three-dimensional localisation experiments have been performed using the miniature tapered-slot antenna mounted on the human body as a mobile station and three Vivaldi antennas as base stations, to comprehend the level of accuracy that can be achieved and assess how precisely the tiny movements of the mobile station could be resolved. Time of Arrival data fusion and peak detection techniques have been used to compute the position of the target node in terms of  $x, y, z$  Cartesian coordinates. The geometry and performance of the UWB Vivaldi antenna designed for the project is also presented.

## **6.1 Ranging Accuracy Investigation of the Miniature UWB Antenna System**

This section presents an experimental study that involves determining how precisely the point-to-point distance between two identical tapered-slot antennas can be deduced through the signal time-of-flight. The range estimation between the transmitter and the receiver antenna has been carried out using the Channel Impulse Response and peak detection techniques [10]. Since the miniature UWB antenna is meant for on-body use, a comparative study has been undertaken to gauge the impact of the human body on the accuracy of the range estimates. Both on-body and free-space scenarios have been considered for this study. Accurate range estimation

between a pair of antennas is very crucial to successfully locate the nodes in a three dimensional coordinate system.

The precise estimation of signal time of arrival (TOA) is the most significant parameter in microwave-based localisation systems [11]. In such an approach, the characteristics of the propagating radio signal are utilized to predict the position of a mobile object. Because of the high time resolution of UWB signals, the range-based TOA approach is one of the most suitable methods for localisation in UWB sensor networks [12], [13]. To accurately estimate the time of arrival of the UWB signal propagating between the transmitter and receiver antenna, channel impulse response and peak detection techniques have been implemented. For experimental convenience the transfer function ( $S_{21}$ ) is measured between the transmitter and receiver antenna using a vector network analyser. Inverse Fast Fourier Transform (IFFT) is then carried out on the measured transfer function to obtain the channel impulse response.

If there are  $N$  propagation channels between a transmitter and a receiver (with the amplitude, phase and delay of the  $k^{th}$  path being  $\alpha_k$ ,  $\varphi_k$  and  $\tau_k$  respectively), the channel impulse response [10] can be written as

$$y(t) = \sum_{k=1}^N \alpha_k e^{j\varphi_k} \delta(t - \tau_k) \quad (6.1)$$

where  $\delta(\cdot)$  is an impulse function. Using the peak detection algorithm, the strongest peak of the channel impulse response is used to obtain an estimate of the signal time of arrival. In the absence of measurement error, the range value (denoted as  $r$ ) based on the estimated signal time of arrival (denoted as  $t$ ), which is the one-way propagation time for the signal to travel from the transmitter to the receiver, can be computed as

$$r = t \cdot c \quad (6.2)$$

where  $c$  is the speed of light in air ( $2.998 \times 10^8$  m/s).

### 6.1.1 Measurements with Antennas in Free-space

For the first set of measurements in this analysis, a pair of identical tapered-slot UWB antennas are placed in free-space, aligned in two different orientations, namely

face-to-face and side-by-side to each other, as shown in Figure 6.1. Several range measurements are carried out, with the distance (denoted as  $d$ ) between the two antennas selected to be in the range of 10 cm to 200 cm (with increments of 10 cm) for each orientation setup. For side-by-side orientation, the physical distance between the two antennas was measured from the middle part of the antenna structure. The measurements were carried out inside the Antenna Lab at Queen Mary University of London using an Agilent N5232A PNA-L vector network analyser [14]. The transmitter and receiver antenna are connected to the two-port network analyser and the transfer function is measured, which is a frequency response of the system. One transfer function measurement is done for each given location. The Inverse Fast Fourier Transform (IFFT) is then carried out on the measured transfer function data (within the VNA). This transforms the data from frequency domain to the time domain and gives the channel impulse response.

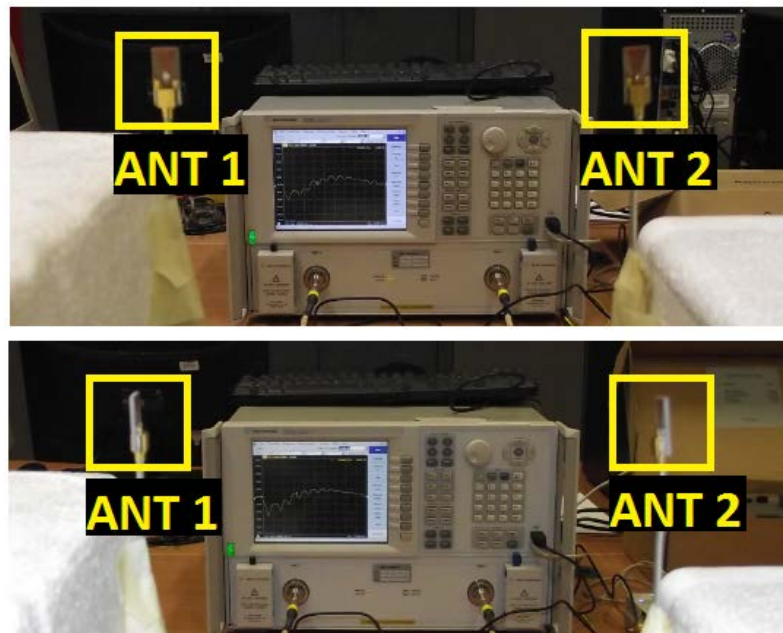


Figure 6.1: Measurement setup for free-space ranging experiment with the two antennas aligned face-to-face and side-by-side to each other.

For direct line-of-sight signal propagation, peak of the channel impulse response provides the time it takes for the signal to reach the receiver from the transmitter i.e., the Time of Arrival. This signal time of arrival is then used for the range estimation by multiplying it with the speed of light. The absolute error values obtained in the range estimation for both face-to-face and side-by-side orientations of the antennas at

varying distances are presented in Figure 6.2. The probability density distribution of the ranging error obtained for these free-space measurements has been illustrated in Figure 6.3.

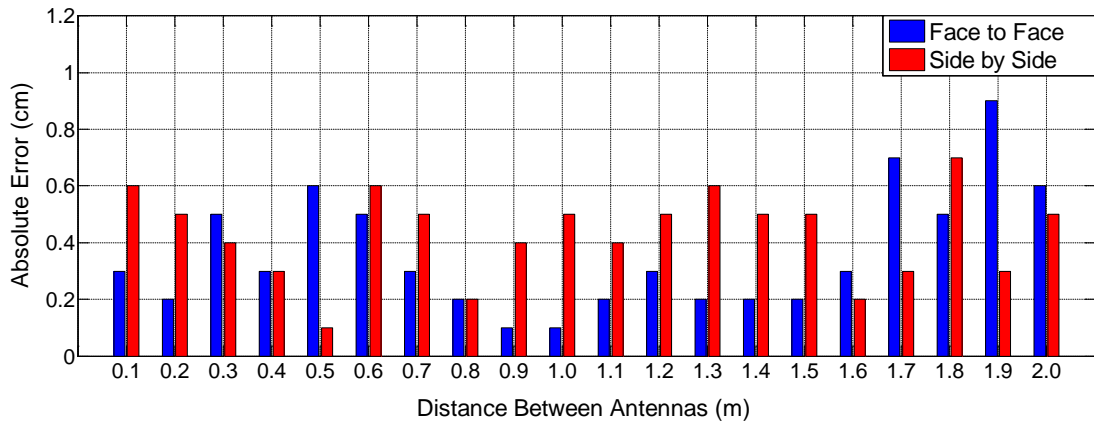


Figure 6.2: Absolute error values in range estimation for two different antenna orientations at varying separation distance  $d$  between the antennas in free-space.

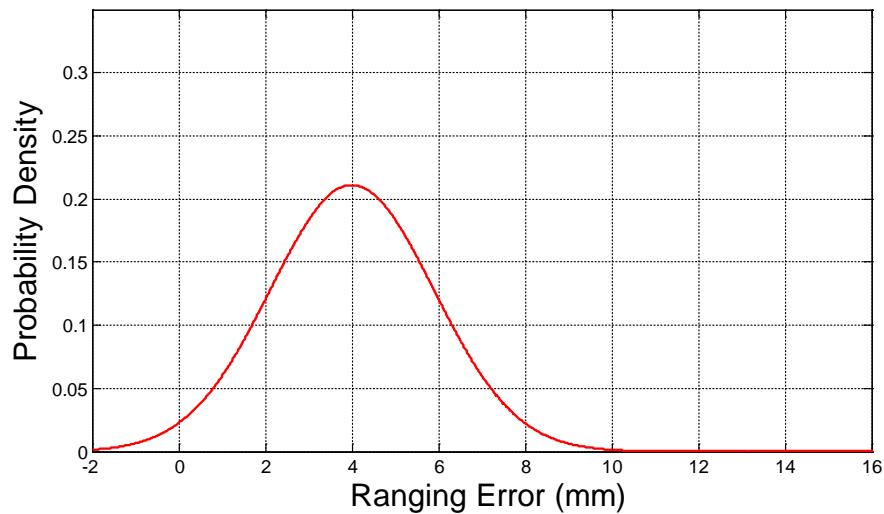


Figure 6.3: Probability density distribution of the ranging error obtained when the antennas were placed in free-space.

It can be noticed from Figure 6.2 that the range estimates between the two antennas have been accomplished with millimetre accuracy at various separation distances for both the antenna orientations. The maximum error in estimating the range was 0.9 cm when the antennas were 190 cm away, aligned face-to-face. The average error in estimating the range values was 0.01 cm. The average range estimation error for

face-to-face alignment was 0.105 cm and for side-by-side alignment was -0.095 cm. The Root Mean Square (RMS) error in range estimation was 0.44 cm.

Similarly, an investigative analysis was undertaken to study the influence of the miniature UWB antenna's alignment in the vertical plane on the estimated range values. Ranging estimates were carried out with the transmitter antenna slightly tilted in the vertical plane in different directions while keeping the receiver antenna erect and unmoved. For these set of measurements, two miniature UWB antennas were placed in free-space in different alignments; face-to-face and side-by-side to each other. The transmitter antenna was rotated in different directions in the vertical plane and the receiver antenna was always kept stationary in the vertically upright position ( $0^\circ$  direction). The coordinate frame used to represent the rotation of the miniature antenna in various directions is provided in Figure 6.4.

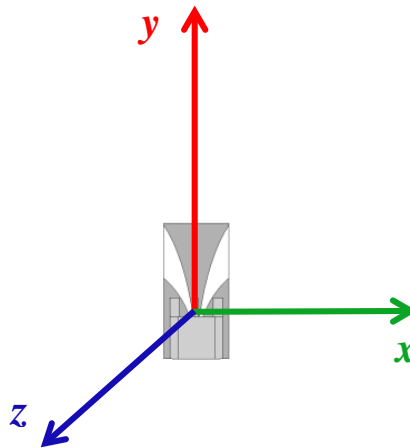


Figure 6.4: Coordinate frame used to represent rotation of the miniature UWB antenna in various directions.

Firstly, the two antennas were aligned face-to-face. The transmitter antenna was then rotated along the z-axis in the vertical plane from its normal upright position by tilting it sideways towards its left and right sides, i.e. in the  $xy$ -plane. Five different measurements were done, one with the antenna kept upright and the rest with the antenna tilted at different angles. The antenna was tilted by  $30^\circ$  and  $45^\circ$  angles, both towards its left and right side. The axis of rotation was along the centre point of the antenna structure. In this analysis, antenna rotation towards the left side is represented with a negative sign, i.e.  $-30^\circ$  and  $-45^\circ$  and towards its right side is represented by positive angles  $30^\circ$  and  $45^\circ$ . The upright position of the antenna is indicated by  $0^\circ$

(See Figure 6.5). The receiver antenna was kept in the stationary vertical position during the entire course of these measurements.

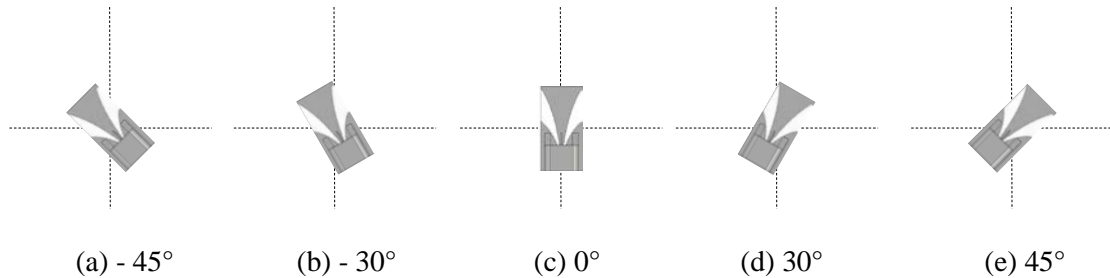


Figure 6.5: Miniature UWB antenna tilted sideways by varying angles. It is to be noted that the tilt angles towards left side are represented by a negative sign.

Similarly, four other range measurements were carried out, this time with the transmitter antenna being rotated along the  $x$ -axis. For this, the antenna was tilted forwards and backwards (i.e. in the  $yz$ -plane) with the same angles of  $30^\circ$  and  $45^\circ$ . Likewise, the antenna's rotation towards the back side is represented by negative angles  $-30^\circ$  and  $-45^\circ$  while towards the front side is indicated by positive  $30^\circ$  and  $45^\circ$  (See Figure 6.6). All the measurements were performed with the distance between the two antennas selected to be 50 cm and 100 cm for each orientation setup.

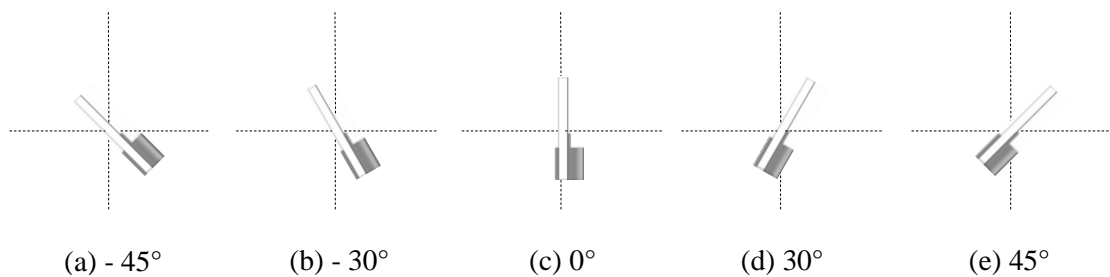
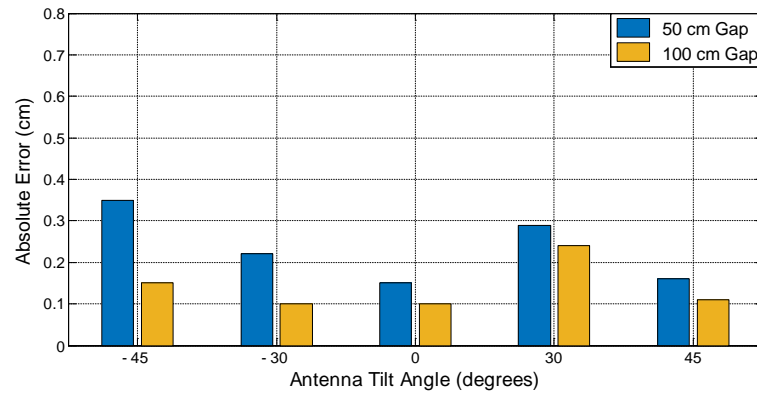


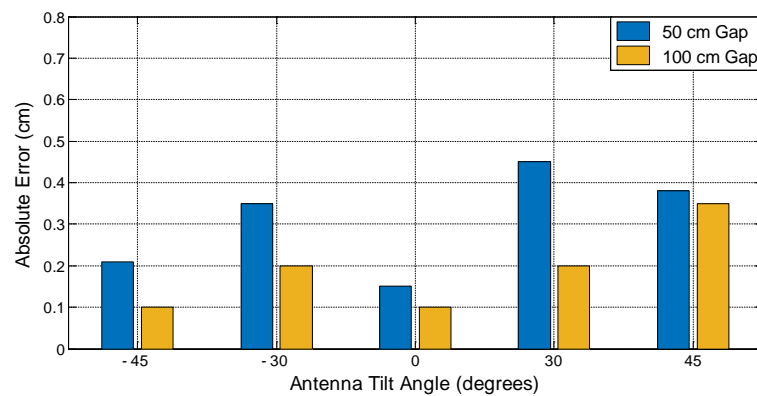
Figure 6.6: Miniature UWB antenna tilted forwards and backwards by varying angles. It is to be noted that the tilt angles towards antenna's back side are represented by a negative sign.

In the same way, the two antennas were kept side-by-side to each other and the same set of measurements were repeated by tilting the transmitter antenna sideways as well as forwards and backwards. This analysis helps to evaluate the effect of vertical orientation of the antenna on the signal time-of-flight based range estimates between

the antenna pair. The absolute error values obtained in the range estimation for side-by-side orientation of the antenna pair at varying tilt angles in the vertical plane are provided in Figure 6.7.



(a) Antenna tilted sideways.

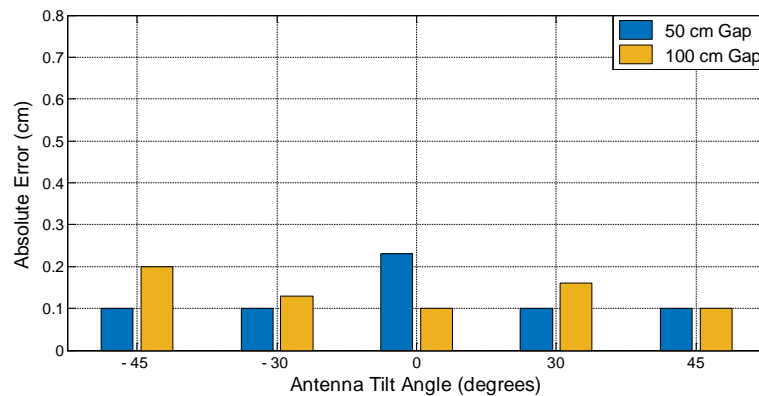


(b) Antenna tilted forwards and backwards.

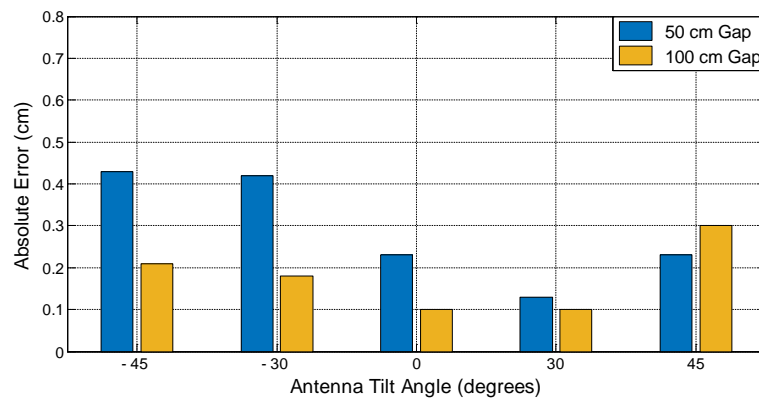
Figure 6.7: Absolute error values in range estimation for varying tilt angles of the transmitter antenna for side-by-side orientation.

It can be observed from Figure 6.7 that for side-by-side orientation, range values between the transmitter-receiver antenna pair have been estimated with millimetre accuracy, even when the transmitter antenna is tilted in various directions in the vertical plane. The maximum range error obtained was 0.45 cm when the antenna was tilted forwards in the  $yz$ -plane by  $30^\circ$  and kept 50 cm away from the receiver. The average error in estimating the range values was -0.19 cm and the RMS error was 0.25 cm. When the transmitter antenna was tilted sideways in the  $xy$ -plane, the average error in range estimation was -0.11 cm. When the antenna was tilted forwards and backwards (in  $yz$ -plane), the average error was -0.25 cm. Thus, the range estimation

accuracy gets slightly less affected when the transmitter antenna is tilted in the  $xy$ -plane.



(a) Antenna tilted sideways.



(b) Antenna tilted forwards and backwards.

Figure 6.8: Absolute error values in range estimation for varying tilt angles of the transmitter antenna for face-to-face orientation.

The absolute error values in the range estimation obtained for face-to-face alignment of the antennas at varying tilt angles in the vertical plane are provided in Figure 6.8. It can be noticed from Figure 6.8 that when the two antennas were aligned face-to-face, all range estimates were once again achieved with millimetre accuracy. The maximum error of 0.43 cm was observed when the transmitter antenna was tilted backwards by  $45^\circ$  and kept 50 cm away from the receiver. The average error in estimating the range values was 0.08 cm and the RMS error was 0.21 cm. When the transmitter antenna was tilted sideways, the average error in range estimation was -0.01 cm. When the antenna was tilted forwards and backwards, the average error was 0.14 cm. Hence, similar to the side-by-side orientation results, the range estimation accuracy gets less

affected when the transmitter antenna is tilted sideways as compared to the antenna tilted forwards and backwards. The average and standard deviation of the error values obtained in these ranging measurements have been summarised in Table 6.1.

Table 6.1: Average and standard deviation of error values obtained for ranging experiments with the transmitter antenna tilted in the vertical plane.

<b>Antenna Orientation</b>	<b>Tilt Direction</b>	<b>Average Error (cm)</b>	<b>Standard Deviation (cm)</b>
Face-to-face	Sideways	-0.11	0.18
	Forwards & backwards	-0.25	0.22
Side-by-side	Sideways	-0.01	0.15
	Forwards & backwards	0.14	0.23

All these results have demonstrated that even when the miniature UWB antenna is tilted in various directions in the vertical plane, range estimates are achievable with millimetre accuracy for free-space measurements. The point-to-point distance between the two antennas has been estimated with an error of less than 1 cm for all the cases. The overall RMS error for all these measurements taken as a single set is 0.23 cm. Slightly better range estimation accuracy was obtained with the antennas aligned face-to-face in comparison to the side-by-side orientation.

This analysis has demonstrated that it is possible to achieve millimetre accuracy in range estimates between a pair of miniature UWB antennas even when they are aligned in various orientations and angles with each other. This is an essential and highly desired characteristic from the transmitter-receiver antenna pair. The antennas will be expected to provide accurate range estimates even when aligned at different angles and orientations for their successful usage in a UWB based motion tracking system.

### **6.1.2 Measurements with Antennas Mounted on the Human Body**

Further range estimation analysis was carried out taking into account the impact of human body on the accuracy of the results obtained. The first set of measurements in

this study involved placing one of the antennas on the human body and analysing its effect on the estimated range values. For this, the transmitting antenna was kept in free-space while the receiving antenna was fixed on the arm of a human male test subject, keeping both the antennas at the same height. The antennas were aligned facing each other; with the body mounted antenna placed flat to the skin using a 2 mm thick cotton pad. The experimental setup for these measurements is illustrated in Figure 6.9. Measurements were taken with the test subject standing at twenty different locations such that the separation gap between the two antennas varied from 10 cm to 200 cm with increments of 10 cm.

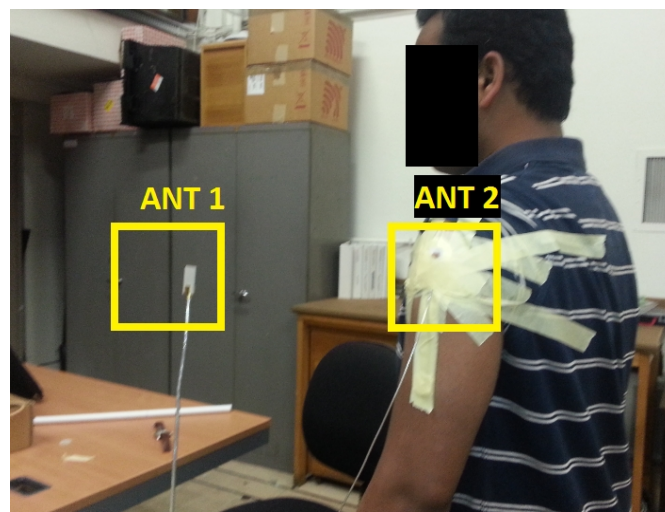


Figure 6.9: Measurement setup with the receiver antenna attached to a test subject's body and the transmitter antenna in free-space.

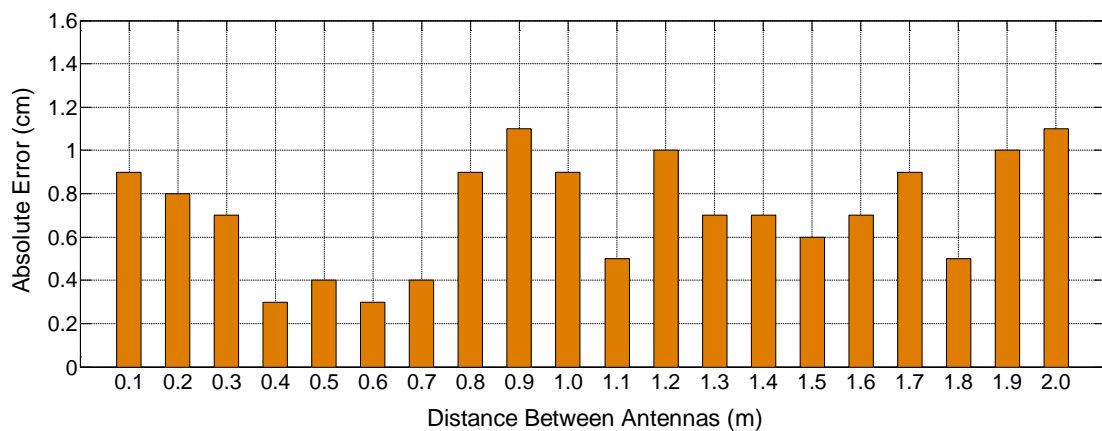


Figure 6.10: Absolute error values in range estimation with one antenna attached to a test subject's body and another antenna in free-space.

The absolute error values obtained in range estimation for this measurement setup at varying distances are presented in Figure 6.10. It can be understood from Figure 6.10 that most range estimates have been done with millimetre-level accuracy. The maximum error in range estimation was 1.1 cm when the antennas were 90 cm and 200 cm away from each other. The average range estimation error was 0.58 cm while the RMS error was 0.76 cm. The probability density distribution of the ranging error obtained for these measurements is shown in Figure 6.11.

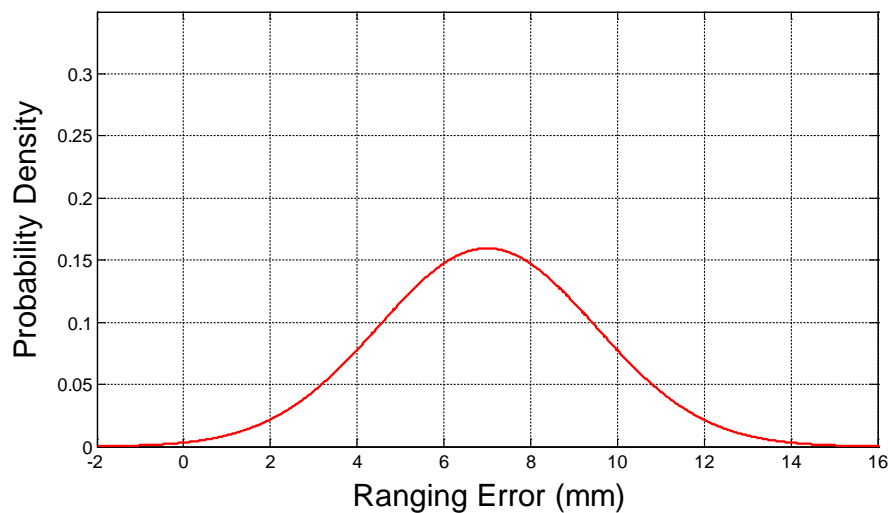


Figure 6.11: Probability density distribution of the ranging error obtained when one antenna was attached to a human test subject’s body.

It can be noticed from these results that there has been a slight increase in the range estimation error as compared to the free-space measurements. Also, it is observed from the probability density plots shown in Figure 6.3 and Figure 6.11 that on placing one of the antennas on the human body, the spread of the ranging error increases slightly. But the effect is trivial, and the average error has increased only by a few millimetres, and could be partly accounted for by subject movement. Thus, it could be inferred from these measurements that placing one of the antennas in this ranging system on the human body had an insignificant effect on the accuracy of the range estimates.

Since the miniature UWB antenna is meant to operate in the vicinity of the human body, more investigations of the range estimation accuracy were carried out with both the transmitter and receiver antennas fixed on a human test subject. The measurement setup involved mounting two identical tapered-slot UWB antennas on a test subject’s

arm, placed flat to the skin with a 2 mm thick cotton pad as ‘air gap’. The transmitting antenna was placed on the wrist and receiving antenna on the shoulder. The target for the measurements was to bend the arm around the elbow at various angles, thereby changing the distance between the two antennas at each step, and performing a range estimation using the signal Time of Arrival approach. The measurement setup with the antennas mounted on the test subject’s arm and different bend-angles of the elbow has been shown in Figure 6.12.



Figure 6.12: Experimental setup for on-body ranging measurements with the two antennas and different bend-angles of the elbow.

The test subject was made to place his arm with the antennas on a table top for stability. Seven sets of measurements were taken, starting with the elbow bent at an angle of  $90^\circ$  and then slowly straightening the arm to reach an angle of  $180^\circ$  at the elbow joint with intervals of  $15^\circ$ . To get the real point-to-point distance between the two antennas, a telescopic rod was used. This rod was adjusted to precisely fit between the two antennas at each measurement interval, with the length of the rod thus providing the real distance between the two antennas.

The absolute error values in range estimation between the antenna pair for different bend angles of the elbow have been presented in Figure 6.13. It can be seen from the

figure that even when both the transmitter and receiver antennas are attached to the human body and orientated at varying angles, the range estimates can be obtained with a high level of accuracy. The maximum error of 1.5 cm was observed when the elbow was straightened (i.e. both antennas lying approximately flat on the plane of the arm). The average range estimation error for all the elbow positions was 0.89 cm. The RMS error in calculating the range estimates was 0.95 cm.

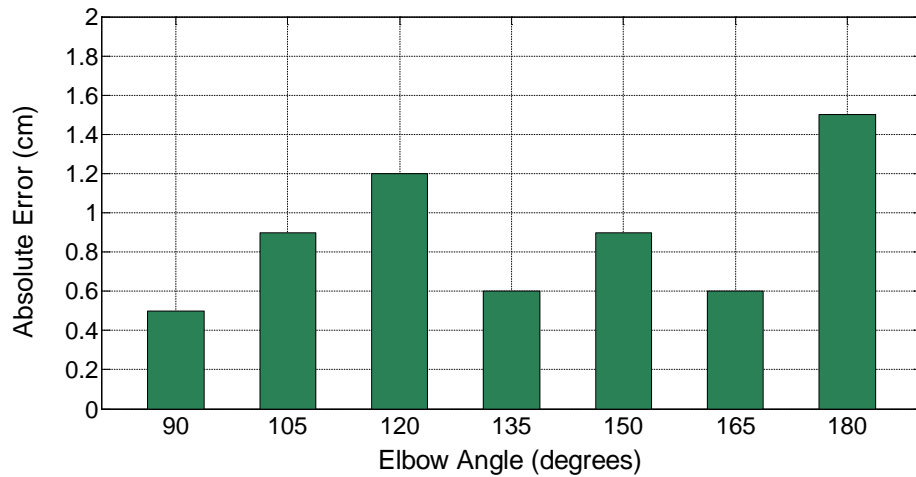


Figure 6.13: Absolute error values in range estimation with both the antennas mounted on-body for different bend angles of the elbow.

Similarly, some more on-body ranging measurements were performed but this time the forearm was moved sideways. The objective of these measurements was to tilt the forearm around the elbow in the vertical plane and study the effect of this tilting on the range estimates. For these set of measurements, the test subject was made to place his right arm with the antennas on a table top, with his elbow bent at an angle of  $90^\circ$ . The measurement setup has been demonstrated in Figure 6.14.

Ten sets of measurements were taken, starting with the forearm kept perpendicular to the table top. The forearm was then slowly tilted by the test subject towards his left side with steps of  $10^\circ$  to make the forearm rest on the table top at the last step. Hence ten different range measurements were done to cover the full  $90^\circ$  movement of the forearm. This procedure has been illustrated in Figure 6.14, which shows the forearm being slowly tilted at different angles in the vertical plane. For all the cases, the antenna mounted on the shoulder was kept unmoved and the elbow was kept bent at angle of  $90^\circ$ . Hence, the actual point-to-point distance between the transmitter and the receiver antenna remained approximately the same at each step of the measurement.

Just like the previous on-body range measurements, a telescopic rod was utilized for getting the actual point-to-point distance between the two antennas mounted on the arm.

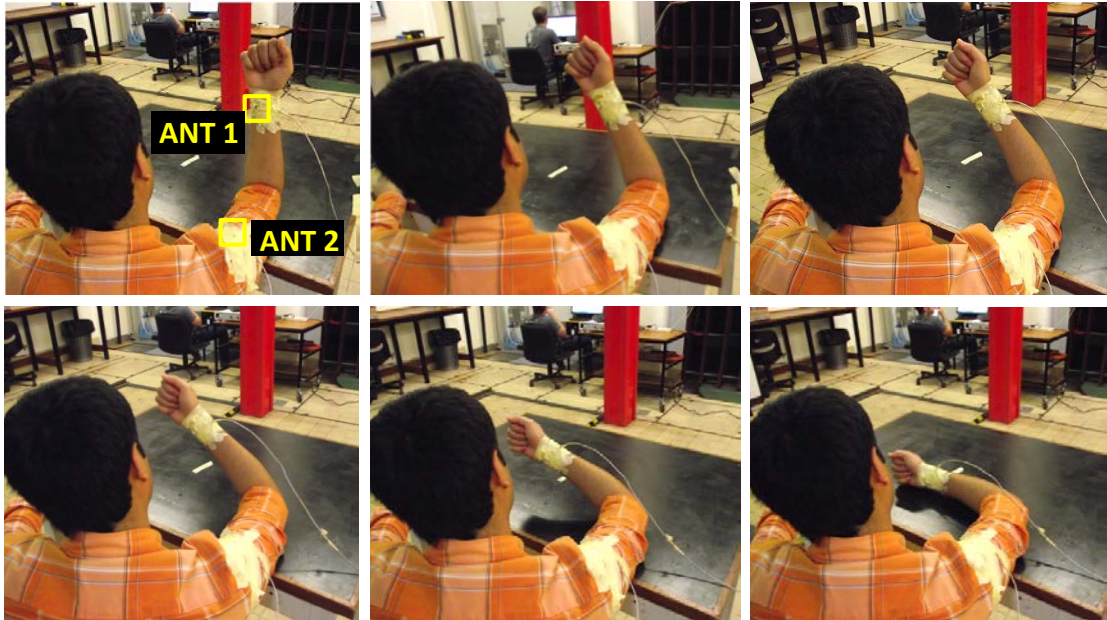


Figure 6.14: Measurement setup for on-body ranging measurements with the two antennas mounted on a human test subject's arm and the forearm bent by different angles in the vertical plane.

Figure 6.15 presents the absolute error values obtained in range estimation between the two antennas, with the forearm tilted by different angles in the vertical plane. The forearm positioned perpendicular to the table is denoted by an angle of  $0^\circ$ . The tilting of the forearm in the vertical plane is indicated by increments of  $10^\circ$ , thus the arm lying flat on the table is represented by  $90^\circ$ .

It can be noticed from Figure 6.15 that with both the transmitter and receiver antennas placed on the human body and the transmitter antenna positioned at varying angles in the vertical plane, the range estimates can be obtained with a good level of accuracy. Accuracy of 1 cm or better was achieved for majority of the cases, except for the scenarios where the forearm was tilted by  $70^\circ$  and above. The maximum range error of 2.45 cm was observed when the forearm was lying flat on the table. The greater ranging errors for higher tilt angles could be attributed to the effect of cross-polarisation between the transmitter and receiver antenna and also possibly due to the influence of close proximity of the antenna to the table surface. The average error in

range estimation for all the forearm positions was 0.75 cm and the RMS error was 1.25 cm.

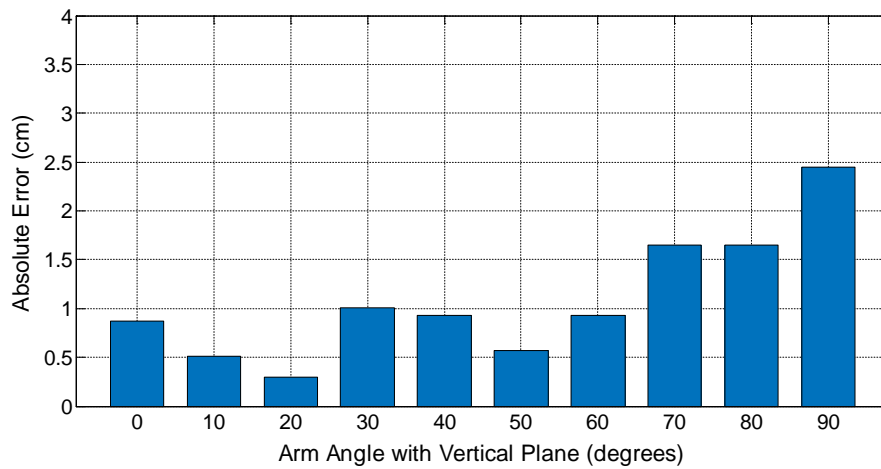


Figure 6.15: Absolute error values in range estimation for on-body measurements, with the forearm tilted by different angles in the vertical plane.

It can be noticed from this analysis that for on-body measurements, the range estimation error has slightly increased as compared to the free-space setup. Some part of this increase in error can be attributed to subject movement. The absolute ranging error varying between 0.3 cm and 2.45 cm clearly exhibit the capacity to obtain centimetre level ranging accuracy using the miniature UWB antennas on the human body. The overall RMS error for all the above on-body measurements taken as a single set was 1.14 cm.

For a time-of-flight based positioning system, in order to locate the sensor nodes in a three dimensional coordinate scheme using the data fusion techniques, an accurate range estimation value is the most crucial parameter. Since such a system will involve a continuously varying orientation of the body-mounted antennas, it is highly desirable that range estimates could be calculated between them with high-precision, irrespective of their alignment with regards to each other. The above investigations have clearly demonstrated this capability of the miniature UWB antenna. Variation in the antenna's physical orientation has a limited effect on the accuracy of the range estimates. An extensive analysis on the 3D localisation of mobile nodes has also been undertaken and provided in later sections of this chapter.

### 6.1.3 Non-line-of-sight Range Measurements

The ranging analysis was also carried out taking into consideration the non-line-of-sight setting between the transmitter and receiver antennas. For this, four different obstructions were placed between the two antennas, impeding their direct line-of-sight communication. Range estimates were then done between the two antennas using the signal Time of Arrival approach. A piece of wood with 1.7 cm thickness, a cardboard sheet with 0.8 cm thickness, a 0.6 cm thick plastic sheet and an adult human's hand were the four different obstructions placed between the antennas. All the measurements were done with the separation gap between the two antennas chosen to be 50 cm and 100 cm. The measurement setup consisting of the two antennas along with the obstructing materials placed in the middle has been illustrated in Figure 6.16.

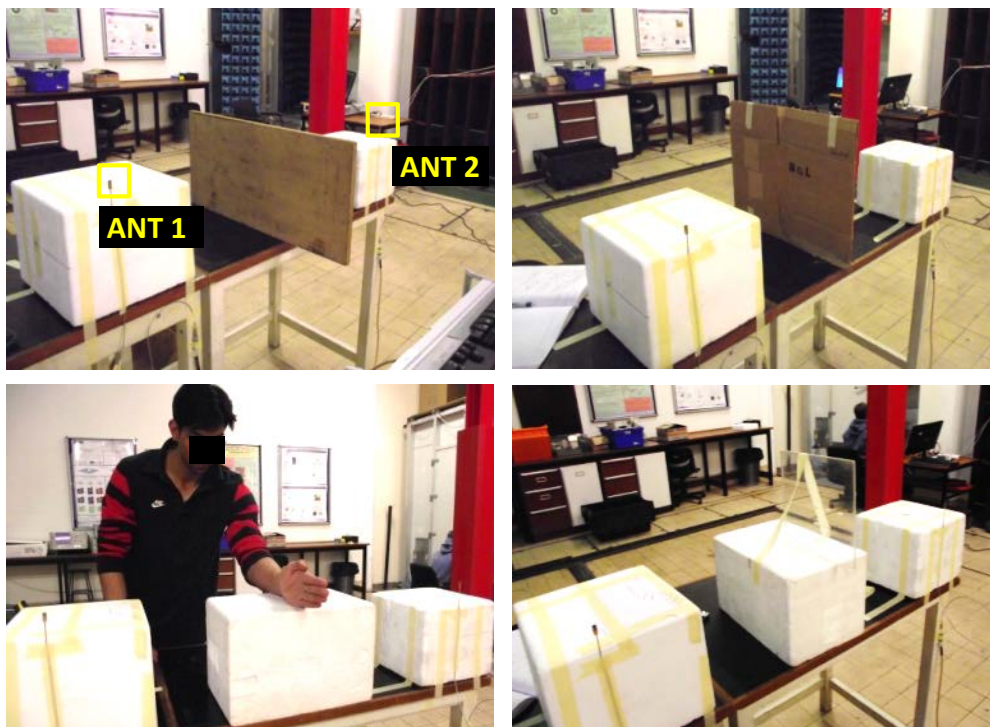


Figure 6.16: Different types of materials: wood, cardboard, human hand and plastic, used as obstruction between the antenna pair for non-line-of-sight ranging analysis.

Figure 6.17 presents the absolute error values obtained in estimating the range values using different obstructions between the antenna pair. It can be noticed from the figure that the maximum ranging error of 1.92 cm was obtained when the human hand was obstructing the line-of-sight between the transmitter-receiver antenna pair. In

contrast, placing a cardboard sheet between the antennas had minimal effect on the range estimates, giving errors of 0.1 cm and 0.24 cm when the antennas were placed 50 cm and 100 cm away respectively.

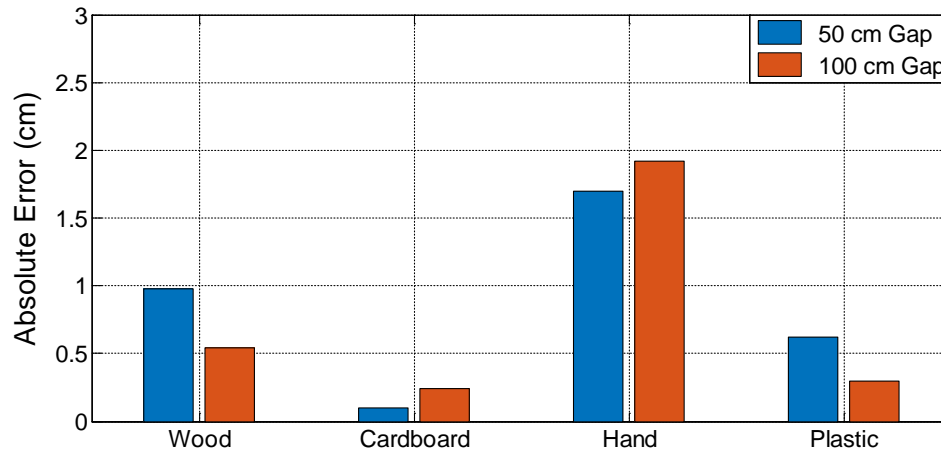


Figure 6.17: Absolute error values for non-line-of-sight ranging measurements of UWB antenna pair using different materials as obstructions.

Sheets of wood and plastic gave slightly higher ranging error as compared to cardboard but the error values were still less than 1 cm for both the cases. As expected, the electromagnetic radiation from the transmitter antenna was able to penetrate the thin cardboard with least amount of delay or distortion. The human hand had the most profound effect on the range estimates. This is understandable since the higher relative permittivity and complex electromagnetic properties of human body tissues affect the antenna's radiation more significantly.

## 6.2 Three Dimensional Localisation Analysis

In this section, an experimental analysis of the three dimensional localisation of the body-mounted miniature UWB antenna has been undertaken using several base station antennas. The study involves determining how precisely location of the on-body mobile antenna can be resolved with the help of several base station receivers through the signal time-of-Flight. Time-of-Arrival data fusion and peak detection techniques have been implemented to locate the on-body antenna, acting as a mobile tag, in terms of  $x, y, z$  cartesian coordinates [5], [15], [16].

### 6.2.1 Base Station Antenna Design

As part of this study, a wideband Vivaldi antenna was designed to be used as the base station receiver, along with the miniature UWB antenna as the mobile transmitter for the three-dimensional localisation experiments. The Vivaldi antenna has an FR-4 substrate with a relative permittivity of 4.3 and thickness of 1.6 mm. The antenna is fed through a 50  $\Omega$  SMA coaxial connector.

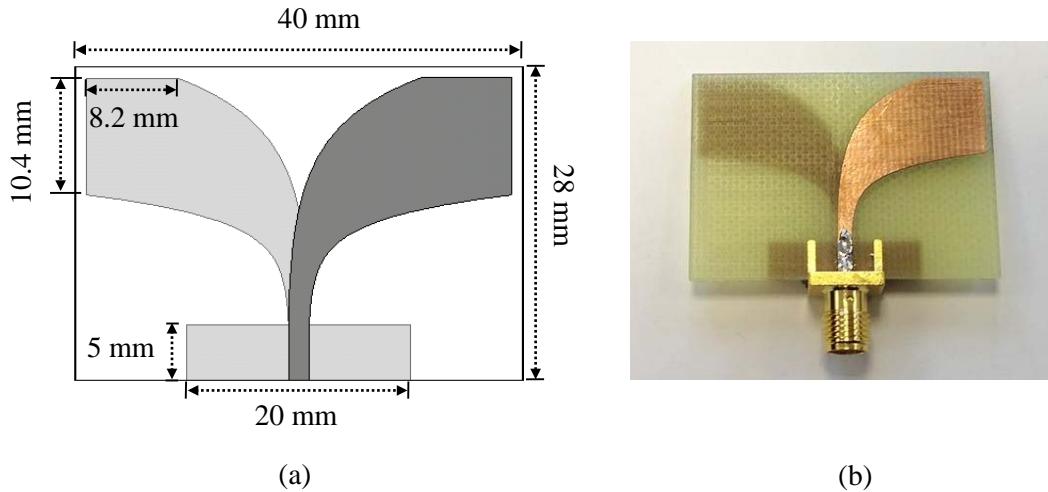


Figure 6.18: The Vivaldi antenna (a) geometry and its (b) fabricated prototype.

The Vivaldi antenna has been designed to operate in the upper UWB band of 6 GHz to 10.6 GHz, just like the miniature UWB antenna. The inner and outer edge tapers of the Vivaldi antenna are characterized by two exponential curves  $I(t)$  and  $O(t)$  respectively, which are defined as

$$I(t) = 0.1 * e^{(0.45 * t)} - 0.82 \quad (6.3)$$

$$O(t) = 1.5 * e^{(0.0045 * t^2)} - 2.42 \quad (6.4)$$

The geometry of the Vivaldi antenna and its fabricated prototype are illustrated in Figure 6.18 (a) and (b) respectively. Figure 6.19 shows the measured and simulated reflection coefficients of the Vivaldi antenna. The measured -10 dB impedance bandwidth of the antenna ranges from 5.7 GHz to > 10 GHz and in simulations is from 6 GHz to > 10 GHz.

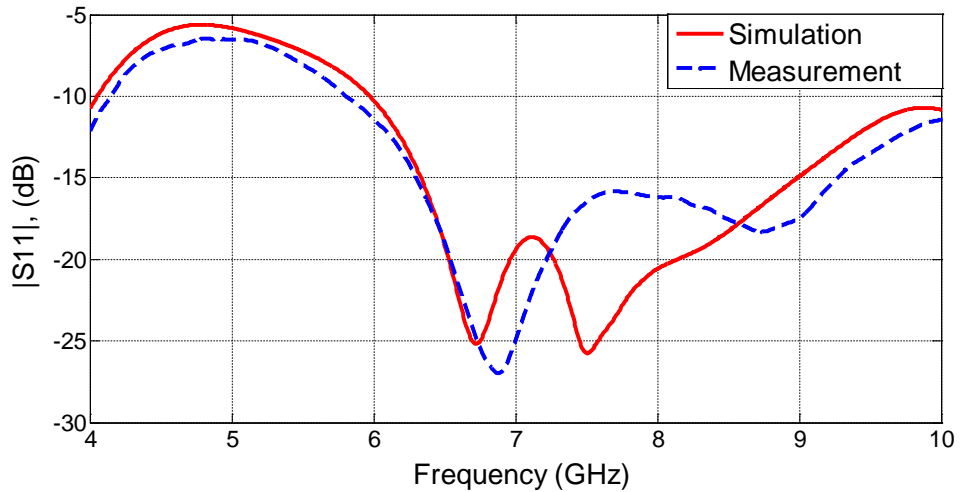


Figure 6.19: Measured and simulated S11 of the Vivaldi antenna in free-space.

To learn about the radiation characteristics of the fabricated Vivaldi antenna, some radiation pattern measurements were also carried out. The radiation patterns were measured at the Antenna Lab in Queen Mary inside an anechoic chamber, using an HP 8720ES vector network analyser [17]. The coordinate frame used for the radiation pattern measurements is illustrated in Figure 6.20. The Vivaldi antenna acted as a receiver and the range horn antenna, connected to the second port of the vector network analyser acted as the transmitter. The radiation patterns were measured at 6, 7.5 and 9 GHz frequencies inside the chamber.

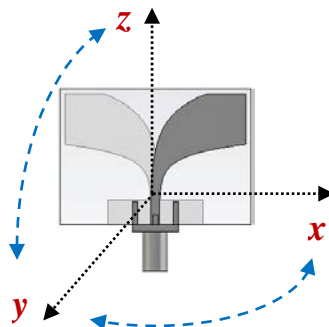


Figure 6.20: Coordinate frame used for the radiation pattern measurements of the Vivaldi antenna.

Figure 6.21 illustrates the normalized radiation patterns for the Vivaldi antenna at 6, 7.5 and 9 GHz for the  $xy$  and  $yz$ -planes respectively. The patterns clearly display the directional nature of the Vivaldi antenna's radiation.

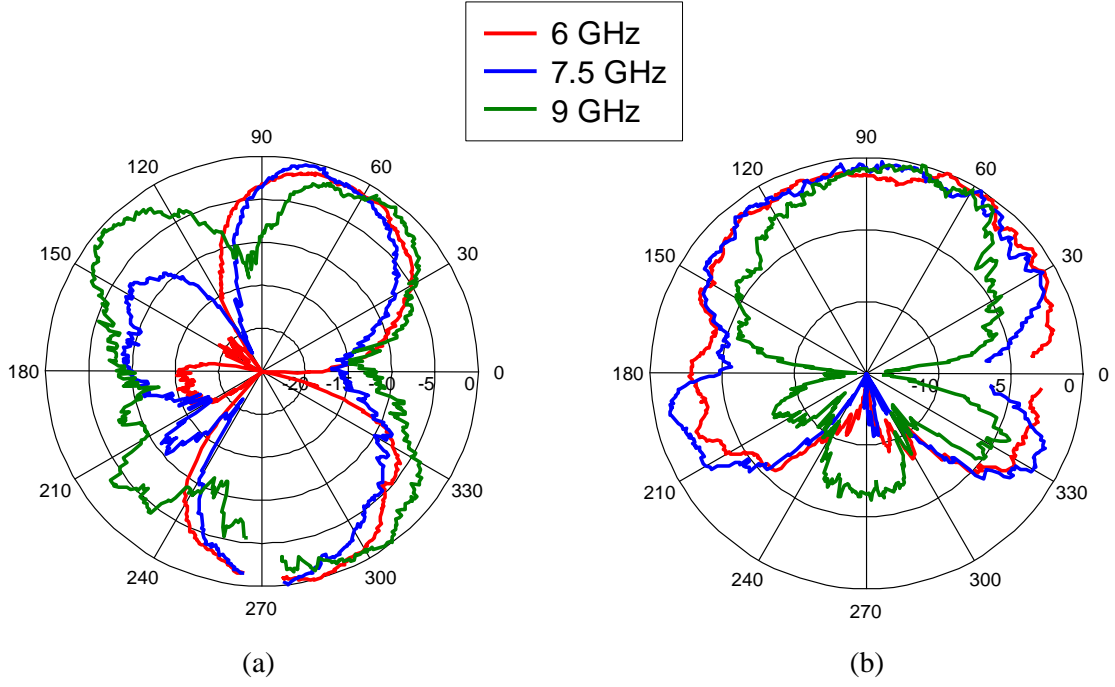


Figure 6.21: Normalized radiation patterns of the Vivaldi antenna at 6, 7.5 and 9 GHz in (a)  $xy$ -plane ( $0^\circ$  is in  $x$ -direction) and (b)  $yz$ -plane ( $0^\circ$  is in  $y$ -direction).

## 6.2.2 Localisation Method and Measurement Setup

The Time-of-Arrival (TOA) data fusion method was implemented in order to compute the coordinates of the mobile station. This method is based on combing the TOA estimates of the signal transmitted from the mobile station, which is received by the different base stations. TOA is then used for range estimation between the mobile station and each base station receiver by multiplying it with the speed of light ( $2.998 \times 10^8$  m/s). Determination of the target position from a set of range measurements is called trilateration.

Let  $d_1$ ,  $d_2$  and  $d_3$  represent the range measurements obtained from three TOA measurements. Then, the following three equations must be solved jointly in order to estimate the position of the mobile station  $(x, y)$  via trilateration:

$$d_i = \sqrt{(x_i - x)^2 + (y_i - y)^2}, \quad i = 1, 2, 3 \quad (6.5)$$

where  $(x_i, y_i)$  is the known position of the  $i^{th}$  reference node, and  $(x, y)$  is the position of the target node. These equations can be solved by using the least square method.

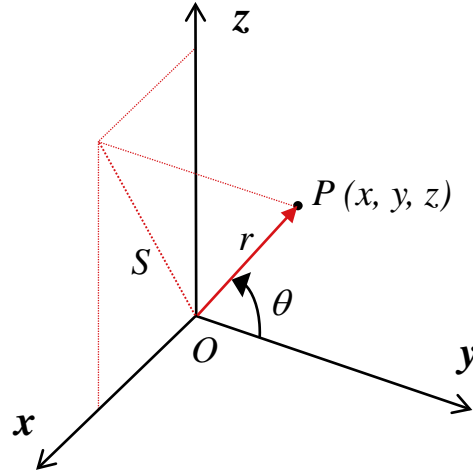


Figure 6.22: The coordinate system for three dimensional localisation of the unknown coordinates of point  $P$ .

The L-shaped configuration makes use of just three base stations to achieve three-dimensional localisation. Firstly, the  $x$  and  $y$  coordinates of the mobile station are calculated by using the time of arrival data fusion method [16] discussed above. Then, the following trigonometric equations are used to compute the mobile station's  $z$  coordinate:

$$\theta = \cos^{-1} \frac{y}{r} \quad (6.6)$$

$$S = y \tan(\theta) \quad (6.7)$$

$$z = \sqrt{S^2 - x^2} \quad (6.8)$$

where  $\theta$  is the elevation angle from the  $y$ -axis,  $r$  is the estimated distance of the mobile station from BS1 (origin  $O$  in Figure 6.22),  $x$  and  $y$  are the estimated coordinates of the mobile station using time of arrival data fusion method and  $S$  is the projected distance of the mobile station from origin in the  $xz$  plane. The coordinate system is illustrated in Figure 6.22.

The localisation measurements involved the usage of three Vivaldi antennas arranged in an L-shaped configuration as receivers, each antenna acting as a base station (BS) and the miniature UWB antenna as a mobile transmitter that needs to be localised. The miniature antenna to be localised was fixed on top of a human test subject's finger. The measurements were carried out inside the Body-Centric Wireless Sensor

Lab at Queen Mary University of London. The L-shaped configuration of the base stations for localisation measurements is presented in Figure 6.23.

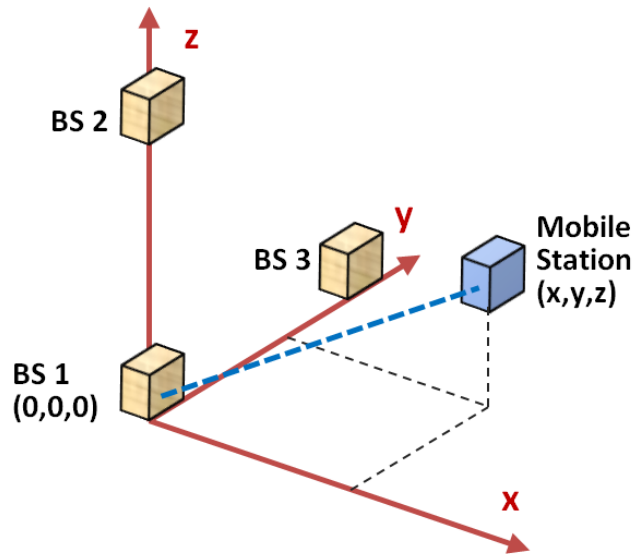


Figure 6.23: L-shaped configuration of the base stations (BSs) for 3D localisation of the mobile station (MS).

For ease of measurement, we have chosen to operate in the frequency domain using a four-port Agilent PNA-X vector network analyser [14]. Channel impulse response is measured between the transmitter and each of the three receivers, by sweeping over the frequency band of 3 to 11 GHz and using the IFFT. For direct line-of-sight signal propagation, peak of the channel impulse response provides the time it takes for the signal to reach the receiver from the transmitter i.e. the TOA. As discussed in the previous section, TOA is then used for range estimation between the transmitter and each of the three base station receivers, by multiplication of the TOA values with the speed of light. Time of arrival data fusion method is then implemented to estimate the location of the mobile station. BS1 is selected as the origin and acts as the reference point to obtain the 3D coordinates of the MS and the other two BSs.

The distances between the three BSs were selected prior to the measurements. The horizontal distance between BS1 and BS3 was chosen to be 1 m, both placed at the same height, with BS2 fixed 0.5 m above BS1. Thus, considering BS1 as the origin, the  $(x, y, z)$  coordinates of the fixed base stations BS1, BS2 and BS3 could be assigned as  $(0,0,0)$ ,  $(0,0,0.5)$  and  $(0,1,0)$  respectively. The 3D coordinates of the BSs along with the signal TOA data were then used to compute the 3D coordinates of the

MS. The actual 3D coordinates for the MS were measured beforehand for each position (using BS1 as reference) and were used later on for comparison with the computed coordinates. The actual location of the mobile station was deduced by creating a coordinate system in the  $xy$  plane on the measurement floor and placing the mobile station at several pre-determined locations. This provided the  $x$  and  $y$  coordinates of the actual location of the mobile station. The  $z$  coordinate was obtained by placing the antenna at a known height from the floor.

The feeds of the antennas were used as the reference points to determine their actual positions. Hence the feed port of BS1 was (0,0,0) in the coordinate system and the positions of other base stations and mobile station were deduced as the distance of their individual feeds from the BS1 feed. Since the coordinate system has to be created manually, this leads to some degree of unavoidable error in defining the actual location of the mobile station. The measurement accuracy of the actual 3D coordinates of the mobile station is estimated to be about  $\pm 0.5$  cm. Figure 6.24 illustrates a photograph of the measurement setup for the 3D localisation experiment, with the MS fixed on a human test subject's finger and the three base stations in the vicinity.

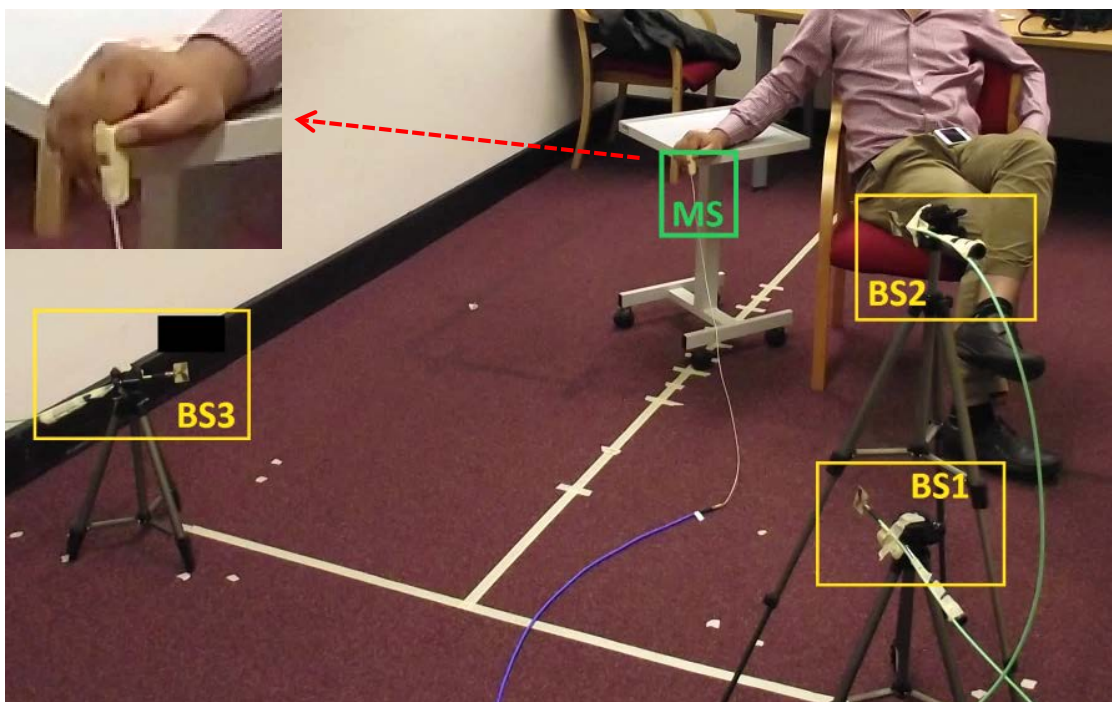


Figure 6.24: 3D localisation experimental setup with the finger-mounted mobile station (MS) and the three base stations (BS1 - 3). Miniature antenna mounted on the finger is shown in the inset.

## 6.3 3D Localisation Measurements and Results

This section provides results of the various three dimensional localisation experiments undertaken in this investigative study. Numerous localisation measurements were carried out by using the body-worn miniature ultra-wideband antennas as transmitters and off-body Vivaldi antennas in the vicinity as the receivers. Experiments have been performed by moving the tag antenna in various directions and the precision with which these slight movements could be resolved has been studied. Some more complex localisation experiments were also carried out, involving the tracking of more than one transmitter tag simultaneously. This helps in quantifying the ease with which this system could be scaled up for realising a full body motion tracking system, having multiple transmitter tags. Moreover, some repeatability measurements were also carried out to measure the variation in the localisation results for the same set of measurement scenarios on two different occasions, which helps to assess the reliability and stability of the system.

### 6.3.1 Localisation of Mobile Tag Being Moved Along the $x$ -axis

These measurements were done with the mobile station (MS) being gradually moved in small steps away from the plane containing the three base stations ( $yz$  plane), i.e. along the  $x$ -axis. Two sets of measurements were performed. In first case, the MS was moved away from the  $yz$  plane with increments of 10 cm and second with increments of 3 cm. The initial distance of the MS was selected to be 1 m from the  $yz$  plane for both the cases.

The height at which the MS was placed was always kept constant. Eight measurements were done for the first scenario and six measurements were done for the second. The localisation results showing a comparison of the actual and estimated locations of the mobile station from the two measurements are presented in Figure 6.25 (a) and (b). It can be noticed from the localisation results in Figure 6.25 that the position estimation of the MS has been achieved with good accuracy. The average error in calculating the 3D coordinates of the MS for the  $x$ ,  $y$  and  $z$  axes was 3.65 cm, 1.16 cm and 1.15 cm respectively.

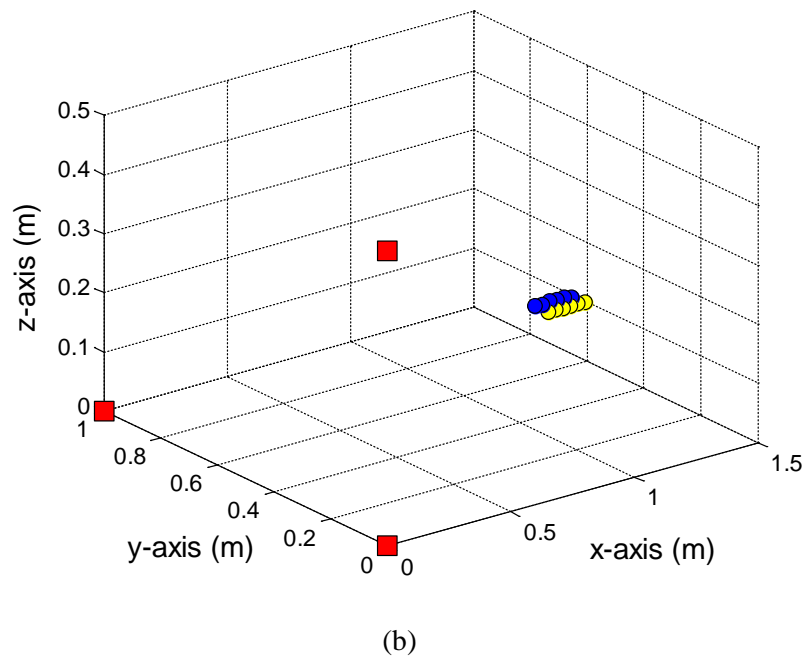
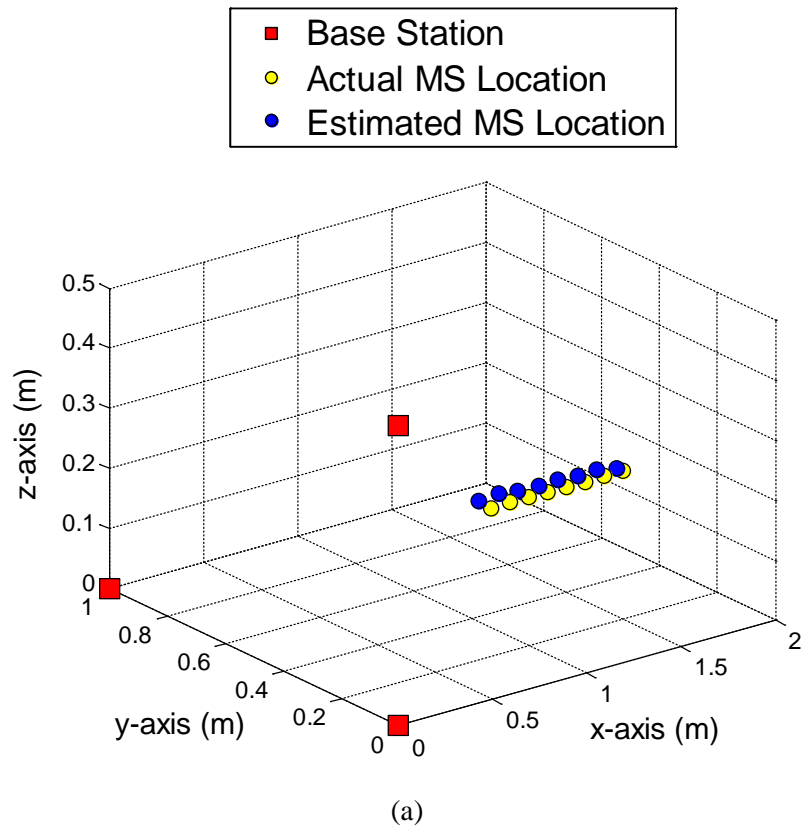


Figure 6.25: Three dimensional plots of the estimated and actual positions of the mobile station for (a) 10 cm increments and (b) 3 cm increments.

It is evident from the above results that the mobile station is localised with a very high degree of precision and the gradual movement of the MS in the direction of the  $x$ -axis can be noticed clearly. Some part of the localisation error could actually be accounted

for by the subject movement as well, since it is very difficult for a real human to remain absolutely still during course of the measurements. An interesting phenomenon that was noticed from the localisation results was that there was a consistent shift between the estimated and actual positions of the mobile station. Further localisation experiments were carried out to study more about this and how this error could be mitigated.

### 6.3.2 Localisation of Mobile Tag Being Moved in the $xy$ and $xz$ planes

For this analysis, the MS was moved in the  $xy$  and  $xz$  planes. For the first case, the MS was shifted with increments of 3 cm along the  $y$ -axis. Five such measurements were taken, with the initial distance of the MS from the plane containing the three BSs being 0.7 m. Then the antenna was shifted 10 cm further away from the plane containing the three BSs ( $yz$  plane) and the same measurements (with increments of 3 cm in  $y$ -axis) were repeated. In this way, four sets of measurements were performed, each having the MS at a specific distance away from the  $yz$  plane for five increments in the  $y$ -axis. The results of the localisation experiment where the mobile tag was being moved in the  $xy$  plane are presented in Figure 6.26. For these measurements, the average error in calculating the 3D coordinates of the MS for the  $x$ ,  $y$  and  $z$  axes was 4.08 cm, 1.32 cm and 1.42 cm respectively.

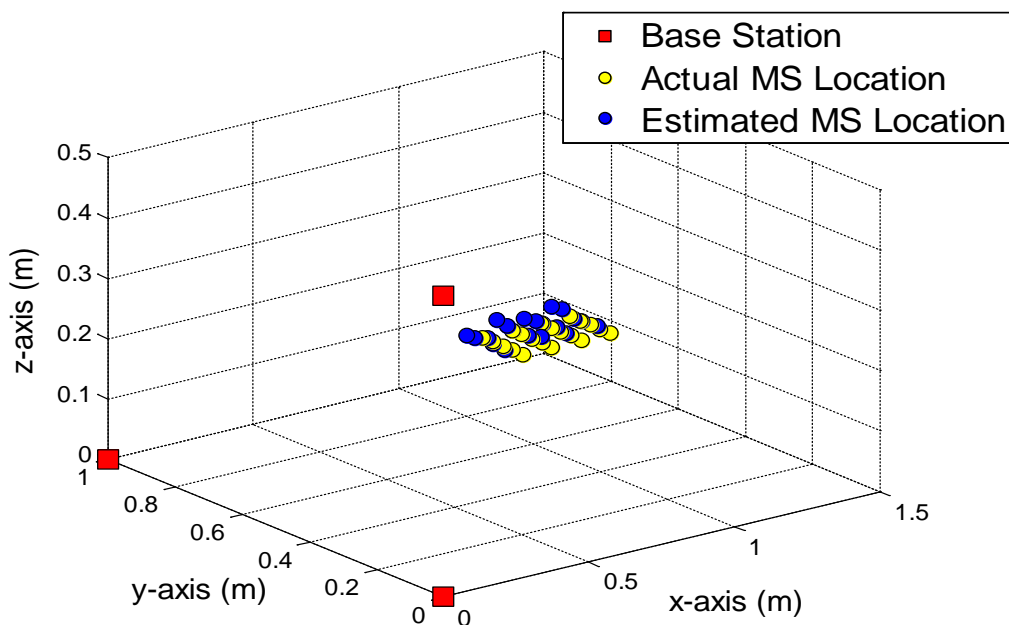


Figure 6.26: Three dimensional plots of the estimated and actual positions of the mobile station being moved in the  $xy$  plane.

In a similar manner, another localisation experiment was performed with the mobile station being moved in the  $xz$  plane. Here, the MS was shifted with increments of 3 cm along the  $z$ -axis. Four such measurements were done with the distance of the MS from the  $yz$  plane equal to 0.7 m. Then the antenna was shifted 10 cm further away from the  $yz$  plane and the same measurements (with increments of 3 cm in  $z$ -axis) were repeated. In this manner, six groups of localisation measurements were performed, each having the MS at a specific distance away from the  $yz$  plane for four increments in  $z$ -axis. The localisation results for the second experiment have been presented in Figure 6.27.

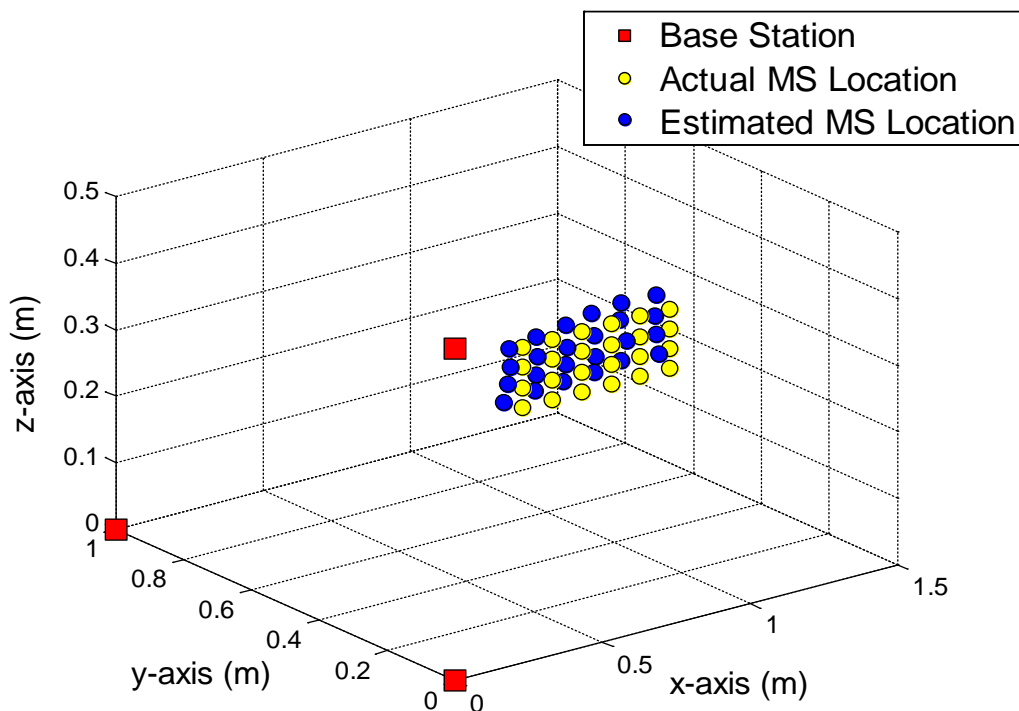


Figure 6.27: Three dimensional plots of the estimated and actual positions of the mobile station being moved in the  $xz$  plane.

For the second case, the average error in estimating the 3D coordinates of the MS for the  $x$ ,  $y$  and  $z$  axes was 4.35 cm, 0.95 cm and 1.62 cm respectively. It can be noticed from Figure 6.26 and Figure 6.27 that there is a consistent shift in all the estimated positions of the mobile station as compared to the actual positions, exactly as in the initial localisation experiment. When the estimated MS positions are compared to each other, it can be clearly seen from the plots that the tiny increments of the MS are sensed by the base stations very smoothly and accurately for both the experiments.

### 6.3.3 Localisation of Two Mobile Tags Simultaneously

For this experiment, two mobile stations (MS) were localised simultaneously, both fixed on a human test subject's hand. One MS was attached to the thumb and the other to the index finger. The first measurement was taken with the thumb and index finger fully stretched. The index finger was then slowly brought near the thumb in five steps, keeping the thumb position constant. Localisation measurements were performed for the thumb location as well as each position of the index finger. Figure 6.28 illustrates the actual and estimated positions of the thumb and the index finger being moved towards the thumb.

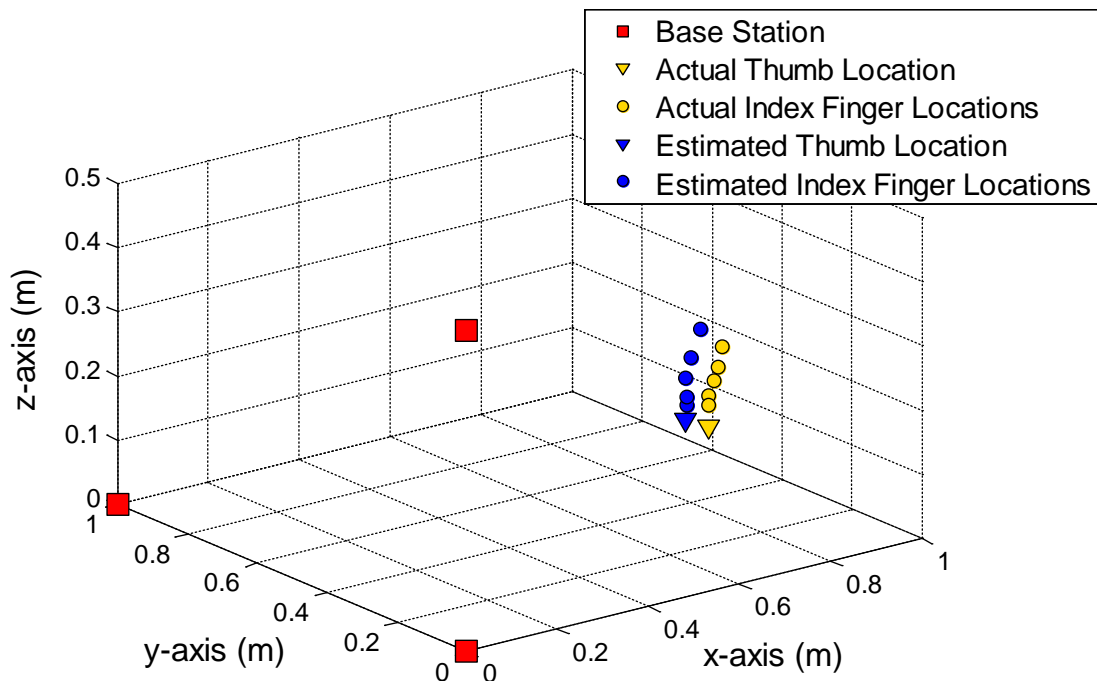


Figure 6.28: Three dimensional plots of the estimated and actual positions of two mobile stations fixed on thumb and index finger, being localised simultaneously.

It can be observed from Figure 6.28 that the mobile station position on the index finger has been tracked with very good accuracy. The trajectory of the gradual movement of the index finger towards the thumb can be clearly noticed from the figure. However, as noticed in all the previous localisation experiments, there is a consistent shift in the estimated positions of the MS as compared to the actual locations. For this experiment, the average error in calculating the 3D coordinates of the MS for the  $x$ ,  $y$  and  $z$  axes was 4.28 cm, 1.31 cm and 1.37 cm respectively.

### 6.3.4 Repeatability of the Localisation Measurements

In this section, the repeatability of the localisation of the mobile tag using the techniques presented in the previous sections of this chapter has been examined. The aim of this analysis was to study how the localisation results differ for the measurements done on two different occasions, when the measurement environment and all the other parameters were kept unchanged. For this, four arbitrary locations were chosen for placing the mobile tag and these positions were localised through the base station receivers using time of arrival data fusion techniques. A repeat of the four measurements was then carried out to analyse how the estimated locations of the mobile station change when the same measurements are repeated on a second occasion. Figure 6.29 illustrates the estimated locations of the mobile station on two different instances.

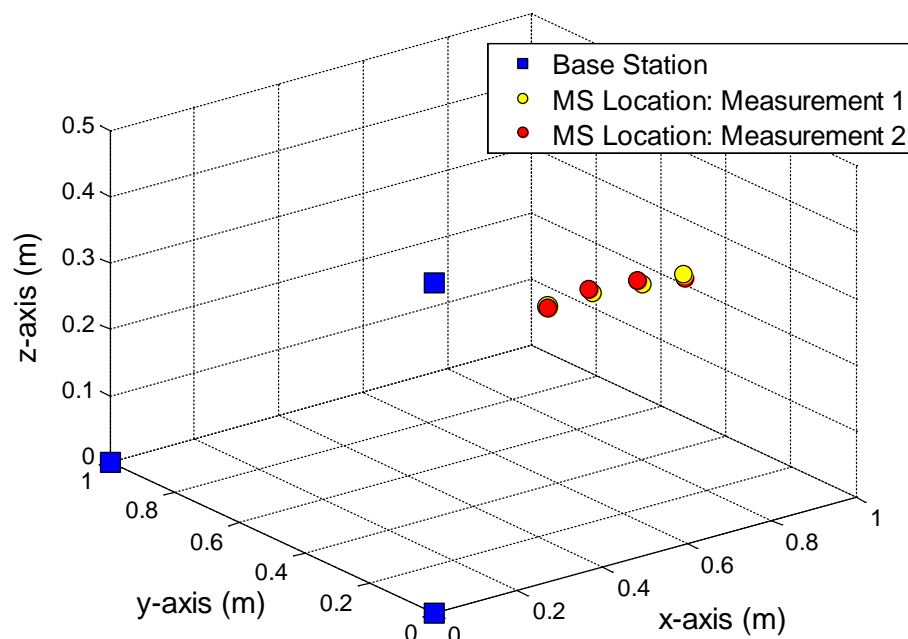


Figure 6.29: Deviation in the estimated locations of the MS from the localisation measurements done on two different occasions.

It can be noticed from Figure 6.29 that the localisation estimates of the MS have been repeated with a very little change. The average difference between the estimated  $x$ ,  $y$  and  $z$  coordinates between the first and second set of measurements was 0.67 cm, 0.34 cm and 0.62 cm respectively. Hence, this analysis demonstrates that the localisation measurements carried out by making use of the three Vivaldi base stations are repeatable within a deviation of only a few millimetres.

### 6.3.5 Calibration of Localisation System to Minimise Error

From the results of all the localisation experiments presented in the previous sub-sections, it has been observed that there was a small degree of consistent shift in all the estimated positions of the mobile station as compared to the actual positions. Although localisation of the MS has been successfully done with average errors mostly in the range of 1 to 4 cm, the consistency in the magnitude of the error values provides the opportunity to calibrate out this error. By removing the consistent error obtained in the localisation measurements, we could potentially achieve sub-centimetre localisation accuracy. The average errors in estimating the  $x$ ,  $y$  and  $z$  coordinates of the MS for each of the localisation experiments discussed in the previous sections, along with the overall average error values for all the experiments have been summarized in Table 6.2. It can be observed from these values that the localisation error was the least for the  $y$  and  $z$  axes for all the experiments as compared to the  $x$ -axis. This could be attributed to the fact that all the base stations are situated in the  $yz$  plane, leading to a better localisation accuracy for the  $y$  and  $z$  axes.

Table 6.2: Average error in estimating the  $x$ ,  $y$  and  $z$  coordinates of the MS for various localisation experiments.

Localisation Experiment	Average Error (cm)		
	$x$	$y$	$z$
MS moved along $x$ -axis	3.65	1.16	1.15
MS moved in $xy$ plane	4.08	1.32	1.42
MS moved in $xz$ plane	4.35	0.95	1.62
Two MSs localised together	4.28	1.31	1.37
<b>(Overall Average)</b>	<b>4.09</b>	<b>1.19</b>	<b>1.39</b>

As discussed earlier, the feeds of the antennas were used as the reference points to get the actual and estimated positions of the mobile station. In order to calibrate the error obtained in estimating the MS location and to get more accurate and reliable measurement results, the locations of the mobile station as well as the base stations

were adjusted by taking the phase centres of the antennas as the reference points instead. Since the phase centre of an antenna is the apparent point from which the electromagnetic radiation appears to emanate, making use of the phase centre as the reference could actually help in obtaining more accurate estimation of the time-of-flight values and also ensure the actual positions of the mobile station and the three base stations are considered more realistically. The locations of phase centres of the Vivaldi and the miniature UWB antenna were computed through numerical simulations in CST Microwave Studio software at 8.3 GHz frequency, which is the centre frequency of the 6 to 10.6 GHz operational band for the antennas. Figure 6.30 shows the positions of the simulated phase centres of the two antennas with respect to the antenna structures.

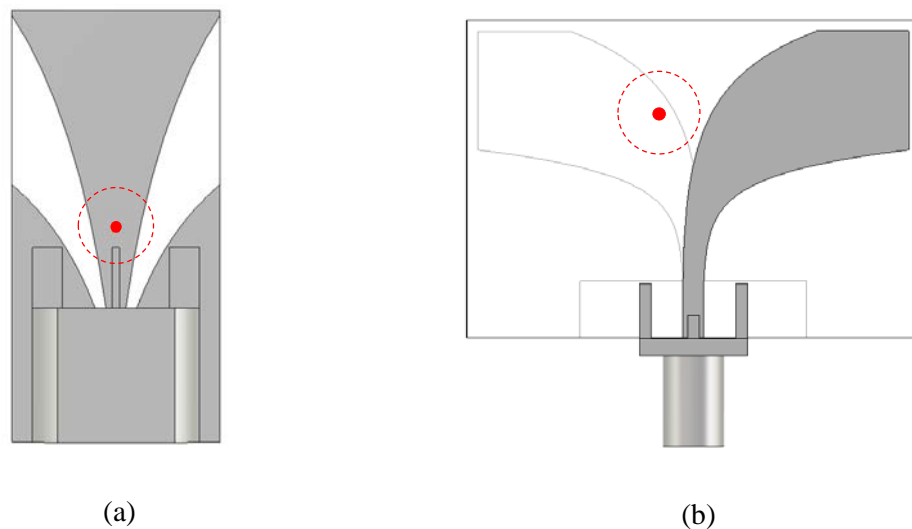


Figure 6.30: Simulated phase centres of the (a) miniature UWB antenna and the (b) Vivaldi antenna at 8.3 GHz frequency.

Figure 6.31 illustrates estimated locations of the MS after calibration of the average error, along with the actual MS locations, when the MS was being moved along the  $x$ -axis. It can be noticed from Figure 6.31 that after calibration, the MS has been localised with a very high precision. After following the calibration procedure, the average absolute error in the estimation of the  $x$ ,  $y$  and  $z$  coordinates of the MS was 0.27 cm, 0.84 cm and 0.15 cm respectively. This is in sharp contrast to the localisation errors of 3.65 cm, 1.16 cm and 1.15 cm obtained for the  $x$ ,  $y$  and  $z$  axes respectively before applying the calibration. Hence, it has been possible to achieve sub-centimetre localisation accuracy by taking into consideration the phase centres of the antennas.

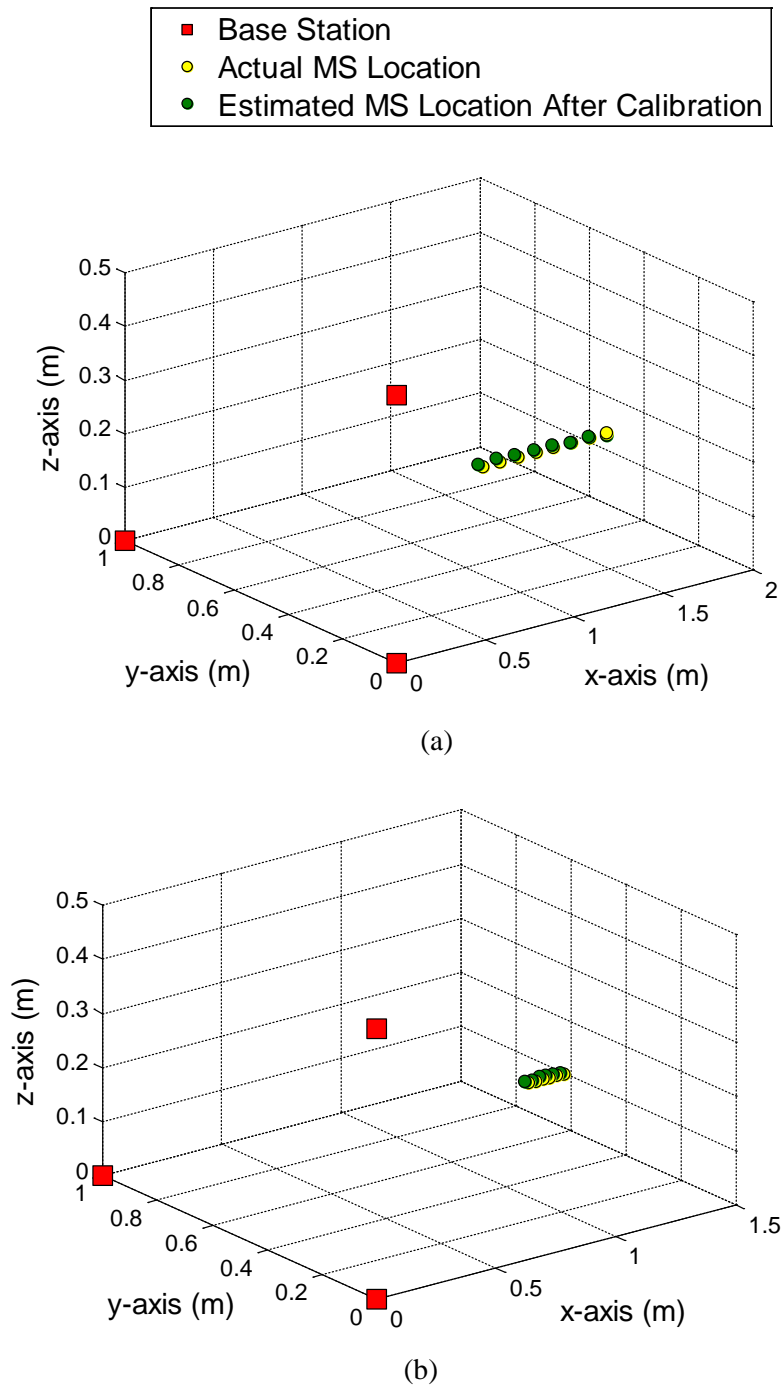


Figure 6.31: Three dimensional plots of the actual positions of the mobile station along with its calibrated estimated positions, with the MS being moved along  $x$ -axis, for (a) 10 cm increments and (b) 3 cm increments.

The same method of utilizing the antenna phase centres for calibrating out the localisation error was repeated for the experiments where the mobile station was moved in the  $xy$  and  $xz$  planes. Figure 6.32 and Figure 6.33 illustrate the estimated locations of the MS after calibration, along with the actual MS locations, when the MS was being moved in the  $xy$  and  $xz$  planes respectively.

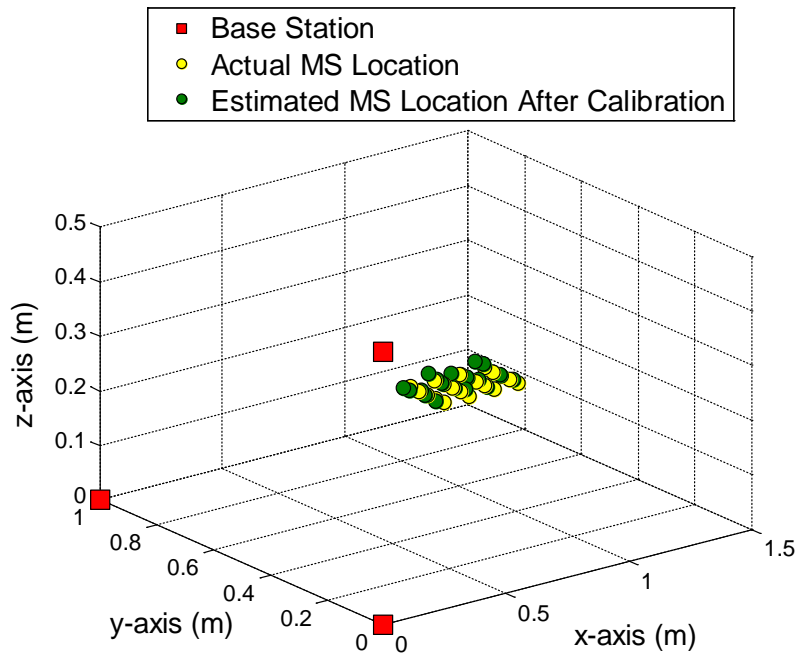


Figure 6.32: Three dimensional plots of the actual positions of the mobile station along with its calibrated estimated positions, with the MS being moved in the  $xy$  plane.

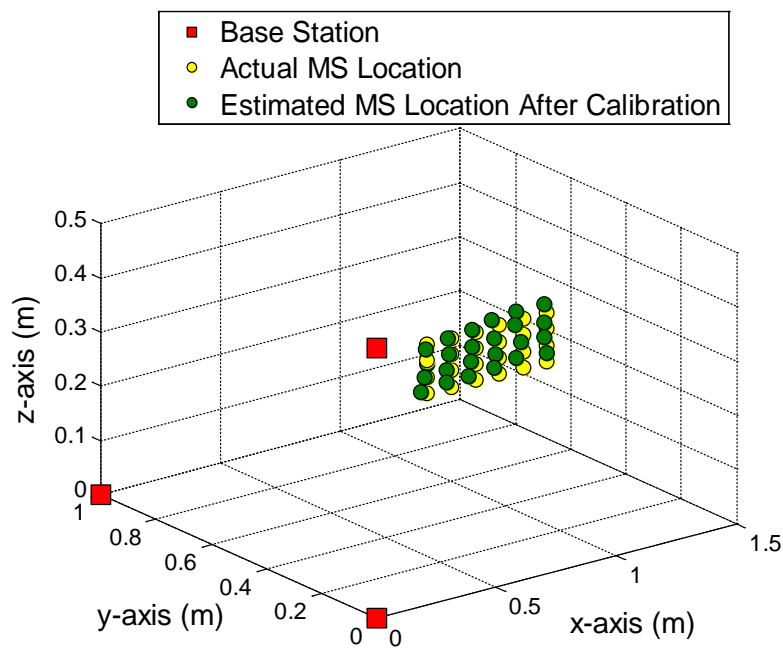


Figure 6.33: Three dimensional plots of the actual positions of the mobile station along with its calibrated estimated positions, with the MS being moved in the  $xz$  plane.

It can be noticed from the above figures that after calibration, the positions of the mobile station have been estimated with very high precision. The average absolute error in estimating the 3D coordinates of the MS for the  $x$ ,  $y$  and  $z$  axes became 0.48

cm, 0.69 cm and 0.42 cm respectively for movement in the  $xy$  plane and 0.79 cm, 0.77 cm and 0.62 cm respectively for movement in the  $xz$  plane. Hence, once again we have been able to achieve millimetre-level accuracy in localising the mobile station by taking into consideration the antenna phase centres as the reference points for determination of the antenna positions. In a similar fashion, the error obtained in the measurements involving localisation of two mobile tags simultaneously was also calibrated out. Figure 6.34 illustrates the estimated positions of the thumb and the index finger after calibration, along with their actual locations.

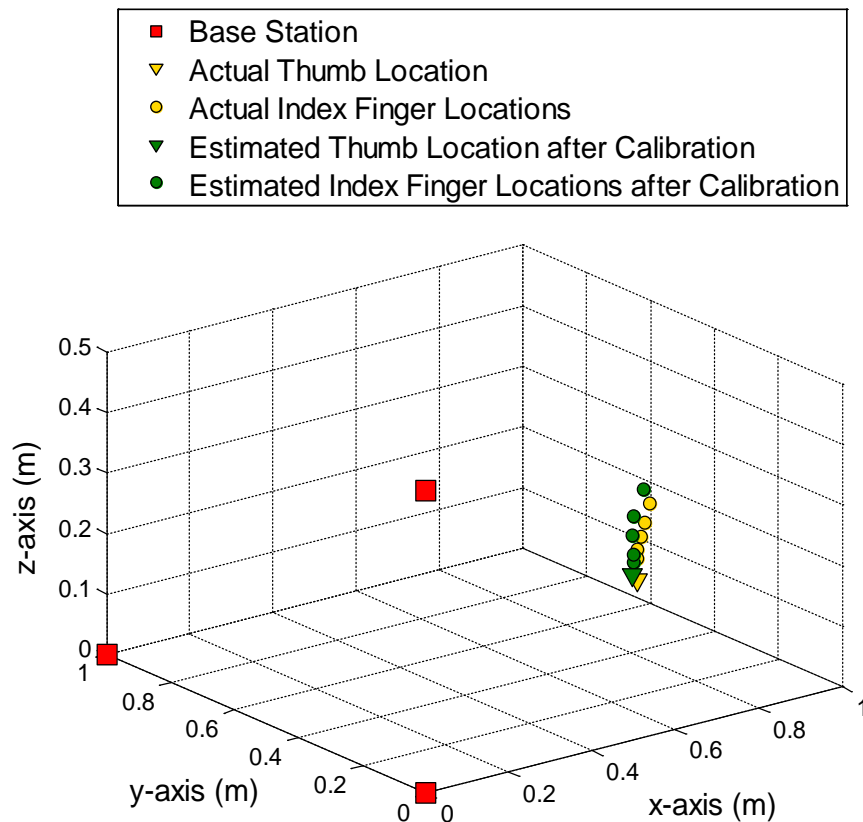


Figure 6.34: Three dimensional plots of the actual positions of thumb and finger mounted mobile stations, along with the calibrated estimated positions.

Yet again, it can be seen from Figure 6.34 that by making use of the antenna phase centres as the reference points, it was possible to predict the position of the two MSs very accurately. After going through the calibration process, the average error in estimating the 3D coordinates of the two mobile stations for the  $x$ ,  $y$  and  $z$  axes becomes 0.69 cm, 0.98 cm and 0.37 cm respectively. This approach has demonstrated that millimetre-level localisation accuracy could be achieved with UWB technology if the antennas are assumed to be point sources and their phase centres are utilized for

obtaining the actual as well as estimated locations. In this way, a major portion of the consistent error being encountered in estimating the MS location could be taken care of. The overall average error for all the above measurements taken as a single set is 0.59 cm. Hence, these investigations have revealed that through taking into consideration the phase centres of the antennas in a positioning system, very precise localisation of a target node could be realised.

## **6.4 Summary**

In this chapter, a detailed analysis involving several range measurements has been provided. The accuracy with which the point-to-point distance between a transmitter-receiver pair of the miniature UWB antennas could be estimated is studied. Time-of-Flight of the signal propagating from the transmitter antenna to the receiver was used for range estimation. Effect of the human body and antenna orientation on the accuracy of range estimates was also investigated. By means of this analysis, it has been demonstrated that for free-space measurements, range estimates can be done with millimetre accuracy by making use of UWB technology.

An experimental investigation of the three dimensional localisation of the body mounted miniature UWB antenna is presented. The design and geometry of a compact wideband Vivaldi antenna are discussed, along with its simulation and measurement results. The Vivaldi antenna has been designed to be used as a base station receiver for the localisation measurements. Several three dimensional localisation experiments have been carried out using the miniature antenna as a mobile station and three Vivaldi antennas as base stations to understand the level of accuracy with which the location of the mobile station could be estimated. Good uncalibrated localisation accuracy of 1-4 cm has been achieved in these measurements. Besides, a unique approach for achieving sub-centimetre localisation accuracy has been demonstrated successfully. In this approach, the antennas in a localisation system are considered as point sources and their phase centres are used as reference points for determining the real locations of the nodes and computing the estimated locations of the mobile station. This study has effectively validated the capability of ultra-wideband technology for use in high precision localisation.

## References

- [1] P. S. Hall and Y. Hao, Eds., *Antennas and Propagation for Body-Centric Wireless Communications*, 2nd ed. Artech House, 2012.
- [2] N. Chahat, M. Zhadobov, R. Sauleau, and K. Ito, "A compact planar UWB antenna for on-body communications," in *Proceedings of the 5th European Conference on Antennas and Propagation (EUCAP)*, 2011, pp. 3627–3630.
- [3] L. Taponocco, A. A. D'Amico, and U. Mengali, "Joint TOA and AOA Estimation for UWB Localization Applications," *IEEE Trans. Wirel. Commun.*, vol. 10, no. 7, pp. 2207–2217, Jul. 2011.
- [4] D. Valderas, J. I. Sancho, D. Puente, C. Ling, and X. Chen, *Ultrawideband Antennas: Design and Applications*. Imperial College Press, 2011.
- [5] Z. Sahinoglu, S. Gezici, and I. Guvenc, *Ultra-Wideband Positioning Systems: Theoretical Limits, Ranging Algorithms, and Protocols*. Cambridge University Press, 2008.
- [6] L. Guo, "Study and Miniaturisation of Antennas for Ultra Wideband Communication Systems," PhD Thesis, Queen Mary University of London, 2009.
- [7] S. Licul, J. Noronha, W. Davis, D. Sweeney, C. Anderson, and T. Bielawa, "A parametric study of time-domain characteristics of possible UWB antenna architectures," in *58th Vehicular Technology Conference (VTC)*, 2003, vol. 5, pp. 3110–3114.
- [8] "Ultra Wide Band Be Spoon." [Online]. Available: <http://bespoon.com/technology/ultra-wide-band/>.
- [9] W. P. Siriwongpairat and K. J. R. Liu, *Ultra-Wideband Communications Systems : Multiband OFDM Approach*. John Wiley and Sons, 2007.
- [10] D. Humphrey and M. Hedley, "Prior Models for Indoor Super-Resolution Time of Arrival Estimation," in *IEEE 69th Vehicular Technology Conference*, 2009, pp. 1–5.

- [11] R. Bharadwaj, C. Parini, and A. Alomainy, "Ultrawideband-Based 3-D Localization Using Compact Base-Station Configurations," *IEEE Antennas Wirel. Propag. Lett.*, vol. 13, pp. 221–224, 2014.
- [12] S. Gezici and H. V. Poor, "Position Estimation via Ultra-Wide-Band Signals," *Proc. IEEE*, vol. 97, no. 2, pp. 386–403, Feb. 2009.
- [13] G. Shen, R. Zetik, H. Yan, O. Hirsch, and R. S. Thoma, "Time of arrival estimation for range-based localization in UWB sensor networks," in *IEEE International Conference on Ultra-Wideband*, 2010, vol. 2, pp. 1–4.
- [14] "Agilent 2-Port and 4-Port PNA-L Network Analyzer," 2013. [Online]. Available: <http://cp.literature.agilent.com/litweb/pdf/N5235-90004.pdf>.
- [15] Z. Sahinoglu and I. Guvenc, "Threshold-Based TOA Estimation for Impulse Radio UWB Systems," in *IEEE International Conference on Ultra-Wideband*, 2005, pp. 420–425.
- [16] A. H. Sayed, A. Tarighat, and N. Khajehnouri, "Network-based wireless location: challenges faced in developing techniques for accurate wireless location information," *IEEE Signal Process. Mag.*, vol. 22, no. 4, pp. 24–40, Jul. 2005.
- [17] "Agilent 8720E Family Microwave Vector Network Analyzers," 2004. [Online]. Available: <http://literature.cdn.keysight.com/litweb/pdf/5968-5163E.pdf>.

# **Measurements and Experimental Analysis using the UWB Localisation System**

Accurate determination of the location of wireless devices forms the basis of many new and interesting applications. Ultra-wideband (UWB) signals enable such positioning, especially in wireless body area networks [1]. Microwave-based localisation systems could be used to track and determine the location of wireless mobile tags. These tags could be attached to moving objects or the human body to locate their position in real time. The mobile tags then transmit wireless signals to receiver devices in the vicinity, called readers or base stations, which process these received signals to resolve the location of the tags [2], [3].

UWB is an extremely attractive technology for application in the field of body-centric wireless communications. This technology provides the prospect for realising robust communication links and high resolution localisation systems. UWB localisation is usually accomplished in two stages: parameter extraction and data fusion. The parameter extraction stage estimates the required parameters of the signals received

by the sensor nodes for usage in the data fusion step. Typical parameters that are used in microwave-based localisation systems are time of arrival (TOA), time difference of arrival (TDOA), angle of arrival (AOA) and received signal strength (RSS). The range-based schemes TOA and TDOA have been shown to deliver the best localisation accuracy because of the excellent time resolution of UWB signals [4], [5].

Because of its low energy consumption and low complexity, the Impulse-Radio ultra-wideband (IR-UWB) technology is being increasingly utilized in wireless body area network applications and is emerging as an ideal fit for the requirements of the next generation wireless sensor networks [6], [7]. This is due to its fine time resolution, energy efficiency and robustness to interference in harsh environments [8]. This technology employs short pulses of nanosecond-order duration, which enables aggressive duty cycling at the transmitters and hence allowing ultra-low power transmission in portable and body mounted devices [9]. IR-UWB radios are suitable for use in precise location systems and high data rate communication links due to the large bandwidths that can be realised with them [10].

In this chapter, the experimental and investigational work carried out towards the development of a prototype ultra-wideband localisation system demonstrating the feasibility and potential of UWB technology for precise location of body mounted mobile tags has been provided. The final antenna designs for the locator and base station sensor nodes, presented in Chapters 4 and 6 respectively, were integrated with the identified UWB chip (from *DecaWave*) and development board, in order to evaluate the real time performance of this standalone demonstrator localisation system.

## **7.1 DecaWave Ultra Wideband Chip**

### **7.1.1 Overview**

The *DW1000 ScenSor* from DecaWave is a fully integrated low power single chip UWB transceiver IC, compliant to the IEEE 802.15.4-2011 standard. It is optimized for applications in Real Time Location Systems and Wireless Sensor Networks across a variety of applications. It can support communication at high data rates of up to 6.8 Mbps. The chip has an excellent communication range of 300 m in line-of-sight

(LOS) and 35 m in non-line-of-sight (NLOS) case. It enables location of objects to an accuracy of 10 cm using either two-way ranging time-of-flight (TOF) measurements or one-way time difference of arrival schemes [11].

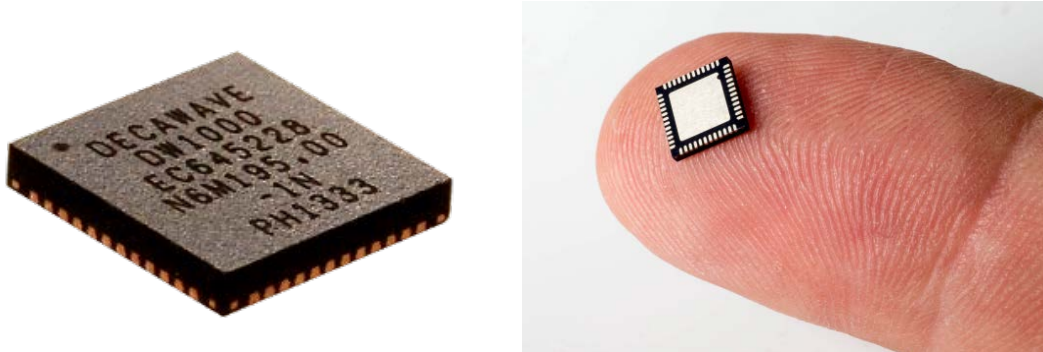


Figure 7.1: DecaWave's DW1000 location and communication chip [12], [13].

The DW1000 chip supports six frequency bands with centre frequencies from 3.5 GHz to 6.5 GHz. The chip has a maximum receive bandwidth of 900 MHz. Because of its short packet durations, the chip can allow high tag densities, which could be up to 11,000 within a 20 m radius. Also, it is very immune to multipath fading and permits reliable communication even in high fading scenarios. These capabilities of the chip to effectively handle severe multipath setting make it very suitable for utilization in reflective RF environments. The high data rates allow the chip to keep on-air time short, which helps in saving power. Its low power consumption allows the chip to be operated from a battery for prolonged periods depending upon mode and helps in minimizing system lifetime costs. The chip has a very low silicon area which will allow the implementation of cost-effective solutions for the localisation system and also helps in keeping the sensor node compact in size. The chip supports both two-way ranging and one-way ranging, using time of arrival (TOA) and time difference of arrival (TDOA) methods respectively [11], [14], [15].

Some key advantages of the DW1000 chip from DecaWave have been discussed below [11]:

- Supports precise location of the tagged objects as well as data transfer simultaneously.
- Good range in both line-of-sight and non-line-of-sight scenarios, which reduces amount of infrastructure necessary for system deployment.

- Low chip cost and small PCB footprint aid in cost effective implementation of hardware.
- Its low power consumption reduces the necessity of changing batteries regularly and also curtails system lifetime costs.
- The chip being based on IEEE compliant standards facilitates proliferation.

Some disadvantages of this chip for the motion tracking solutions are:

- The device only has a limited bandwidth of 900 MHz, thus limiting the ultimate precision of range detection (see Section 7.1.2 below).
- Centre frequencies of the chip are limited to the lower part of the UWB band. For motion tracking purposes, the top end of the UWB band is seen to be more suitable as it offers more compact antennas and improved accuracy via the shorter wavelength.

### **7.1.2 Range Estimation Mechanisms**

The DW1000 chip uses a set of three messages to complete two round trip measurements from which the range is calculated. In the two-way ranging algorithm there are two roles, one end is nominated to act as an Initiator, initiating a range measurement, and the other end acts as a Responder (anchor), listening and responding to the Initiator and calculating the range.

A single ranging operation is started by the Initiator sending a poll message addressed to the Responder and notes the send time,  $T_{SP}$ . The Initiator then listens for the response message. When the Responder receives the poll, it notes the receive time  $T_{RP}$  and sends a response message back to the Initiator. The Initiator then receives the response message and sends a final message with embedded transmit and receive timestamps for the poll, response and the final message itself. The Responder uses this information along with its own transmission and reception timestamps to calculate two round-trip times which are then averaged and halved to get the one-hop time-of-flight. The time-of-flight value provides the distance between the Initiator and Responder by multiplication with the speed of light in air [11], [16]. The complete

range estimation mechanism of the DW1000 chip using the two-way ranging algorithm has been illustrated in Figure 7.2.

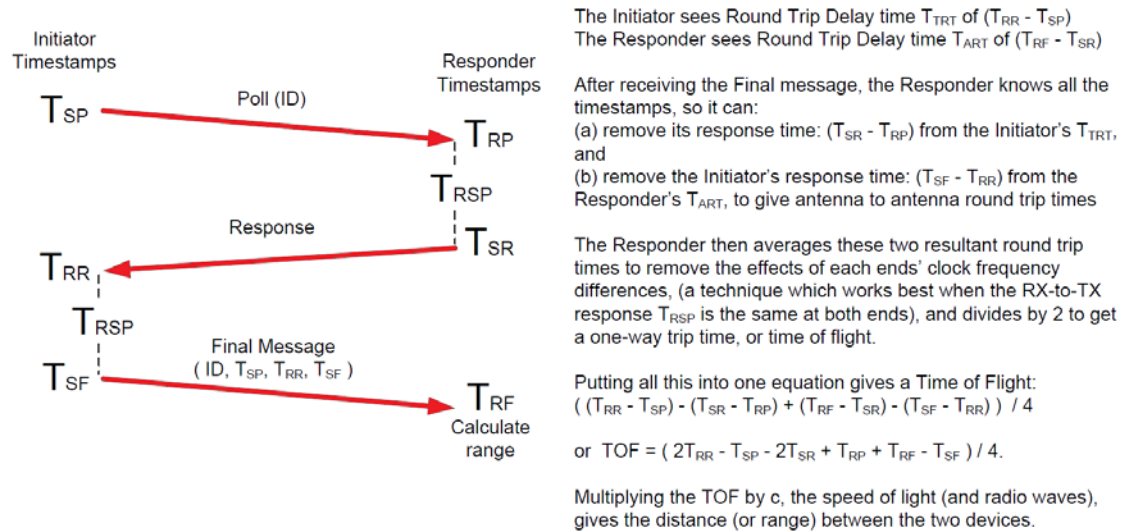


Figure 7.2: Range calculation mechanism of the DecaWave chip using the two-way ranging algorithm [11].

In order to localise a mobile node within an operating space, measurements have to be carried out referenced to a number of fixed base station nodes. In general, at least three base station nodes are required for locating a mobile node in two dimensions and at least four non-coplanar base stations are required for three dimensional localisation of the mobile node. The spacing of the base station nodes in a measurement setup has to be in such a way that all of them are always within the communication range of the mobile node, no matter where it is in the operating area. Using the DW1000 chip, there are two general methods for carrying out three dimensional localisation. These are the time-of-flight and time difference of arrival based methods.

The time-of-flight method in the DW1000 chip entails two-way communication between the mobile tag and each of the anchor nodes. The round-trip time is obtained by the means of periodic message exchanges (as explained above), from which the one-way time-of-flight is calculated between the mobile tag and each fixed anchor. The time-of-flight values are then multiplied by the speed of light, thus providing the

distance between each anchor and the mobile tag. Each of the calculated distance value defines a spherical surface centred on the respective anchor, on which the mobile tag must lie. The intersection of the spheres resulting from the time-of-flight measurements with the four anchors provides the three dimensional location of the mobile tag [11].

For localisation using TDOA method, the mobile tag transmits signals periodically and this signal is received by all the base station nodes in the vicinity. All the base station nodes need to have synchronized clocks so that the arrival time of the transmitted signal from the mobile tag to each base station could be compared. For every pair of base stations, the time difference between the arrival of the signal from the mobile transmitter defines a hyperbolic surface on which the transmitting mobile tag must lie. The three dimensional position of the mobile tag is obtained by the intersection of the hyperbolic surfaces defined by the TDOA values of the received signal at different pairs of base stations.

The TDOA mechanism is beneficial for realisation of a low power localisation system, as the mobile tag needs to send only a single message in order for it to be localised. When using the TDOA scheme, a wired clock distribution could be used to realise clock synchronization of multiple base station nodes. On the other hand, for the TOF scheme, the tag needs to transmit and receive several messages with multiple fixed anchors to be localised successfully. Moreover, the mobile tag needs to know what anchors are in the vicinity so it can address each of them in turn correctly. In the TOF mechanism, there is no requirement for the anchors to be synchronized with each other. Due to lesser number of messages involved, TDOA scheme is a simpler and low power solution as compared to the TOF scheme and is also suitable for applications with high tag density [11].

Time of Arrival (TOA) based measurements provide information about the distance between two nodes by estimating the time-of-flight of a signal that travels from one node to the other. Therefore, a TOA measurement at a node provides an uncertainty region in the shape of a circle. To prevent ambiguity in TOA estimates, the two nodes must have a common clock, or they must exchange timing information via certain protocols, such as the two-way ranging mechanism. The conventional TOA

estimation technique is performed by means of matched filtering or correlation operations. Let the received signal at a node be expressed as

$$r(t) = \alpha s(t - \tau) + n(t), \quad (7.1)$$

where  $\tau$  represents the TOA,  $\alpha$  is the channel coefficient, and  $n(t)$  is additive white Gaussian noise (AWGN). Then, a conventional correlator based scheme searches for the peak of the correlation of  $r(t)$  with a shifted version of the template signal,  $s(t - \hat{\tau})$ , for various delays  $\hat{\tau}$ . Similarly, a matched filter scheme, in which the filter is matched to the signal, estimates the instant at which the filter output attains its largest value. These schemes are optimal for single-path AWGN channels. The accuracy of a TOA measurement can be improved by increasing the SNR and/or the effective signal bandwidth. Since a UWB signal has a very large bandwidth, this property allows highly accurate distance estimation using TOA measurements via UWB radios [1], [17].

On the other hand, TDOA measurements can be obtained even in the absence of synchronization between the target node and the reference nodes, if there is synchronization among the reference nodes. In this case, the difference between the arrival times of two signals travelling between the target node and the two reference nodes is estimated. This locates the target node on a hyperbola, with foci at the two reference nodes.

One way to obtain a TDOA measurement is to estimate TOA at each reference node and then to obtain the difference between the two estimates. Specifically, if the received signals are given by  $r_1(t)$  and  $r_2(t)$  as in equation (7.1),  $\tau_1$  is estimated from  $r_1(t)$  and  $\tau_2$  is estimated from  $r_2(t)$ . Since the target node and the reference nodes are not synchronized, the TOA estimates at the reference nodes include a timing offset in addition to the time-of-flight. As the reference nodes are synchronized, the timing offset is the same for each TOA estimation [1]. Therefore, the TDOA measurement can be obtained as

$$\hat{\tau}_{TDOA} = \hat{\tau}_1 - \hat{\tau}_2, \quad (7.2)$$

where  $\hat{\tau}_1$  and  $\hat{\tau}_2$  denote the TOA estimates at the first and second nodes, respectively.

The TDOA associated with  $BS_i$  is  $t_i - t_1$ ; i.e., it is the difference between the arrival time of the MS signal at  $BS_i$  and  $BS_1$ . Thus, the difference between the distance values can be defined as [5]:

$$\begin{aligned} r_{i1} \triangleq r_i - r_1 &= (t_i - t^0)c - (t_1 - t^0)c \\ &= (t_i - t_1)c \end{aligned} \quad (7.3)$$

It should be noted that these differences do not get affected by the errors in the MS clock time ( $t^0$ ) as it cancels out when subtracting the two time of arrival measurements.

How accurately a TOA estimate for impulse UWB signal can be obtained is quantified by a lower bound, called the Cramer-Rao lower bound (CRLB), which is given by [18]:

$$\sigma_\tau^2 \geq \frac{1}{8\pi^2 \beta^2 SNR} \quad (7.4)$$

where  $\sigma_\tau^2$  represents the variance (equivalently error) of the time of arrival estimate, SNR is the signal-to-noise ratio and  $\beta$  is the bandwidth of the received signal. The CRLB for the ranging distance can be obtained as the product,  $c \cdot \sigma_\tau$  where  $c$  is the speed of light.

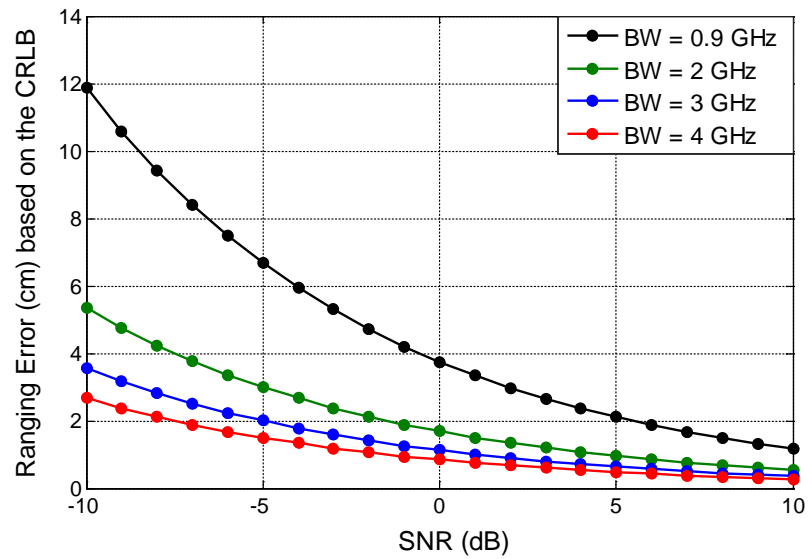


Figure 7.3: Cramer-Rao Lower Bounds on the ranging error in terms of SNR for four different frequency bandwidths.

The CRLB expression indicates that the accuracy of range estimates increases with SNR and the signal bandwidth. Hence, the large bandwidths of UWB signals can facilitate very precise range measurements. Figure 7.3 shows the CRLBs on the ranging error in terms of SNR for the four different bandwidths, 0.9 GHz, 2 GHz, 3 GHz and 4 GHz.

The figure indicates that the theoretical low bounds on the range estimation error are less than 3 cm for the entire range of the investigated SNR (-10 dB to 10 dB) and is less than a centimetre at an SNR of 0 dB when using the bandwidth of 4 GHz. When the TDOA estimates are obtained from the TOA estimates as described in the previous section, the range accuracy limits for such a scenario can be similarly deduced from the CRLB expression in (7.12). Hence, it can be established that the accuracy of TDOA estimation also improves with increase in SNR or the effective bandwidth [17]. The DW1000 chip has a maximum receiver bandwidth of 900 MHz. This constraint of using a limited bandwidth restricted the range accuracy that could be achieved with this chip. Nevertheless, the DW1000 chip was the best available option at the time and was seen as a useful research development tool for this study regardless of its limited receiver bandwidth.

## **7.2 Ultra Wideband 3D Localisation System**

This section provides the details about the base station and mobile tag sensor nodes, which are the core constituting elements of the UWB localisation system. Also, the experimental setup information of the whole system for carrying out various 3D localisation measurements is presented.

### **7.2.1 Base Station and Mobile Tag PCBs**

The UWB localisation system comprised of four base station receivers aligned in a Y-shaped configuration, and a mobile transmitter tag whose position is to be determined. The receivers in the localisation system comprised of the ultra-wideband Vivaldi Antenna (presented in Chapter 6) integrated with the DecaWave DW1000 chip onto a PCB, as an expansion board to implement the base station sensor nodes.

The size of these PCB boards was 27 mm by 30 mm. The PCB carrier board for the DW1000 chip and the hardware interfacing were fabricated in collaboration with *Shadow Robot Company* [19] due to their expertise in circuit building and designing. The datasheet of the DW1000 chip provided by DecaWave was followed in order to build the PCB carrier board [11]. A fabricated prototype of the base station sensor node, along with the Vivaldi Antenna has been illustrated in Figure 7.4.

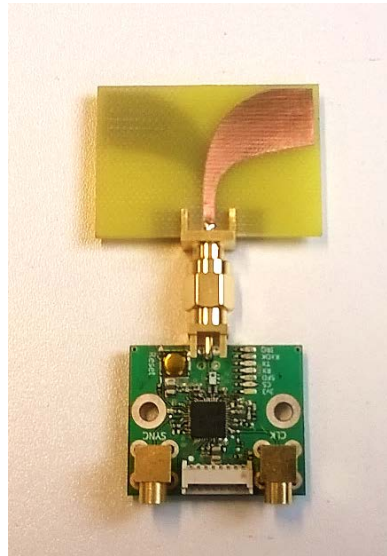


Figure 7.4: Fabricated prototype of the base station sensor node along with the Vivaldi antenna.

The mobile transmitter tag in this prototype localisation system comprised of the miniature UWB antenna (presented in Chapter 4) integrated with DecaWave's EVB1000 board. The EVB1000 is an evaluation board for the DW1000 IC chip supplied by DecaWave, which can be utilized for the development of applications in real time location systems and wireless sensor networks. The evaluation board supports all the features of the DW1000 chip.

The off-board antenna connection in the EVB1000 gives the option to test different antennas. The evaluation board could be configured by means of dipswitch settings to work as a transmitter and controlled by a PC through a USB connection. The EVB1000 board has a size of 7 cm  $\times$  7 cm, equipped with DecaWave's 6 mm  $\times$  6 mm DW1000 chip [20], [21]. One such evaluation board, along with the miniature ultra-wideband antenna has been presented in Figure 7.5.



Figure 7.5: DecaWave’s EVB1000 evaluation board connected to the miniature UWB antenna.

Figure 7.6 shows a block diagram of the prototype UWB localisation system. For clarity, the block diagram of the localisation system shows only two of the four base stations. Each of the four base station nodes is connected to the interfacing circuitry (developed by Shadow Robot Company) via Serial Peripheral Interface (SPI) cables.

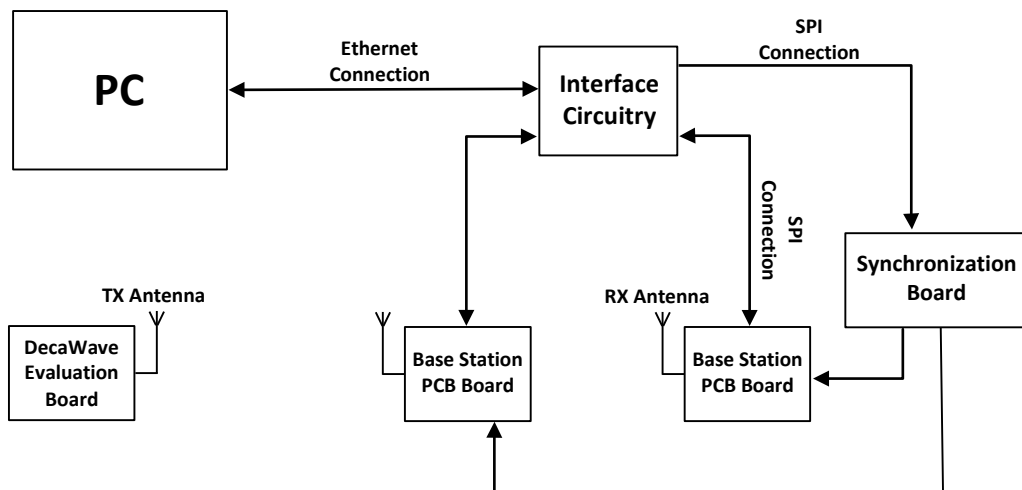


Figure 7.6: Block diagram of the prototype ultra-wideband localisation system (shows just two base stations for clarity).

The interfacing circuit is a hardware platform which allowed the communication and control of the base stations with a PC using the Ethernet port. SPI is a high-speed

interface bus commonly used to send data between microcontrollers and small peripherals such as sensors and shift registers [22]. The synchronization board provides the clock synchronization of the base station nodes through a wired clock distribution. A general outline of the whole system has been discussed here. However, the comprehensive details of the system circuitry are outside the scope of this thesis.

### 7.2.2 Measurement Setup for UWB Localisation System

In the localisation system, time difference of arrival (TDOA) of the signal propagating from the mobile station to the four different base station receivers was used for estimating the mobile station location. Use of TDOA meant that there was no need of synchronization between the mobile station and the base station receivers, as there was synchronization among the clocks of the four base stations. Thus, by using the TDOA approach, the difference between the arrival times of two signals travelling between the mobile node and the two reference nodes was estimated. For this localisation system, the distance between each base station was selected to be 50 cm, aligned in a Y-shaped arrangement. The Y-shaped configuration of the base stations of the UWB localisation system has been illustrated in Figure 7.7.

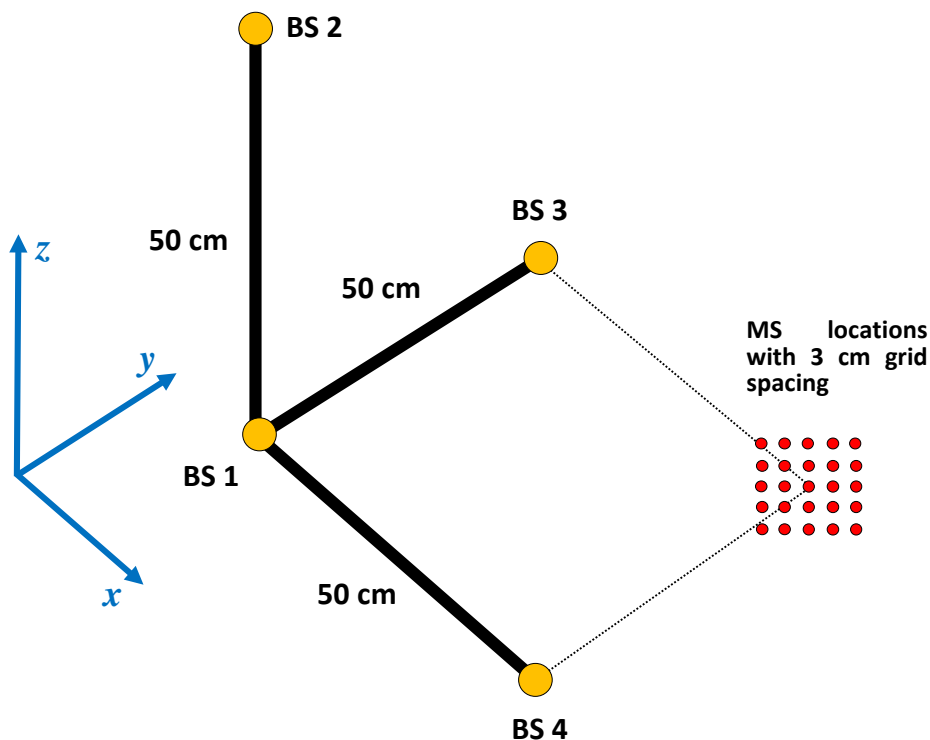


Figure 7.7: Base station receivers aligned in a Y-shaped configuration along with the mobile station positions.

The localisation measurements were carried out inside the Body-Centric Wireless Sensor Lab at Queen Mary University of London. For this, the UWB localisation system was placed on a table surface. In order to make the localisation system physically stable, the base station receivers were fixed on to a wooden frame. This also helped to improve system deployability by reducing the overall setup time for the localisation system and ensured that the base stations remained sturdy during the entire course of the measurements.

A 50 cm by 50 cm square was drawn on the table surface, with three of the four corners of the square been occupied by the base station receivers. The base station antennas were kept about three centimetres above the table top in order to minimize the effect of the table surface on the antennas. The mobile station transmitter was placed near the fourth corner of the square. The measurements were done with the mobile station being moved on a 5-by-5 matrix near the fourth corner of the square created on the table top. Thus, the mobile station was placed at 25 different locations. The matrix had a grid spacing of 3 cm. The actual physical distances between the antennas were measured from their phase centres.

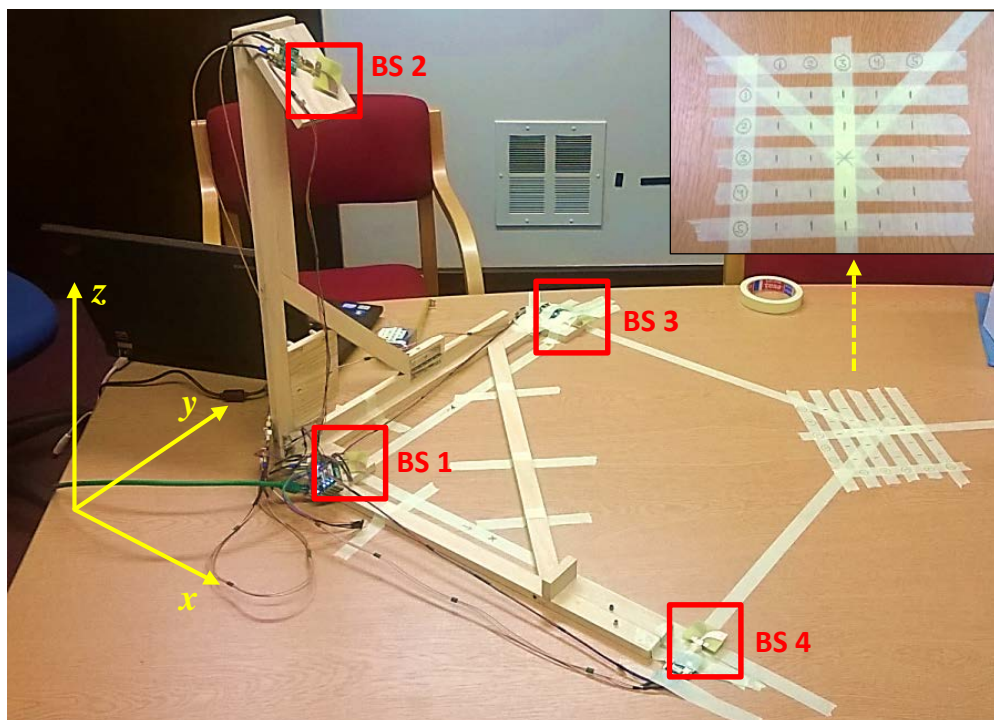


Figure 7.8: Measurement setup of the UWB localisation system placed on top of a table. The 5-by-5 matrix used to place the mobile station is shown in the inset.

Figure 7.8 illustrates a photograph of the measurement setup for the 3D localisation measurements, with the UWB localisation system fixed on top of a table and the 5-by-5 matrix locations used to place the mobile station shown in inset. The matrix point (3, 3) lies on the corner of the 50 cm by 50 cm square created on the table top. The measurements were done using the DW1000 chip's 900 MHz wide frequency channel centred at 6.5 GHz. The localisation system provided the TDOA values between BS<sub>1</sub> and each of the other three base stations, namely BS<sub>2</sub> - BS<sub>1</sub>, BS<sub>3</sub> - BS<sub>1</sub> and BS<sub>4</sub> - BS<sub>1</sub>.

### 7.2.3 Three Dimensional Localisation Method

Let the coordinates of the four base stations (BS<sub>1</sub>, BS<sub>2</sub>, BS<sub>3</sub> and BS<sub>4</sub>) be denoted as  $(x_1, y_1, z_1)$ ,  $(x_2, y_2, z_2)$ ,  $(x_3, y_3, z_3)$  and  $(x_4, y_4, z_4)$  respectively and  $(x_m, y_m, z_m)$  represent the unknown coordinates of the mobile station in a Cartesian coordinate system. Without loss of generality, the origin of the Cartesian coordinate system is set at BS<sub>1</sub>, i.e.,  $(x_1, y_1, z_1) = (0, 0, 0)$ . Let  $r_1$ ,  $r_2$ ,  $r_3$  and  $r_4$  represent the distance between the mobile station and BS<sub>1</sub>, BS<sub>2</sub>, BS<sub>3</sub> and BS<sub>4</sub> respectively. Then, using the distance formula, the following four equations could be obtained

$$r_1^2 = x_m^2 + y_m^2 + z_m^2 \quad (7.5)$$

$$r_2^2 = (x_2 - x_m)^2 + (y_2 - y_m)^2 + (z_2 - z_m)^2 \quad (7.6)$$

$$r_3^2 = (x_3 - x_m)^2 + (y_3 - y_m)^2 + (z_3 - z_m)^2 \quad (7.7)$$

$$r_4^2 = (x_4 - x_m)^2 + (y_4 - y_m)^2 + (z_4 - z_m)^2 \quad (7.8)$$

Equations (7.6), (7.7) and (7.8) can be rewritten in terms of the TDOA measurements  $r_{21}$ ,  $r_{31}$  and  $r_{41}$  (i.e. BS<sub>2</sub> - BS<sub>1</sub>, BS<sub>3</sub> - BS<sub>1</sub> and BS<sub>4</sub> - BS<sub>1</sub> respectively), as

$$(r_{i1} + r_1)^2 = K_i^2 - 2x_i x_m - 2y_i y_m - 2z_i z_m + r_1^2 \quad (7.9)$$

for  $i = 2, 3$  and  $4$ , where

$$K_i^2 = x_i^2 + y_i^2 + z_i^2 \quad (7.10)$$

By expanding and rearranging the terms, these equations can be rewritten in matrix form as

$$Hx = r_1c + d \quad (7.11)$$

where

$$H = \begin{bmatrix} x_2 & y_2 & z_2 \\ x_3 & y_3 & z_3 \\ x_4 & y_4 & z_4 \end{bmatrix}, \quad x = \begin{bmatrix} x_m \\ y_m \\ z_m \end{bmatrix}, \quad c = \begin{bmatrix} -r_{21} \\ -r_{31} \\ -r_{41} \end{bmatrix}, \quad d = \frac{1}{2} \begin{bmatrix} K_2^2 - r_{21}^2 \\ K_3^2 - r_{31}^2 \\ K_4^2 - r_{41}^2 \end{bmatrix}$$

We can rearrange equation (7.11) to solve for  $x$  in terms of the unknown  $r_1$ , to get

$$x = (H^T H)^{-1} H^T (r_1 c + d) \quad (7.12)$$

Substituting this intermediate result into (7.5) leads to a quadratic equation in  $r_1$ . Solving for  $r_1$  and substituting the positive root back into (7.12) gives the final solution for  $x$ .

### 7.3 Three Dimensional Localisation Experiments

This section presents the results of the experiments carried out using the demonstrator UWB localisation system. The mobile station was moved on a 5-by-5 matrix with 3 cm grid spacing. The localisation analysis was carried out with the mobile station placed both in free-space and on the human body. Also, the effect of mobile station orientation and disruption to line-of-sight communication on the localisation results has been studied.

#### 7.3.1 Mobile Tag Placed in Free-space

Firstly, localisation measurements were performed with the mobile station always kept in free-space. The mobile transmitter was placed on each point of the 5-by-5 matrix created on the table surface, thus covering 25 different locations. Figure 7.9 illustrates the measurement setup of the localisation system with the mobile station placed on one of the matrix points in free-space. Actual physical distances were measured from the phase centres of the mobile tag and base station antennas. From this the  $x, y, z$  coordinates were determined and the error table was constructed.

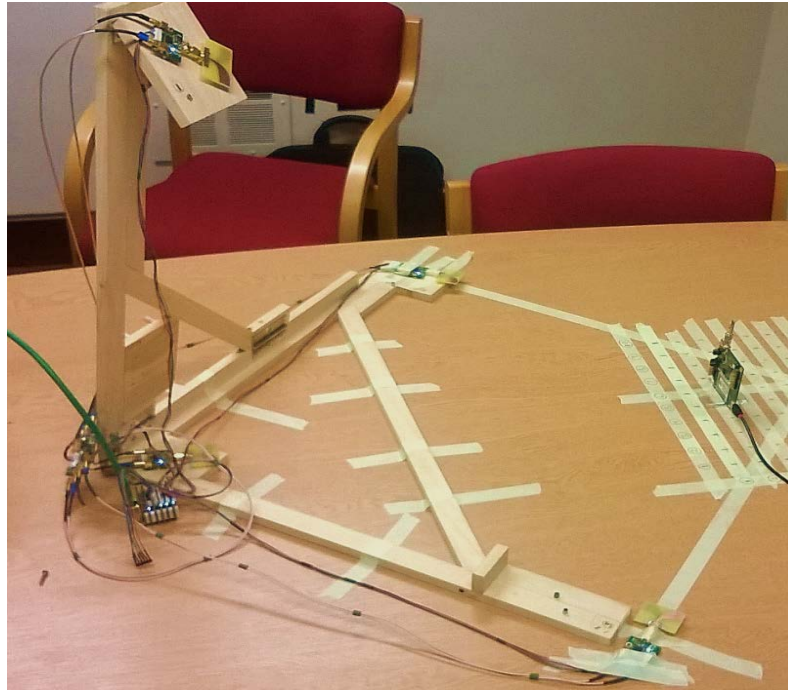


Figure 7.9: Measurement setup for 3D localisation of the mobile station kept in free-space.

The average error values in estimating the  $x$ ,  $y$  and  $z$  coordinates of the mobile tag for each row of the 5-by-5 matrix have been provided in Table 7.1. It could be noticed from Table 7.2 that the localisation error varied between 2 and 7 cm when the mobile tag was kept in free-space. The overall average error in calculating the 3D coordinates of the MS for the  $x$ ,  $y$  and  $z$  axes for all the matrix positions was 2.91 cm, 4.63 cm and 4.68 cm, with a standard deviation of 2.28 cm, 2.64 cm and 2.74 cm respectively.

Table 7.1: Average error in estimating the  $x$ ,  $y$  and  $z$  coordinates of the mobile tag in free-space for each row of the matrix locations.

	<b>Average Error (cm)</b>		
	<b><math>x</math></b>	<b><math>y</math></b>	<b><math>z</math></b>
Row 1	1.84	5.09	5.91
Row 2	2.33	4.44	2.31
Row 3	3.04	4.96	2.08
Row 4	3.22	3.27	6.30
Row 5	4.13	5.41	6.78
Overall Mean	2.91	4.63	4.68
Standard Deviation	2.28	2.64	2.74

### 7.3.2 Mobile Tag Placed on the Human Body

Since the mobile tag was meant to be used while mounted on the human body, further localisation experiments were carried out to take into consideration the impact of human body on the accuracy of the results obtained. For this, the free-space localisation measurements of the previous section were repeated with the mobile tag mounted on the hand of a real human test subject.

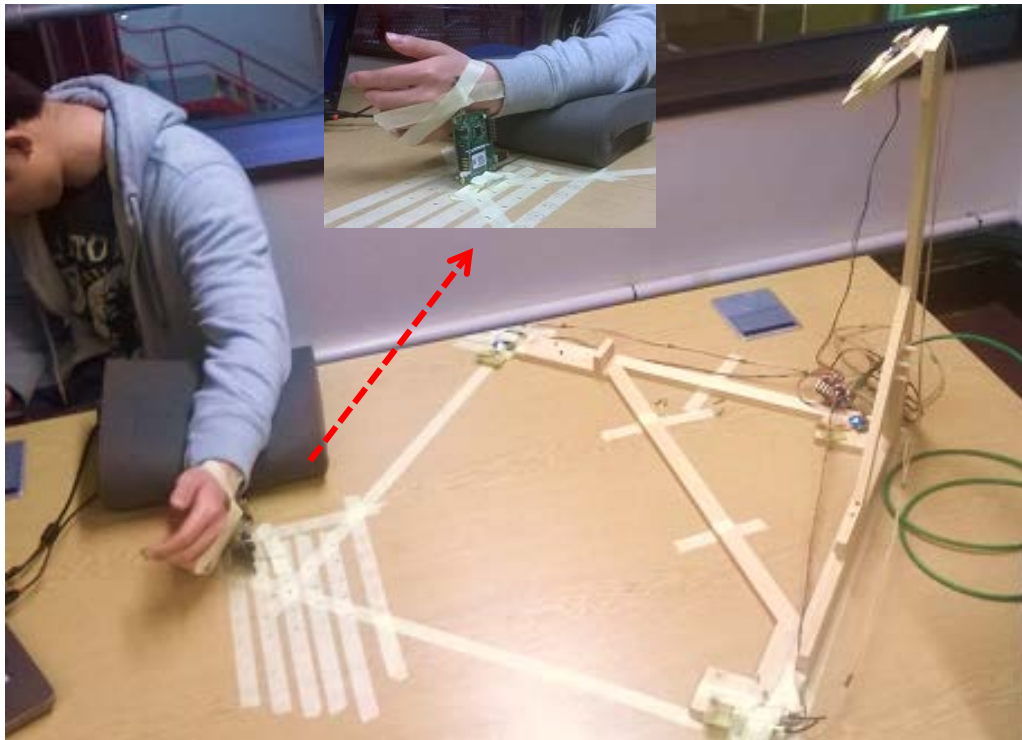


Figure 7.10: Localisation measurements with the mobile tag fixed on the hand of a real human test subject.

A 2 mm thick cotton pad was placed between the antenna and the skin as ‘air gap’. Figure 7.10 illustrates the measurement setup of the localisation system, with the mobile tag attached to the test subject’s hand. The hand-mounted mobile tag was then placed on each point of the 5-by-5 matrix sequentially, to cover each of the 25 different locations. The average error values in locating the position of the body mounted mobile tag for each row of the matrix locations have been provided in Table 7.2. Overall, the localisation error varied between 1 and 5 cm on average, when the mobile tag was mounted on the hand of a human test subject. It could be noticed that placing the mobile tag on the human body did not have any significant impact on

the error values. The localisation error was varying with a similar range of values, both when the mobile tag was kept in free-space and when placed on the human body.

Table 7.2: Average error in estimating the  $x$ ,  $y$  and  $z$  coordinates of the hand mounted mobile tag for each row of the matrix locations.

	<b>Average Error (cm)</b>		
	<b><math>x</math></b>	<b><math>y</math></b>	<b><math>z</math></b>
Row 1	4.18	2.92	0.92
Row 2	2.97	5.03	2.44
Row 3	3.88	3.57	1.89
Row 4	3.60	4.76	3.07
Row 5	2.47	4.71	3.05
Overall Mean	3.42	4.19	2.27
Standard Deviation	2.41	2.58	1.60

For these measurements, the overall average error in estimating the 3D coordinates of the MS for the  $x$ ,  $y$  and  $z$  axes was 3.42 cm, 4.19 cm and 2.27 cm, with a standard deviation of 2.41 cm, 2.58 cm and 1.60 cm respectively. Thus, the presence of human body did not degrade the performance of the system. This could be attributed to the fact that the miniature UWB antenna used in the mobile tag was optimised for on-body use. The antenna had a decent performance even when mounted on the human body. Hence, placing the mobile tag on the hand of the test subject just had a minor effect on the localisation error.

### 7.3.3 Hand Mounted Mobile Tag Tilted by 90°

The free-space and on-body localisation measurements provided in the previous sections were all done with the mobile tag placed erect, i.e. perpendicular to the table surface. An interesting scenario could be to analyse what effect the orientation of the mobile tag has on the localisation results. For this, the mobile tag was tilted by 90° towards one side and fixed on the hand of a human test subject and the same localisation experiment was carried out again. The setup of the mobile tag on a test

subject's hand has been illustrated in Figure 7.11. The hand-mounted mobile tag was then placed on each point of the 5-by-5 matrix again and localisation measurements were performed at each of the matrix points.

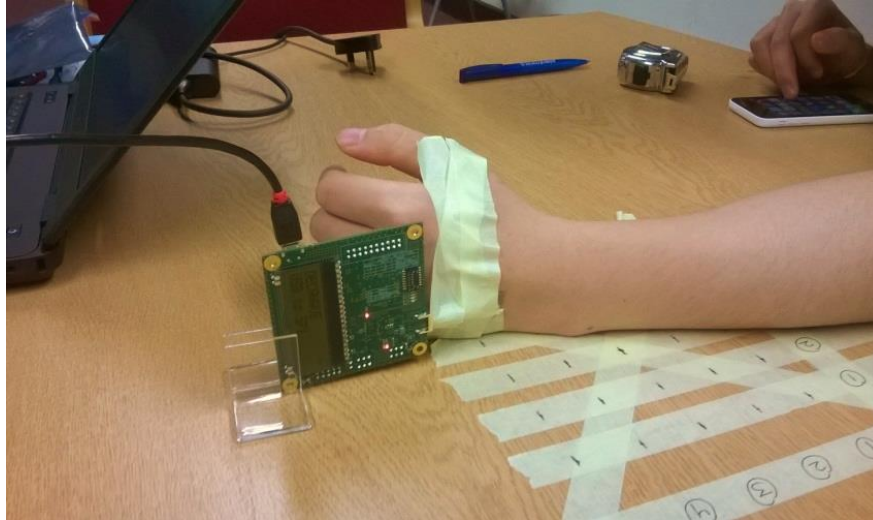


Figure 7.11: Localisation measurements with the hand-mounted mobile tag tilted by 90°.

Table 7.3: Average error in estimating the  $x$ ,  $y$  and  $z$  coordinates of the hand-mounted mobile tag when tilted by 90° for each row of the matrix locations.

	<b>Average Error (cm)</b>		
	<b><math>x</math></b>	<b><math>y</math></b>	<b><math>z</math></b>
Row 1	2.91	1.82	2.33
Row 2	3.85	3.40	3.10
Row 3	2.53	3.34	2.37
Row 4	4.29	7.02	3.85
Row 5	4.91	8.17	6.18
Overall Mean Error	3.70	4.75	3.57
Standard Deviation	2.52	3.32	2.49

Table 7.3 provides the average error values in locating the position of the tilted mobile tag mounted on the test subject's hand, for each row of the matrix locations. It can be noticed from Table 7.3 that the localisation error values varied between 2 and 8 cm on average, when the on-body mobile tag was kept tilted by 90° towards its side. The

overall average error in estimating the 3D coordinates of the MS for the  $x$ ,  $y$  and  $z$  axes was 3.70 cm, 4.75 cm and 3.57 cm, with a standard deviation of 2.52 cm, 3.32 cm and 2.49 cm respectively. Thus, there was a small increase in the localisation error as compared to the localisation results with the mobile tag kept erect. As the mobile tag was moved away from the base station receivers, the localisation error also kept on increasing. This increase in error results from the effect of cross-polarisation between the antennas, leading to a reduction in SNR of the transmission path (*cf.* equation 7.4). Some of this rise in localisation error could be attributed to the influence of the table surface since the mobile tag lies very close to the surface of the table when tilted towards its side.

### 7.3.4 Non-line-of-sight Measurements

The localisation analysis was also carried out taking into consideration the non-line-of-sight situation for the mobile tag. For these sets of measurements, the human hand was placed in front of one of the base station receivers, kept at a distance of 10 cm. The hand acted as an obstruction to the direct line-of-sight communication between the base station BS<sub>4</sub> and the mobile tag.

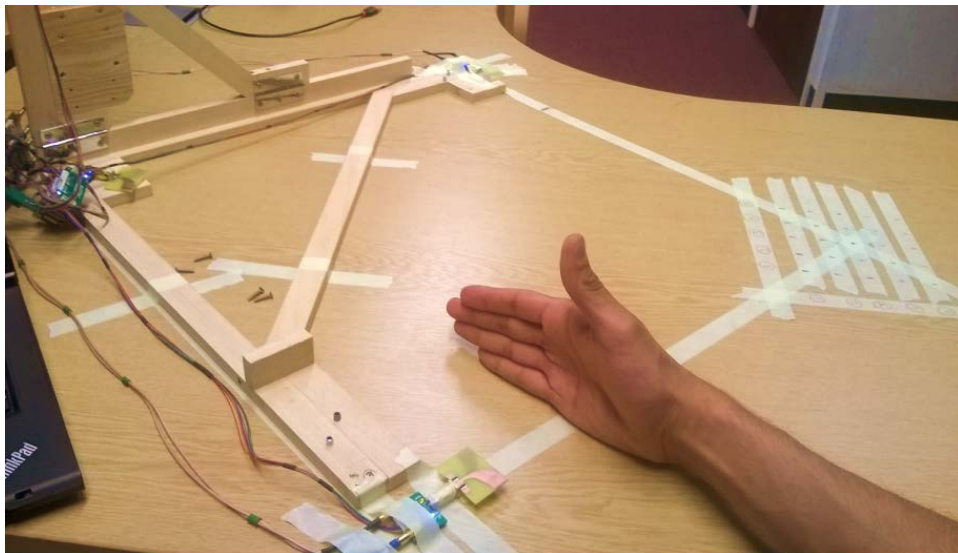


Figure 7.12: Localisation measurements setup with a human hand kept 10 cm away from one base station receiver, blocking its direct line-of-sight communication with the mobile station.

Figure 7.12 illustrates the measurement setup with the hand placed near one of the base station receivers of the UWB localisation system. The mobile tag was fixed on

the hand of a human test subject and kept erect on the table surface, similar to the setup shown in Figure 7.10. The average error values in locating the position of the mobile tag with the hand blocking direct line-of-sight communication of the mobile tag with one base station are provided in Table 7.4.

Table 7.4: Average error in estimating the  $x$ ,  $y$  and  $z$  coordinates of the hand-mounted mobile tag for non-line-of-sight measurements.

	Average Error (cm)		
	$x$	$y$	$z$
Row 1	3.22	2.61	5.29
Row 2	5.38	3.30	4.77
Row 3	9.05	3.37	9.23
Row 4	10.19	4.36	4.20
Row 5	10.49	6.04	2.53
Overall Mean Error	7.67	3.94	5.20

The localisation error values varied between 2.5 and 10.5 cm on average. It could be clearly noticed that placing the human hand in front of BS<sub>4</sub> had an adverse impact on the position estimation of the mobile tag. The overall average error in estimating the 3D coordinates of the MS for the  $x$ ,  $y$  and  $z$  axes was 7.67 cm, 3.94 cm and 5.20 cm respectively. The presence of human hand as an obstruction degraded the localisation results by a few centimetres. This is understandable since the higher relative permittivity and complex electromagnetic properties of human body tissues affect the antenna radiation both in terms of reduced SNR and effective phase velocity in the region of the hand being less than the speed of light, leading to some increase in the localisation error. It can be observed from Table 7.4 that the localisation error increased noticeably for the  $x$ -axis as compared to the  $y$  and  $z$  axes. This could be attributed to the fact that the hand was obscuring the base station which was situated along the  $x$ -axis (i.e. BS<sub>4</sub>), leading to an increased error in estimation of the  $x$ -coordinate of the mobile station.

## 7.4 Summary

In this chapter, experimental and investigational work towards the development of a prototype UWB localisation system has been presented. The operating principles of the localisation system and results of various three dimensional localisation measurements undertaken using the system are provided. Details of the DecaWave DW1000 chip, the core component of this system have been discussed. This work has been undertaken as part of a feasibility study project and the localisation system built acts as a technology demonstrator to highlight the potential of creating a simple and inexpensive standalone system using UWB technology for locating the position of a body-mounted mobile sensor node.

The system was able to estimate the position of the on-body mobile tag with an accuracy ranging between 1 and 8 cm. The overall average error of all the measurement results in Tables 7.1 to 7.3 taken as a single set is 3.8 cm as compared to the overall average error of 0.59 cm obtained from the measurements presented in Chapter 6. Although it has been demonstrated in Chapter 6 that UWB technology has the capability to achieve sub-centimetre level localisation accuracy, the relatively higher localisation error obtained with the prototype system is related to the inherent limitation of the DW1000 chip. As demonstrated through the Cramer-Rao Lower Bound (CRLB) in equation (7.4), the TOA estimation error is directly related to the inverse of the bandwidth. Consequently, the limited receiver bandwidth of 900 MHz available in the DW1000 chip constrained the range accuracy that could be achieved with it. This suggests that a four-fold increase in bandwidth would see the 3.8 cm error reduce by approximately four times to less than 1 cm, confirming the validity of the overall approach. Thus, the feasibility of using Impulse-Radio UWB technique to realise a high-precision location system has been successfully demonstrated. An ultra-wideband chip with a wider operation bandwidth could make full use of the high time-resolution capacity of the UWB pulses and would thus be able to achieve even higher localisation accuracy. The work presented in this chapter has successfully validated that the pulsed UWB technology can be easily utilized to track small movements of human limbs and thus this simple system could be easily scaled up to realise a full body motion tracking system, comprising of multiple body-mounted mobile tags.

## References

- [1] Z. Sahinoglu, S. Gezici, and I. Guvenc, *Ultra-Wideband Positioning Systems: Theoretical Limits, Ranging Algorithms, and Protocols*. Cambridge University Press, 2008.
- [2] G. Villarrubia, J. Bajo, J. F. De Paz, and J. M. Corchado, “Real time positioning system using different sensors,” in *16th International Conference on Information Fusion (FUSION)*, 2013, pp. 604–609.
- [3] Clarinox Technologies Pty Ltd, “Real Time Location Systems.” [Online]. Available: <https://www.nottingham.ac.uk/grace/documents/resources/marketreports/realtimelocationsystems09.pdf>.
- [4] R. Thomä, R. H. Knöchel, J. Sachs, I. Willms, and T. Zwick, Eds., *Ultra-Wideband Radio Technologies for Communications, Localization and Sensor Applications*. Rijeka: InTech, 2013.
- [5] A. H. Sayed, A. Tarighat, and N. Khajehnouri, “Network-based wireless location: challenges faced in developing techniques for accurate wireless location information,” *IEEE Signal Process. Mag.*, vol. 22, no. 4, pp. 24–40, Jul. 2005.
- [6] C. K. Ho, T. S. P. See, and M. R. Yuce, “An ultra-wideband wireless body area network: Evaluation in static and dynamic channel conditions,” *Sensors Actuators A Phys.*, vol. 180, pp. 137–147, Jun. 2012.
- [7] B. Latré, B. Braem, I. Moerman, C. Blondia, and P. Demeester, “A survey on wireless body area networks,” *Wirel. Networks*, vol. 17, no. 1, pp. 1–18, Nov. 2010.
- [8] T. Ye, M. Walsh, P. Haigh, J. Barton, and B. O’Flynn, “Experimental impulse radio IEEE 802.15.4a UWB based wireless sensor localization technology: Characterization, reliability and ranging,” in *22nd IET Irish Signals and Systems Conference*, 2011.

- [9] M. Crepaldi, M. Paleari, A. Bonanno, A. Sanginario, P. Ariano, D. H. Tran, and D. Demarchi, “A quasi-digital radio system for muscle force transmission based on event-driven IR-UWB,” in *IEEE Biomedical Circuits and Systems Conference (BioCAS)*, 2012, pp. 116–119.
- [10] J. R. Fernandes and D. Wentzloff, “Recent advances in IR-UWB transceivers: An overview,” in *Proceedings of IEEE International Symposium on Circuits and Systems*, 2010, pp. 3284–3287.
- [11] “DecaWave DW1000 ScenSor - User Manual,” 2014. [Online]. Available: [http://www.decawave.com/sites/default/files/resources/dw1000\\_user\\_manual\\_2\\_02.pdf](http://www.decawave.com/sites/default/files/resources/dw1000_user_manual_2_02.pdf).
- [12] “ScenSor Radio Communication Products Overview | DecaWave.” [Online]. Available: <http://www.decawave.com/products/overview>.
- [13] “DecaWave ScenSor News | VentureBeat.” [Online]. Available: <http://venturebeat.com/tag/decawave-scensor/>.
- [14] “DecaWave Product Information: DW1000,” 2013. [Online]. Available: <http://www.decawave.com/sites/default/files/resources/dw1000-product-brief.pdf>.
- [15] “DecaWave DW1000 Datasheet,” 2014. [Online]. Available: [http://www.decawave.com/sites/default/files/resources/dw1000-datasheet-v2.03\\_0.zip](http://www.decawave.com/sites/default/files/resources/dw1000-datasheet-v2.03_0.zip).
- [16] “DecaRanging (PC) User Guide,” DecaWave Ltd, 2013.
- [17] S. Gezici and H. V. Poor, “Position Estimation via Ultra-Wide-Band Signals,” *Proc. IEEE*, vol. 97, no. 2, pp. 386–403, Feb. 2009.
- [18] Woo Cheol Chung and Dong Sam Ha, “An accurate ultra wideband (uwb) ranging for precision asset location,” in *IEEE Conference on Ultra Wideband Systems and Technologies*, 2003, pp. 389–393.
- [19] “Shadow Robot Company Ltd.” [Online]. Available: <http://www.shadowrobot.com/>.

- [20] “Product Information: EVB1000,” 2013. [Online]. Available: [http://www.decawave.com/sites/default/files/resources/evb1000-product-brief\\_3.pdf](http://www.decawave.com/sites/default/files/resources/evb1000-product-brief_3.pdf).
- [21] “EVK1000 User Manual,” 2014. [Online]. Available: [http://www.decawave.com/sites/default/files/resources/evk1000\\_user\\_manual\\_v107.pdf](http://www.decawave.com/sites/default/files/resources/evk1000_user_manual_v107.pdf).
- [22] “KeyStone Architecture Serial Peripheral Interface (SPI) User Guide,” 2012. [Online]. Available: <http://www.ti.com/lit/ug/sprugp2a/sprugp2a.pdf>.

# Conclusions and Future Work

## 8.1 Conclusions

Ultra-wideband has emerged as a technology that offers great promise to satisfy the growing demand for low-cost, high-speed digital wireless networks. Accurate determination of the location of wireless sensors forms the basis of many new and interesting applications of UWB. Because of its ultra-short pulses, the Impulse-Radio ultra-wideband (IR-UWB) technology has the ability to be used in high-precision ranging and localisation applications.

This thesis presented the experimental investigations and research studies aimed towards the formulation of new techniques to enable the development of a simple, inexpensive and low cost UWB sensor-based localisation system for human motion tracking. The upper part of the UWB frequency spectrum from 6 GHz to 10.6 GHz was chosen as the operating band since it is less cluttered and provided the required broad spectrum necessary to ensure high accuracy, and also to realise the need for compact antennas and hence compact sensor nodes. IR-UWB has the potential to overcome the limitations of current motion tracking technologies and in the near

future, will lead to the development of more compact, user-friendly and accurate solutions for motion tracking at reasonable costs.

A novel miniature tapered-slot antenna designed for usage in the UWB sensor node has been presented. The antenna has been specifically designed for on-body use and has an overall size of 7.9 mm by 16.38 mm including the antenna feed. The antenna has been investigated in free-space as well as on-body. In addition, an investigational analysis involving different kinds of simplified multi-layered human equivalent phantoms was carried out. This study aimed at understanding which body model provides the simulation results closest to the actual measurements with a real human body without being too demanding in terms of complexity, computation time and resources. It was concluded from the investigations that a flat dispersive body model estimated the antenna impedance bandwidth performance with real human body most truly. It was also established that during the numerical modelling stage, the size of the simplified body models can be reduced to be just slightly bigger than the antenna structure without exhibiting any noticeable changes to the simulation results. The results of this investigation could eventually help in reducing design timescales and development costs of a wearable antenna.

A fidelity analysis of the miniature antenna was carried out using different kinds of input pulses in order to characterise the antenna's overall performance for pulse-based transmission. The effect of the vicinity of the human body on the level of distortion experienced by the received pulse was also examined. It has been concluded that very high pulse fidelity could be achieved if the spectrum of the input pulse was to be fully located within the operating band of the antenna system transfer function. The human body had a limited effect on the pulse fidelity of the miniature UWB antenna. Besides, comprehensive free-space and on-body fidelity patterns of the antenna were evaluated to study the pulse distortion in various spatial directions of the antenna. This analysis demonstrated the capacity of the miniature UWB antenna to achieve very high pulse fidelity in a very wide range of angular directions, which confirmed its suitability for pulse-based systems. Investigations were carried out on the miniature UWB antenna from a system perspective. By using the antenna's measured channel impulse responses, the effect of antenna fidelity on the communication performance of a pulse-based UWB system was examined, based on the BER and

$E_b/N_0$  parameters. It was revealed that the sent data could be retrieved with better accuracy for higher pulse fidelity scenarios.

This thesis also presented an in-depth study involving numerous ranging and three-dimensional localisation measurements using the miniature UWB antenna. The effect of human body, antenna orientation and non-line-of-sight scenario on the estimated range values was investigated. This analysis demonstrated that with the help of UWB technology, range estimates could be achieved with millimetre accuracy in free-space. Variation in antenna's physical orientation and vicinity of the human body had a limited effect on the accuracy of range estimates. The 3D localisation experiments involved using several compact Vivaldi antennas as base station receivers and body-mounted miniature UWB antennas as transmitters. Good uncalibrated localisation accuracy of 1-4 cm has been achieved in these measurements. The ability of UWB technology for achieving high precision localisation was proven by means of this analysis. Moreover, a unique approach of considering the antennas in a localisation system as point sources and making use of their phase centres as reference points, for achieving sub-centimetre localisation accuracy has been presented successfully.

The investigational work towards the development of a prototype ultra-wideband localisation system is also presented in this thesis. The DW1000 chip from DecaWave was identified for utilization in the UWB sensor node. This chip, whilst not fulfilling all the requirements, was seen as a useful research development tool for creating a prototype system. The standalone demonstrator localisation system successfully estimated the position of the on-body mobile tag with an accuracy ranging between 1 and 8 cm. The inherent bandwidth limitation of the DW1000 chip restricts the localisation accuracy that could be achieved using the prototype system. However, the capacity of using IR-UWB technology to achieve sub-centimetre localisation accuracy has been demonstrated in the earlier investigations presented in Chapter 6. The accuracy of a range estimate is directly related to the inverse of the bandwidth. Thus, a suitable UWB chip with a wider operation bandwidth could make full use of the high time-resolution of the UWB pulses and can certainly help in realising high-precision localisation. This work has successfully validated that the Impulse Radio UWB technology can be easily utilized to track small movements of human limbs.

Although more research work is required to apply this technology in clinical practice, the feasibility of the concept has been demonstrated successfully.

## 8.2 Key Contributions

The major contributions of the work presented in this thesis are as follows:

- A novel CPW-fed miniature UWB antenna design has been presented. This unique antenna uses an SMP connector and is small enough that it can fit on a fingertip. To the best of the author's knowledge, this is the smallest planar UWB antenna in the 6 to 10.6 GHz frequency range. The compact size, wideband characteristics and decent on-body performance support the suitability of this antenna for wearable UWB applications.
- An investigational study of utilizing simplified human body phantoms instead of the complicated full body models when designing wearable antennas is provided. This approach could ultimately help to reduce design timescales and development costs of a body-mounted antenna. Actual on-body measurements demonstrated that a dispersive flat body model could estimate the antenna impedance bandwidth performance with the real human body very closely.
- Experimental investigations of the fidelity factor of the miniature UWB antenna have been undertaken. Different excitation pulse types were employed to study the effect of the antenna and the propagation channel on the received pulse quality. The fidelity factor analysis of the antenna has been carried out in both the azimuth and elevation planes, thereby creating complete antenna fidelity patterns.
- The effect of fidelity on the communication performance of an ultra-wideband antenna system has been investigated. To this aim, an impulse-based UWB system incorporating the measured channel impulse response data was modelled. To the author's knowledge, a detailed investigation of the impact of pulse fidelity on a UWB system's communication performance, such as BER has not been reported in the open literature.

- The effect of antenna orientation and the presence of human body on the range estimation accuracy are studied. Various three dimensional localisation experiments of the body-mounted miniature UWB antenna have been carried out by using three Vivaldi antennas as base stations in an L-shaped configuration and making use of time of arrival data fusion techniques.
- The viability of using UWB technology for high-precision 3D localisation is established. Millimetre-level localisation accuracy has been achieved with UWB technology by making use of the phase centre information of the antennas in location estimation. A standalone prototype of a three-dimensional localisation system demonstrating the potential of impulse-radio ultra-wideband technique for precise location of body mounted mobile tags has been developed and tested successfully.

### **8.3 Future Work**

Based on the conclusions drawn and the limitations of the work presented, the following research initiatives could provide prospective progression to the accomplished work in this thesis:

- In order to achieve more accurate localisation, an investigation of the number and spatial distribution of the base station receivers could be undertaken. Also, a study involving the usage of both the base station receivers and the mobile stations on the human body should be carried out for realising a fully wearable and portable limb tracking system.
- Designing and modelling of a more sophisticated impulse-radio communication system using network simulator tools like NS2, Opnet etc. for evaluating the communication performance of an ultra-wideband radio system, in order to more accurately and realistically analyse how well the sent data could be retrieved from a received pulse.
- Synchronization is one of the key challenges when working with ultra-wideband localisation systems. Using the two-way ranging based

estimation of the signal time of arrival could help in removing the need for node synchronization in the system.

- Construction of a prototype three-node system based on the DecaWave chip employing the two-way ranging technique. The system can then be tested on-body for different scenarios of limb movement to further validate the concept.
- An extensive study of non-line-of-sight (NLOS) setting and techniques for its mitigation to obtain accurate three dimensional localisation needs to be undertaken, since NLOS condition is one of the main causes of error in microwave-based localisation.
- Localisation of limbs at various positions and postures of the human body in dynamic as well as static scenarios for different kinds of measurement environments needs to be investigated as they could significantly influence the performance of the localisation system.
- The discussion of Cramer-Rao Lower Bound indicates that bandwidth is the most significant element to influence the accuracy of localisation measurements. Therefore, employment of a better ultra-wideband chip having a wider bandwidth needs to be carried out in the system. Such a chip will make full use of the high time-resolution capacity of the UWB pulses and deliver very precise localisation.
- In the longer term, the IEEE 802.15.6 standard will also be relevant for implementation of this system when chips compliant to this standard will become available. IEEE 802.15.6 is specifically optimised to serve wireless communication needs for ultra-low power devices operating in or around the human body. The standard is designed to compensate the effects of human body on network performance, providing benefits like low power consumption, Quality of Service, high data rate, reliability, interference protection etc., which are essential to address the necessities of WBAN applications.

- Investigation and development of motion interpretation algorithms, involving translation of the acquired spatial and temporal data of the localised body mounted nodes on to a virtual body model for precise reconstruction of body motions. This will require modelling a generic human body model as a set of rotational joints connected by bones, on which inverse kinematics will be used based on the acquired spatial data to estimate the joint angles.